# High-resolution Structured Illumination Solid Immersion Fluorescence Microscopy

**Lin Wang, MSc.**

**Thesis submitted to the University of Nottingham**

**for the degree of Doctor of Philosophy**

**April 2010**

## Contents

## List of Figures

## List of Tables

# Abstract

The use of aplanatic solid immersion lenses (ASILs) made of high refractive index optical glasses provides a route to wide-field high-resolution optical microscopy. Structured illumination microscopy (SIM) can double the spatial bandwidth of a microscope to achieve high-resolution imaging. This research aims to investigate the combination of the ASILs and SIM in fluorescence microscopy, which we call structured illumination solid immersion fluorescence microscopy (SISIM), to pursue a microscopic system with very large numerical aperture and high lateral resolution. The first stage of the research shows the development of solid immersion fluorescence microscopy (SIF) employing an ASIL allows us to obtain a fluorescence microscope with effective numerical aperture of 1.85. The aberration issues, especially chromatic aberration, that need to be circumvented are analysed by both optical simulation and experimental verification. The near-field imaging property is also discussed and demonstrated. Then the SIM using a diffraction grating to generate structured illumination pattern via two-beam interference is developed. Finally, the SISIM system is constructed by combining the structured illumination with the SIF, and an effective numerical aperture of 3 has been obtained. Future developments of the SISIM system to make it achieve higher resolution and suit routine use are proposed. SISIM is a promising high-resolution microscopic technique with extensive potential applications in cell biology.

# Acknowledgements

I would like to acknowledge so many people who helped me accomplish this thesis. First of all, I would like to thank my supervisor, Professor Mike Somekh, for his constant guidance, support and encouragement throughout this research, and for giving me a wonderful opportunity to study in the UK. I would also like to thank my other supervisor, Dr. Mark Pitter, for the tremendous technical guidance on this project. I am also grateful to Dr. Chung W. See for mentoring me with great patience.

I would like to thank every staff and research student in the Institute of Biophysics Imaging and Optical Science (IBIOS). Ken Hsu worked along with me in the investigation on structured illumination microscopy (SIM) and kindly provided me the MATLAB codes for SIM image reconstruction; Jing Zhang helped me work out the correct method to align aplanatic solid immersion lens in an experimental system; Gerard Byrne and Kevin Webb gave me generous help with the biological sample preparation. Other people who I particularly appreciate include Chen Qian, Noah Russell, Yu Huang, Chunhua Li, Jo Richens, Beth Lunt, Tim Smith, Kelly-Ann Vere, and Laura Nightingale. A special thank must be given to Shugang Liu who took care of me all the time. I would also like to thank many people outside the IBIOS who helped

me with this research, especially Dr. Shihong Jiang and Dr. Xuesheng Chen in the Applied Optics Group, and Dr. Jingxian Yu in the School of Chemistry.

I would like to thank Overseas Research Student (ORS) Award Scheme and University of Nottingham for providing me the scholarship, thank School of Electrical and Electronic Engineering for funding my living expenses as well.

I would like to thank my lovely wife, Fang, for leaving behind her relaxing job in China and coming with me to Nottingham. She not only gave me consistent help and support during my PhD study, but also made the last few years a truly wonderful time with her love and company. I wish her all the best with her own PhD study here in Nottingham.

Finally, I would like to thank my parents for believing in me and supporting me in all that I have done. Without their love and support, I could not have made it this far. This thesis is dedicated to them.

# Chapter 1 Introduction

## 1.1 Research motivation

This thesis focuses on the development of hybrid fluorescence microscopy with high lateral resolution based on the combination of solid immersion fluorescence microscopy employing an aplanatic solid immersion lens and structured illumination microscopy.

Fluorescence microscopy is a universal and irreplaceable imaging tool of modern biology and has been made more so by recent progress in immunolabelling such as the advent of the green fluorescent protein (GFP) [1]. However, to observe the detail of each molecule inside an organism by fluorescence microscopy is traditionally regarded as a mission impossible because the diffraction of light makes the structures too blurry to be resolved once they are smaller than approximately half the wavelength of light. This resolution limit determined by the diffraction limit, at 200-300 nm, is nearly two orders of magnitude larger than the size of a typical protein molecule [2]. In the past ten years or so, some practical super-resolution optical microscopic techniques, including stimulated emission depletion (STED) microscopy [3], stochastic optical reconstruction microscopy (STORM) [4] and structured illumination microscopy (SIM) [5] [6], emerged to obtain the resolution surpassing the classical resolution limit. The

development of super-resolution microscopy leads to the rapid emergence of many more new, improved or modified microscopic techniques. Our research on hybrid microscopy based on the combination of SIM and solid immersion fluorescence microscopy (SIF), as one contribution to this rapid growing field, aims to develop a new microscopic technique with lateral resolution down to about 100 nm.

The application of aplanatic solid immersion lenses (ASILs) in non-fluorescence optical microscopy has been investigated in the Applied Optics Group at the University of Nottingham [7] [8]. It turns out it is possible to fulfil wide-field high-resolution imaging by applying an ASIL with a conventional objective lens with moderate numerical aperture. Wide-field high-resolution fluorescence imaging in a microscope applying an ASIL has not been reported, although the application of ASILs in photoluminescence (PL) microscopy has been investigated [9-11]. PL imaging is different from fluorescence imaging because it is label-free and has much narrower radiation spectrum than fluorescence. PL imaging naturally avoids the occurrence of severe chromatic aberration (CA), however CA is a major hurdle to applying ASILs to fluorescence microscopy. The research tasks in this project include the investigation on the application of ASILs in fluorescence microscopy, the implementation of SIM and the combination of SIM and solid immersion fluorescence microscopy (SIF) applying an ASIL.

## 1.2 Thesis structure

This thesis is organised along the following lines.

Chapter 2 describes the fundamental concepts of resolution and aberration in optical microscopy, and reviews two independent high-resolution microscopic techniques – structured illumination microscopy and solid immersion microscopy. We bring out the idea to combine them for the purpose of developing a new type of fluorescence microscopy with high lateral resolution in this chapter.

Chapter 3 presents our investigation on SIF employing an ASIL to fulfil wide-field high-resolution imaging. In this chapter, we describe the design of ASILs, the instrumental realisation of the fluorescence microscopy employing an ASIL and the corresponding high-resolution experimental results. We also analysis and discuss two important topics in connection with the resolution performance of this technique – the aberration issues and the near-field imaging property.

Chapter 4 presents our investigation on SIM. We explain a four-phase-step algorithm used to reconstruct high-resolution images in SIM with a one-dimensional simulation. The key work in this chapter includes the instrumentation of SIM working in one dimension and the acquisition of corresponding experimental results to demonstrate the theory of SIM and the feasibility of our algorithm, which paves the way to the

implementation of the combination of SIM and SIF employing an ASIL happening in the next chapter. Furthermore, we also discuss the artefact issue, especially the artefacts induced by raw image displacements, in SIM.

Chapter 5 presents our research on the combination of SIM and SIF employing an ASIL. The experimental considerations, implementations and results of structured illumination solid immersion fluorescence microscopy (SISIM) are presented in detail. We also discuss the total internal reflection (TIR) illumination intrinsically happening in the SISIM.

Chapter 6 summarises the research contributions with regard to SIF, SIM and SISIM. It also discusses the future work to be carried out in order to obtain higher resolution in SISIM and make this technique more feasible in routine biological research. Total internal reflection fluorescence microscopy (TIRF) applying an ASIL (ASIL-TIRF), as a spin-off from SISIM, is also described.

# Chapter 2 Review

## 2.1 Introduction

This chapter examines fundamental concepts and research related to high-resolution fluorescence microscopy. Firstly, we give a brief description of the history and the common configuration of optical microscopy, with more emphasis on fluorescence microscopy that is the main target in this thesis. Secondly, we present an introduction to the optical resolution that is the key parameter we address in this research. Thirdly, we describe geometrical optical aberrations which directly affect the resolution of an optical microscope. Fourthly, we briefly review current mainstream high/super-resolution microscopic techniques including confocal fluorescence microscopy (CFM), stimulated emission depletion (STED) microscopy, stochastic optical reconstruction microscopy (STORM) and structured illumination microscopy (SIM). Then we particularly stress the theory and development of structured illumination microscopy because it has several advantages which make it superior to other techniques in many ways. After that, we introduce the theory and development of solid immersion lens (SIL) capable of improving the numerical aperture of the system and SIL application in optical microscopy. Finally, we express the concept of combinatorial microscopy and bring out the idea to combine structured illumination microscopy with solid immersion

lens for the purpose of developing a new type of fluorescence microscopy with high lateral resolution, which is the ultimate goal in this research.

## 2.2 Optical microscopy and fluorescence microscopy

Optical microscopy, also referred to as light microscopy, involves passing visible light that is transmitted or reflected from the sample through a single or a group of lenses to allow a magnified view of the sample. Optical microscopy is naturally related to the development of cell biology. In the latest BBC documentary The Cell, the Dutch scientist Anton van Leeuwenhoek (1632-1723) is credited as the inventor of optical microscopy. However, it is believed the English scientist Robert Hooke (1635-1703) was the first to publish work based on the use of an optical microscope in 1665 [12]. Leeuwenhoek used a single lens in his simple microscope, while Hooke developed a rather complete microscope containing two lenses. Leeuwenhoek is considered to have made a greater contribution of the microscopy than Hooke mainly because he has made massive observations on bacteria, plants, blood cells and minerals with his microscope. By 1900 the optics theory and principles of the microscope were well understood and the optical microscopes had become a well-established research tool. Further development in optical and mechanical design and manufacture, together with the development of digital imaging techniques, have led to the modern optical microscopes used as an essential tool in laboratories all around the world.

A conventional compound microscope (Figure 2.2.1) consists of an objective lens and an eyepiece in its basic form. The objective lens produces an inverted magnified image of the specimen. The eyepiece treats this image as an object and images it again with further magnification. Usually a light source is required to illuminate the specimen. Light from the light source, for example a lamp, passes through a condenser and then through the specimen. After that, it is gathered by the objective lens. In an infinity-corrected system, the tube lens gathers the parallel beams of light emerging from the objective and forms the intermediate image as shown in Figure 2.2.2. The objective lens and the tube lens focus the image of the specimen at the front focal plane of the eyepiece. The intermediate image is then imaged by the eyepiece and human eyes.

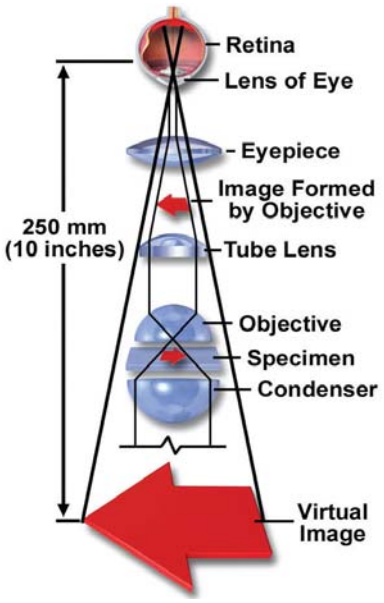


**Figure 2.2.1 Basic configuration of a compound optical microscope [13]**

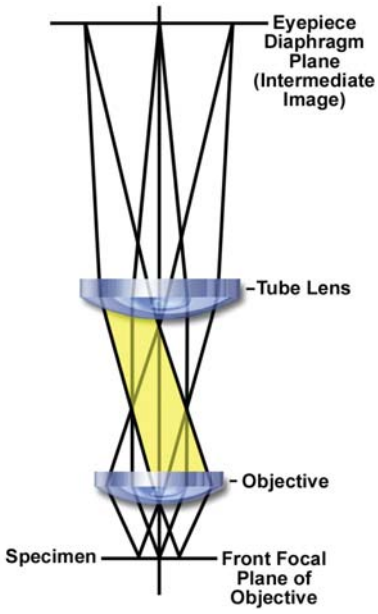


**Figure 2.2.2 Infinity-corrected system [13]**
An infinite conjugate objective is designed to project the image to an infinite distance

In the family of optical microscopy, fluorescence microscopy is a powerful tool to provide internal observation of cells and tissues with exceptional detail. Fluorescence is the effect that some molecules can absorb light of a certain wavelength and emit light at

longer wavelength. The shift of the emission light to longer wavelengths is referred to as Stokes shift [14]. The measure of the emission efficiency of the fluorophore is defined as the ratio of photons emitted to photons absorbed, which is known as quantum yield [14]. An important quenching phenomenon in fluorophores is photobleaching that comes from photon-induced chemical damage and covalent modification. Due to photobleaching, a fluorophore could permanently lose the ability to be fluorescent. On average, a fluorescein molecule will emit 30000-40000 photons during its photochemical life-time [15]. The protection against photobleaching includes eliminating exposure time or excitation energy, or adding antifade reagents to fixed specimens.

Samples that are intrinsically fluorescent or which are coupled to extrinsic fluorescent molecules can be imaged by a fluorescence microscope. The fundamental function of a fluorescence microscope is to deliver excitation light to the fluorophore in the specimen and to separate the much weaker emitted fluorescence light from the brighter excitation light. In this way, only the emitted light reaches the imaging detector and a high contrast dark-field image is generated. The wavelength selection is fulfilled by the combination of excitation filter, dichroic filter and emission filter. A typical epi-fluorescence microscope configuration containing a filter set is shown in Figure 2.2.3. The excitation filter is used to select the excitation wavelength of light from a light source. It can be a short-pass filter or a band-pass filter. When the light source is a laser, it is usually unnecessary to employ the excitation filter. The dichroic filter, usually a long-pass filter, reflects the short wavelength excitation light to the objective. It allows the long

wavelength emitted fluorescence to pass to the detector, but prevents the passage of the shorter excitation wavelength. The emission filter that is usually a band-pass filter specifically selects the emission wavelength of the light emitted from the sample and removes the traces of residual excitation light.

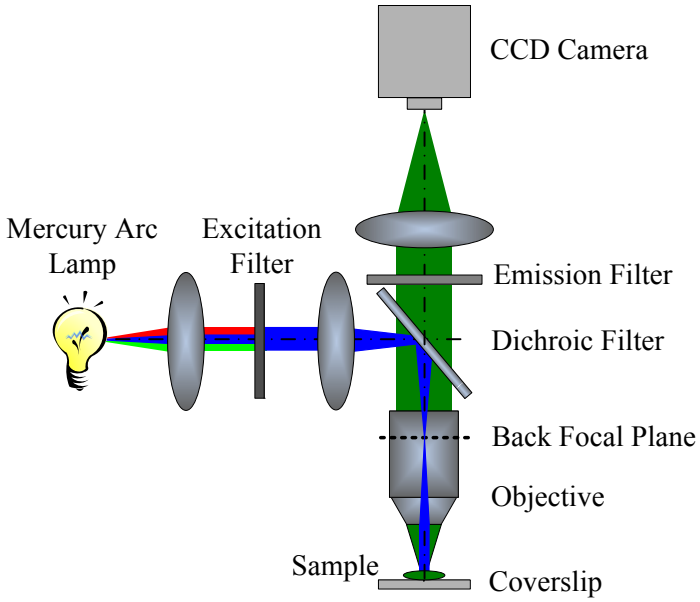


**Figure 2.2.3 A typical epi-fluorescence microscope configuration**
The mercury arc lamp working as a light source emits light with multiple wavelengths; excitation filter is used to separate the excitation wavelength light from the light from the lamp; emission filters is used to isolate the emission wavelength light of fluorophores and residual excitation wavelength light; dichroic filter reflects shorter wavelength light and allows longer wavelength light to pass. The epi-illumination configuration is used to create a dark background so that the fluorescence can be easily seen.

## 2.3 Resolution

Resolution is defined as the smallest distance between two point objects that can be distinguished as two separate objects in an optical imaging system. In a diffraction-limited optical microscope, the image of an infinitely small point object formed on the

image plane is made up of the diffraction pattern of the original object (Figure 2.3.1). This diffraction pattern is known as the Airy disc which can be described by [16]:

$$I = I_0 \left[ \frac{J_1(k \cdot NA \cdot r)}{k \cdot NA \cdot r} \right]^2 \tag{2.3.1}$$

Where $I$ is the intensity distribution, $I_0$ is the intensity at the centre of the pattern, $J_1$ is the first order Bessel function of the first kind, $k=2\pi/\lambda$, $\lambda$ is the wavelength of the imaging light, $r$ is the radial coordinates of the image plane, $NA$ is the numerical aperture of the system that is expressed as:

$$NA = n \cdot \sin u \tag{2.3.2}$$

where $n$ is the refractive index of the medium between the specimen and the objective lens, $u$ is the light collecting angle of the objective lens. The function that describes the distribution of intensity in an Airy disc is called point spread function (PSF). According to Equation 2.3.1, the radius of a PSF is expressed as:

$$r = \frac{0.61\lambda}{NA} \tag{2.3.3}$$

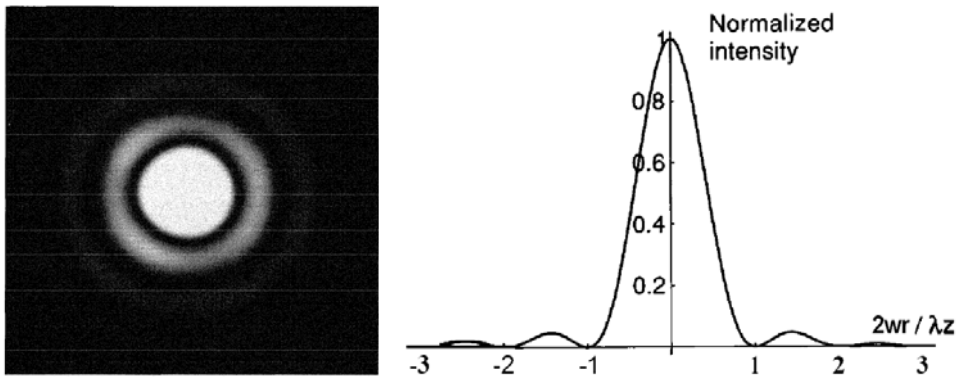


**Figure 2.3.1 Airy disc and its cross-section profile [17]**
w: radius of the circular aperture; r: radius coordinate in the image plane; λ: wavelength; z: normal distance from the object plane to the image plane.

According to Rayleigh criteria [17], when the central maximum of one Airy disc lies over the first minimum of the other, two points that produce Airy discs can just be resolved in the image plane. Under this condition, the distance between the two objects equals the radius of the Airy disc, that is, the resolution is defined as:

$$R = \frac{0.61\lambda}{NA} \tag{2.3.3}$$

When the diffraction patterns of two point objects are just distinguishable, there is a 26.5% dip in intensity between the two diffraction patterns (Figure 2.3.2 right). If their diffraction patterns further overlap and the distance between them becomes less than the Rayleigh criteria, the two objects cannot be distinguished as individual objects. Because the radius of the Airy disc is determined by the objective NA and the wavelength of the imaging light, the higher the NA of the objective, the finer the resolution. A shorter imaging wavelength is obviously beneficial for higher resolution as well.

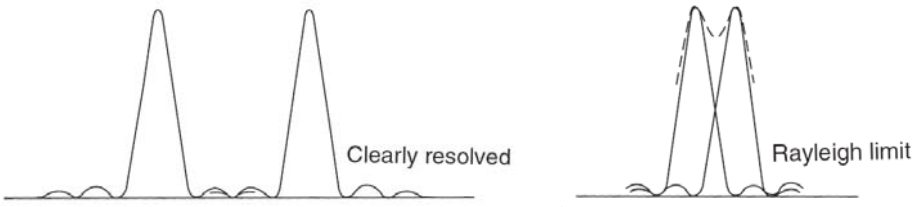


**Figure 2.3.2 The profiles of two Airy discs clearly resolved (left) and just resolved (right) in the image plane as Rayleigh criteria defines [18]**

Besides Rayleigh criteria, another classical resolution criteria is Sparrow criteria [17], which defines when the intensity of the mid-point of two point images has the same value as the peak value of the Airy disc, two points that produce Airy discs can just be

resolved in the image plane (Figure 2.3.3 right). Under this condition, the distance between the two objects is:

$$R = \frac{0.5\lambda}{NA} \tag{2.3.4}$$

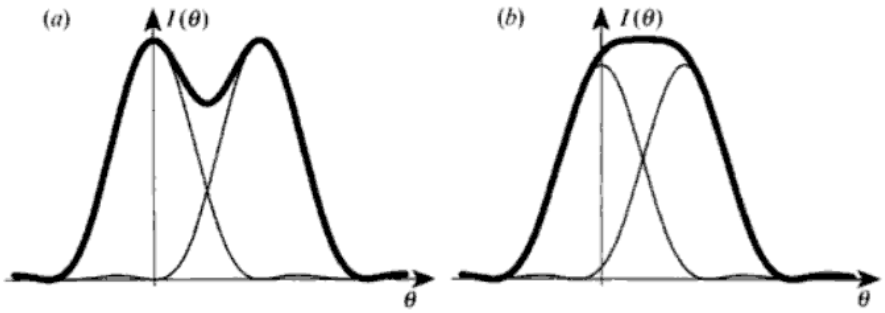


**Figure 2.3.3 Comparison of Rayleigh criteria (left) and Sparrow criteria (right) [19]**

According to the mathematic expressions of these two criterions, it is clear Sparrow criteria leads to a minimum distance that can be resolved 18% smaller than the one defined by Rayleigh criteria, which means the resolution criteria is actually somewhat subjective. A more objective method to define and measure the resolution of an optical microscope is Abbe limit that exactly explains which information component is delivered by a microscope. Abbe limit corresponds to the distance of the finest periodic structure that can be imaged by an optical microscope. If we regard an arbitrary sample as an additive superposition of a lot of periodic structures, as a linear system, an optical microscope will generate an image made up of the sum of these individual images of each periodic structure. The light coming from the sample is required to be collected by the objective lens in order to form the final image. Due to the diffraction, a finer periodic structure will generate the light leaving the sample at a higher angle. However, the aperture of the objective is finite so that it may not be able to collect the light from a

very fine periodic structure. In this way, the aperture of the objective determines the resolution. When the NA of the objective lens is large enough to collect the first order diffraction light of the finest periodic structure (Figure 2.3.4), the spacing in this structure, i.e. the resolution defined by Abbe limit, is:

$$d = \frac{\lambda}{2NA} \tag{2.3.5}$$

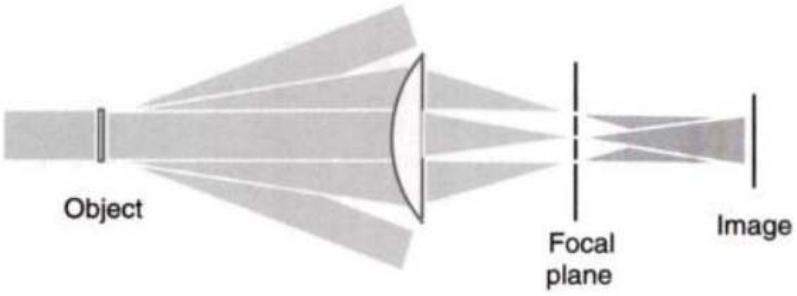


**Figure 2.3.4 Abbe theory of image formation [17]**

Following the Abbe theory of image formation, we can also derive the resolution of a microscope in frequency domain. Different periodic structures, which are made into an arbitrary sample, correspond to different spatial frequency components. The response of an imaging system to different spatial frequency components is known as optical transfer function (OTF). For an incoherent diffraction-limited imaging system, the OTF distribution is like a Chinese hat (Figure 2.3.5). In this case, the cut-off frequency of an OTF is determined as:

$$f_c = \frac{2NA}{\lambda} \tag{2.3.6}$$

which is the reciprocal of the Abbe limit. OTF is substantially the Fourier transform of PSF. Apparently a wider OTF or a narrowed PSF corresponds to a higher resolution.

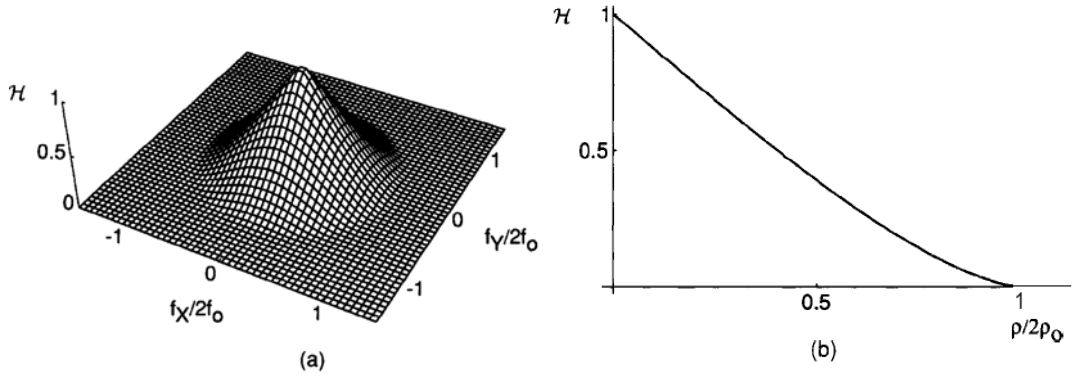


**Figure 2.3.5 The optical transfer function of an incoherent diffraction-limited system [17]**
Three-dimensional plot (left) and half cross-section profile (right). $f_0$, $\rho_0$: cutoff frequency; $\rho$: radial distance in the frequency plane.

The above description on resolution is on the basis of a diffraction-limited system, however, the resolution of a practical optical system is still dependent on aberrations and signal to noise ratio (SNR). We will describe the basic concepts of aberrations in the next section.

## 2.4 Aberrations

For a diffraction-limited optical system, the image-forming characteristics are considered in the paraxial region in which the image is a faithful copy of the object. However, real lenses have finite apertures and fields of view so that their behaviour always deviates from the imaging property in the paraxial region, and this deviation is called aberration. The aberration issues will be extensively discussed in the investigation on the application of solid immersion lens in fluorescence microscopy in

the following chapter, so we describe the concepts of them here clearly for future references.

Aberrations can be measured by the amount by which real rays miss the paraxial image point. For a monochromatic imaging system, generally speaking, there are five types of aberrations which are spherical aberration (SA), coma, astigmatism, field curvature and distortion. When thinking about polychromatic imaging, another aberration called chromatic aberration (CA) turns up.

Spherical aberration is defined as the variation of focus with aperture. In Figure 2.4.1, we can see the rays close to the optical axis come to a focus very near the paraxial focus, while the rays further from the optical axis are brought to a focus away from the paraxial focus. Coma is defined as the variation of magnification with aperture. In Figure 2.4.2, we can see when the oblique rays are incident on a lens with coma, the rays passing through the edge portions of the lens are imaged at a different height than those passing through the centre portion. Astigmatism appears when the tangential and sagittal images separate as shown in Figure 2.4.3. When field curvature is present, all rays will cross at a point along the chief ray which does not lie in the paraxial plane as shown in Figure 2.4.4. When distortion is present, all rays cross at a point in the paraxial plane but not at the ideal chief ray pierce as shown in Figure 2.4.5.

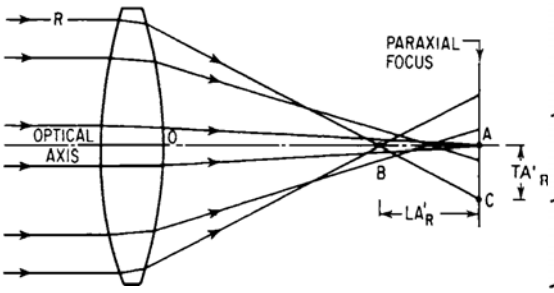


**Figure 2.4.1 Illustration of spherical aberration [20]**
The rays further from the axis are brought to a focus nearer the lens.

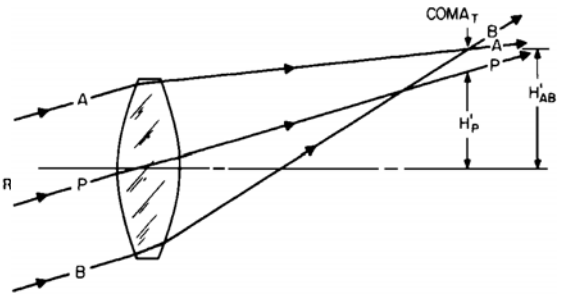


**Figure 2.4.2 Illustration of coma [20]**
The rays through the outer portions of the lens focus at a different height than the rays through the centre of the lens.

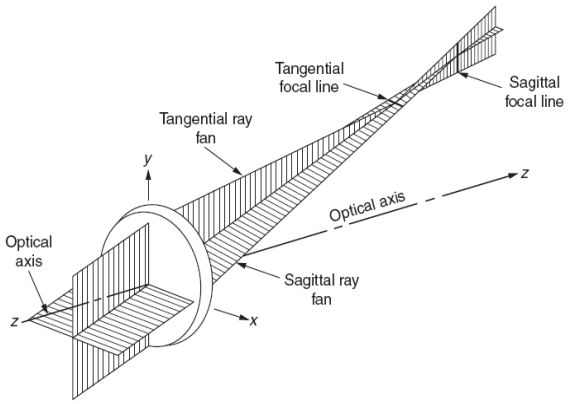


**Figure 2.4.3 Illustration of astigmatism [20]**

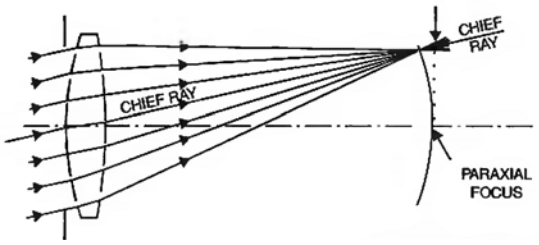


**Figure 2.4.4 Illustration of field curvature [21]**

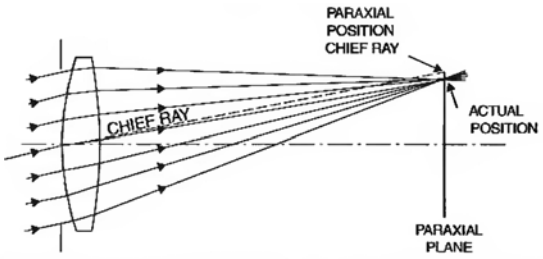


**Figure 2.4.5 Illustration of distortion [21]**

The above is the description of monochromatic aberrations. Since the refractive index of optical glass is a function of the wavelength, the imaging property of a lens also varies with different colours. The refractive index of optical glass is higher for shorter wavelengths, thus the shorter wavelengths is about to be refracted more strongly at lens surfaces. The difference of the focal points for different wavelengths along the optical axis is called axial chromatic aberration as shown in Figure 2.4.6. Similarly, the

difference of the image heights for different wavelengths is called lateral chromatic aberration as shown in Figure 2.4.7.

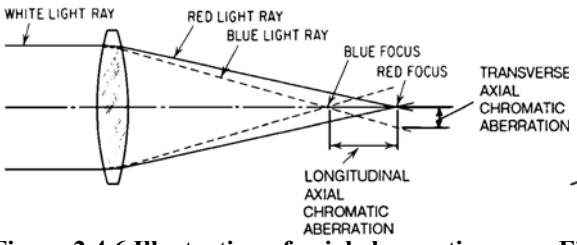


**Figure 2.4.6 Illustration of axial chromatic aberration [20]**

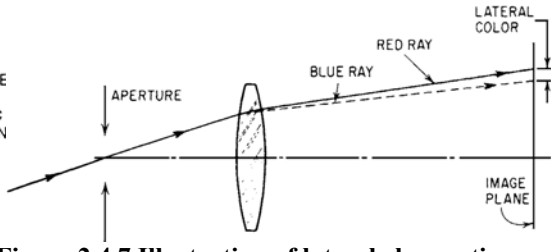


**Figure 2.4.7 Illustration of lateral chromatic aberration [20]**

In a practical optical imaging system, the monochromatic aberrations are usually mixed with chromatic aberrations, which could result in a severely blurred image. In order to achieve high-resolution imaging in an optical system, aberrations in the system must be eliminated or balanced to a negligible level.

## 2.5 High/super-resolution microscopic techniques

The resolution of a conventional optical microscope is limited to about half of the imaging wavelength due to the diffraction of the light. However, with the rapid development in cell biology in recent years, conventional microscopes started to be inadequate when biologists expanded their research on biological processes at the cellular and molecular scales. The increasing requirements for higher resolution urge physicists and engineers to explore new ideas to break the classical resolution limit. Although the physical principle of the light diffraction intrinsically cannot be broken, researchers have found some methods to bypass the resolution barrier, and in this way, a

concept called super-resolution turned up and has been successfully demonstrated in several research groups all around the world in last decade. Not surprisingly, this exciting prospect has driven the Nature journal to choose super-resolution microscopy or nanoscopy as Method of the Year 2008 [22]. In the crowd of high/super-resolution microscopic techniques, the most prominent ones are stimulated emission depletion (STED) microscopy, stochastic optical reconstruction microscopy (STORM) and structured illumination microscopy (SIM). All of these techniques belong to fluorescence microscopy.

The concept of STED microscopy was first presented by Hell and Wichmann in 1994 theoretically [3], and then was experimentally demonstrated in 1999 [23]. In STED microscopy (Figure 2.5.1), fluorescent light coming from the periphery of the focused excitation beam is suppressed by a second laser beam (STED) that depletes the excited state population through stimulated emission. In this way, the PSF of the microscope can be effectively narrowed and the resolution can be increased. STED beam is spatially modulated to be a doughnut shape in which the light intensity is zero in the centre and there is no stimulated emission. The STED beam should possess a high spatial gradient to make the non-depleted area as small as possible. Molecules in the region of zero STED intensity and also in an excited state are left to decay by spontaneous emission. Fluorescence coming from this region can be confined in an area that could be smaller than the diffraction limit, which is the basic principle of STED microscopy to achieve super resolution. STED microscopy inherently is a scanning technique because only one point is examined at a time, and then the focal point needs to be scanned all over the

sample for a wide-field image. The speed of STED microscopy can be improved with multi focal point scanning [2].

Super-resolution microscopy based on single-molecule localisation is enabled by detecting fluorescent emission from a single fluorophore and then determining the molecular position. For a single fluorescent dye molecule, its position can be determined with a precision as high as ~ 1 nm [24]. The localisation-based super-resolution microscopy technique was independently developed and named as stochastic optical reconstruction microscopy (STORM) [4], photoactivated localization microscopy (PALM) [25], and fluorescence photoactivation localization microscopy (FPALM) [26]. In STORM, the imaging area is filled with many dark fluorophores that can be photoactivated by a flash of light. Because photoactivation is stochastic, only a few molecules that are well separated are switched on each time. This process is repeated many times, and finally a super-resolution image is constructed frame by frame (Figure 2.5.2).

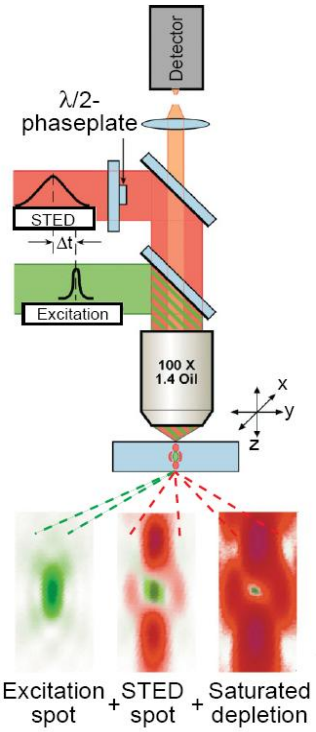


**Figure 2.5.1 Schematic of STED microscopy setup [27]**
Excitation and STED are accomplished with synchronized laser pulses focused by a lens into the sample, sketched as green and red beams, respectively. Fluorescence is registered by a detector. Below, note the panels outlining the corresponding spots at the focal plane: the excitation spot (left) is overlapped with the STED spot featuring a central naught (centre). Saturated depletion by the STED beam reduces the region of excited molecules (right) to the very zero point, leaving a fluorescent spot of sub-diffraction dimensions.

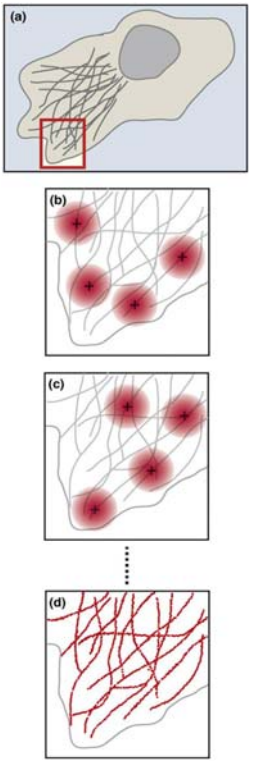


**Figure 2.5.2 Concept of STORM [28]**
(a) Schematic of the structure of interest in a cell labelled with photo-switchable fluorophores. (b) An activation cycle: a sparse set of fluorophores is activated to the fluorescent state, the position of each activated fluorophore is determined by centroid fitting. (c) A subsequent activation cycle: a different set of fluorophores is activated and their positions are determined as before. (d) After a sufficient number of fluorophores have been localized over the course of multiple activation cycles, a super-resolution image is constructed by plotting the measured positions of the fluorophores.

Another promising super-resolution microscopic technique is structured illumination microscopy (SIM) [29] [5] [6]. When a fluorescent sample is illuminated by a structured pattern, the excitation pattern mixes with the spatial information in the sample and shifts high frequency structural information to within the bandwidth of the microscope. SIM effectively expands the transfer function of the conventional microscope and thereby reaches a higher resolution. This method increases the resolution by up to a factor of

two considering excitation wavelength, as the periodicity of the excitation pattern is itself limited by diffraction. When structured illumination is used at saturating intensities, excitation patterns with arbitrarily high spatial frequencies may be generated, extending the resolution of SIM significantly beyond the diffraction limit [30] [31]. Different from STED microscopy or STORM, SIM is totally a wide-field method to fulfil super resolution. A single super-resolution SIM image can be reconstructed by simply capturing several raw wide-field images in a sequence. Among the super-resolution methods described above, SIM is the fastest one to image a rather large field of view. Therefore, we are more interested in this technique. Lateral structured illumination can also be applied to provide optical sectioning that leads to high axial resolution [32] [33]. However, in this thesis, we just concentrate on the development in lateral resolution.

Besides these recently developed super-resolution microscopic techniques, another method capable of obtaining higher resolution than classical resolution limit is confocal fluorescence microscopy (CFM) that first appeared in the late 1970s [34]. In CFM (Figure 2.5.3), the excitation light is a laser beam that is focused to a very tiny point. The emission light is detected through a pinhole located at the image of that point. The final image is built up point by point by scanning either the sample or the excitation beam. This illumination and detection in combination with a linear response of the sample leads to the resulting PSF of the overall system to be the product of the illumination and detection PSFs. Thus, the lateral resolution is improved over that of a conventional wide-field microscope by a factor of about 1.4, although this only occurs if

the pinhole is substantially smaller than the image of the focus point. The increased sectioning ability of confocal microscopes is rather more important and leads to their success.

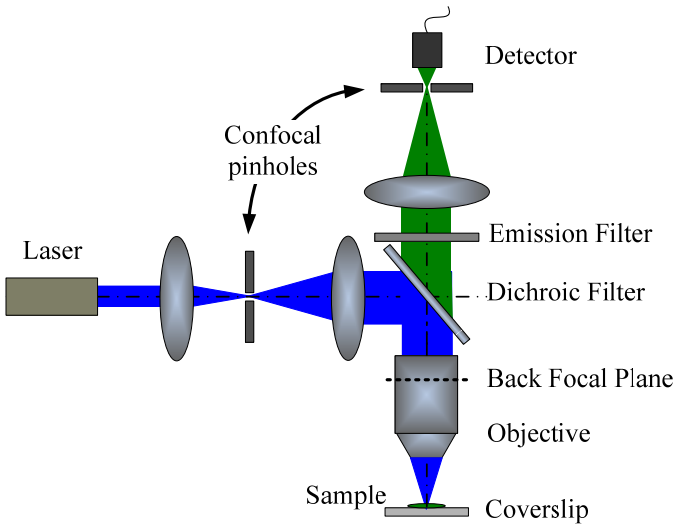


**Figure 2.5.3 Schematic of confocal fluorescence microscopy setup**
Excitation and emission are depicted by blue and green shadings respectively. A fraction of the fluorescence emitted by the fluorophores in the specimen is collected by the microscope objective and imaged onto the detection pinhole in form of a photon detector.

The practical resolution performance of CFM, STED, STORM and SIM nowadays is listed in Table 2.5.1 for comparison.

**Table 2.5.1 Resolution comparisons of high/super-resolution fluorescence microscopy**

| Type | Best (lateral) resolution (nm) | References |
|---|---|---|
| Confocal fluorescence microscopy (CFM) | ~180 | [15] |
| Stimulated emission depletion (STED) microscopy | 5.8 (fluorescent tag: nitrogen vacancies in diamond);15-20 (fluorescent tag: dye) | [35], [36] |
| Stochastic optical reconstruction microscopy (STORM) | ~20 | [4], [37] |
| Structured illumination microscopy (SIM) | ~100 (linear) or ~50 (nonlinear) | [5], [6],[31], [38],[39] |

## 2.6 Structured illumination microscopy

Generally speaking, structured illumination microscopy uses a spatial frequency mixing approach to overcome the classical Abbe limit that defines the resolution of an optical microscope. In SIM, the product of the fluorescent sample and the structured illumination pattern with known spatial frequency is made up of the sum and difference of the spatial frequencies of the sample and structured pattern. In this way, the high frequency information from the fine fluorescent sample is carried in the conventional images from a fluorescence microscope. It is possible to retrieve these high spatial frequencies belonging to the sample from several conventional images by mathematically manipulating the frequency shifts in frequency domain. The physical phenomenon of this frequency mixing can be easily understood in terms of well-known Moiré effect as shown in Figure 2.6.1. When overlapping two fine patterns (Figure 2.6.1 a, b), a rough pattern called Moiré fringes (Figure 2.6.1 c) appears. If we regard the fine patterns with unknown and known spatial frequency as the fluorescent sample and structured illumination pattern respectively, Moiré fringes express the resolvable product of the sample and structured illumination pattern carried in the conventional images.

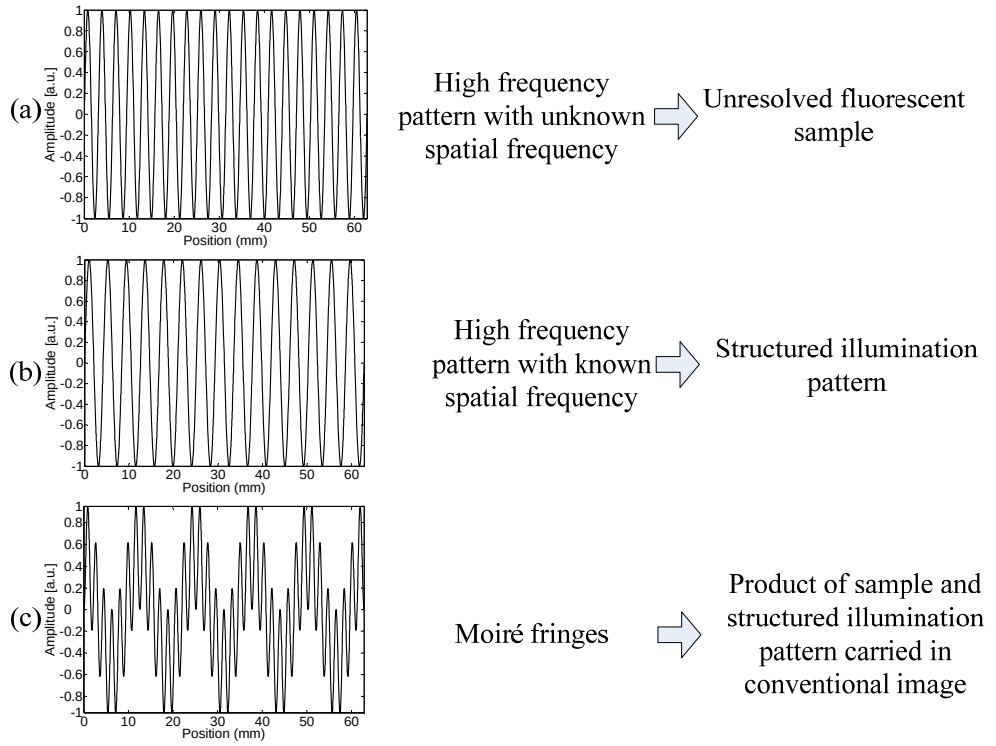


**Figure 2.6.1 Physical phenomenon behind structured illumination microscopy-Moiré effect**

In order to retrieve the high frequency information from the sample, the spatial phase of the structured illumination pattern needs to be altered. The procedure of altering the spatial phase of the illumination pattern is called phase stepping. The resolution enhancement in SIM happens in the direction of phase stepping, i.e. the direction perpendicular to the grid stripes used as structured illumination pattern. The number of phase alteration steps is dependent on the algorithm used to restore the original sample. In one dimension, it could be three steps or four steps, from which three or four conventional raw images are obtained. To fulfil two-dimensional image reconstruction, the phase stepping needs to be implemented in at least three directions to acquire all the necessary information in two dimensions.

The best resolution enhancement performance of SIM is doubled resolution in terms of excitation wavelength compared with the original conventional microscope, which happens when the spatial frequency of the structured illumination pattern is approaching the bandwidth of the conventional microscope defined by the excitation wavelength and numerical aperture. The spatial frequency of the structured illumination pattern itself is still limited by the diffraction limit of the conventional microscope.

The concept of using structured illumination to achieve a resolution exceeding the classical resolution limit was first proposed by Lukosz and Marchand in 1963 [40] and further explained in 1966 [41]. In 1998, Heintzmann and Cremer presented the idea to use a diffraction grating to improve the lateral resolution of a microscope [29]. The first experimental demonstration of SIM was performed by Gustafsson in 2000 [5] [6]. In his system (Figure 2.6.2), a multi-mode optical fibre delivers scrambled 532 nm laser beam. The collimated linearly polarised light is directed to a phase grating, which diffracts the beam into a large number of orders. Only ±1 orders are used; all other orders are blocked. The phase grating is located on a piezoelectric translation stage, which in turn is mounted on a rotation stage. The ±1 order beams are focused so as to form images of the fibre end face near opposite edges of the rear aperture of the objective lens. The resulting structured illumination pattern is a set of parallel lines of period 0.23 μm that is approaching the theoretical resolution limit of the objective. In this system, lateral resolution exceeding the classical diffraction limit by a factor of two was achieved. After that, Gustafsson and co-workers continuously develop the SIM. In 2005, they introduced nonlinear high frequency harmonics into the SIM and accomplished 5.5-fold

improvement of lateral resolution with saturated structured illumination [31]. In 2008, they used a grating to generate three mutually coherent light beams which interfere in the specimen to form an illumination pattern that varies both laterally and axially (Figure 2.6.3). In this way, they achieved three-dimensional doubled resolution approaching 100 nm laterally and less than 300 nm axially by structured illumination [38] and successfully applied 3D SIM in the observation of the nuclear periphery [39]. They also combined SIM with $I^5M$, a well established high axial resolution microscopic technique, to form a microscope called $I^5S$ to yield 3D imaging resolution in the 100 nm range (Figure 2.6.4) [42]. The imaging speed of SIM was also improved recently by applying liquid crystal on silicon spatial light modulator to produce structured illumination pattern. They demonstrated a high-speed SIM by video imaging of tubulin and kinesin in living cells [43] [44].

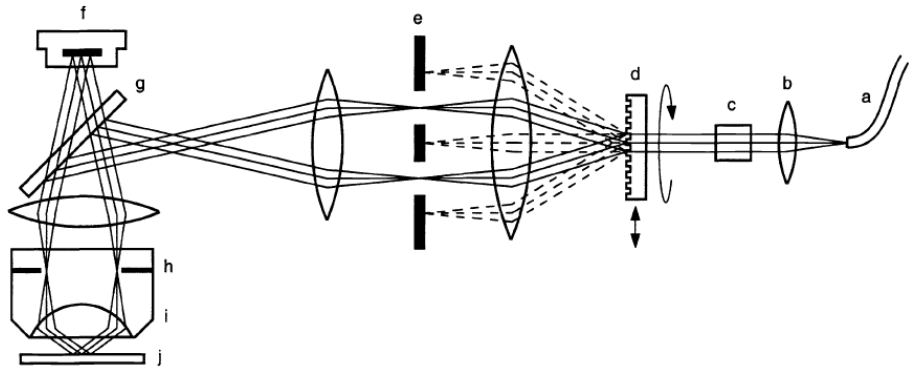


**Figure 2.6.2 Schematic of the structured illumination system [6]**
(a) Multi-mode optical fibre from light source, (b)collimation lens, (c) linear polarizer, (d) phase grating, (e) beam block for order selection, (f) CCD camera, (g)dichroic mirror, (h) back focal plane aperture of objective, (i) objective lens, (j) sample.

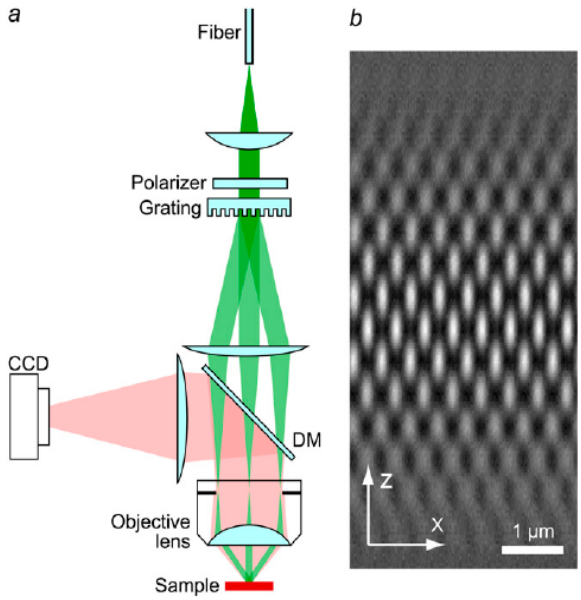


**Figure 2.6.3 Simplified diagram of the 3D structured illumination apparatus (a) and the intensity pattern with both lateral and axial structure (b) [38]**
In (a), laser light from a multimode fiber is collimated onto a linear phase grating. Diffraction orders –1, 0 and +1 are refocused into the back focal plane of an objective lens. The beams, recollimated by the objective lens, intersect at the focal plane in the sample, where they generate an intensity pattern with both lateral and axial structure (b). Emission light from the sample is observed by a CCD camera via a dichroic mirror (DM).

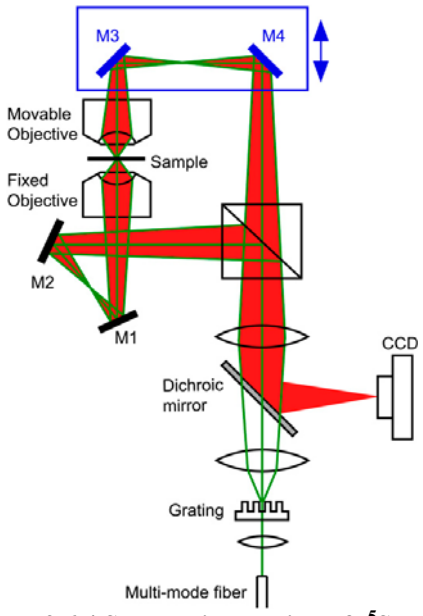


**Figure 2.6.4 Schematic drawing of I$^5$S microscope [42]**
The illumination light passes firstly through a transmission grating, which diffracts it into three beams (green lines), and then through a beam splitter, which splits each beam and directs three beams to each of the two opposing objective lenses. The same beam splitter combines the two beams of emission light (red) from the sample onto the camera. The movable objective lens can be positioned in X, Y, and Z with respect to the stationary objective lens. Mirrors M3 and M4 can be translated together to adjust the path-length difference. The grating can be rotated and laterally translated to control the orientation and phase of the illumination pattern.

SIM is also developed in other research groups under different names, such as harmonic excitation light microscopy (HELM) [45-47], standing-wave total-internal-reflection fluorescence microscopy (SWTIRF) [48-51], laterally modulated excitation microscopy or patterned excitation microscopy [29] [30] [52] [53].

SIM is not only capable of operating in far-field fluorescence microscopy, but also capable of working in near-field fluorescence microscopy by contacting the physical

device used to generate structured illumination to the sample. The benefit of near-field SIM is a greater degree of resolution enhancement than the far-field cases can be achieved because the periodicity of the near-field device is not limited by the diffraction through the illuminating optics. Sentenac *et al.* proposed to illuminate the fluorescent sample by a sub-diffraction light grid generated by a periodically nano-structured substrate [54], as shown in Figure 2.6.5. The periodic substrate, i.e. the near-field grating, generates a high-frequency light grid that changes when the azimuthal incident angle of the illumination beam is varied. The sample is illuminated with different angles of incidence, and an appropriate reconstruction scheme is used to restore the distribution of fluorescence density from a series of images recorded by the microscope. The resolution performance in this technique is limited by the period of the near-field grating. The optimisation process of the grating was also discussed in the authors' another paper [55].

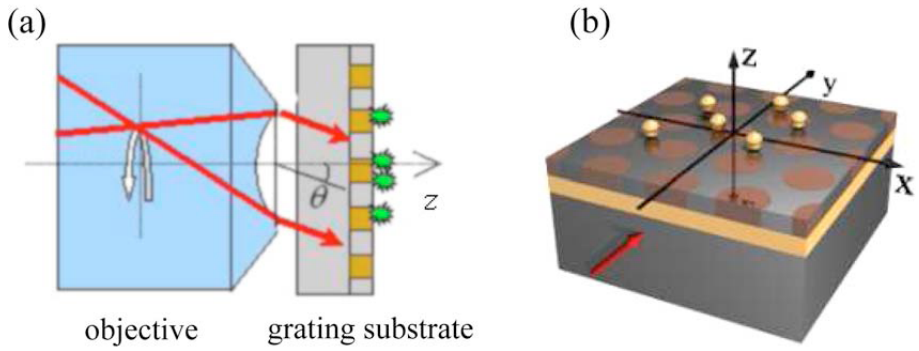


**Figure 2.6.5 Schematic of the periodically nano-structured substrate for high-resolution imaging [54]**
(a) The fluorescent sample is deposited on a grating that is illuminated by a plane wave in total internal reflection configuration. The fluorescence is collected through the same objective. A total of 24 images are recorded by successively illuminating the sample under different incident angles. (b) Three-dimensional diagram of the grating substrate.

Another technique developed by the researchers in the Applied Optics Group at the University of Nottingham makes the grating contact to the sample as well [56]. It employs an array of elongated nano-particles as a physical grating placed close to the sample. The localised surface plasmon resonance of the array is dependent on the illumination polarisation. By arranging the particle orientation to vary with position the grating can be moved by changing the input polarisation, then the spatial phase can be changed. Moreover, the near-field grating is combined with a conventional diffraction grating, as shown in Figure 2.6.6, to perform an even larger resolution enhancement. This double-grating structured-illumination microscope (DGSIM) can potentially extend the bandwidth of the conventional microscope by a factor of 5.

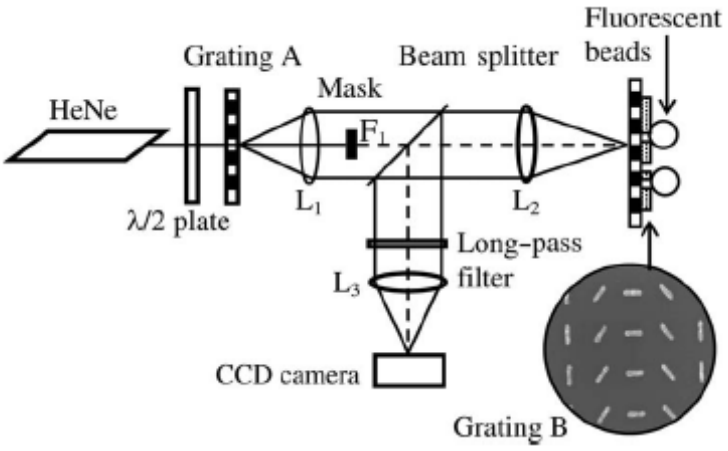


**Figure 2.6.6 Schematic of the DGSIM setup [56]**
Grating A: conventional diffraction grating; Grating B: near-field grating that is an array of elongated nano-particles; inset: micrograph of the near-field grating, period = 1μm.

SIM is one of the most prominent super-resolution microscopic techniques nowadays, therefore a lot of technical details of it have been investigated, such as the methods and apparatus to generate structured illumination [57-59] [54] [60] [55] [61] [56]; the effects of inhomogeneous fields in SIM [62] and the way to tackle it [63]; image reconstruction

and artefact analysis in SIM [64-66]. SIM is also combined with other optical techniques for certain imaging function, which leads to structured illumination confocal scanning microscopy (SICSM) [67], endomicroscopy with structured illumination [68], nanoprofilometry using structured illumination [69].

## 2.7 Solid immersion microscopy

Different from the ideas to bypass the classical resolution limit as SIM, the other way to improve the resolution of an optical microscope is to physically enlarge the NA. A well-developed technique based on this idea is liquid immersion objective. By filling the gap between the sample and the objective with liquid, the system NA can be increased thanks to the higher refractive index of the liquid medium compared to that of the air. The liquid immersion idea was first proposed in as early as the 17th century by Robert Hooke [7]. In 1840, an Italian scientist Giovanni Battista Amici invented the first oil immersion objective [7]. Amici is also considered to be the inventor of the water immersion objective [70]. Around the middle to late 20th century, many optical companies like Edmund and Carl Zeiss started to produce liquid immersion objectives. In modern optical microscopes, liquid immersion objectives have been widely used to obtain high NA and resolution. Currently, the highest NA achieved by an oil immersion objective is 1.65 [71] from the optics company Olympus. The idea to use high refractive index medium certainly can be extended from liquid to solid materials, as shown in Figure 2.7.1. Generally speaking, solid materials have higher refractive indices than

those of liquids, which means a higher NA and resolution could be achieved by using solid immersion medium.

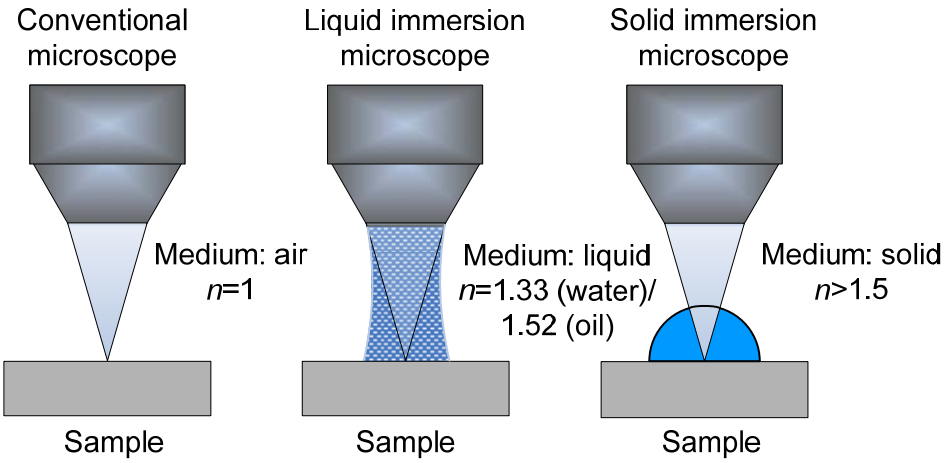


**Figure 2.7.1 The development of immersion medium in optical microscopy**
(a) conventional microscope, immersion medium: air; (b) liquid immersion microscope, immersion medium: liquid (usually water or immersion oil); (c) solid immersion microscope, immersion medium: solid material.

A lens made of a solid material that is used to improve the NA of an optical microscope is known as solid immersion lens (SIL) [7]. In a traditional view, there are two types of SILs according to their outer shapes, which are hemisphere SIL (HSIL) and aplanatic SIL (ASIL) [72]. When combining a SIL with conventional optical microscopy, a new microscopic technique called solid immersion microscopy is formed. The combinations of two types of SILs with a conventional objective, named as SIL-objective, are shown in Figure 2.7.2. For an HSIL-objective, the effective NA is increased by a factor of $n$, here $n$ is the refractive index of the HSIL material, compared to the NA of the conventional objective lens applied here, according to the definition of numerical aperture. For an ASIL-objective, the effective NA is increased by a factor of $n^2$, because not only the wavelength in the ASIL is reduced by a factor of $n$ due to the high

refractive index of the ASIL material, but also the beam from the sample is refracted at the curved surface of the ASIL.

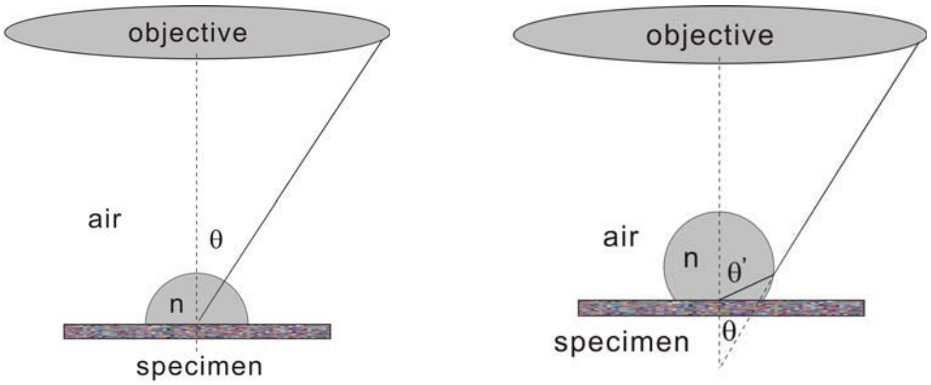


**Figure 2.7.2 SIL-objective configuration by employing a hemisphere SIL (left) and an aplanatic SIL (right) [7]**

The first solid immersion microscopy was reported by Mansfield and Kino in 1990 [73, 74]. In their configuration (Figure 2.7.3) they employed an HSIL, made of glass with refractive index of 1.92 at 436 nm, with a 100×, 0.8 NA objective lens. By scanning the sample, they demonstrated the resolution improvement by a factor of two over a confocal microscope according to the edge response of 100 nm lines. From then on, many scanning microscopes based on HSILs were developed [75-79]. In 1994, Terris *et al.* applied an ASIL in a microscope (Figure 2.7.4) to fulfil near-field optical data storage [72]. Their ASIL was made of high index glass LaSFN9 ($n_{780nm}$ = 1.83) and worked under the wavelength 780 nm with a 0.6 NA objective, accordingly they achieved a 317 nm spot size. In 1997, Stotz and Freeman reported an ASIL-based high-resolution scanning microscope (Figure 2.7.5) [76]. They applied an ASIL, made of glass LASF9 with refractive index of 1.887 at 441.6 nm, with a 0.55 NA objective to achieve a resolution of λ/2.2. Scanning microscopes employing ASILs were also investigated in other forms [80-85]. Also in 1997, Sasaki *et al.* applied an ASIL in

wide-field photoluminescence (PL) microscopy to image patterned GaAs quantum wells [9]. With the help of a 750 μm diameter ASIL made of TaF-3 glass ($n_{587.6nm}$ = 1.8) and a 0.55 NA objective, an effective NA of 1.25 was realised. After that, the application of ASILs in wide-field PL microscopy continued in Sasaki's research group [10] [11]. The application of HSILs in a non-scanning wide-field fluorescence microscope (Figure 2.7.6) was developed by Wu *et al.* in 1999 [86] [87]. They realised a NA of 2 by employing a gallium phosphide ($n$ = 3.42 at wavelength 560 nm) HSIL with a 0.8 NA objective. Zhang *et al.* theoretically and experimentally studied the performance of an ASIL in a non-fluorescence wide-field microscope (Figure 2.7.7) during her PhD study finished in 2006 [7] [8], and they proved solid immersion microscopy employing an ASIL performs much better than the system employing an HSIL in terms of both the spatial resolution and the valid field of view (FOV). At around the same time, Ippolito *et al.* compared the performances of HSILs and ASILSs theoretically [88] [89] and obtained similar results as those of Zhang. Therefore, it is promising to apply an ASIL in fluorescence microscopy in order to achieve wide-field high-resolution imaging. As far as we know, wide-field high-resolution fluorescence imaging in an optical microscope applying an ASIL has not been reported, although the improved fluorescence collection efficiency in a microscope with the help of an ASIL was studied by Yoshita *et al.* [90] and Zwiller *et al.* [91] independently in 2002.

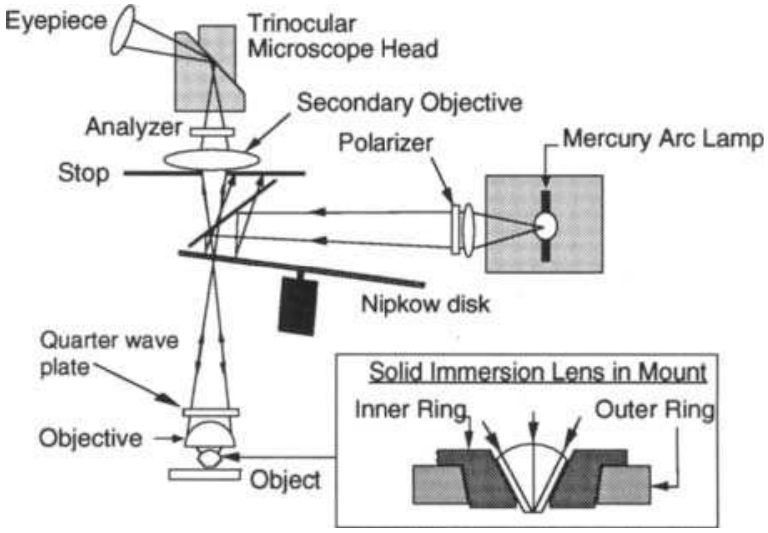


**Figure 2.7.3 Schematic of the scanning microscopy employing an HSIL and the mounting apparatus for the HSIL (inset) [73]**

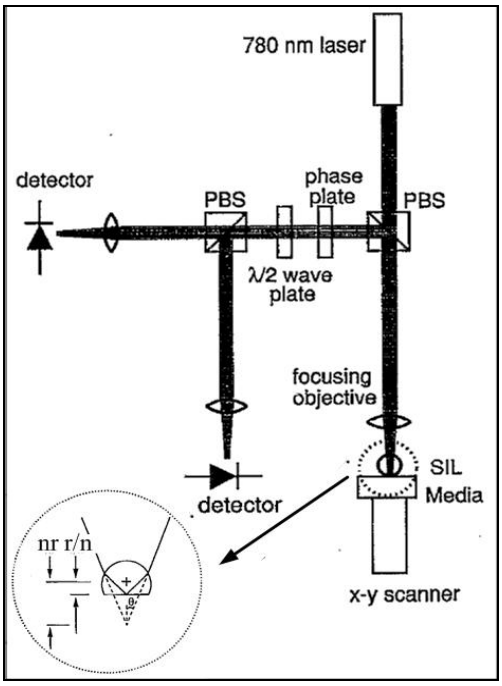


**Figure 2.7.4 Schematic of the optical storage setup employing an ASIL [72]**

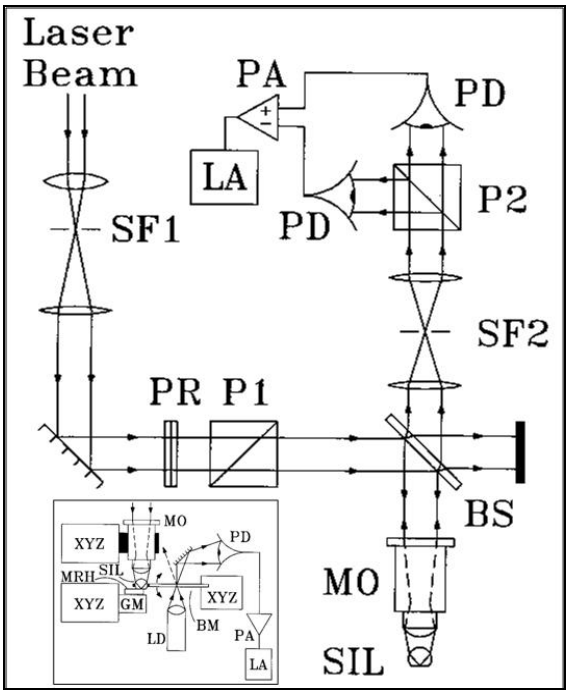


**Figure 2.7.5 Schematic of the scanning microscopy employing an ASIL and the mounting apparatus for the ASIL (inset) [76]**

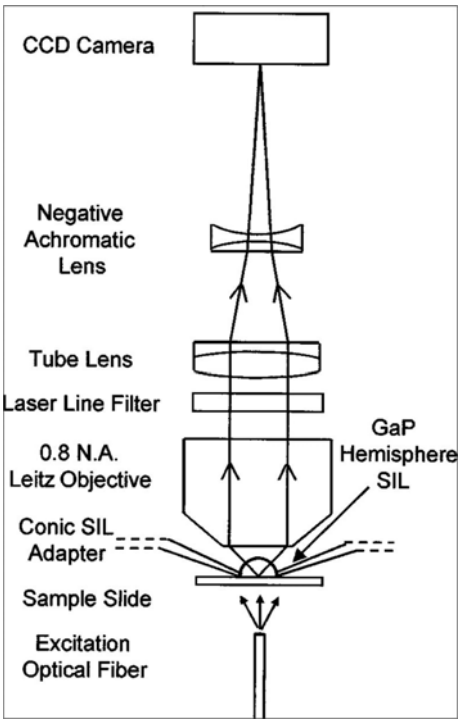


**Figure 2.7.6 Schematic of the wide-field fluorescence microscopy employing an HSIL [86]**

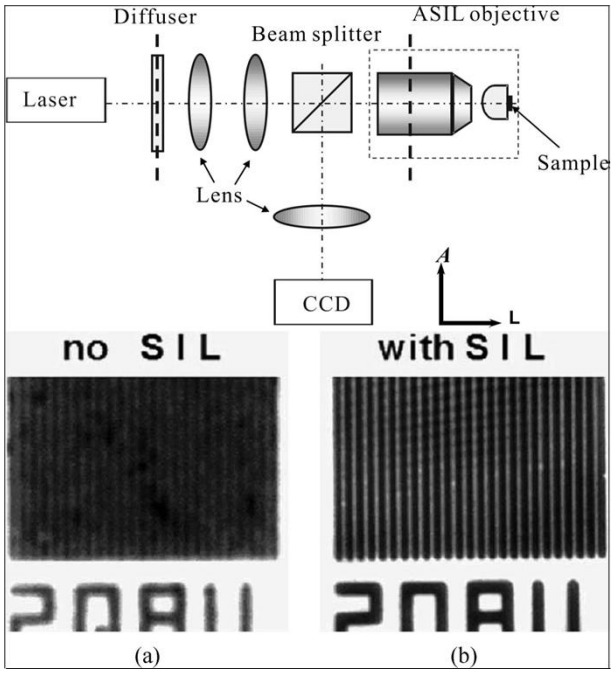


**Figure 2.7.7 Schematic of the non-fluorescence wide-field microscopy employing an ASIL (top) and the comparison of the images of a 25 μm period grating obtained with and without the ASIL (bottom) [8]**

Some new types of SILs are recently developed in order to tackle the aberrations inherently associated with HSILs or ASILs, such as diffractive SIL [92-94] (see more in Subsection 3.2.1 and 3.5.3), or to balance the aberrations from fabrication errors, such as optimum SIL [95] and replicated SIL [96]. Choi *et al.* designed the optimum SIL (Opti-SIL) which has large thickness error tolerance [95]. This design is based on the stable point of the spherical aberration curve rather than the aberration-free points. The spherical aberration induced by non-aplanatic configuration of Opti-SILs is compensated by the aberration from customer-designed objectives (Figure 2.7.8). Opti-SILs have the favourable amount of tolerance towards the thickness error that can meet

the manufacturing requirement while maintaining a high NA. Yoon *et al.* presented the idea to add an aspherical replicated lens to an ASIL, which is called replicated SIL (Figure 2.7.9), in order to obtain a large SIL thickness tolerance for easy fabrication and high NA [96]. Due to the aspherical surface of the replicated lens, the refractive angles of propagating lights can be increased and the sensitivity to spherical aberration with respect to the SIL thickness error can be reduced.

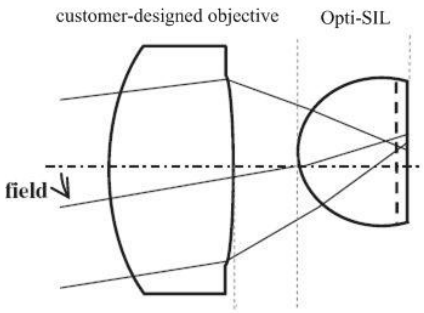


**Figure 2.7.8 Configuration of Opti-SIL and customer-designed objective [95]**
The spherical aberration induced by Opti-SILs is compensated by the aberration from customer-designed objectives.

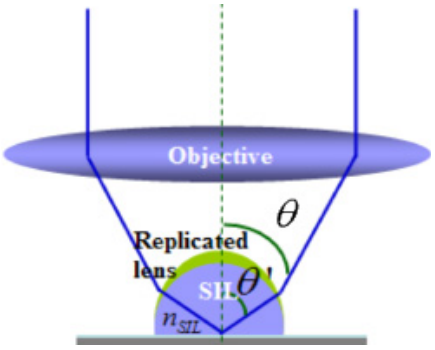


**Figure 2.7.9 Configuration of the replicated SIL and objective [96]**
The sensitivity to spherical aberration with respect to the SIL thickness error can be reduced by using the aspherical surface of the replicated lens.

Throughout the development of SIL technique, a lot of important issues have been investigated, such as the resolution of SIL systems [97] [98]; the aberrations and their allowances [67, 99-108]; optical tunnelling effect in SILs [109]; roles of propagating and evanescent waves in SILs [110-113]; roles of polarisation, phase and amplitude in SILs [114]; light collection efficiency in SIL fluorescence microscopy [115] [90] [91] and non-fluorescence microscopy [116].

SIL technique is also combined with other techniques for certain application purposes, such as the combination of an ASIL and laser tweezers for microfluidic systems [117] [118]; SILs with induced polarisation evanescent imaging for Si wafer inspection[119] [120]; laser induced fault localisation technique with SILs [121]; Raman spectroscopy with SILs [122]; two-photon techniques with SILs [123] [124]; fluorescence correlation spectroscopy with SILs [125] [126] ; transient optical elements with SILs [127]; SILs in imaging system based on negative refraction photonic crystals [128]; SIL system with a multiphase Fresnel zone plate [129]; the combination of SIL with tip-enhanced optical fields [130] and surface plasmon microscopy with SILs [131] [132].

## 2.8 Combinatorial microscopy

The field of microscopy has entered a new frontier in cell biology in which greater spatial resolution is required. To pursue higher resolution in optical microscopy, one development route is to explore new ideas to bypass the physical resolution limit, just like the newly emerged super-resolution microscopic techniques; meanwhile, the other way is to make the most of the established high-resolution techniques and seek a possible way to combine them for a higher resolution than that can be obtained in any individual techniques. A typical case that proves the latter point is the successful combination of solid immersion microscopy and surface plasmon microscopy which was developed in our research group.

Surface plasmons (SP) are electromagnetic surface waves confined to the region between two dielectrics and a conductor. SP are especially sensitive to the properties of any material or discontinuities at or close to the interface between the conductor and one of the dielectrics. Zhang *et al.* developed a wide-field surface plasmon microscope which employs a solid immersion lens (Figure 2.8.1) to produce images of very thin protein structures deposited on a metal surface; resolution of approximately 1 μm has been achieved [7] [131]. The advantage of using SILs in SP microscopy rests with the very high NA obtained with the help of SILs. In the SP microscope, this gives better contrast due to the ability to generate surface waves that would be difficult to excite with conventional objective lenses.

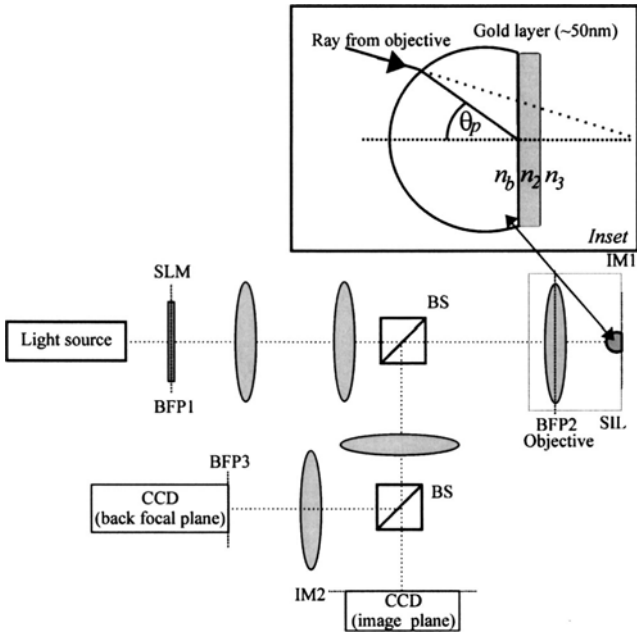


**Figure 2.8.1 Schematic diagram of wide-field surface plasmon microscopy applying a solid immersion lens [131]**
Inset: ray path in aplanatic SIL used for exciting surface plasmons.

Solid immersion microscopy provides a large NA that cannot be obtained in conventional microscopes, thus it is promising to apply solid immersion microscopy as

a platform to support any microscopic techniques that need a large NA. In our research, we intend to combine structured illumination microscopy with solid immersion microscopy in order to develop hybrid fluorescence microscopy to pursue high lateral resolution.

## 2.9 Conclusions

In this chapter, we summarised a wide range of background concepts and techniques connected with high-resolution optical microscopy, especially fluorescence microscopy, in order to help promote a better understanding of the research undertaken in this thesis.

Lateral resolution is one of the most important parameters in optical microscopy, however, the classical resolution limit, rooted in the diffraction phenomenon of optical wave, dictates a barrier on the resolution that can be achieved by an optical microscope. Modern biology stands in need of cellular and even macromolecular scale resolution in order to produce fundamental insights into the inner workings of cells. Fortunately, advances in fluorescent probes pave the road to push the resolution barrier. The rapid development of super-resolution techniques in the last decade makes the resolution that was previously impossible possible. Structured illumination microscopy, as one of the promising super-resolution techniques, is non-scanning wide-field fluorescence microscopy capable of imaging large field of view with rather high speed. Meanwhile, solid immersion lens is able to physically expand the numerical aperture of optical

microscopy. The combination of them has great potential to achieve high lateral resolution beyond that the best conventional microscope can realise.

The application of aplanatic solid immersion lens in wide-field non-fluorescence microscopy has been investigated recently in our research group; however, how to make ASILs work in wide-field fluorescence microscopy is still a question. Structured illumination microscopy is a developing technique, there was no related research embarked upon in our research group. Therefore, in our research, we will firstly investigate solid immersion fluorescence microscopy employing an aplanatic solid immersion lens, and then examine structured illumination microscopy, at last explore the combination of them.

# Chapter 3 Solid Immersion Fluorescence Microscopy (SIF)

## 3.1 Introduction

### 3.1.1 Overview

Solid immersion fluorescence microscopy (SIF) refers to a fluorescence microscopic technique employing a solid immersion lens (SIL) to increase the numerical aperture (NA) and spatial resolution. The appropriate combination of a conventional objective lens and a SIL can achieve a higher effective NA ($NA_{eff}$) than the NA of the conventional objective lens. The first microscope employing a SIL was a scanning system working in non-fluorescence condition [73]. Afterwards, researchers developed a non-scanning wide-field fluorescence microscope employing a SIL [86] [87]. These two types of solid immersion microscopes both applied a hemisphere solid immersion lens (HSIL). Recently, researchers established a wide-field microscope employing an aplanatic solid immersion lens (ASIL) operating in non-fluorescence condition [7] [8]. This solid immersion microscope performed much better than previous ones employing HSILs in terms of both the spatial resolution and the valid field of view (FOV). In our

research, following the previous steps, we intend to develop a wide-field high-resolution fluorescence microscope employing an ASIL.

In this chapter, firstly we give a systematic introduction to the SILs. Secondly we present a comprehensive description of the experimental realisation of the SIF employing an ASIL. Thirdly we describe the high resolution results from our SIF system. Fourthly we discuss the aberration issues in the application of the SIF employing an ASIL. Finally, the near-field imaging property of the SIF is analysed from different viewpoints, and the experimental verification results are presented as well.

### 3.1.2 Sign conventions

In this chapter, the optical properties of SILs are mainly analysed using geometrical optics, and all this analysis follows a specific sign convention in order to make the description clear. Figure 3.1.1 serves as a guide and reminder of these conventions.

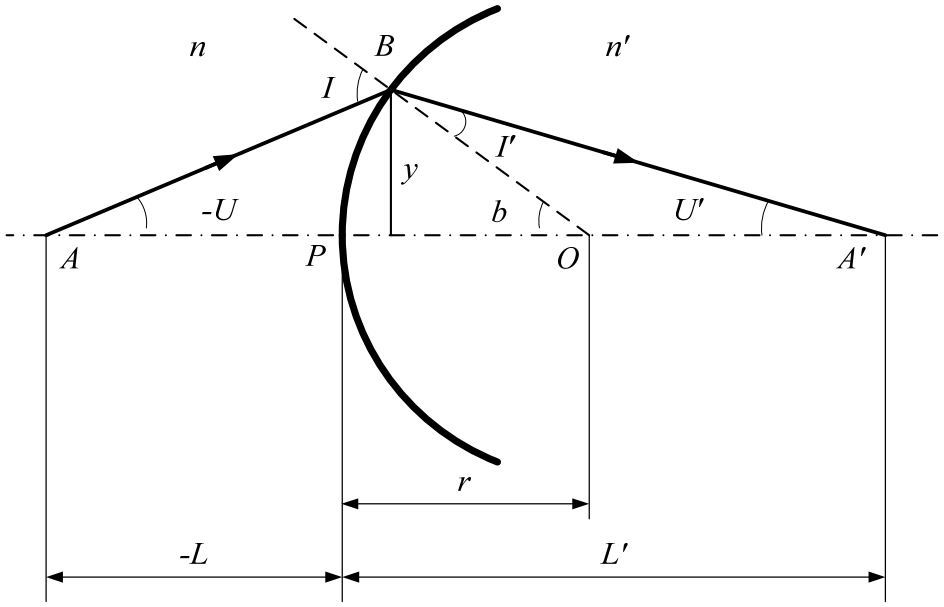


**Figure 3.1.1 Depiction of the sign conventions**
The signs of distances and angles in different directions are indicated here, serving as a guide of our geometrical optics analysis.

In this figure, the single refractive surface *BP* is the interface of two different media with the refractive index *n* and *n′* respectively. *O* is the centre of curvature; *PO* is the radius of curvature denoted as *r*, and its reciprocal, i.e. the curvature, is denoted as *c*. The optical axis *AA′* intersects with the spherical surface at the vertex *P*. Our sign conventions are defined as follows:

(1) Longitudinal direction: The distance, measured from the vertex of the refractive spherical surface to the meeting point of the ray and the optical axis, is positive when its direction coincides with the direction of the propagation of the ray; negative if they are opposite. Similarly, the distance, measured from the vertex of the refractive spherical surface to the centre of curvature, is positive when its direction coincides with the direction of the propagation of the ray; negative if they are opposite. The direction of the propagation of the ray is permanently defined as from left to right.

(2) Lateral direction: The distance, measured from the optical axis, is positive when it is above the optical axis; negative when it is below the optical axis.

(3) The angles between the ray and the optical axis: The angle from the optical axis to the ray is positive when it is clockwise; negative when it is counter-clockwise.

(4) The angles between the ray and the normal: The angle from the ray to the normal is positive when it is clockwise; negative when it is counter-clockwise.

(5) The angles between the optical axis and the normal: The angle from the optical axis to the normal is positive when it is clockwise; negative when it is counter-clockwise.

Furthermore, the distance between different refractive spherical surfaces is denoted as *d*, and the distance, measured from the front refractive spherical surface to the rear refractive spherical surface, is positive when its direction coincides with the direction of the propagation of the ray; negative when they are opposite. In the optical system entirely made up of refractive elements, the *d* is always positive.

## 3.2 Solid immersion lens (SIL)

### 3.2.1 Configurations

Generally speaking, there are two types of SILs according to their outer shapes, which are hemisphere SIL (HSIL) and aplanatic SIL (ASIL) [72]. The HSIL, as the name suggests, is a half ball shape lens as shown in Figure 3.2.1. The thickness *t* of the HSIL

is equivalent to its radius *r*. Different from the HSIL, the ASIL is a truncated ball lens whose thickness is larger than its radius as shown in Figure 3.2.2. The thickness *t* of an ASIL is determined by its radius *r* and the refractive index *n*, which is equivalent to $r + r/n$. These two types of SILs both belong to the traditional spherical optical lenses that work on the basis of the refractions.

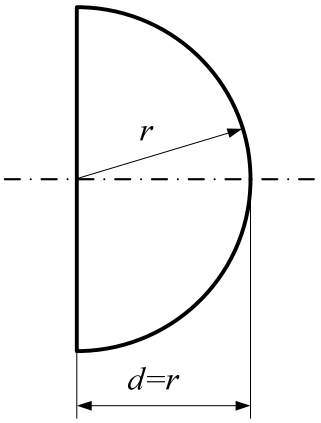


**Figure 3.2.1 Configuration of a hemisphere solid immersion lens (HSIL)**

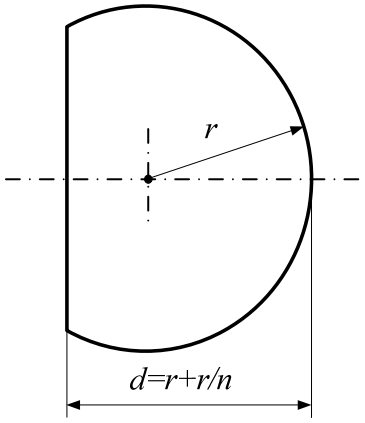


**Figure 3.2.2 Configuration of an aplanatic solid immersion lens (ASIL)**
Here *n* is the refractive index of the ASIL material.

In recent years, a new type of SILs operating primarily by diffraction, with the name of diffractive solid immersion lens (DSIL), has emerged [92] [94]. The DSILs work in the manner of a Fresnel zone plate as shown in Figure 3.2.3. This binary phase element is fabricated by direct electron-beam (e-beam) writing and subsequent reactive ion etching. DSILs have the potential to reduce the chromatic aberration induced by highly dispersive SIL materials (see Subsection 3.5.3), but their non-spherical configuration makes the fabrication much more difficult than that of HSILs or ASILs. Considering the same theoretical resolution achievable using DSILs and ASILs, which is determined by the refractive indices of the SIL materials (see Subsection 3.2.2), we can optimise the

application of ASILs with regard to chromatic aberration for high-resolution imaging. Therefore it is not necessary to fabricate and use DSILs in our research at this stage.

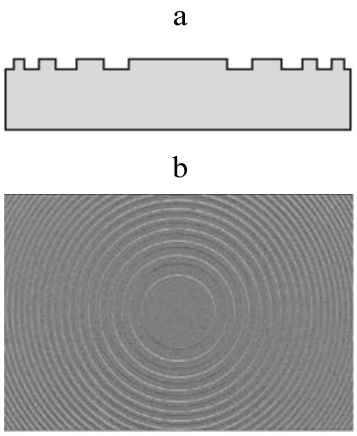


**Figure 3.2.3 Configuration of a diffractive solid immersion lens (DSIL).**
(a) cross-section profile; (b) top view.

### 3.2.2 Two characteristics: Aberration-free imaging and NA enhancement

SILs are very unusual lenses. One special feature is their aberration-free imaging capability thanks to their particular configurations. Here, aberration-free imaging is strictly defined as monochromatic imaging without spherical aberration and other axial aberrations. Chromatic aberrations in SILs will be discussed later in this chapter.

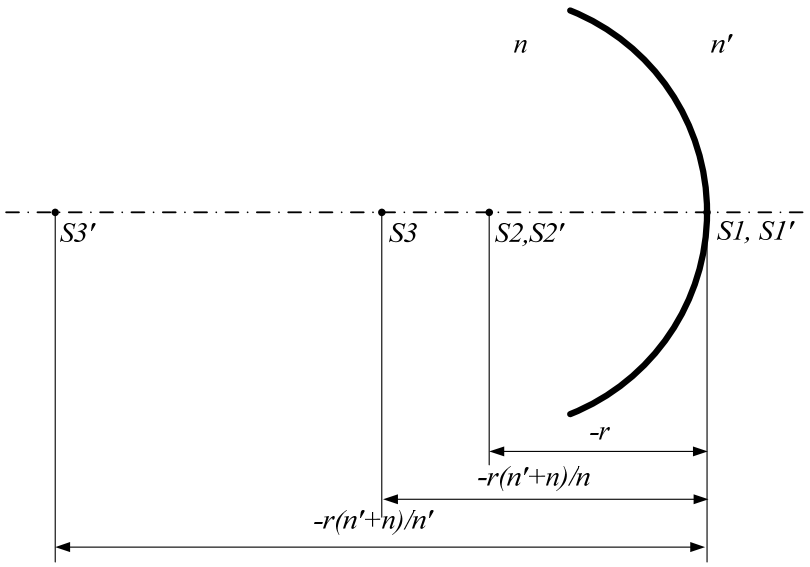


**Figure 3.2.4 Three conjugate pairs free from spherical aberration with a single refractive spherical surface**

For a single refractive spherical surface (Figure 3.2.4), there are three conjugate pairs that are free from spherical aberration (See Appendix I). They are summarised as follows:

(1) The first group is the object point *S1* and its virtual image point *S1′* which both lie on the vertex of the spherical surface.

(2) The second group is the object point *S2* and its virtual image point *S2′* which both lie on the centre of curvature of the spherical surface.

(3) The third group is the object point *S3*, which lies on the concave side of the spherical surface at the distance of

$$L = r\frac{n' + n}{n} \tag{3.2.1}$$

from the vertex of the surface, here $n$ and $n'$ are the refractive indices on the left and right of the spherical surface respectively, and the conjugate image point *S3′* lying on the same side at the distance of

$$L' = r\frac{n'+n}{n'} \tag{3.2.2}$$

from the vertex of the surface. This conjugate pair is called aplanatic points. The situations that satisfy these two equations are called aplanatic conditions [16].

For an HSIL, its configuration satisfies the second condition as described above, which means the imaging from the centre of the flat surface of the HSIL does not suffer any spherical aberration. At this point, the HSIL has the capability of fulfilling aberration-free imaging.

For an ASIL, its configuration satisfies the third condition as Equation (3.2.1) shown, which means the imaging from the centre of the flat surface of the ASIL does not suffer any spherical aberration. At this point, when system operates with single wavelength, the ASIL has the capability to fulfil aberration-free imaging.

So far, the conclusion is, for both HSILs and ASILs, the aberration-free imaging area of a SIL is limited to the central point on the flat surface. This limitation means the aberration-free field of view is very limited. Fortunately, according to the following analysis, it turns out the ASIL has much wider area available with acceptable tolerance of aberrations.

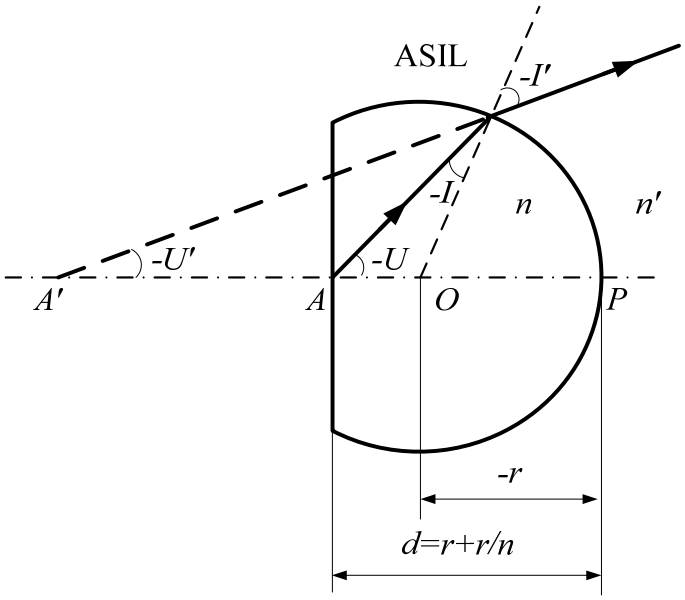


**Figure 3.2.5 Ray propagation model of an ASIL**
Here, *r* is the radius of the ASIL, *n* is its refractive index, *n'* is the refractive index of the medium (usually air) outside the ASIL, *d* is the thickness of the ASIL.

A ray propagation model of an ASIL is shown in Figure 3.2.5. The object situated at the point $A$ conjugates to its virtual image situated at the point $A'$. According to the trigonometric relations, we know:

$$U + I = U' + I' \tag{3.2.3}$$

It is also known, for the aplanatic points, there is (See Appendix I):

$$I' = U \tag{3.2.4}$$

Then

$$I = U' \tag{3.2.5}$$

In this way, it can be concluded that:

$$\sin I = \sin U' \tag{3.2.6}$$
$$\sin I' = \sin U \tag{3.2.7}$$

Dividing the second by the first, we obtain:

$$\frac{\sin I}{\sin I'} = \frac{\sin U'}{\sin U} \tag{3.2.8}$$

According to the Snell's law, there is:

$$n \sin I = n' \sin I' \tag{3.2.9}$$

here $n$ is the refractive index of the ASIL material, $n'$ is the refractive index of the medium (usually air) between the ASIL and the objective lens.

From the above two equations, we know:

$$\frac{\sin I}{\sin I'} = \frac{\sin U'}{\sin U} = \frac{n'}{n} \tag{3.2.10}$$

This means:

$$\frac{\sin U'}{\sin U} = \frac{n'}{n} = k \text{ (constant ratio)} \tag{3.2.11}$$

According to equation (3.2.11), we can draw a very important conclusion: the classic Abbe sine condition [16] is fulfilled in ASILs. This means the sines of the angles of convergence before and after refraction are in a constant ratio, in other words, the lateral magnification is independent of which annular zone in the lens that rays pass through. This leads to a well-defined image not only for the point on the optical axis, but also for the surrounding area without coma.

Besides the aberration-free imaging capability of the SILs, another attractive characteristic of them is the NA of a microscope can be increased by combining the SILs with a conventional objective lens, and in this way, the spatial resolution can be increased.

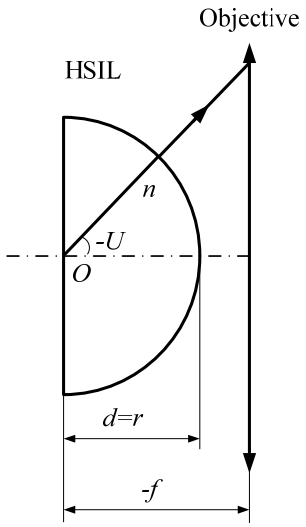


**Figure 3.2.6 Ray propagation model of the combination of an HSIL and a conventional objective lens**
Here, *r* is the radius of the HSIL, *n* is its refractive index, *f* is the focal length of the conventional objective lens.

Let us investigate the combination of an HSIL and a conventional objective lens first (Figure 3.2.6). The HSIL is placed on the left side of the conventional objective lens. The medium between the HSIL and the objective lens is usually air with the refractive index of 1. Here, if the NA of the conventional objective lens is denoted as *NA*, we know for the conventional objective lens, there is:

$$NA = \sin U \tag{3.2.12}$$

If the refractive index of the HSIL is *n*, we define the effective NA of the combination of the SIL and the conventional objective lens as $NA_{eff}$, from Figure 3.2.6, it is clear that:

$$NA_{eff} = n \sin U = nNA \tag{3.2.13}$$

Then we know the NA can be increased *n* times when applying the combination of an HSIL and a conventional objective lens.

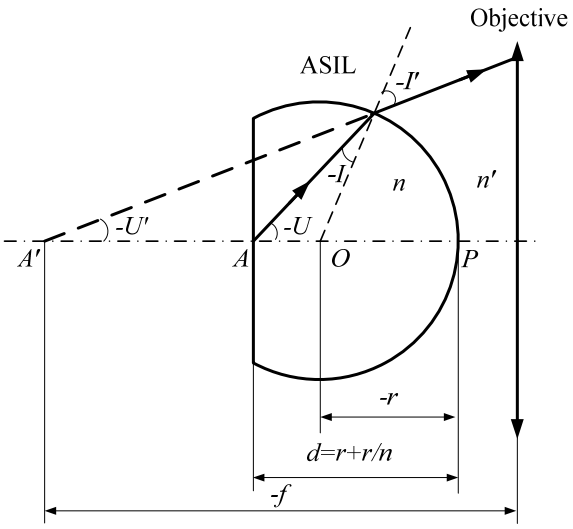


**Figure 3.2.7 Ray propagation model of the combination of an ASIL and a conventional objective lens**
Here, *r* is the radius of the ASIL, *n* is its refractive index, *n′* is the refractive index of the medium (usually air) between the ASIL and the conventional objective lens, *f* is the focal length of the conventional objective lens.

The ray propagation model of the combination of an ASIL and a conventional objective lens is shown in Figure 3.2.7. The ASIL is placed on the left side of the conventional objective lens. When using an infinite conjugate objective lens, the aplanatic point in the image space of the ASIL overlaps the front focal point of the conventional objective lens. The medium between the ASIL and the objective lens usually is air with the refractive index of 1. From Equation (3.2.11) we know:

$$\sin U = \frac{n}{n'} \sin U' = n \sin U' \tag{3.2.14}$$

Then there is:

$$NA_{eff} = n \sin U = n \cdot n \sin U' = n^2 \sin U' \tag{3.2.15}$$

Because the NA of the conventional objective lens is:

$$NA = \sin U' \tag{3.2.16}$$

We can conclude

$$NA_{eff} = n^2 NA \tag{3.2.17}$$

Therefore, the NA can be increased $n^2$ times when applying the combination of an ASIL and a conventional objective lens.

It is necessary to note that the $NA_{eff}$, regardless of the SIL configuration, is subject to a maximum value of the refractive index *n* of the SIL material, which is self-evident from the definition of numerical aperture. This maximum limit can be expressed as:

$$NA_{eff_{\max}} = n \tag{3.2.18}$$

By comparing the HSILs and ASILs (Table 3.2.1), it is very clear the ASILs have more advantages than the HSILs considering both the valid aberration-free area and $NA_{eff}$. For this reason, we decide to employ an ASIL to fulfil our wide-field high-resolution solid immersion fluorescence microscopy (SIF).

**Table 3.2.1 Comparisons of different types of the SILs**

| SIL type | Valid aberration-free area | Effective NA |
|---|---|---|
| HSIL | Limited to the centre of the flat surface | *n*NA, subject to the maximum value of *n* |
| ASIL | Extended to the surrounding area of the centre of the flat surface | $n^2$NA, subject to the maximum value of *n* |

Here, we also intend to discuss the selection of the conventional objective lens to match the ASIL. According to Equation (3.2.18), we know the maximum $NA_{eff}$ is limited to

the ASIL's refractive index *n*. In this situation, the NA of the conventional objective lens from Equation (3.2.17) is:

$$NA = \frac{NA_{eff}}{n^2} = \frac{n}{n^2} = \frac{1}{n} \tag{3.2.19}$$

In order to achieve a maximum $NA_{eff}$, we need a NA of at least $\frac{1}{n}$ for the conventional objective lens.

### 3.2.3 ASIL material, design and manufacture

Our motivation to apply the ASIL in fluorescence microscopy is to pursue high $NA_{eff}$ and corresponding high lateral resolution. According to Equation (3.2.17), the $NA_{eff}$ is dependent on the refractive index of the ASIL material when the conventional objective lens is pre-determined. Even considering the maximum limit of the $NA_{eff}$ as expressed in Equation (3.2.18), the refractive index still plays the key role in increasing the system $NA_{eff}$. Therefore it is beneficial to select the ASIL material with a rather high refractive index.

The solid materials used to manufacture refractive optical components can be glasses, crystalline materials (insulators and semiconductors) and polymeric materials. Among these, the optical glasses are mostly used due to their high transmittance in visible spectral region as well as stable mechanical and thermal properties. Optical glasses are characterised and designated by their refractive index and dispersion. The most common measure is the refractive index at the wavelength of the He *d* line (587.6 nm) or the Na

*D* line (589.3 nm). The difference in the refractive index at the hydrogen *F* (486.1 nm) and *C* (656.3 nm) lines, i.e. $n_F - n_C$, is called the average or principal dispersion [133]. The ratio $(n_F - n_C)/(n_d - 1)$ is called the relative dispersion; the reciprocal of this quantity is the Abbe number $\nu_d$, i.e.,

$$\nu_d = (n_d - 1)/(n_F - n_C) \tag{3.2.20}$$

There are more than 200 types of optical glasses in market. For our needs, the highest refractive index glass readily available is S-LAH79 from Ohara which has $n_d$ = 2.0033 and $\nu_d$ = 28.3. The full technical information of this type of glass can be found in Appendix II.

The selection of the ASIL size needs an extensive discussion because it has broad implications with many aberration issues, which will be discussed in detail in Section 3.5. Considering the fluorescence spectral width and feasible field of view (FOV) we need, we choose 5 mm as the diameter of the ASILs.

In Subsection 3.2.1, we have pointed out the thickness of an ASIL as determined by the radius *r* and refractive index *n*:

$$d = r + r/n \tag{3.2.21}$$

In a fluorescence microscope, due to the fluorescence Stokes shift [14] of the fluorophores, the fluorescence wavelength is different from the illumination

wavelength. However, in an epi-fluorescence microscope, the objective is shared by the illumination path and the florescence imaging path. In this way, the size of the ASIL needs to be designed to be compatible for both of these wavelengths. Practically, we choose the median value between the theoretical sizes corresponding to the excitation and emission wavelengths as the designed thickness. In our experiments, the excitation wavelength is 632.8 nm, and the emission is centred at 670 nm. According to the data sheet of optical glass S-LAH79 (Appendix II), the refractive indices under these two wavelengths are 1.99613 and 1.99135. According to Equation 3.2.21, the thicknesses should be 3.752 mm and 3.755 mm. Considering manufacturing precision, the designed thickness of our AILs is 3.75±0.005 mm. The thickness deviation from the ideal value could lead to the appearance of spherical aberration, however practically most of the aberration can be balanced by defocusing from the paraxial focus. This point is discussed in Subsection 3.5.5. The S-LAH79 ball lenses with diameter of 5 mm were purchased, and then they were sent to an optics workshop to grind and polish to our desired thickness. A photograph of our ASIL is shown in Figure 3.2.8.

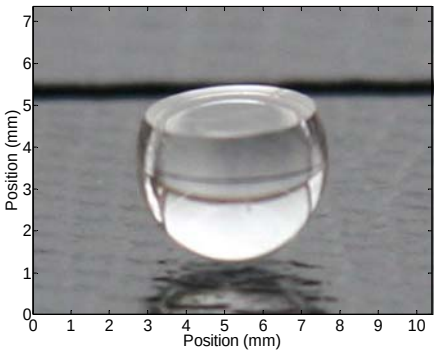


**Figure 3.2.8 Photograph of an ASIL**

### 3.2.4 ASIL-objective specification

The most important optical parameters, such as focal length and magnification, of ASILs and the combination of an ASIL and a conventional objective lens, so-called ASIL-objective, are derived in Appendix III. In conclusion, the focal length of an ASIL is:

$$f' = \frac{r}{n-1} \tag{3.2.22}$$

where $r$ is the radius of the ASIL, $n$ is the refractive index.

The magnification of an ASIL is:

$$m = n^2 \tag{3.2.23}$$

The focal length of an ASIL-objective is:

$$f' = \frac{f_0'}{n^2} \tag{3.2.24}$$

where $f'_0$ is the focal length of the conventional objective lens.

The magnification of an ASIL-objective is:

$$m = n^2 m_0 \tag{3.2.25}$$

where $m_0$ is the magnification of the conventional objective lens.

To match our ASIL, the conventional objective lens should at least have the NA of:

$$NA = \frac{1}{n} \approx 0.5$$

We use a conventional objective lens with 0.55 NA to combine with our ASIL. The specification of this conventional objective lens is shown in Table 3.2.2. We use a long working distance objective lens here to ensure that there is enough space to accommodate the ASIL.

**Table 3.2.2 Specification of Mitutoyo infinity-corrected long working distance objective lens**

| | |
|---|---|
| **Magnification** | 50× |
| **Numerical Aperture (NA)** | 0.55 |
| **Working Distance, WD** | 13.0mm |
| **Focal Length** | 4mm |
| **Resolving Power(λ=550nm)** | 0.5μm |

According to the above conclusions, we can work out some important optical parameters of our ASIL-objective. From Equation (3.2.17), we know the $NA_{eff}$ of our ASIL-objective goes to:

$$NA_{eff} = n^2 NA = 2.2 > n$$

So we need to apply Equation (3.2.18) and then the $NA_{eff}$ is:

$$NA_{eff} = n \approx 2$$

The focal length of our ASIL-objective, which we call effective focal length, is:

$$f_{eff} = \frac{f_o}{n^2} = 1mm$$

The theoretical resolution at wavelength $\lambda$= 670nm defined by Rayleigh criteria is:

$$R = \frac{0.61\lambda}{NA} = 204nm$$

We list these parameters in Table 3.2.3.

**Table 3.2.3 Major parameters of our ASIL-Objective**

| | |
|---|---|
| **Numerical Aperture (NA)** | 2 |
| **Focal Length** | 1mm |
| **Resolving Power (λ=670nm)** | 0.2μm |

The distance between the ASIL and the objective lens and other related geometrical parameters are shown in Figure 3.2.9.

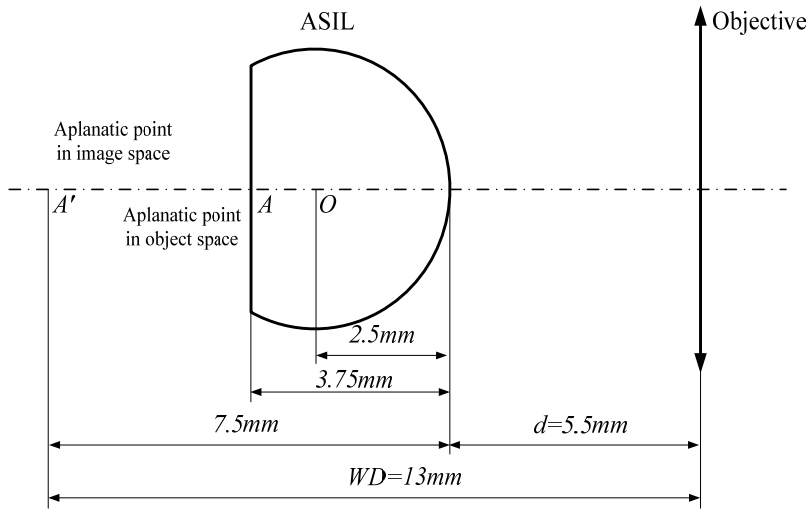


**Figure 3.2.9 Geometrical parameters of our ASIL-objective**
Here *WD* is the working distance of Mitutoyo objective, *A* is the object position, *A′* is its image position.

## 3.2.5 Discussion

Optical glasses are not the only possible materials to make SILs, semiconductor materials usually have higher refractive indices than optical glasses. Other researchers have successfully applied gallium phosphide (GaP), which has a refractive index of 3.420 at 560 nm, to fabricate HSILs to fulfil high-resolution fluorescence microscopes

[86] [87]. However, GaP has very low internal transmittance (up to 20% over 1mm thickness) in visible spectrum range (Figure 3.2.10), while S-LAH79 has higher than 80% internal transmittance over 10 mm thickness in the same spectrum range (See Appendix II). So, if the SIL is designed to work in the visible spectrum range, especially under the condition of weak emission detection, high-index optical glasses like S-LAH79 are still the better choices.

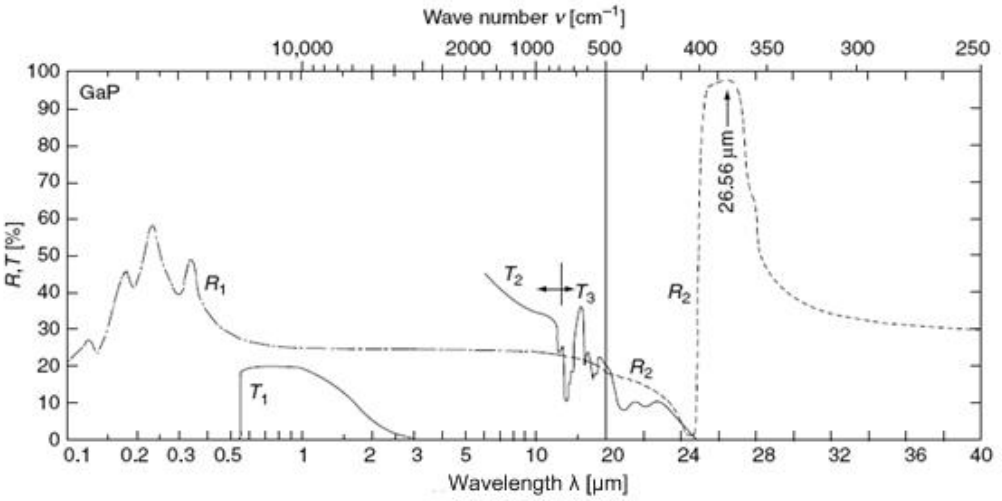


**Figure 3.2.10 Internal transmittance and reflectance spectra of GaP**
Transmittance: T1 at 1 mm, T2 at 0.386 mm, T3 at 0.18 mm; Reflectance: R1, R2 at normal incidence.[133]

# 3.3 SIF instrumentation

## 3.3.1 System design

The epi-illumination method gives a stronger signal to background ratio than the transmission configuration, since most of the excitation light is transmitted through the specimen, only a small amount of reflected excitation light reflects back to the objective

lens together with the emission light. For this reason, we decide to implement epi-fluorescence microscope configuration to set up our SIF system. We also adopt Köhler illumination in order to obtain an even excitation around the specimen.

Besides necessary illumination and imaging paths, we also set up a back focal plane (BFP) imaging path for the purpose of estimating the NA of our SIF system. For an aplanatic objective lens, there exists a linear relationship between the radius $r$ (or diameter $d$) of the BFP and its NA [134]:

$$r = f \cdot NA \tag{3.3.1}$$

or

$$d = 2f \cdot NA \tag{3.3.2}$$

Here, $f$ is the focal length of the objective lens. From these equations, we know the angular distribution of the emission of a fluorescent specimen can be converted into an intensity distribution over the BFP. Because the collection angle of the emission is limited by the NA of the objective lens, it is possible to estimate the NA by measuring the size of the BFP. Moreover, we also set an adjustable aperture on the conjugate plane of the BFP of the ASIL-objective in order to control the NA accordingly. It is worth noting that Equations (3.3.1) and (3.3.2) are based on paraxial approximation, which means, for a high NA system, the NA is over-estimated slightly when evaluating it from the measured size of a BFP image.

The above considerations lead to a SIF system design as shown in Figure 3.3.1. The laser beam is expanded by a lens relay, and then reflected by the dichroic filter into the

ASIL-objective. This illumination excites samples in a collimated form, as the sharp red shading illustrates, to fulfil Köhler illumination. The fluorescent samples situated at the flat surface of the ASIL emit fluorescent light as the dark red shading illustrates. A two-stage lens relay is applied to make a conjugate plane of the BFP physically available. On this conjugate plane, a calibrated iris diaphragm is mounted. After the diaphragm, an emission filter is used to ensure only the fluorescent emission enter CCD camera. A beam splitter is placed in front of the CCD camera in order to separate half of the fluorescent emission to form the image of the BFP on the other CCD camera, as shown by the green dashed lines. All the lenses are settled as telecentric configuration in order to obtain the best image quality, that is to say, the distance between every two lenses is equivalent to the sum of their focal lengths.

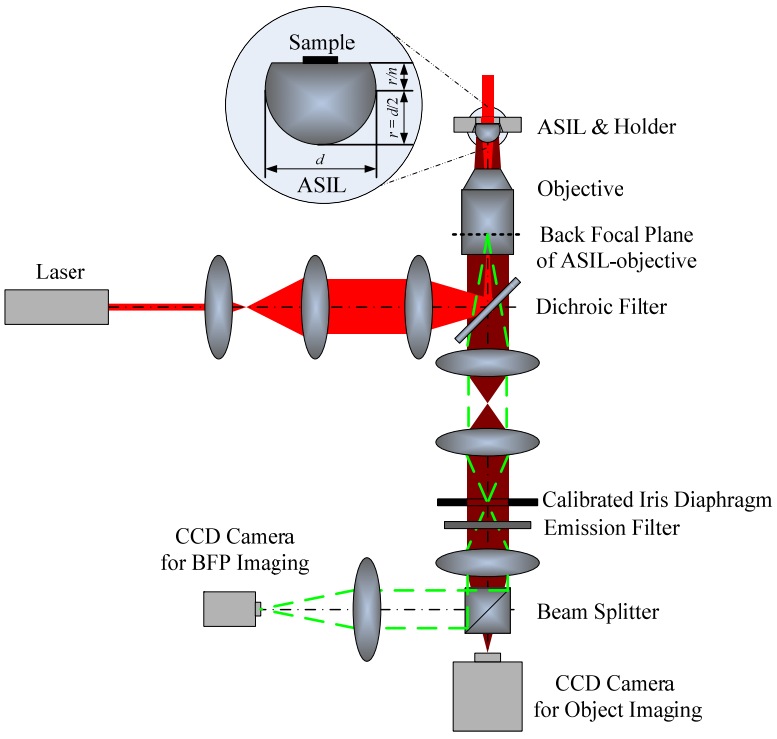


**Figure 3.3.1 Schematic of the SIF system**
The sharp red shading illustrates Köhler illumination beam; the dark red shading illustrates the fluorescent light forming the specimen image; and the green dashed lines illustrate the fluorescent light forming the BFP image. The ASIL configuration is also shown in the enlarged inset.

Now we need to do some calculations in order to implement a real system. First, we should work out the necessary magnification in the imaging path. In our setup, a digital charge-coupled device (CCD) camera was used. The ability of a CCD camera to accurately capture all the details of samples is dependent on the sampling frequency. The features of specimen presented through a microscope that are smaller than the digital sampling frequency are not able to be represented accurately in the digital image. The Nyquist criterion [15] requires a sampling frequency equal to twice the highest specimen spatial frequency to accurately preserve the spatial resolution in the resulting digital image. Therefore, to capture the smallest degree of detail in a specimen, pixel size must be small enough so that a minimum of two pixels are covered for each feature, guaranteeing the whole spatial period are gathered by the imaging device. From Subsection 3.2.4, we know the theoretical resolution of our ASIL-objective is about 200 nm (λ=670nm); meanwhile the pixel size of our CCD camera is 8 μm× 8 μm. According to Nyquist criterion, the necessary, i.e. the minimum, magnification is:

$$M = \frac{8\mu m \times 2}{200nm} = 80$$

Practically, we intend to make the magnification about twice as great as the minimum value, and then we adopt the magnification of 200.

Second, we need to calculate the appropriate magnification in the illumination path. In epi-configuration, the illumination beam could be easily shrunk to an impractically small size due to the strong optical power of the objective. Then a beam expander is

commonly employed to expand the illumination beam before it goes through the objective lens. On the other hand, to make the best of the illumination, it is necessary to restrict the illumination area to match the FOV. The image area of our CCD is 8 mm× 8 mm, correspondingly, the FOV in the object plane is:

$$FOV = \frac{8mm \times \sqrt{2}}{200} \approx 57\mu m$$

The minimum (de)magnification is determined by the result of FOV dividing the laser beam size:

$$DM = \frac{57\mu m}{1mm} = 0.057$$

Practically, we adopt the (de)magnification of 0.06.

At last, we need to choose the magnification of BFP imaging path. The theoretical BFP diameter of our ASIL-objective can be calculated by Equation (3.3.2):

$$d = 2f \cdot NA = 2 \times 1 \times 2 = 4mm$$

For simplicity, we set the magnification of BFP imaging path as 1, which will produce an image with the identical size as the real BFP. Thus we need a CCD camera which has at least 4 mm × 4 mm imaging area; fortunately, CCD in this size is conveniently available.

## 3.3.2 Apparatus

According to the system design described in the previous subsection, a prototype SIF system was built as shown in Figure 3.3.2. In this photograph, the illumination, object imaging and BFP imaging paths are indicated by bright red, dark red and green dash-dot lines respectively. A photograph of the ASIL-objective is shown in Figure 3.3.3. The distance between the ASIL and the objective lens needs delicate alignment that is described in Appendix IV.

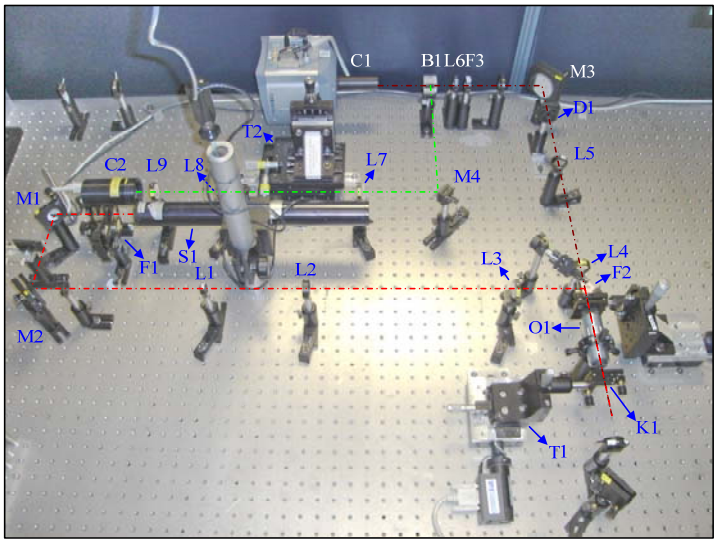


**Figure 3.3.2 Photograph of the SIF system**
Bright red dash-dot line: illumination path; dark red dash-dot line: object imaging path; green dash-dot line: BFP imaging path.

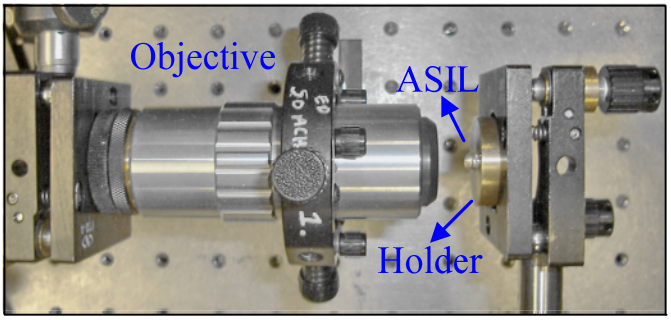


**Figure 3.3.3 Photograph of the ASIL-objective**

The key apparatus in this setup include:

(1) Laser

The light source (S1 in Figure 3.3.2) is a He-Ne laser from JDS Uniphase Corporation. Its brief specifications are given in Table 3.3.1.

**Table 3.3.1 Specifications of JDS Uniphase He-Ne laser**

| | |
|---|---|
| **Wavelength** | 632.8 nm |
| **Output power** | 7 mW |
| **Beam diameter(1/$e^2$ points)** | 0.81 mm |
| **Beam divergence(full angle)** | 1 mrad |
| **Maximum noise (rms, 30Hz to 10MHz)** | 0.2% |
| **Beam pointing stability(after 15 minutes warm-up)** | <0.02 mrad |

(2) Electron Multiplying CCD (EMCCD) camera

The camera (C1 in Figure 3.3.2) used to image samples is an EMCCD camera from Andor Technology plc. This camera is capable of amplifying weak photon signals to a signal level well above the readout noise floor of the camera at any readout speed, despite the fact that the noise level practically deviated from the nominal value [135]. Importantly, this 'on-chip' amplification process is realised without sacrificing the photon collection capability of the sensor. The major parameters of this camera from the manufacturer are given in Table 3.3.2.

**Table 3.3.2 Specifications of Andor EMCCD camera**

| | |
|---|---|
| **Active pixels** | 1004×1002 |
| **Pixel size** | 8×8 μm |
| **Image area** | 8×8 mm |
| **Spectral response** | QE max at 600 nm(typical 65%), 50% roll-off at 380nm and 880 nm |
| **Active area pixel well depth** | 30000($e^-$, typical) |
| **Gain register pixel well depth** | 80000($e^-$, typical) |
| **Max readout rate** | 35 MHz |
| **Frame rate @ full resolution** | 31.4 frames per second |
| **Readout noise** | 25($e^-$) @ 35 MHz; < 1 ($e^-$) with EM gain |

(3) CCD camera

The camera (C2 in Figure 3.3.2) used to image the BFP of the system is a CCD camera from Starlight Xpress Ltd. The major parameters are given in Table 3.3.3.

**Table 3.3.3 Specifications of Starlight Xpress CCD camera**

| | |
|---|---|
| **Active pixels** | 752×580 |
| **Pixel size** | 8.6×8.3 μm |
| **Image area** | 6.47×4.83 mm |
| **Spectral response** | QE max at 540 nm(~70%), 50% roll-off at 400 nm and 650 nm |
| **Active area pixel well depth** | 70000($e^-$, typical) |
| **Image download time** | 0.3 seconds full resolution using USB2.0 |
| **Readout noise** | 10 ($e^-$) |

(4) Objective lens

The objective lens (O1 in Figure 3.3.2) we used is a 0.55 NA 100 × infinite conjugate long working distance objective from Mitutoyo Ltd. The details about it can be found in Table 3.2.2 in Subsection 3.2.4.

(5) Dichroic filter

The dichroic filter (F2 in Figure 3.3.2) is a notch filter from Edmund Optics Inc., which has 90% transmission for the spectrum range from 350nm to 2500 nm combined with 99.5% reflectivity at the centre wavelength 632.8 nm.

(6) Emission filter

The emission filter (F3 in Figure 3.3.2) is a laser interference filter centred at 670 nm with 3 nm passband (FWHM) from Edmund. This super-narrow bandpass filter is used not only to specifically select the emission light and remove excitation light, but also to reduce chromatic aberration induced by the ASIL to a negligible level. The chromatic aberration issue will be discussed in detail in Section 3.5.

(7) ASIL holder

The ASIL holder needs careful design. The situation when maximum $NA_{eff}$ can be achieved is shown in Figure 3.3.4.

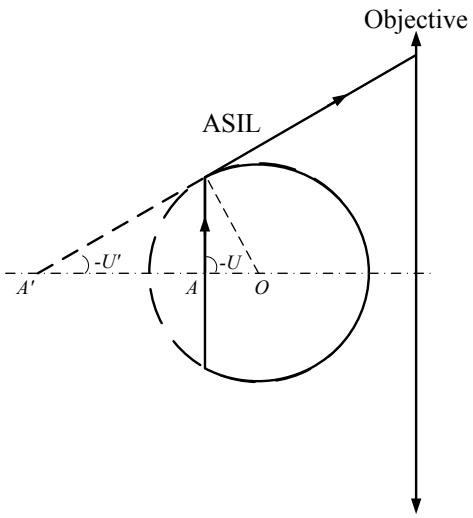


**Figure 3.3.4 Schematic of the emission ray propagation when achieving maximum $NA_{eff}$**

In this schematic diagram, we can see when $NA_{eff}$ goes to its theoretical value of 2, the maximum emission angle collected by the ASIL is:

$$U = \arcsin\frac{NA_{eff}}{n} = 90°$$

In order to achieve theoretical $NA_{eff}$, the holder cannot block any part of the curved surface of the ASIL. For this reason, we designed a holder with a central conical hole as shown in Figure 3.3.5. The assembly of the ASIL and its holder was completed by gluing the peripheral area of the ASIL flat surface on the bottom platform of the central conical hole. Samples could be made upon the flat surface of the ASIL through the central hole from the back side of the holder. The holder was made of brass with which the mechanical strength was guaranteed in usage while with easy fabrication. A further discussion on holder aperture and $NA_{eff}$ was reported by Goh *et al.* [105].

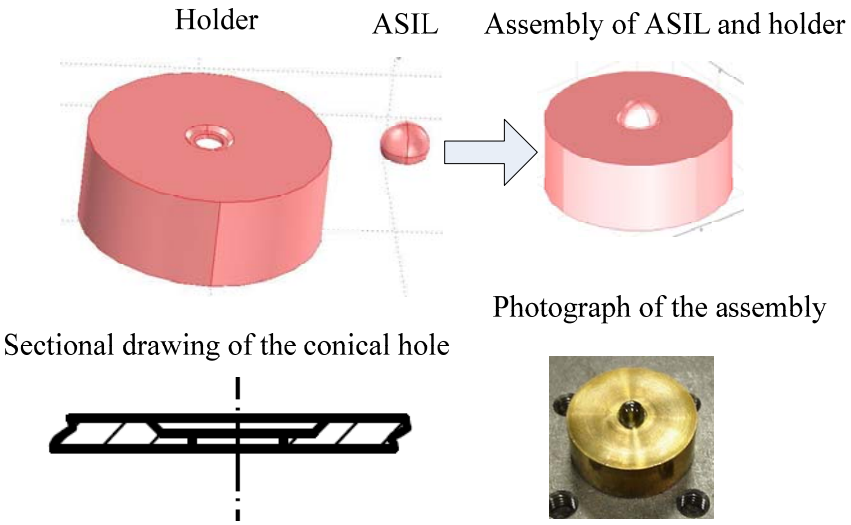


**Figure 3.3.5 ASIL, holder and their assembly**
Top left: schematic of the holder; top middle: schematic of the ASIL; top right: schematic of the assembly of the ASIL and holder; bottom left: sectional drawing of the central conical hole; bottom right: photograph of the assembly of the ASIL and holder

### 3.3.3 Magnification calibration

The magnification is undoubtedly one of the most important parameters of a microscope. There are two major reasons we need to calibrate the practical magnification: one is to examine if the optics are properly aligned; the other is to precisely verify the magnification for the later use of resolution investigation.

A common way to calibrate microscope magnification is to image a standard calibration target. A regular target is usually a glass plate with chrome deposit in standard pattern and size. However, the ASIL holder only retains 3 mm diameter space on the flat surface of the ASIL to accommodate samples, it is nearly impossible to apply any type of traditional magnification targets in our SIF system. So, we need to find a new way to

accomplish this calibration. The method we applied to calibrate the magnification of our SIF is micro contact printing (μCP) [136]. The μCP uses the relief patterns on an elastomeric stamp to form patterns of self-assembled monolayer of inks on the surface of a substrate through direct contact. The elastomeric stamp can be cut to any size as we want, so it is perfect for the application in a small space as in the case of the SIF. In our experiment, the elastomeric stamps were made from polydimethylsiloxane (PDMS). The master we used was a 25 μm pitch grating. Its structure was copied on the PDMS stamp in a similar way as described in the literature [136]. The patterned surface of the stamp was stained in a drop of fluorescent dye of Oxazine1 (Sigma-Aldrich). Oxazine1 has an absorption peak at 642.5 nm and an emission peak at 648 nm (in methanol) that are suitable to our case. The stained relief grating pattern was printed on the flat surface of the ASIL to form a standard fluorescent target for the purpose of magnification calibration. Before applying this method in SIF, it is sensible to examine the accuracy of dye grating pattern size. A dye grating sample was made on a regular coverglass and imaged under a Zeiss Axio Imager microscope, from which the measured value of one pitch is 24.7 μm as shown in Figure 3.3.6. In comparison with the nominal pitch of 25 μm, the error is just 1.2%. Repeating this measurement several times with other batches of dye grating samples, the error is always in this range. Therefore, we regard the μCP as a reliable method for making standard fluorescent calibration patterns.

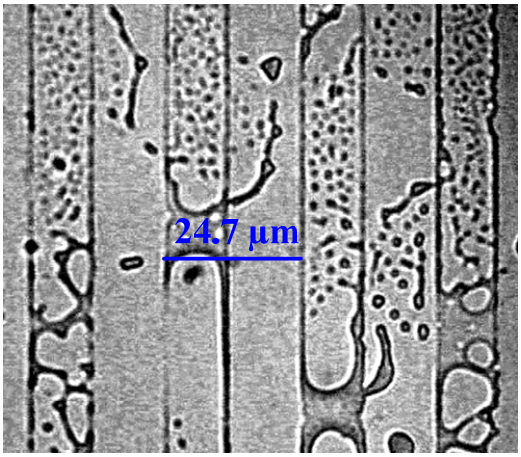


**Figure 3.3.6 Image of 25 µm pitch dye grating obtained with the Zeiss microscope**
According to the measurement fulfilled through the measurement software provided in this Zeiss microscope, the pitch distance of this dye grating is 24.7 µm.

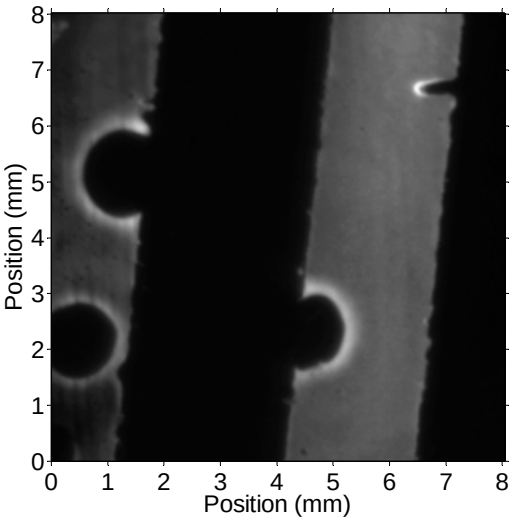


**Figure 3.3.7 Image of 25 µm pitch dye grating obtained with the SIF**
The coordinates correspond to the image plane on the CCD.

The dye grating image obtained with the SIF is shown in Figure 3.3.7. By measuring the edge to edge distance from its cross-section profiles, the dye grating pitch value can be quantified. According to the measurements of three randomly picked profiles, the average length of one pitch is 5239 ± 53 µm in the image plane. Since the real dye grating period is 25 µm, it is identified through their ratio that the practical magnification of the SIF is 210. The small difference between theoretical and practical magnifications, which are 200 and 210 respectively, comes from the defocusing for best image quality. In the fabrication of ASILs, the thickness error deviated from perfect value determined by the ASIL material and size is inevitably generated due to the limitation of current manufacturing precision. For ASILs, the appearance of spherical aberration is rather sensitive to the thickness error in contrast to HSILs [104]. To balance the residual spherical aberration, slight defocusing from the paraxial focus is

necessary, leading to the variation of magnification from the theoretical value. Further discussion on thickness error and its tolerance can be found in Subsection 3.5.5.

The SIF can be easily converted to a conventional fluorescence microscope by removing ASIL from the system. It is also convenient to examine the same specimen with both the SIF and the conventional fluorescence microscope by flipping the ASIL. In other words, when the curved surface of the ASIL facing the objective lens, it works as a SIF system; while reversing the ASIL to make its flat surface face the objective lens, it is transformed to a conventional microscope. At this point, we also calibrated the magnification of this conventional microscope for future use. A 20 μm period Ronchi grating was used as standard calibration target. To avoid speckle in the images, a red LED, working as the light source, was put into the original lens relay in the illumination path to form a Köhler illumination. The image of this Ronchi grating is shown in Figure 3.3.8. With the same measurement method as used before, the average length of one period is measured to 1003.5 ± 0.87 μm. By dividing this over the actual period length 20 μm, it is found the magnification is 50, just as same as the theoretical value.

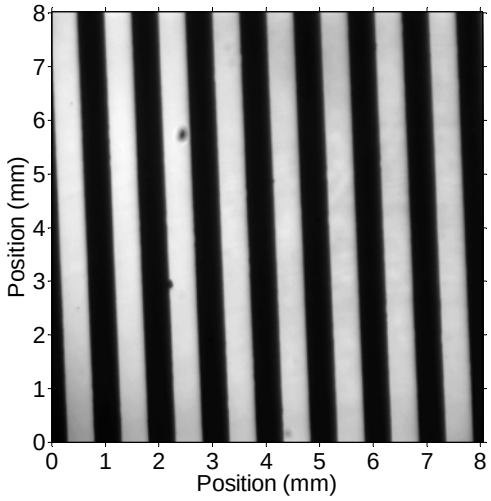


**Figure 3.3.8 Image of 20 µm period Ronchi grating obtained with conventional microscope**
The coordinates correspond to the image plane on the CCD.

# 3.4 Experimental realisation of high-resolution SIF

## 3.4.1 Resolution evaluation method

The resolution of an optical microscope can be evaluated in both the spatial domain and the frequency domain. In the spatial domain, an accurate method to evaluate the resolution is to investigate the point spread function (PSF) of the microscope. According to the classical Rayleigh criteria, two point sources are just resolved if the central maximum of the intensity diffraction pattern produced by one point source coincides with the first zero of the intensity diffraction pattern produced by the other. In other words, if identical point objects are within the Rayleigh criteria distance, the objects cannot be resolved in the images. Therefore, a higher resolution is equivalent to

a smaller size of the PSF. On the other hand, in the frequency domain, a wider optical transfer function (OTF) of the microscope means a higher resolving power.

To evaluate the resolution of a practical microscope in the spatial domain, it looks like we need point objects and then get their images in order to retrieve the PSF of this microscope. With the measured PSF, we are able to conclude the NA and resolution of the microscope according to Equation (2.3.3). Unfortunately, an ideal point object has zero size. Obviously real objects have finite sizes. In reality, although sometimes very tiny fluorescent beads are regarded as point objects, depending on how much the size of these beads is smaller than the theoretical PSF of the microscope, we actually cannot retrieve the genuine PSF in experiments directly.

A widely used method to quantify the resolution of an optical microscope is to image a sample with regular shape of known size, for example, a small fluorescent latex bead, then the known sample shape is removed by deconvolution to retrieve the PSF. In practice, the deconvolution sometimes is simplified to make it easy to perform. For example, it could be performed using a simple equation [86] [87] :

$$\Delta x^2_{observed} = \Delta x^2_{system} + \Delta x^2_{dyeball} \qquad (3.4.1)$$

to calculate the size of the PSF (here $\Delta x_{observed}$, $\Delta x_{system}$ and $\Delta x_{dyeball}$ denote the sizes of observed image, system PSF and object, i.e. dye ball, correspondingly), or using simple linear deconvolution to remove the known bead shape [31]. However, these simplified deconvolution methods do not take into account the noise in the experimental images. To recover a signal that is embedded in noise, Wiener filter is known to be optimal in

the minimum mean square error (MSE) sense [137]. In an optical microscope, the observed data $D(r)$ is the convolution of the distribution of a sample $E(r)$ with the PSF $H(r)$ of the microscope:

$$D(r) = E(r) \otimes H(r) \tag{3.4.2}$$

Considering the effect of additive noise $N(r)$, the above equation is rewritten as:

$$D(r) = E(r) \otimes H(r) + N(r) \tag{3.4.3}$$

In frequency domain, the Wiener filter can be expressed as [137]:

$$\tilde{G}(k) = \frac{1}{\tilde{H}(k)} \left[ \frac{\left|\tilde{H}(k)\right|^2}{\left|\tilde{H}(k)\right|^2 + \frac{\tilde{N}(k)}{\tilde{E}(k)}} \right] \tag{3.4.4}$$

here tildes (~) indicate the Fourier transform of the corresponding quantities in spatial domain and $k$ is the spatial frequency component. The item $\frac{\tilde{N}(k)}{\tilde{E}(k)}$ is the inverse of the signal to noise ratio (SNR), which indicates that the Wiener filter is highly sensitive to the estimated noise. To circumvent the complicated noise estimation in the Wiener filter deconvolution algorithm, instead of doing deconvolution, we model the convolution of the known sample shape and the computed PSF of a noise-free microscope, then derive the modelled image of the sample from this hypothetical microscope. By comparing the modelled image and experimental image from a practical system, we are able to quantify the resolution performance of this practical microscope. In detail, the method we used follows these steps:

(1) We model the convolution of a spherical object of known size, corresponding to a fluorescent bead, and the PSF of a virtual microscope. The diffraction-limited PSF is calculated from the square of *jinc* function. By changing the NA used in the calculations, a series of simulated images corresponding to different NAs are produced;

(2) We obtain the images of single fluorescent beads with our bench-top microscope;

(3) We calculate two-dimensional (2D) correlation coefficients between the simulated images and the experimental image of single fluorescent bead, and find the simulated image with the highest correlation coefficient with the experimental image. Since the NA of the simulated microscope is known, we can accordingly conclude the NA of the bench-top microscope.

The benefit of our approach is that it circumvents the complicated noise estimation in traditional Weiner filter deconvolution, meanwhile it accounts for the noise effect in the imaging through the numerical values of correlation coefficients. The precision of this method is still strongly limited by the noise level in the experimental images, which is reflected by the fact that the high correlation coefficients can only be acquired when a high SNR experimental image is used, therefore in practice the noise should be kept as low as possible. For a low NA system, due to the ease of acquiring high SNR experimental images, the resolution evaluation method employed here readily produces very high correlation coefficients between the simulated and experimental data, which indicates a more accurate evaluation on the resolution than that for a high NA system.

Actually, when evaluating the resolution of a low NA system, the simplified deconvolution methods applied in other literatures [31, 86, 87] usually show a good agreement with the results from our approach, thus the simplified deconvolution may be preferred due to its simplicity in this case.

With our resolution evaluation approach, the genuine NA of the experimental system is effectively converted to the value of a hypothetically noise-free microscope system, therefore the genuine NA of the experimental system may be underestimated in terms of the ignorance of the noise-induced resolution degradation, which is a distinct weakness of this method. It is worth noting that we employed a simplified model of an optical microscope to simulate its PSF. Rigorously, there are many more factors that should be considered when modelling the solid immersion fluorescence microscopy. For example, image formation models in fluorescence microscopy should take into account polarisation effects because the fluorescent molecules work as a dipole emitter [138]. When large mismatches occur in the refractive indices of the media of the objective lens and specimen, the PSF may differ from the imaging model used here [139]. For a high NA imaging system, the vectorial analysis is better to be used and a wide variety of imaging conditions, for example, aberrations, vectorial beam illumination and arbitrary scattering of the object, need to be considered [140]. However, despite these factors, it has been demonstrated that the approximate physical model based on wave optics, which is implemented in our approach, is usually possible to obtain accurate predictions as that from rigorous vectorial theories of diffraction [141].

### 3.4.2 Resolution evaluation experiments and results

In our research, 20 nm fluorescent beads (excitation/emission: 625/645 nm) were used to evaluate the resolution of our prototype SIF system. These beads are carboxylate-modified polystyrene microspheres coated with hydrophilic polymer. They are loaded with dyes to make them fluorescent. These 20nm fluorescent beads are supplied as suspensions in water in high density. For the purpose of imaging separate beads, the original bead solution is diluted with distilled water in the ratio of 1:50000 followed by minutes of mixing using a vortex mixer. The diluted solution is pipetted on the flat surface of the ASIL, and then placed in an oven to heat-dry at 60°C for 15 minutes.

Due to the tiny size of these fluorescent beads, the fluorescent emission from each bead is rather weak. In order to improve the SNR of the image, 1000 frames with 0.5 seconds exposure time for each frame were captured by the SIF, and then all of these single frames were averaged to form the final image. The image of a separate 20 nm fluorescent bead from SIF is shown in Figure 3.4.1. For comparison, the simulated image of a 20 nm fluorescent bead from a NA 1.85 microscope system is shown in Figure 3.4.2. By calculating 2D correlation coefficients between the experimental image and a series of simulated images of a 20 nm bead, and locating the simulated image with the highest correlation coefficient with the experimental image, the practical NA of our SIF was established. The simulation was executed with NA of from 1.5 to 2.1 at 0.05 intervals. The coefficient data and quadratic curve fitting are shown in Figure 3.4.3. According to these data, we can conclude the practical NA of the SIF is 1.85 ± 0.01.

When evaluating the NA of the SIF, in order to reduce the effect of random noise in each correlation coefficient, each data point of the coefficient was composed of the average of 5 original data from 5 individual 20 nm fluorescent bead images. These bead images were chosen randomly from different areas in one SIF image. Moreover, random noise was generated in each data point based on a normal distribution, in which the initial correlation coefficient data worked as the mean value of the normal distribution, and the norm of residuals from quadratic curve fitting worked as the standard deviation of the normal distribution. With these noisy data, quadratic curve fitting was performed and repeated for 100 times, at last the average peak value of the fitting curves was calculated. This value is regarded as the practical NA of the SIF.

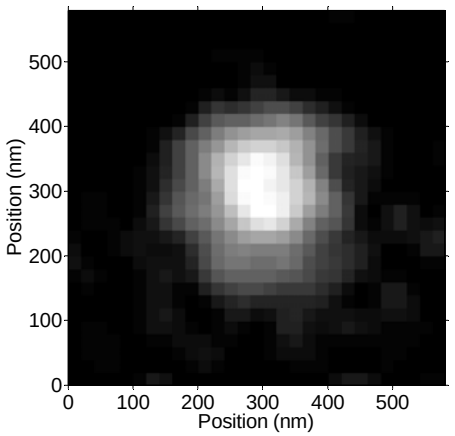


**Figure 3.4.1 20 nm fluorescent bead image obtained with SIF**

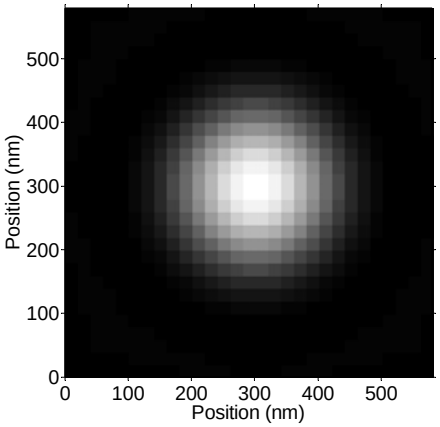


**Figure 3.4.2 Simulated 20 nm fluorescent bead image with NA of 1.85**

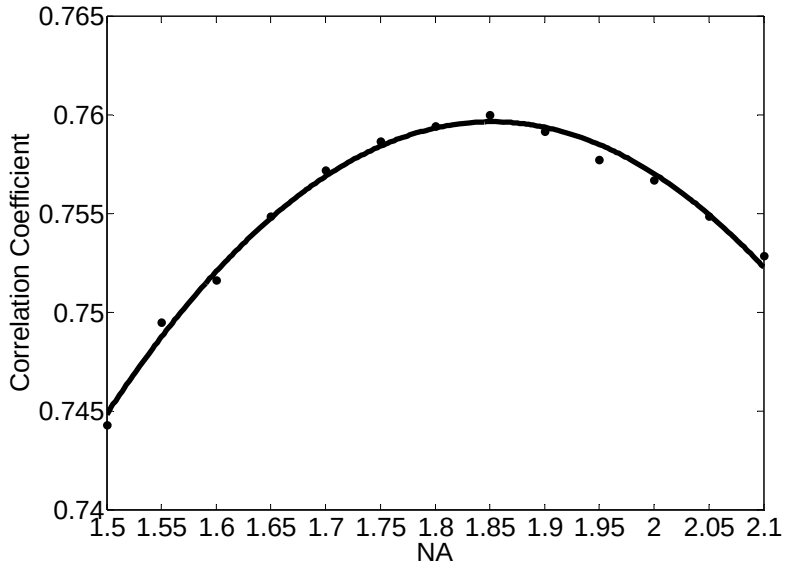


**Figure 3.4.3 Resolution evaluation data/curve of the SIF based on correlation coefficient method**
2D correlation coefficient data and quadratic fitting curve between the experimental SIF image and a series of simulated images of a 20 nm bead under different NA, the peak value is found at (1.85, 0.7597).

From another perspective, the NA of a microscope can be estimated from the size of the BFP as discussed in Subsection 3.3.1. When imaging 20 nm fluorescent beads, the BFP (Figure 3.4.4) of our SIF was also imaged by the BFP camera. From the cross-section profile of the BFP (Figure 3.4.5), the measured value of its outer diameter is 3.99 mm. According to Equation (3.3.2), the NA is:

$$NA = \frac{d}{2f} = 1.995 .$$

The result from BFP measurement tells us our SIF has the potential to approach NA of nearly 2, which is exactly the theoretical value of our ASIL-objective, however, the practical NA has been demonstrated to be 1.85. This difference mainly comes from the resolution degradation induced by the sample thickness and the difficulty for rays to propagate when collection angle approaching 90°. More discussion on this issue, i.e. the near-field imaging property of the ASIL, will be presented in Section 3.6.

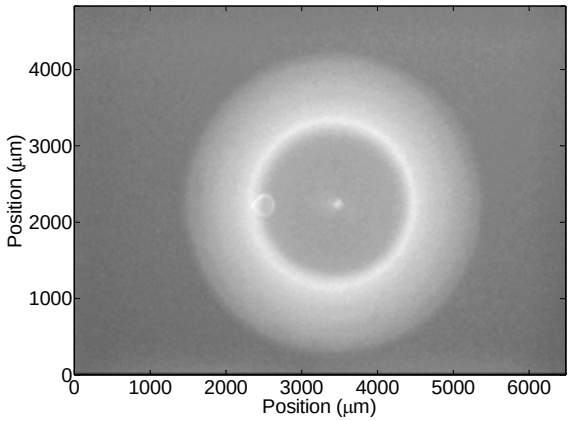


**Figure 3.4.4 BFP image of 20 nm fluorescent beads in SIF**

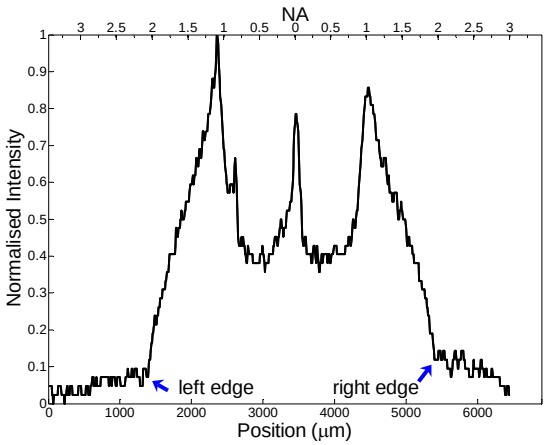


**Figure 3.4.5 Cross-section profile of the BFP image of 20 nm fluorescent beads in SIF**
The estimated NA from this distribution is 1.995 by measuring the distance from edge to edge (as indicated by the arrows); the central peak is the residual excitation reflection.

## 3.4.3 Supplementary resolution evaluation experiments and results

The resolution of our SIF is the most important characteristic we intend to investigate, so it will be beneficial if we examine it from different perspectives in order to draw a more reliable conclusion. Besides 2D correlation coefficient method and BFP estimation to evaluate the resolution of the SIF, another idea is to directly image some sort of standard resolution target, just as the regular method to examine conventional microscopes. However, common resolution targets, like glass slide resolution target with the 1951 USAF test pattern, are not applicable for the SIF due to the limited space to accommodate samples. We therefore need to find other feasible targets.

In Subsection 3.3.3, micro contact printing (μCP) has been successfully applied to make dye grating for the purpose of magnification calibration. Following this idea, if some standard resolution target structure can be replicated with a fluorescence sample by the μCP, it is possible to use this sample as a resolution target for the SIF. The structure of the mold, i.e. the standard resolution target, should be periodic because once it is printed on the ASIL, it is impossible to adjust sample position laterally as the sample is bound to the ASIL. A periodic structure is capable of being replicated in a rather large area, and in this way the possibility of sample coverage in effective FOV of the SIF can be greatly enhanced. For this purpose, we obtained an AFM (Atomic Force Microscopy) calibration grid (Nanosurf AG) with chessboard-like structure of holes in 679 nm pitch. With this calibration grid, fluorescent dye grid samples, working as standard resolution targets, were made with μCP method. A sample of these dye grids was examined under an AFM (EasyScan, Nanosurf AG) and its image is shown in Figure 3.4.6. The finest structures in this dye grid sample are the horizontal grid rows which have the width of 191 ± 30 nm as indicated in Figure 3.4.6. Some parts of these structures in the SIF image can be clearly seen in Figure 3.4.7, which is consistent with the resolution evaluation result obtained in the previous subsection.

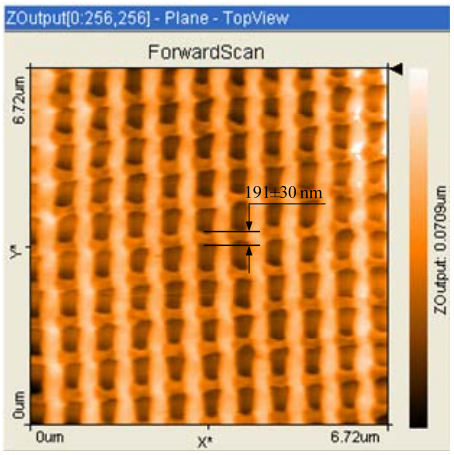


**Figure 3.4.6 AFM image of 679 nm pitch dye grid**

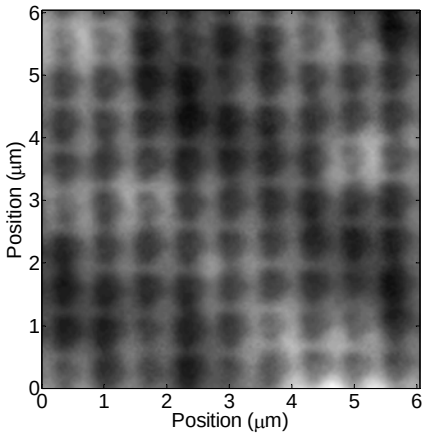


**Figure 3.4.7 Image of 679 nm pitch dye grid obtained with SIF**
Some parts of the structure of the horizontal rows can be clearly seen.

When measuring the dye grid size under the AFM, we also measured its thickness. The measured value of the thickness is about 30 nm. In Section 3.6, we will see it is this small thickness that ensures the high resolution performance of the SIF.

The BFP image (Figure 3.4.8) of the dye grid was also captured. The measurement of its cross-section profile (Figure 3.4.9) shows the identical value as the measurement of the BFP image of 20 nm fluorescent beads.

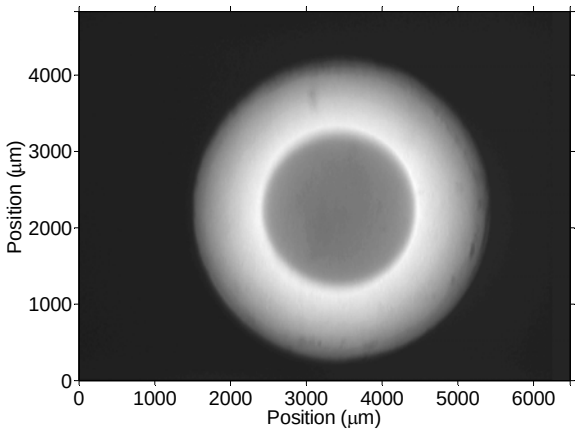


**Figure 3.4.8 BFP image of 679 nm pitch dye grid in SIF**

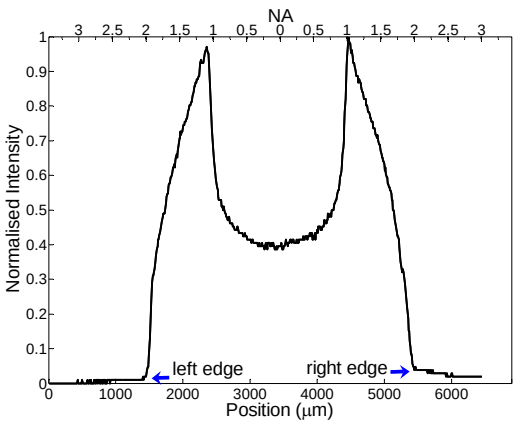


**Figure 3.4.9 Cross-section profile of the BFP image of 679 nm pitch dye grid in SIF**
The estimated NA from this distribution is 1.995 by measuring the distance from edge to edge (as indicated by the arrows), which is as same as the result of BFP image measurement of 20 nm fluorescent beads.

## 3.4.4 Cell imaging

Fluorescence microscopy is widely used in biology in which fluorescent stains are applied to the specimen in order to image a specific protein or other molecule of interest. In a like manner, our SIF is designed to perform high-resolution imaging on biological specimen, especially cells. In our research, we imaged Jurkat cell membrane by SIF. Jurkat cells are an immortalized line of T lymphocyte cells from human blood.

The labelling material used to stain cell membrane is fluorescent carbocyanine DiD (Invitrogen) that diffuses laterally within the plasma membrane. Its spectral character holds the excitation maxima 644 nm and emission maxima 665 nm. Before labelling, in order to assist adhesion of cells to the substrate, a pre-cleaned ASIL was covered with 0.01% poly-L-lysine (PLL, Sigma-Aldrich) solution for 15 min at 20 ºC followed by

distilled water washes. The procedure of poly-L-lysine covering and distilled water washing was repeated for three times. Then Jurkat cell culture media was overlaid onto the PLL-coated ASIL and cells were allowed to adhere for 3 hours in incubator at 37 ºC. Adherent cells were then fixed by adding 10% buffered paraformaldehyde in phosphate buffered saline (PBS). After fixation for 20 min, the cells were stained with DiD (1:100 in PBS) for 40 min, and then washed several times with PBS. The final PBS wash was removed as much as possible without drying the cells.

The Jurkat cell membrane image is shown in Figure 3.4.10. In this image, the fine feature of pseudopodium indicated by an arrow is clearly seen as a protruding structure. The measured value of the width of the pseudopodium tip is about 350 nm. In order to compare the resolution performance with and without the ASIL, the same Jurkat cell was imaged by the conventional epi-fluorescence microscope, which was fulfilled by flipping the ASIL over, as shown in Figure 3.4.11. In this image, the morphological specificity of the cell membrane including the pseudopodium is unresolvable due to the low NA (0.55) and strong background fluorescence scatter of the conventional microscope. From these two images, it is evident the resolution has been significantly increased by transforming a conventional fluorescence microscope to a SIF system.

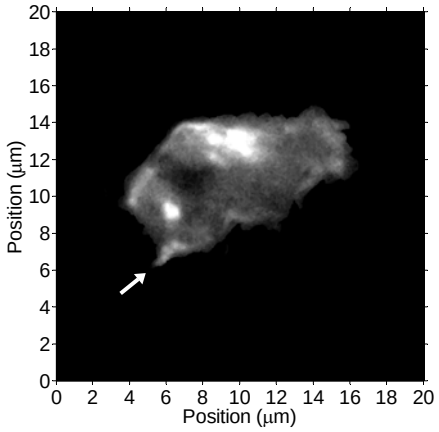


**Figure 3.4.10 Image of Jurkat cell membrane obtained with SIF**
The fine feature of pseudopodium is clearly seen as indicated by the arrow.

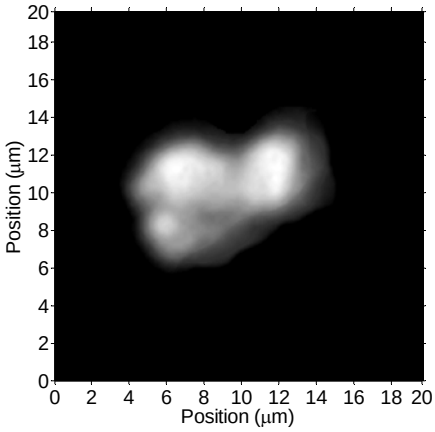


**Figure 3.4.11 Image of Jurkat cell membrane obtained with the conventional epi-fluorescence microscope**
NA of the objective lens: 0.55. The fine feature of pseudopodium is unresolvable due to the low NA and strong background fluorescence scatter.

Another demonstration of cell imaging undertaken by the SIF is Jurkat cell F-actin cytoskeleton imaging. The labelling material used to stain F-actin is Atto655 Phalloidin (Sigma-Aldrich) that works at the excitation maxima 663 nm and emission maxima 684 nm. The cell labelling procedure is very similar to the membrane stain except that the specimen cells were permeabilized with 0.1% Triton X-100 and 5% bovine serum albumin (BSA) in PBS before staining.

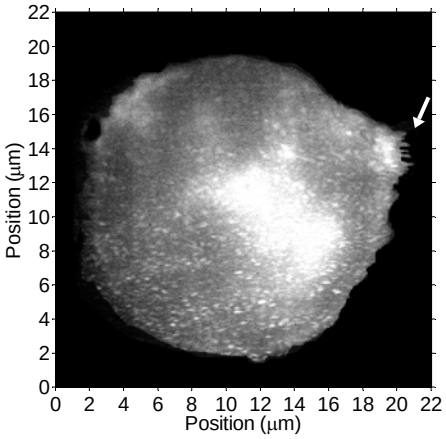


**Figure 3.4.12 Image of Jurkat cell F-actin cytoskeleton obtained with SIF**
Filopodia are observed in the upper right of the cell margins as indicated by the arrow.

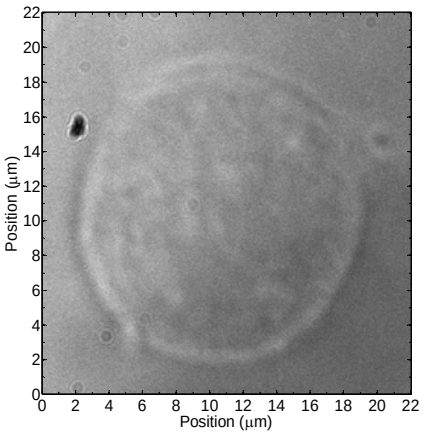


**Figure 3.4.13 Image of Jurkat cell obtained with bright-field transmission microscope**
Filopodia cannot be observed in this image.

The fluorescent image of Jurkat cell F-actin cytoskeleton obtained with the SIF is shown in Figure 3.4.12. From this image, we see that most of the F-actin in this cell is concentrated around the nucleus, while some exist on the periphery of the cell. Significantly, tenuous new filopodia are observed in the upper right of the cell margins as indicated by the arrow in the image. Their widths are estimated to be around 200 nm. Apart from the fluorescent image, a conventional bright-field transmission image (Figure 3.4.13) of the same cell was also obtained by altering the original epi-illumination from a laser to a transmitted illumination from a LED (Phillips). The LED, with central wavelength 625 nm, was placed to face the flat surface of the ASIL to construct a transmitted illumination. The LED beam was collimated by a 20 mm focal length lens to form a Köhler illumination. The bright-field transmission image has low contrast and resolution because not only the cell is rather transparent but also the image quality is degraded by the chromatic aberration induced by wide spectrum of LED

illumination. By comparing these two images, it is shown that the high-resolution SIF is especially suitable to image flat and transparent cell specimen.

### 3.4.5 Discussion

We have experimentally demonstrated the SIF with the effective NA of 1.85. As far as we know, currently the highest NA obtained by an objective lens in market is the NA of 1.65 [71] from Olympus. Apparently the high NA of our ASIL-objective is superior to any kind of commercially available objective lenses so far. In addition, the 1.65 NA objective lens requires the use of expensive 1.78 refractive index coverslips made of either LAFN21 glass or SF11. This objective lens also requires special $n_D$ = 1.78 liquid (Cargille) which is volatile and leaves a crystalline residue [142]. In our SIF, there is no need to use either customised coverslips or volatile high-index liquid, which makes the application of the SIF more convenient than the microscopes applying 1.65 NA Olympus objectives.

In our research, the ASIL is combined with a long working distance objective to form the high NA ASIL-objective. The major concern that we apply this type of objective is to make enough space to accommodate the ASIL. However, it is not necessary to use a long working distance objective lens, which is more expensive than a regular objective lens with same NA, to build an ASIL-objective. An ASIL can be directly combined with a regular objective lens provided that the ASIL size can be fitted in the working distance of this objective. For example, for a regular Olympus UIS2 20× 0.5 NA

objective with a working distance of 2.1 mm, it is still feasible and possible to use an ASIL (material: S-LAH79, working wavelength: 632.8 nm) with the radius of smaller than 0.7 mm to achieve a NA as high as the one reported in this chapter. So, the ASILs have great potential to be applied as an add-on to an existing microscope to realise much higher resolution than its original level.

It is worth noting, besides the high spatial resolution, another advantage of SIF is its high fluorescence collection efficiency. According to the theory on the radiation of dipoles near the surface of two dielectric media, which will be discussed in Section 3.6, the radiation from the dipole located on a flat surface of dielectric medium directs more on the higher index medium. In SIF, the high fluorescence collection efficiency is mainly from the efficient electromagnetic coupling from the fluorophore, working as dipole emitters, to optically dense SIL material via evanescent fields. This property has been analysed and demonstrated in the SIF systems applying either HSILs [115] or ASILs [90] [91]. Although a very narrow bandpass filter was used to eliminate chromatic aberration (CA) in our case, which offsets the high fluorescence collection efficiency in SIF, we could take advantage of this characteristic by using other methods, for example the combination of a negative lens and an ASIL, to eliminate or balance CA. The CA and its elimination or correction will be discussed in detail in the next section.

Another case associated with CA is dual labelled fluorescent sample imaging in SIF. It is possible to image dual labelled fluorescent sample with the same ASIL by slightly

defocusing when changing one wavelength to the other for imaging, provided that the difference between the two wavelengths is minor, otherwise the mismatch between the ASIL configuration and the imaging wavelength can lead to severe CA that degrades the image quality.

## 3.5 Aberrations of SIF

### 3.5.1 Monochromatic aberrations

In a diffraction-limited optical system, the resolution is simply limited by diffraction. However, in a practical optical system, aberrations are always present because the refraction in a real lens diverges the beams from the same object point to different image points. Well-designed lenses can work in a nearly aberration-free state, so practically we regard them as diffraction-limited optical components under certain conditions. In our SIF setup, the objective lens is plano apochromat and all the other lenses are achromatic doublets except the ASIL, which means the SIF can be considered as the combination of a diffraction-limited conventional microscope and an aberrated ASIL. In this way, the aberrations in the SIF are totally induced by the ASIL, that is, we just need to investigate the aberrations in the ASIL rather than the SIF. In Subsection 3.2.2, it has been discussed and concluded that there is no spherical aberration for on-axis objects or coma for off-axis objects when properly imaging with the ASIL. However, the other three monochromatic aberrations, which are astigmatism, field curvature and distortion, still exist and determine the image quality and resolution of the ASIL imaging.

In order to investigate the aberration issues further, our current ASIL configuration (material: S-LAH79; radius: 2.5 mm) has been modelled in optical design software ZEMAX (Zemax Development Corporation) (Figure 3.5.1). In ZEMAX, the aberrations of an optical system can be examined in spot diagrams. Assume a uniform rectilinear grid is put on the entrance pupil of an optical system. From an on-axis or off-axis point object, many rays are launched to pierce each grid point. The rays arrive in image space and converge toward the image plane. A two-dimensional distribution of these ray pierces in the image plane is called a spot diagram [21]. The distribution of spot diagram depends on the aberrations in the system. For a diffraction-limited system, the spot diagram would appear as a single point. The spot diagram of our ASIL in the full FOV of 40μm × 40μm is shown in Figure 3.5.2 in which single wavelength 632.8 nm is considered. From this through-focus (±2 μm) spot diagram, we can perceive the distribution of all the five monochromatic aberrations.

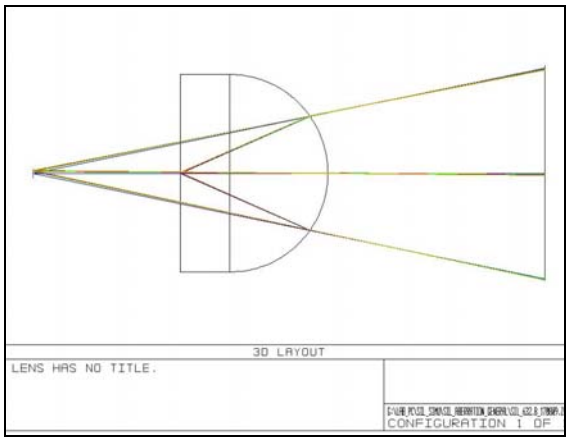


**Figure 3.5.1 Layout of ASIL imaging in ZEMAX modelling**

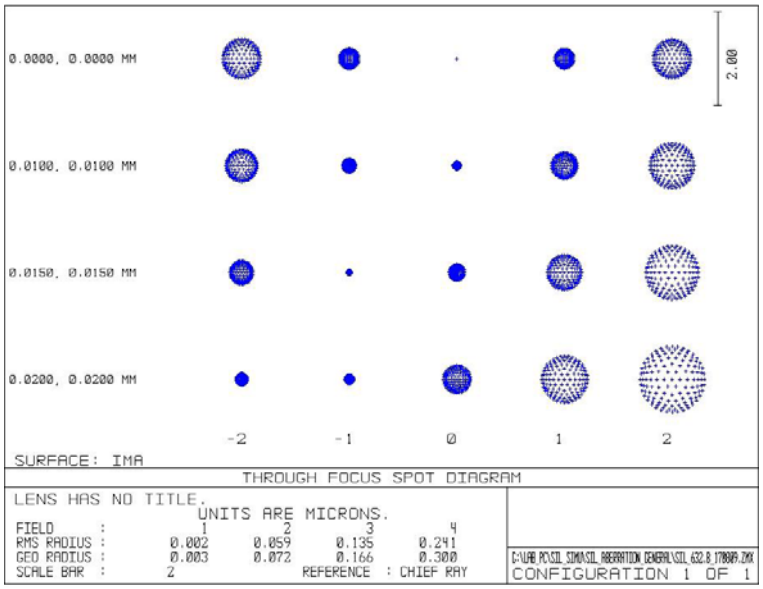


**Figure 3.5.2 Spot diagram of ASIL imaging in ZEMAX modelling**

(1) Spherical aberration (SA): the top row of the diagrams in Figure 3.5.2 is the on-axis through-focus spot diagrams. The plane in the middle marked with '0' is paraxial focus plane. All rays are coincident here and the spot diagram is just a point. In the planes equidistant on either side of the focus plane, the spot diagrams appear symmetric. They get larger as moving away from paraxial focus because the distribution in these defocused planes is a geometrically scaled version of the pupil distribution. From this row, as predicted, we know there is no SA in the ASIL imaging for on-axis objects.

(2) Coma: check the second, third and fourth rows in Figure 3.5.2, which represent the off-axis through-focus spot diagrams of the full FOVs in 20μm×20μm, 30μm×30μm and 40μm×40μm, we can see there is no 'ice cream' cone shape distribution at either focal or defocused planes. All rays from the same zone of the object come to a focus at

the same point. Again, as predicted, there is no coma in the ASIL imaging at full FOV of 40μm × 40μm.

(3)Astigmatism: check off-axis spot diagrams again, we cannot see any line or elliptical shape distribution on either side of focus point, which means there is no noticeable astigmatism at full FOV of 40μm × 40μm.

(4)Field curvature (FC): it is obvious the displacement along the chief ray from the paraxial plane (marked '0' at the bottom) to the left (minus) side increase as the FOV increase, which means the image surface bends in this way. It is also shown that the spot diagrams taken at various FOV in the paraxial plane show a steady increase in diameter. So, FC does exist. Quantitatively, the value of field curvature is 1.2 μm at full FOV of 40μm × 40μm (Figure 3.5.3, left).

(5)Distortion: spot diagrams generated by rim rays are a bit radially displaced from their ideal positions, and this displacement increases with FOV increasing. It can therefore be concluded there is slight distortion. Quantitatively, the value of distortion is 0.08% at full FOV of 40μm × 40μm (Figure 3.5.3, right). This amount of distortion usually can be ignored.

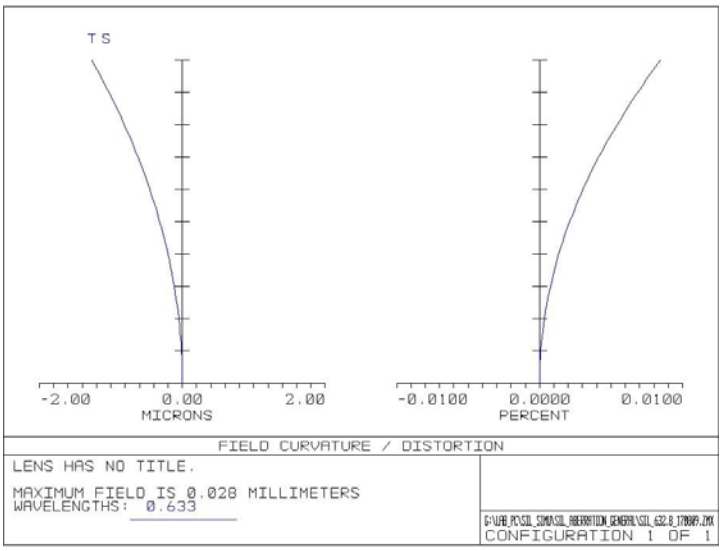


**Figure 3.5.3 Field curvature and distortion curves of the ASIL imaging in ZEMAX modelling**

In summary, the most significant monochromatic aberration existing in our ASIL imaging is field curvature.

## 3.5.2 Chromatic aberration (CA)

Fluorescence microscopes mostly work on multi-colour condition due to the broad emission spectrum of normal fluorescent labels like dyes. In this circumstance, chromatic aberration (CA) will appear and sometimes can degrade the image quality heavily. The ASIL material used in our research is highly dispersive with a considerable Abbe number of 28.3, thus severe CA could be produced in SIF, which might cause major loss of resolution. In ZEMAX, the on-axis spot diagrams of the ASIL (material: S-LAH79; radius: 2.5 mm) in single wavelength at 632.8 nm and 50 nm spectrum centred at 632.8 nm have been modelled and displayed in Figure 3.5.4 and 3.5.5 correspondingly. From these figures, we clearly see the appearance of CA considerably

blurs the image and leads to a low resolution performance. Therefore we must take steps to eliminate CA.

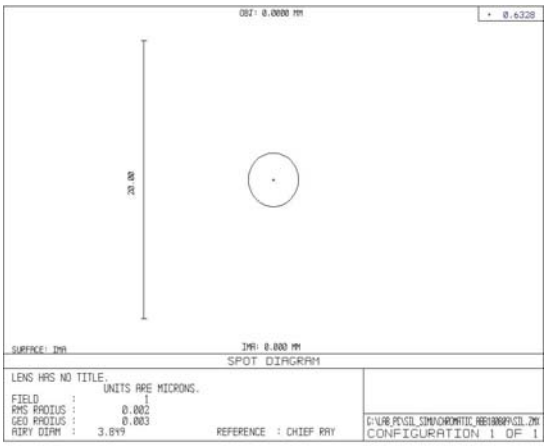


**Figure 3.5.4 Spot diagram of ASIL imaging in single wavelength at 632.8 nm in ZEMAX modelling**
ASIL material: S-LAH79; radius: 2.5 mm. The black circle in the diagram represents the corresponding Airy disk.

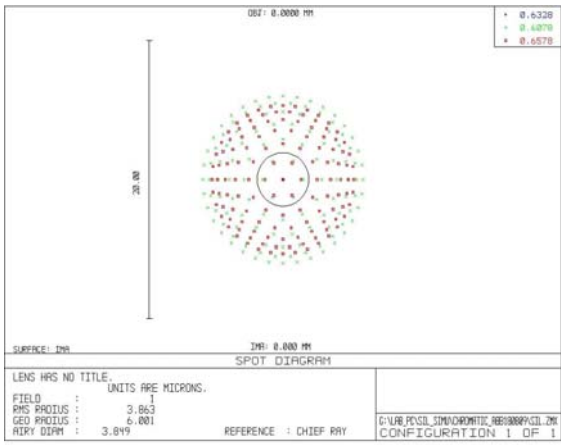


**Figure 3.5.5 Spot diagram of ASIL imaging in 50 nm spectrum centred at 632.8 nm (632.8/50 nm) in ZEMAX modelling**
ASIL material: S-LAH79; radius: 2.5 mm. The black circle in the diagram represents the corresponding Airy disk.

## 3.5.3 CA elimination and correction

In order to maintain the high-resolution performance of SIF, CA must be properly eliminated or corrected. In our research, we try to find the most convenient and effective way to eliminate CA in our prototype SIF system. Several methods have been investigated experimentally or theoretically.

(1) A straightforward method to eliminate CA is to use a narrow passband filter as emission filter. In this way, the imaging spectrum can be constrained in a very limited

range, and then the differences of refractive indices to different wavelengths can be compressed to a tolerable level. In Figure 3.5.6, two SIF images of the same 200 nm fluorescent bead samples are shown. Image (a) and (b) were captured by using 670/3 nm (central wavelength = 670 nm, passband = 3 nm) and 675/50 nm bandpass filters as emission filter separately. The effect of CA elimination by using narrow passband emission filter is apparent according to the comparison.

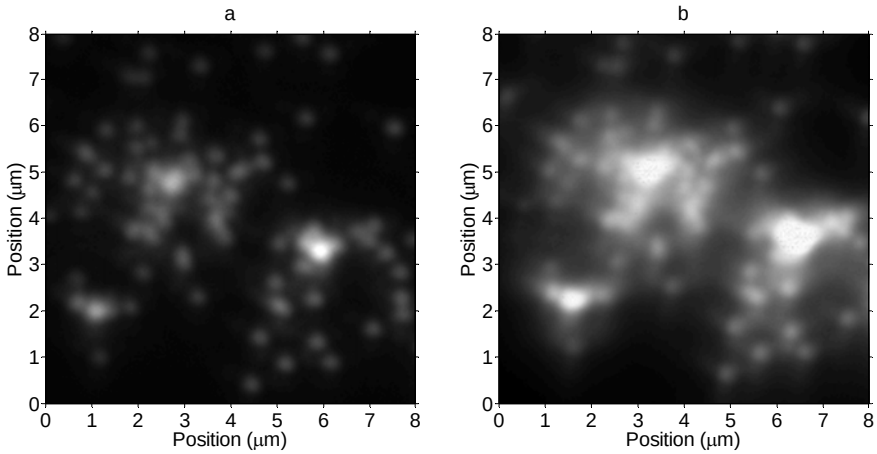


**Figure 3.5.6 Two SIF images of the same field of 200 nm fluorescent beads using (a) 670/3 nm and (b) 675/50 nm bandpass filters as emission filter**

The shortcoming of this method is also obvious. The narrower the passband of the emission filter, the less fluorescent signal can be collected. When the quantum yield of fluorophore is low, the application of a very narrow bandpass filter will make the imaging quite difficult. In our research, thanks to the highly efficient photon collection of our EMCCD camera, the problem of photon budget is usually less critical. Therefore, in practice we use a 670/3 nm laser line interference filter, an extreme narrow bandpass filter, as emission filter to eliminate CA.

(2) A regular way to correct CA in traditional optical design is to carefully choose suitable combination of positive (converging) lenses and negative (diverging) lenses, or of glasses with different refractive indices. The ASIL practically works as a positive lens, so it is possible to combine it with a negative lens made with different glass to balance CA. We simulated the combination of a negative lens with focal length -12 mm and our ASIL in ZEMAX (Figure 3.5.7) in order to correct CA, and it appears they work very well. The negative lens is a plano-concave lens made of optical glass SF11 ($n_d$ =1.78472, $v_d$ =25.76). Comparing its on-axis spot diagram in Figure 3.5.8 with Figure 3.5.5, it is observable this combination efficiently corrects CA coming from 50 nm full fluorescence spectral width centred at 632.8 nm even if a small amount of spherical aberration is produced. Quantitatively, from chromatic focal shift curves with and without negative lens (Figure 3.5.9 and Figure 3.5.10), we know the CA have been reduced to 0.4% of the original amount with the help of the negative lens. Moreover, the simulation also shows that the full fluorescence spectral width can be extended to 100 nm centred at 632.8 nm while maintaining the theoretical NA of 2 for a 40μm × 40μm full FOV. The negative lens with focal length -12 mm used in this ZEMAX simulation was chosen from the optical component catalogue of Edmund Optics, Inc. The distance between the negative lens and the ASIL was adjusted manually in order to find the best imaging performance. Predictably, if we apply custom-designed negative lens and optimize its configuration with merit functions in ZEMAX, an even better imaging performance could be achieved with the combination of an ASIL and a negative lens.

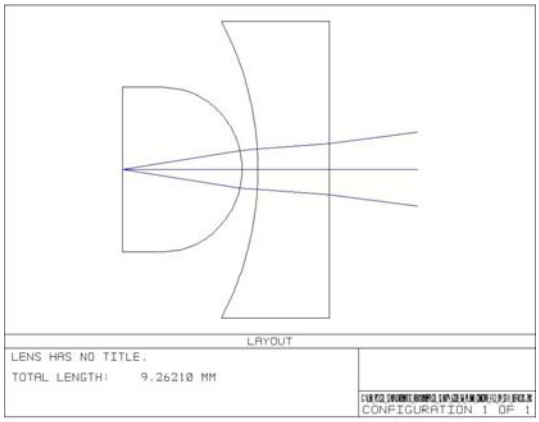


**Figure 3.5.7 Layout of the combination of the ASIL and an f = -12 mm negative lens in ZEMAX modelling**


**Figure 3.5.8 Spot diagram of the imaging of the combination of the ASIL and an f = -12 mm negative lens in 50 nm spectrum centred at 632.8 nm (632.8/50 nm) in ZEMAX modelling**
The black circle in the diagram represents the corresponding Airy disk.

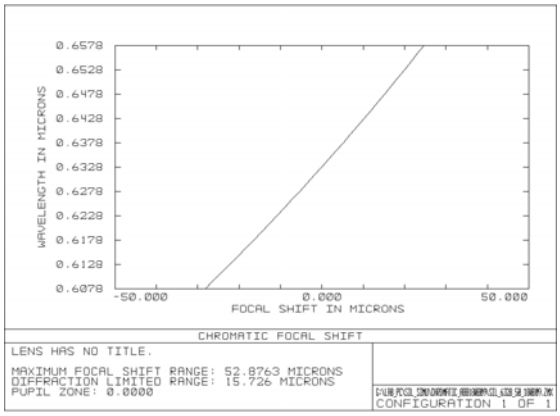


**Figure 3.5.9 Chromatic focal shift curve of the ASIL imaging in 50 nm spectrum centred at 632.8 nm (632.8/50 nm) in ZEMAX modelling**
The maximum focal shift is 52.8763 μm.

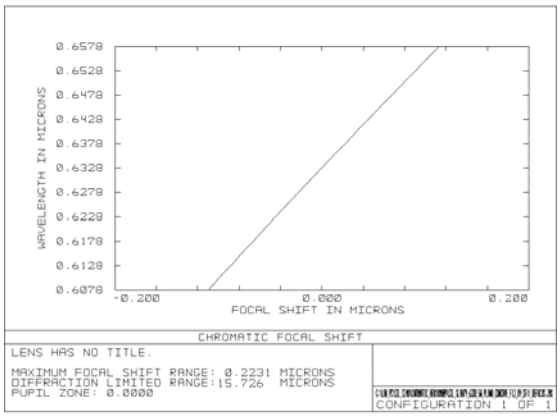


**Figure 3.5.10 Chromatic focal shift curve of the imaging of the combination of the ASIL and an f = -12 mm negative lens in 50 nm spectrum centred at 632.8 nm (632.8/50 nm) in ZEMAX modelling**
The maximum focal shift is 0.2231 μm.

The shortcoming of this method mainly exists in its positioning. For a bench-top system, it is probable that there will be many difficulties in rendering two closely adjacent small optical components, here the ASIL and the negative lens, precisely concentric and axially in position. For this reason, we did not examine this method experimentally. However, this method indicates an efficient way to conquer the occurrence of CA in the application of ASILs.

(3) Other researchers proposed the idea of diffractive optical element (DOE) to correct CA [99]. A simple DOE (Figure 3.5.11) with only weak focusing power has proved to be sufficient to correct the majority of the chromatic focus shift caused by the ASIL dispersion. The DOE is designed to focus in the zero diffraction order, and the weak power of the DOE eases the fabrication requirements for the device. In a special case (ASIL material: ZnS; radius: 1 mm), the correction improves the CA by more than a factor of ten for imaging an on-axis object [99].

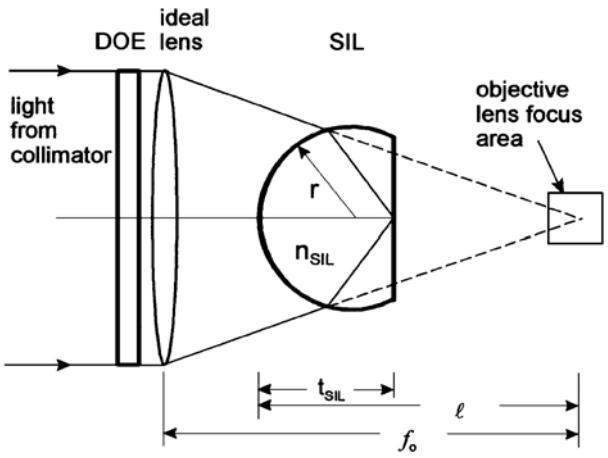


**Figure 3.5.11 Schematic of CA correction using a diffractive optical element (DOE) with ASIL [99]**
DOE with weak focusing power is placed in front of a matched ideal lens to correct CA generated by the ASIL.

From an application point of view, certainly it is better to assemble DOE with ASIL to form one entity. DSIL, which is mentioned in Subsection 3.2.1, is exactly this kind of thing. A well designed DSIL can not only correct CA, but also eliminate other aberrations in a rather large FOV that is beneficial to wide-field imaging. This method still has some fabrication difficulties due to the aspherical fabrication so far.

(4) Another scheme to eliminate CA is to reduce ASIL size. The CA comes from the optical path difference (OPD) of wide imaging spectrum in the ASIL. OPD is proportional not only to the refractive index, but also to the propagation distance. To reduce the size of ASIL is actually to reduce the emission light propagation distance, and then to reduce CA.

We now investigate how much CA can be reduced by decreasing ASIL size, or to put it another way, what are the ranges of imaging wavelengths that can be tolerated while maintaining a high $NA_{eff}$ with different ASIL sizes. The analysis on this issue was carried out by combining ray optics and wave optics simulations. The imaging mechanism of SIF can be separated into two parts. One is the ASIL imaging system that produces aberrations; the other is a diffraction-limited conventional microscope system that is theoretically aberration-free. The former part is simulated in ZEMAX using ray tracing; and the latter part is simulated in MATLAB using the theory of wave optics. Specifically, an ideal on-axis point object, which hypothetically is in the size of zero, is converted into its image with finite size by the ASIL. The prediction from ray optics is convolved with the PSF determined by aberration-free diffraction. The final image

produced in MATLAB is a measure of the PSF of the whole system. The width (FWHM) of the PSF is used to quantify the $NA_{eff}$ of the SIF system.

In these simulations, the central imaging wavelength was 632.8 nm, the ASIL material was S-LAH79 and the conventional microscope system was supposed to have the NA of 2. The curves depicting the relationship between the full fluorescence spectral width of the imaging and the $NA_{eff}$ are presented in Figure 3.5.12, in which the ASILs in different sizes are examined. The simulation results indicate, for on-axis objects, the smaller the ASIL, the broader the fluorescence imaging spectral width that can be tolerated for a given spatial resolution. The idea to eliminate CA by reducing ASIL size appears quite effective.

Reducing ASIL size looks pretty promising for reducing CA. This idea neither sacrifices fluorescence collection efficiency nor needs to add new optical elements. However, using small size ASILs inevitably causes difficulties in the mechanical support for the ASILs. It also makes the sample preparation, especially biological sample preparation, more difficult due to the reduction of available area on the flat surface of the ASIL. To deal with these problems, it would be necessary to modify the ASIL holding mechanics or the ASIL configuration itself.

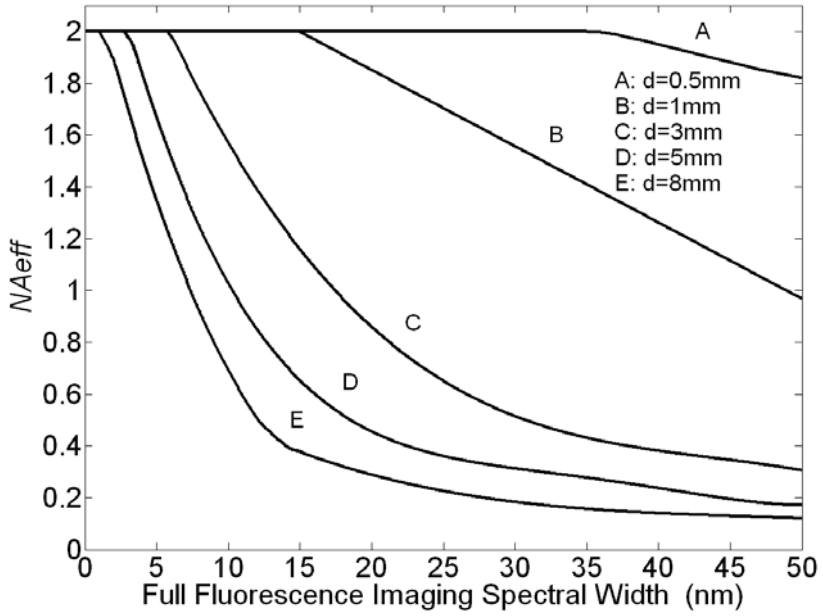


**Figure 3.5.12 Curves between full fluorescence spectral width and $NA_{eff}$ (on-axis) with different ASIL sizes in the SIF from simulations**
ASIL material: S-LAH79; central wavelength: 632.8nm; d: ASIL diameter. It shows the smaller the ASIL, the broader the fluorescence imaging spectral width that can be tolerated for a given spatial resolution.

## 3.5.4 FOV determined by aberrations

The method of using small size ASIL in SIF has many advantages considering the elimination of CA. We drew this conclusion only by investigating on-axis imaging property of the SIF. The off-axis imaging performance of the SIF employing an ASIL also needs to be investigated because we anticipate developing a wide-field microscopic technique. Predictably, reducing the ASIL size would make the optical power of the ASIL stronger. Then some off-axis aberrations, like field curvature and distortion, could become severe. Besides CA, these aberrations could also lead to the degradation of the image quality of the SIF when increasing the FOV.

Employing the same simulation method described in the previous subsection, a series of point objects located at different off-axis positions in the SIF were simulated. The point responses of the SIF in different FOV were converted to the corresponding $NA_{eff}$s in different FOVs, which shaped the relationship curves between FOVs and $NA_{eff}$s.

The fluorescence imaging spectral widths used here are from the simulation results shown in Figure 3.5.12. We choose the upper limitation of imaging spectral width when maintaining NA of 2, that is, the bandwidths are 35, 15, 5, 3 and 1 nm when ASIL diameters are 0.5, 1, 3, 5 and 8 mm correspondingly. The central imaging wavelength is still 632.8 nm. For these off-axis point object images, we do not intend to distinguish each type of aberration from others; instead, we just use the point response as a comprehensive indication of the aberration to evaluate the corresponding $NA_{eff}$s. Figure 3.5.13 shows the curves between FOVs and $NA_{eff}$s, which indicates that the bigger the ASIL, the larger the effective FOV we can achieve. In our research, we chose a 5 mm diameter ASIL to work with a 3 nm passband emission filter to achieve at least 50 μm valid FOV with the theoretical NA of 2 (dashed curve in Figure 3.5.13).

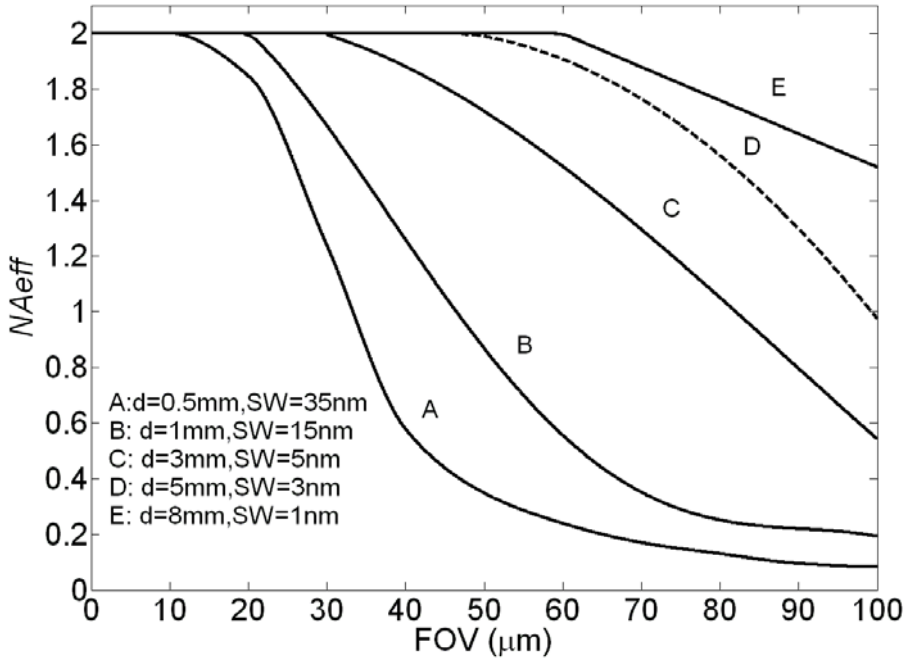


**Figure 3.5.13 Curves between field of view (FOV) and $NA_{eff}$ with different ASIL size in the SIF from simulations**
ASIL material: S-LAH79, central wavelength: 632.8nm, d: ASIL diameter, SW: full fluorescence spectral width. It shows the bigger the ASIL, the larger the effective FOV we can achieve. The dashed curve depicts the relationship between the FOVs and $NA_{eff}$s when ASIL diameter is 5 mm and full fluorescence spectral width is 3 nm which was adopted in our experiments.

Summing up these simulation results described above, we can draw a conclusion on the relationships between ASIL size, fluorescence spectral width and FOV as shown in Figure 3.5.14. When the theoretical NA is maintained at 2, the feasible fluorescence spectral width decreases with increasing ASIL size; on the contrary, the feasible FOV increases with increasing ASIL size. In other words, to reduce CA, we need a fairly small size ASIL; meanwhile, to achieve large FOV, we need a fairly large size ASIL. These results obviously conflict. From the application point of view, it is necessary to find a trade-off between fluorescence spectral width and effective FOV. The green dashed ellipse in Figure 3.5.14 indicates the parameters adopted in our experiments in

which ASIL diameter, full fluorescence spectral width and FOV were designated as 5 mm, 3nm and 50 μm.

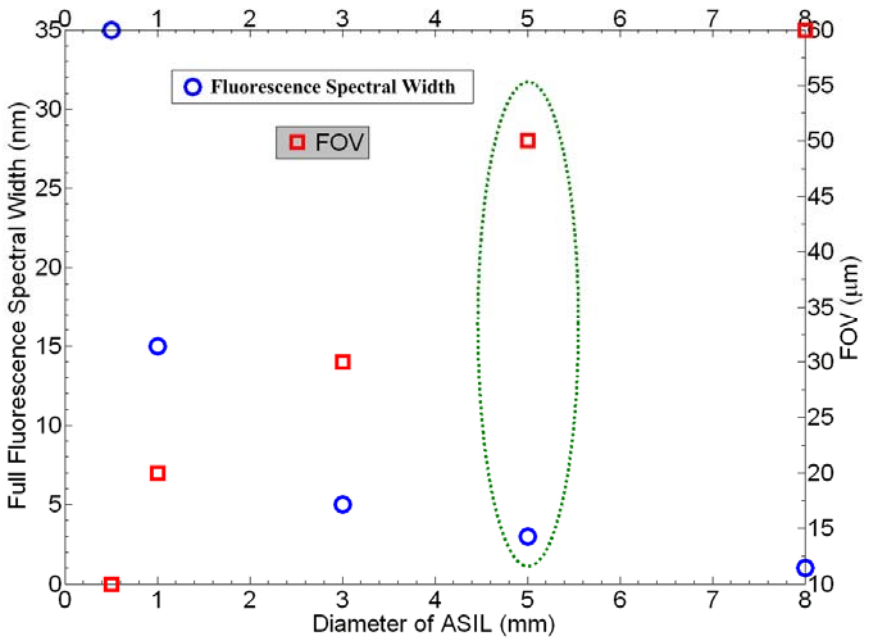


**Figure 3.5.14 Data depicting the relationships between ASIL size, full fluorescence spectral width and field of view (FOV) when $NA_{eff}$ of the SIF is maintained at 2 from simulations**
Blue circle markers: data between ASIL size and full fluorescence spectral width; red square markers: data between ASIL size and field of view (FOV); ASIL material: S-LAH79, central wavelength: 632.8nm. The green dashed ellipse indicates the parameters adopted in our experiments in which ASIL diameter, full fluorescence spectral width and FOV were designated as 5 mm, 3nm and 50 μm.

## 3.5.5 Discussion

In this section, our discussion on aberration issues of SIF is subject to the ignorance of fabrication errors. However, in reality, the deviations of ASILs produced in fabrication from the ideal design degrade the image quality and resolution performance of SIF. Other researchers estimated the aberrations from fabrication errors, including thickness error and aspheric error, and the allowance for these errors [90]. Spherical aberration $W$ caused by thickness error $d$ is given as:

$$W = nd[n^2(\sqrt{1-\sin^2\theta}-1)-(\sqrt{1-n^2\sin^2\theta}-1)] \quad (3.5.1)$$

here, $n$ is refractive index of ASIL martial, $\theta$ is emission angle in the image space. Using Rayleigh's quarter-wave criterion, there is $|W| < \lambda/4$ for $\sin\theta = 1/n$ where $|W|$ reaches its maximum, the allowance for thickness error $d$ is:

$$|d| < \lambda/4n(n\sqrt{n^2-1}-n^2+1) \quad (3.5.2)$$

In the same way, for the aspheric error $b$, as a deviation from a perfect spherical surface, there are:

$$W = b[n\sqrt{1-\sin^2\theta}-\sqrt{1-n^2\sin^2\theta}] \quad (3.5.3)$$

$$|b| < \lambda/4\sqrt{n^2-1} \quad (3.5.4)$$

In our case, for $\lambda$ = 632.8 nm, $n_{632.8nm}$ = 1.99613, the allowance for thickness error is $|d|$ < 0.17μm, and that for aspheric error is $|b|$ < 0.1 μm. The latter value is feasible to achieve in real fabrication, however, the former value is too rigorous to fulfil in real fabrication. The actual thickness errors of our ASILs are within a few microns, which results in some residual spherical aberration. However, most of this spherical aberration can be balanced by slight defocusing from the paraxial focus. An extensive discussion on balancing of defocus aberration with spherical aberration for general optical imaging system can be found in Wolf's book [143]. To tackle the aberrations induced by fabrication errors, other researchers presented some new design ideas on SILs based on aberration theory that can be found in Section 2.7.

# 3.6 Near-field imaging property of SIF

## 3.6.1 Ray tracing analysis

So far, we always suppose the objects are perfectly in contact with the flat surface of an ASIL, that is, we ignore the air gap between the objects and the ASIL. However, a genuine sample or a part of it, depending on its shape and texture, usually has an air gap towards the flat surface of the ASIL. Now we are going to examine the influence of the existence of this air gap on the resolution of a SIF system.

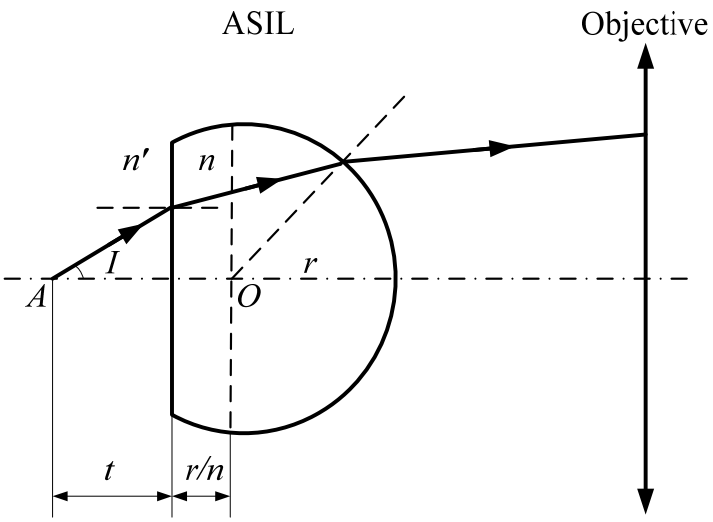


**Figure 3.6.1 Ray propagation model of an on-axis object with a gap towards an ASIL**
The object is situated at point *A*, the gap distance is *t*, the medium in this gap has the refractive index *n'*, the radius and refractive index of the ASIL are *r* and *n*.

At this time, we are going to employ ray tracing method to discuss this issue. A geometric model of the emission propagation from an on-axis fluorescent sample with the gap width *t* towards an ASIL is shown in Figure 3.6.1, here we do not restrict the

medium in this gap to be air, but generalise the medium as anything with a refractive index $n'$. From the figure, it is clear there is:

$$NA_{eff} = n' \sin I \tag{3.6.1}$$

When emission angle $I$ approaches its maximum 90°, the above equation becomes:

$$NA_{eff} \approx n' \sin 90° = n' \tag{3.6.2}$$

which means the $NA_{eff}$ is determined by the refractive index of the gap between the object and the ASIL, rather than the refractive index of the ASIL.

From the analysis above, we can conclude when the sample thickness is rather large, even if it is in close contact with an ASIL, the sample is effectively immersed in the medium made of the same material as the sample itself, then the $NA_{eff}$ of the SIF will be determined by the sample refractive index rather than the refractive index of the ASIL. A thin sample is much better for the SIF to demonstrate its high resolution. According to our experimental examination on the resolution of our SIF described in Subsection 3.4.3, we know when the sample thickness is around 30 nm, our SIF can still perform fluorescence imaging with the $NA_{eff}$ of 1.85. This thickness value could be used as a reference when applying the SIF in practice.

The conclusion above confirms a very important characteristic of SIF – SIF performs the best resolution in near-field imaging mode. This explains why SIL technique is widely used in high-resolution semiconductor inspection [83]. In this application, the semiconductor targets, which usually are made of the same material as SILs, are set to

tightly touch the flat surfaces of SILs without any gaps, and in such condition SILs work in near-field imaging mode without degradation of resolution.

### 3.6.2 Dipole emitter analysis

In a classic electrodynamics framework, fluorophore molecules, the basic components of fluorescent dyes, perform as radiating electrical dipoles. When embedded within a dielectrically homogenous environment, the differential power of the radiating dipoles is expressed by the following equation [144]:

$$\frac{dP}{d\Omega} = \frac{\omega^4 {p_0}^2}{32\pi^2 \varepsilon_0 c^3} \sin^2\theta \qquad (3.6.3)$$

here $\omega$ is the angular frequency of the wave, $p_0$ is the power moment, $\varepsilon_0$ is the electric constant, $c$ is the velocity of light and $\theta$ is the angle between the dipole axis and the chosen direction of emission. Equation (3.6.3) specifies the radiation pattern of an oscillating electric dipole precisely. From further analysis on this equation, it is shown the radiation behaviour alters significantly when a fluorescent molecule is placed close to an interface between two media with different dielectric properties. In our case, at the air($n$=1)/glass(S-LAH79,$n$≈2) interface, the simulation results of the angular distribution of the radiation of a large number of randomly oriented molecule dipole emitters are shown in Figure 3.6.2. In this figure, the left diagram depicts the radiation distribution of dipole emitters located directly at the surface, while the right diagram depicts the radiation distribution of dipole emitters located at a surface distance equal to a third of the emission wavelength. It is shown no matter what the distance between the dipole emitters and the interface, the emission maximum always occurs at the total

internal reflection (TIR) angle of the interface. More importantly, only surface-bound dipole emitters send a substantial part of their intensity into supercritical angles, i.e. angles larger than critical angle, in the glass side. This phenomenon reveals that it is necessary to eliminate the distance between the fluorescent samples and the ASIL flat surface in order to maintain the high resolution performance of SIF. Otherwise the fluorescent emission is mostly constrained in the limited $NA_{eff}$ which is determined as:

$$NA_{eff} = n\sin[\arcsin(\theta_{TIR})] = n\sin[\arcsin(\frac{n'}{n})] = n' \qquad (3.6.4)$$

here $n$ is the refractive index of the ASIL material, $n'$ is the refractive index of the medium surrounding the fluorescent molecules.

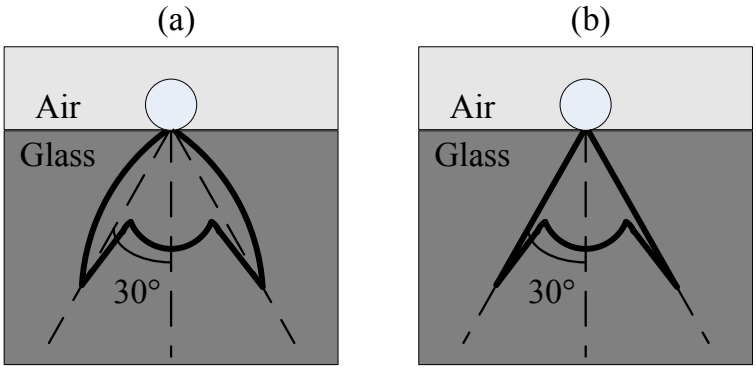


**Figure 3.6.2 Angular distribution of emission propagating into the glass for isotropically oriented molecules in an interface between the air and glass S-LAH79**
(a) Distance from fluorophores to interface is zero; (b) distance from fluorophores to interface is equal to a third of the emission wavelength.

Comparing Equation (3.6.2) and (3.6.4), interestingly we find the same conclusion has been drawn either from ray tracing analysis, which is from the instrument point of view, or dipole emitter analysis, which is from the sample point of view.

### 3.6.3 Experimental examination

Besides theoretical analysis on near-field imaging property of SIF, we also experimentally examined this unique characteristic. Two experiments have been designed and implemented on our prototype SIF system.

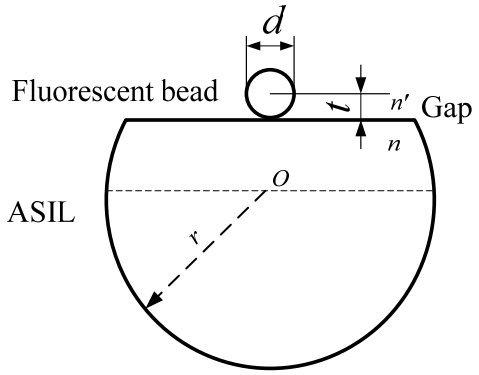


**Figure 3.6.3 Model of a fluorescent bead sample with a gap towards ASIL**
*d*: fluorescent bead diameter; *t*: gap distance; *n′*: refractive index of the medium in the gap; *n*: refractive index of the ASIL material; *r*: radius of the ASIL.

(1) The first experiment is designed to test the effect of an air gap on the resolution of SIF. A number of 170 nm 633/660 fluorescent beads (Invitrogen) were imaged by the SIF. In this circumstance there exists an air gap (width *t*: 85 nm) between the spherical centre of a fluorescent bead and the ASIL (Figure 3.6.3). By changing the aperture size of the calibrated iris diaphragm (see Figure 3.3.1 and D1 in Figure 3.3.2) located at the conjugate plane of the BFP, the NA of the SIF system can be configured deliberately. Meanwhile, the practical NA can be quantified by measuring the size of a fluorescent bead image (see Subsection 3.4.1). According to previous analysis, the resolution of the SIF should be determined by the refractive index of the medium in the gap which is 1 in

this case, then we predict the practical NA should not go beyond 1, even if the NA measured from BFP image is larger than 1.

In Figure 3.6.4, (a) to (i) are the images of a single 170 nm fluorescent bead obtained with the SIF at different aperture sizes of the calibrated iris diaphragm, their corresponding BFP images are (j) to (r) respectively. The NAs are quantified by measuring the FWHM sizes of the bead images from (a) to (i) (more information about this resolution evaluation method can be found in Subsection 4.5.3), and corresponding NAs are also calculated by measuring their BFP sizes from (j) to (r). The relationship between NAs measured from BFPs and NAs measured from single beads is plotted in Figure 3.6.5. From this figure, it is shown at first the NAs measured from single beads increase linearly with increasing the NAs measured from BFPs. However, when NAs measured from BFPs exceed 1, NAs measured from single beads remain at around 1, which verifies our prediction very well. These experimental results confirm the resolution of the SIF cannot go beyond 1, as we predicted, when there is an air gap between the fluorescent sample and the ASIL.

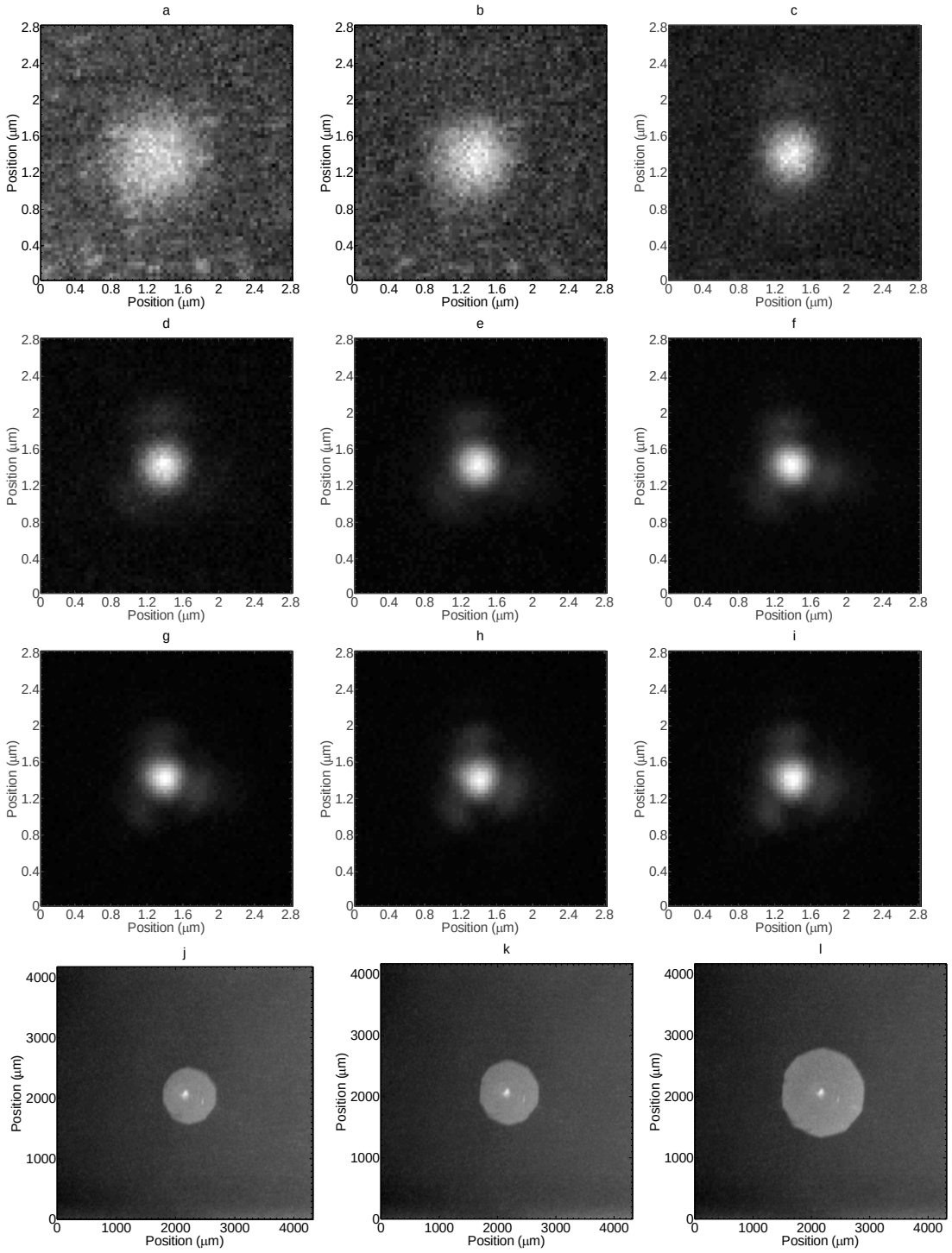


(Part of Figure 3.6.4, continued on the next page)

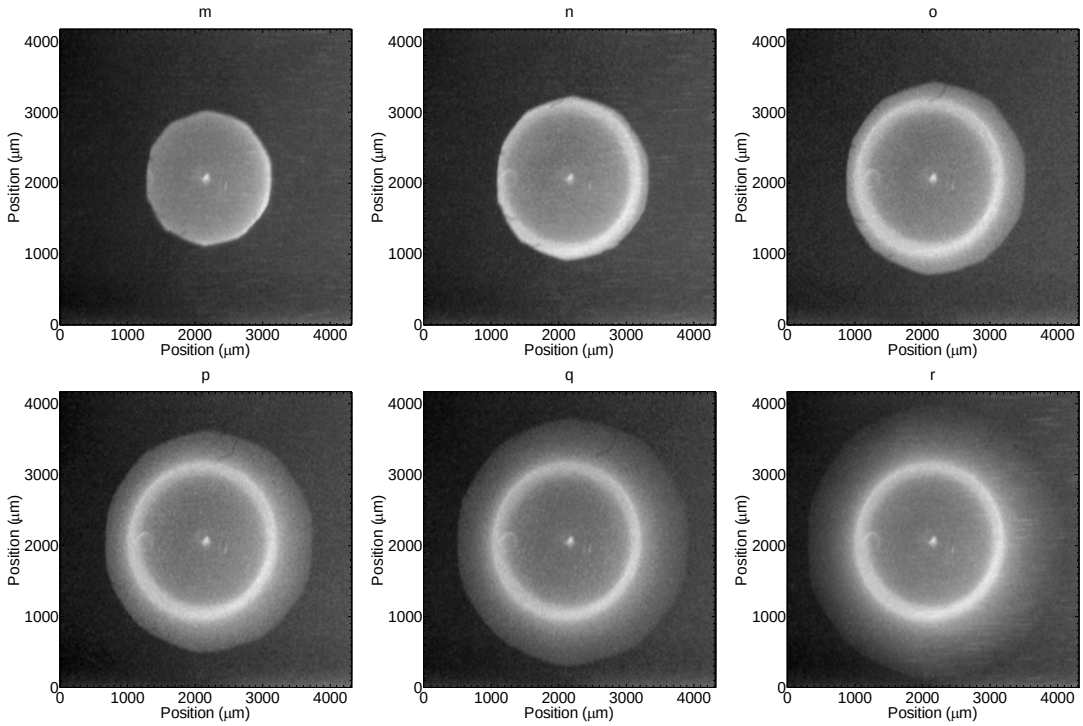


**Figure 3.6.4 Series of images of a 170 nm fluorescent bead from SIF and their BFP images with different NAs**
From (a) to (i), the measured NA is 0.58, 0.64, 0.81, 0.94, 1, 1.05, 1.1, 1.1 and 1.05 respectively; from (j) to (r), the measured NA is 0.47, 0.57, 0.75, 0.99, 1.18, 1.39, 1.6, 1.82 and 1.95 respectively.

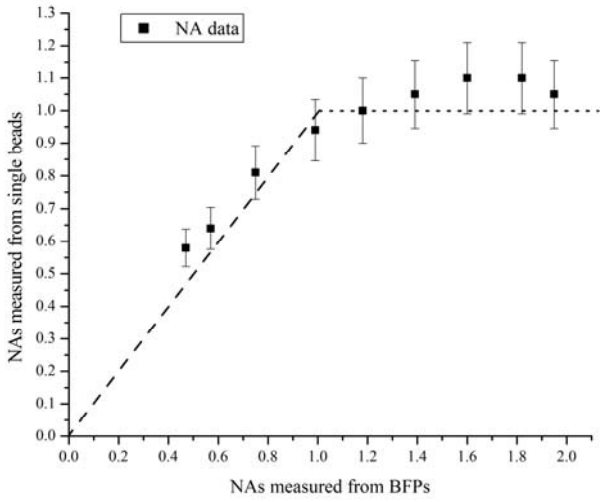


**Figure 3.6.5 Relationship between NAs measured from BFPs and NAs measured from single beads**
The dashed line is the linear fitting of the data points when NAs measured from BFPs are below 1; the dotted line corresponds to NA of 1. This figure shows the NAs measured from single beads cannot go beyond 1 even if the NAs measured from BFPs are larger than 1 when an air gap existing. Error bar: 10% of the NAs measured from single bead.

(2) The second experiment is designed to test the connection between the gap medium and the resolution of the SIF. Again, 170 nm fluorescent beads were used as samples. We imaged these fluorescent beads, with the calibrated iris diaphragm fully open, by the SIF when they were immersed in air ($n'$ =1), distilled water ($n'$ =1.33), immersion oil (Carl Zeiss, $n'$ =1.518) and high-index liquid (Cargille Laboratories, $n'$ =1.78) respectively. In this way, a series of images with different gap medium were obtained. The practical NAs are quantified by measuring the FWHM size of a single fluorescent bead image in each circumstance. According to Equation (3.6.2) and (3.6.4), we predict the practical NA in each case should be equivalent to the refractive index of corresponding gap medium.

In Figure 3.6.6, (a) to (d) are the SIF images of a single 170 nm fluorescent bead immersed in air, distilled water, immersion oil, and high-index liquid respectively. In the same figure, from (e) to (g), the BFP image in each case is also displayed. The BFP image was not able to be taken when using the high-index liquid because the liquid provoked severe fluorescence photobleaching, while the BFP imaging camera in our system had rather low image acquisition speed. The practical NAs measured from single bead images and the achievable NAs measured from BFP images are organised in Table 3.6.1. The determination of NA according to the refractive index of the gap medium is distinct in spite of some slight measurement errors. These findings confirm the resolution of SIF is determined by the refractive index of the gap medium.

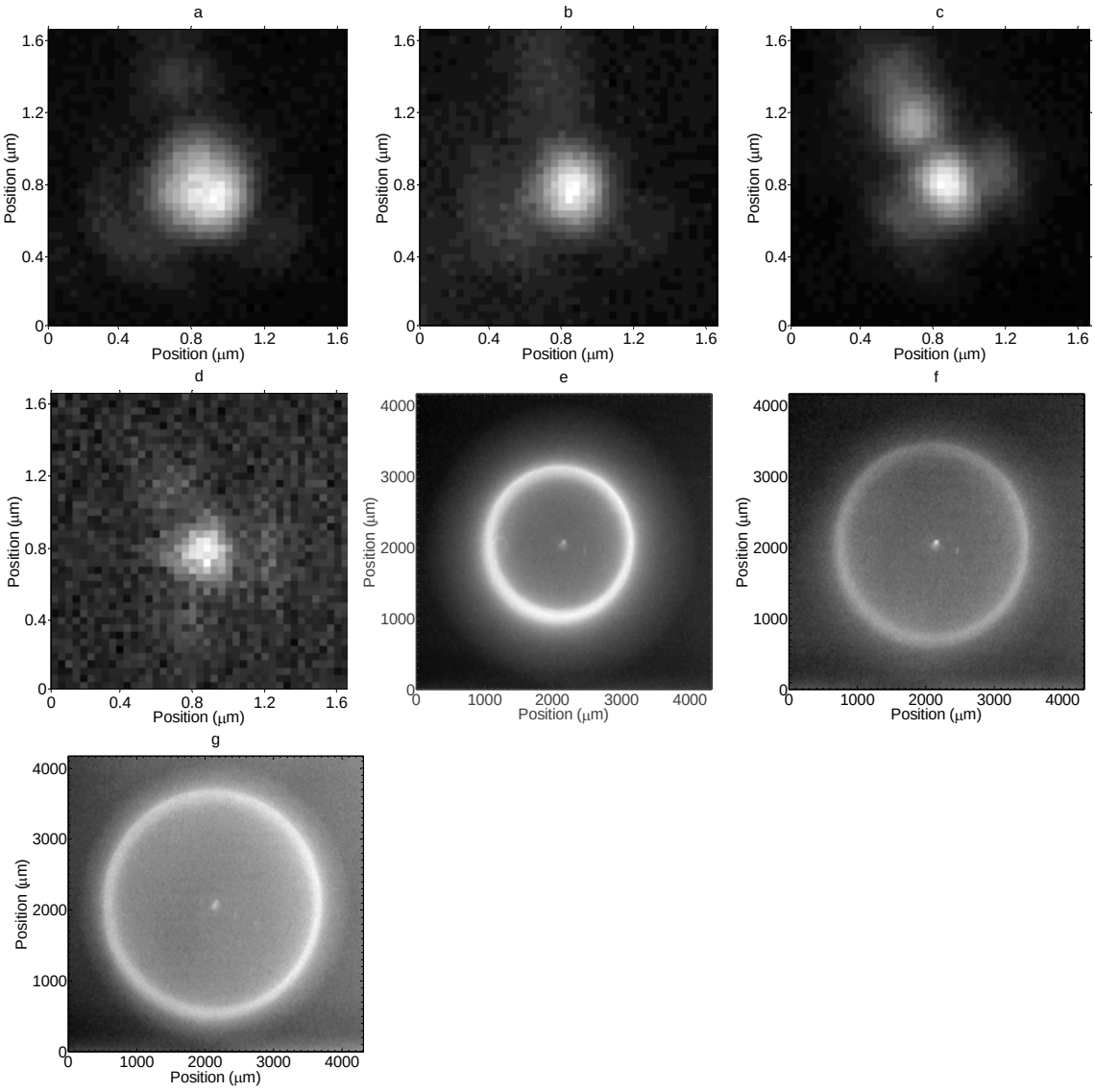


**Figure 3.6.6 Series of images of a 170 nm fluorescent bead captured by SIF and their BFP images with different gap medium**
From (a) to (d), the gap medium is air ($n'$=1), distilled water ($n'$=1.33), immersion oil ($n'$=1.518) and high-index liquid ($n'$=1.78) respectively, and the corresponding measured NA is 1.05, 1.28, 1.47 and 1.7 in sequence. From (e) to (g), the NA measured from BFP is 1, 1.3 and 1.51 respectively.

**Table 3.6.1 Comparisons of refractive indices of medium in the gap, practical NAs and NAs measured from BFPs when changing the gap medium in the SIF**

| Medium in the gap | Refractive index | Practical NA | NA measured from BFP |
|---|---|---|---|
| Air | 1 | 1.05 | 1 |
| Water | 1.33 | 1.28 | 1.3 |
| Immersion oil | 1.518 (at 546 nm) | 1.47 | 1.51 |
| High-index liquid | 1.78 (at 587 nm) | 1.7 | Not available |

### 3.6.4 Discussion

Theoretically, the NA of our SIF system should approach 2, although the BFP images (Figure 3.4.4 and 3.4.8) confirm the bandwidth of the system coincides with the theoretical value, the practical NA of the system was verified as 1.85 according to the measurements in spatial domain. The difference between the theoretical and practical NA values mainly comes from the existence of air gaps that breaks the ideal near-field imaging condition and the difficulty for rays to propagate when collection angle approaching 90°. Another minor factor that influences the practical resolution performance of SIF is the inhomogeneous near-field emission distribution of surface-proximal fluorophores because the maximum emission happens at the TIR angle.

A method to address the issue of sacrificing resolution due to the occurrence of air gaps is to immerse the sample in the medium with the same refractive index as the ASIL material. In this way, the samples are effectively in perfect contact with the ASIL, which makes the near-field imaging condition satisfied. Practically, even the usage of high-index, but lower than the index of the ASIL material, medium is beneficial to the resolution improvement. Meanwhile, using high-index medium also enlarges the TIR angle, which is helpful to make the best of the emission from the fluorophores. However, liquids with such high refractive indices usually are subject to severe photobleaching on fluorescence samples. For example, the high-index ($n_D$=1.78) liquid used in our experiments degraded the fluorescent beads to half of the initial fluorescence emission intensity in about 1.5 seconds. So, it is highly anticipated that high-index liquids with less photobleaching effects are produced. For living cell

samples, the absence of apparent phototoxicity is another important factor of applicable high-index liquids.

## 3.7 Conclusions

In this chapter, we explored the formation of a new wide-field high-resolution fluorescence microscopic technique – solid immersion fluorescence microscopy (SIF) applying an aplanatic solid immersion lens (ASIL). With the help of an ASIL ($r$ = 2.5 mm) made of optical glass S-LAH79 ($n_d$ = 2.0033), we successfully demonstrated a wide-field high-resolution SIF system with effective NA of 1.85 that is superior to any kind of commercially available objective lenses in market so far. We also discussed and demonstrated the aberration issues and near-field imaging property of it, which are extremely crucial for the realisation of high resolution in SIF.

We choose an ASIL to accomplish the SIF instead of a hemisphere SIL (HSIL), because the ASIL has stronger NA enhancement capability and larger valid aberration-free area. The severe dispersion of the high-index material of the ASIL makes the SIF suffer serious chromatic aberration (CA) that degrades the high-resolution performance. We proposed several methods to eliminate or balance CA in SIF, and practically applied a super-narrow passband filter (FWHM = 3 nm) as emission filter to overcome the drawback of CA in the SIF. The size of an ASIL determines the range of fluorescent spectrum suitable for imaging and the valid FOV associated with aberrations when maintaining high-resolution performance. We theoretically analysed their relationships

by using both ray optics and wave optics simulations. The conclusion not only guides us to design the microscope demonstrated in this chapter, but also can be regarded as a convenient reference when applying an ASIL in fluorescence microscopes. According to the analysis based on both ray tracing and dipole emitter simulation, it is demonstrated the SIF can deliver the best resolution performance only if working in near-field imaging mode.

The application of ASILs in fluorescence microscopy is mainly limited by the chromatic aberration induced by the highly dispersive ASIL material; however, we have successfully overcome this problem in our case, so we can get on with our research.

# Chapter 4 Structured Illumination Microscopy (SIM)

## 4.1 Introduction

Structured illumination microscopy (SIM) is a wide-field microscopic technique applying spatially structured excitation illumination to achieve higher resolution than the microscope using conventional illumination. Structured excitation illumination itself can be used to improve the resolution in either lateral or axial directions. Laterally structured illumination has been used particularly to provide axial sectioning [32] [33], however in this case, the spatial frequencies of the structured illumination and the coherence of the illumination in the back focal plane do not increase the lateral resolution but ensure that a uniform object appears dark when it is out of focus [145]. In our research, we specifically focus on the lateral resolution improvement with the help of SIM. The concept of improving lateral resolution by patterned illumination can be traced back to 1963 [40], however, this concept just came into reality in the last 10 years or so. In 1998, Heintzmann and Cremer proposed the idea of using a diffraction grating to improve the lateral resolution of a microscope [29]. Two years later, Gustafsson reported doubled lateral resolution achievement in wide-field fluorescence microscopy using structured illumination [5] [6]. In 2005, Gustafsson accomplished 5.5-fold

improvement of lateral resolution with saturated structured illumination [31], and more recently in 2008, they achieved three-dimensional doubled resolution by structured illumination [38]. All these achievements made the SIM become a key technique in the exploration of higher resolution in optical microscopy. In this chapter we will develop an experimental SIM system with a view to showing how SIM provides increased lateral resolution.

In this chapter, firstly, we generally explain the theory of the resolution enhancement in SIM. Secondly, we mathematically explain a four-phase-step algorithm used to reconstruct high-resolution images with a one-dimensional (1D) SIM simulation. Thirdly, we describe the SIM instrumentation working in one dimension, including the structured illumination generation and phase stepping implementation. Fourthly, we present a thorough description of the 1D SIM experiments and results. Finally, we discuss the artefact issue in SIM, especially the artefacts induced by raw image displacements.

## 4.2 Theory

In a conventional optical microscope, the observed data $D(r)$ is the convolution of the distribution of a sample $E(r)$ with the point spread function (PSF) $H(r)$ of the microscope:

$$D(r) = E(r) \otimes H(r) \tag{4.2.1}$$

According to the convolution theorem, the Fourier transform of this convolution is:

$$\tilde{D}(k) = \tilde{E}(k)\tilde{H}(k) \tag{4.2.2}$$

here tildes (~) indicate the Fourier transform of the corresponding quantities in spatial domain and *k* is the spatial frequency component. Because the optical transfer function (OTF) is the Fourier transform of the PSF $H(r)$ of the microscope:

$$O(k) = \tilde{H}(k) \tag{4.2.3}$$

Substitute this equation into Equation (4.2.2), there is:

$$\tilde{D}(k) = \tilde{E}(k)O(k) \tag{4.2.4}$$

From this expression we can see, in frequency domain, the final observed data are simply made up of the multiplication of the sample and OTF of the microscope.

The classical resolution limit is based on the fact that the OTF has a finite support that defines which spatial frequencies the microscope can detect. In other words, high spatial frequency information outside the OTF cannot pass through a conventional microscope, and then the fine details in spatial domain cannot be resolved.

In a fluorescence microscope, when a fluorescent object with a local concentration $S(r)$ of fluorophores is excited by the illumination intensity $I(r)$, the resultant emission distribution is:

$$E(r) = S(r)I(r) \tag{4.2.5}$$

The Fourier transform of this multiplication is a convolution:

$$\tilde{E}(k) = \tilde{S}(k) \otimes \tilde{I}(k) \tag{4.2.6}$$

This convolution mixes information from different components in frequency domain, and in particular moves some unresolvable high-frequency information into the OTF of the conventional microscope. More precisely, the convolution will generally cause $\tilde{E}(k)$ at each spatial frequency component $k$ to depend on the values of $\tilde{S}(k)$ at other spatial frequency components that may be outside the bandwidth. With appropriate illumination structure $\tilde{I}(k)$, high spatial frequency information of the sample can be encoded in conventional images and then they can be decoded and restored. In this way, the information from outside of the bandwidth defined by conventional OTF can be detected, and then a new synthetic OTF with wider bandwidth is obtained. The derivation of 1D SIM transfer function is depicted in Figure 4.2.1 [145]. For a simple sinusoidal distribution structured illumination pattern, we suppose the spatial frequency of the pattern equals to the cut-off frequency of conventional fluorescence microscope transfer function (dashed curve), and the amplitude of the two contributions (dash-dotted and dotted curves) of the structured illumination pattern is half of that of the conventional transfer function, therefore the sum of the conventional transfer function and these two contributions, which is the transfer function of the SIM, is a triangular transfer function (solid curve) with twice the bandwidth of the conventional one. The comparison of 1D transfer functions of conventional wide-field fluorescence microscope, confocal fluorescence microscope and conceptual SIM is shown in Figure 4.2.2 [145]. Here, the conceptual SIM means the upconverted and the downconverted contributions from structured illumination are shifted by ±2 units of NA/λ, and they have the half the amplitude of the conventional transfer function. Correspondingly, in

spatial domain, the lateral resolution of conventional fluorescence microscope is extended by structured illumination.

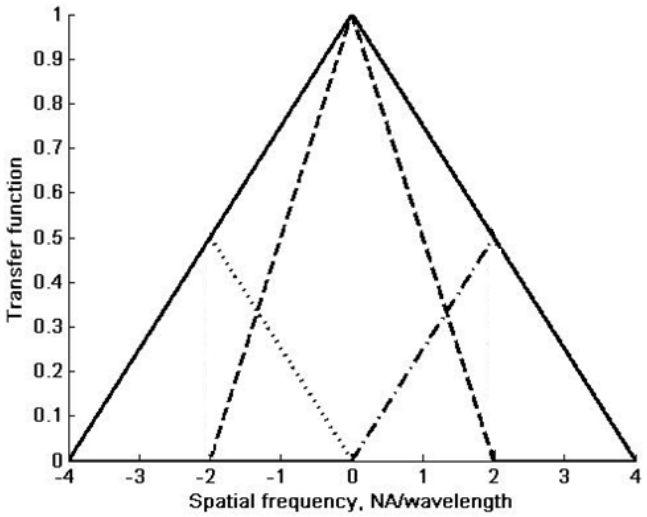


**Figure 4.2.1 Derivation of 1D SIM transfer function [145]**
Dashed curve: conventional fluorescence microscope transfer function; dash-dotted curve and dotted curve: contributions of structured illumination pattern; Solid curve: synthetic transfer function of 1D SIM.

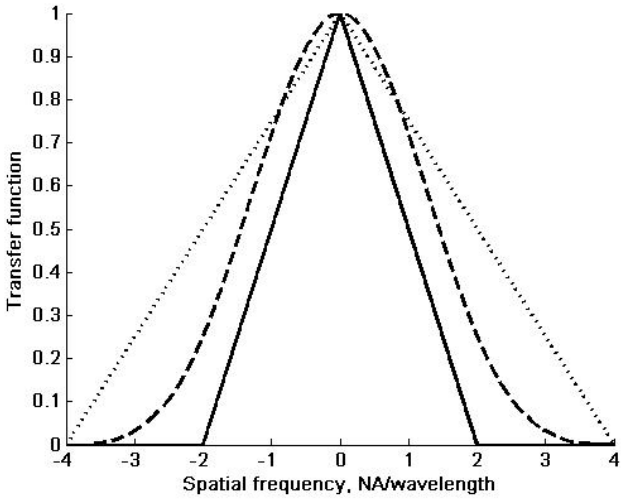


**Figure 4.2.2 Comparison of 1D transfer functions of different microscopic systems [145]**
Solid curve: conventional wide-field fluorescence microscope; dashed curve: confocal fluorescence microscope with small pinhole; dotted curve: conceptual SIM.

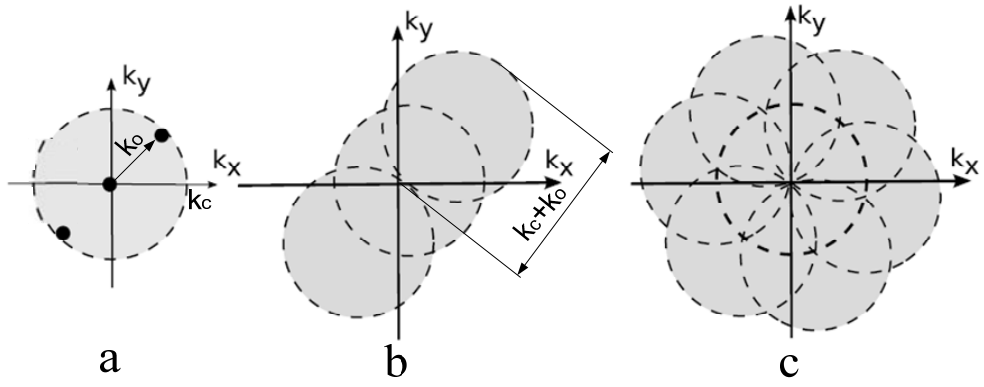


**Figure 4.2.3 Schematic explanation of two-dimensional resolution improvement in SIM in frequency domain**
(a) The sinusoidal distribution structured illumination pattern has three Fourier components and the corresponding wave vector $k_o$, which approaches the bandwidth $k_c$ of conventional fluorescence microscope. (b) The observed data include the usual sample information within the conventional bandwidth and information originating in two regions displaced by $+k_o$ and $-k_o$. This information can be decoded and restored to its proper position. (c) By repeating this procedure at different azimuthal angles, all the information from a circle with twice the radius of the conventional bandwidth can be retrieved and restored. Thus, a doubled lateral resolution image can be reconstructed in spatial domain.

By repeating the procedure for other orientations of the illumination wave vector $k_0$ (suppose the structured illumination pattern has a sinusoidal distribution), we can acquire and restore all the necessary information about the sample from a circular area of radius $k_c + k_0$ in frequency domain, where $k_c$ is the radius of the bandwidth in conventional microscope (Figure 4.2.3). In this way, a two-dimensional (2D) SIM image with improved lateral resolution can be reconstructed. In theory, the best performance of this resolution enhancement happens when the spatial frequency of the illumination pattern equals the bandwidth of the microscope, and thus the resolution can be improved by a factor of two in the lateral direction.

Somekh *et al.* developed a modified formulation of the imaging response of the microscope and a probabilistic analysis to assess the resolution performance of SIM

[145]. By examining the trade-off between achievable lateral resolution and SNR when photon shot noise is dominant, it was concluded that for a given photon budget, SIM invariably achieves better lateral resolution than confocal microscopy for a given SNR. And according to the derivation of the stochastic transfer function (STF) [146] for SIM, it was proved SIM is capable of surpassing the lateral resolution limit by a factor of two [147], which is the best resolution performance of SIM. This point was also experimentally demonstrated by others [5] [6].

## 4.3 1D simulation and image reconstruction algorithm

To gain insight into the operation of SIM, we modelled a SIM system working in one dimension in MATLAB. Through the following description on this simulation, a four-phase-step method for extracting high frequency information and reconstructing high-resolution image is explained.

As described in Section 2.3, fluorescence microscopy, as an incoherent imaging system, should have a Chinese-hat distribution OTF. However in the following model, for simplicity, it is supposed we have a fluorescence microscope with a hypothetical transfer function, OTF being 1 everywhere in the bandwidth and 0 outside the bandwidth as shown in Figure 4.3.1. The bandwidth is set as $3\times10^6$ $m^{-1}$ (corresponding to NA 0.75 if the imaging wavelength is 500 nm).

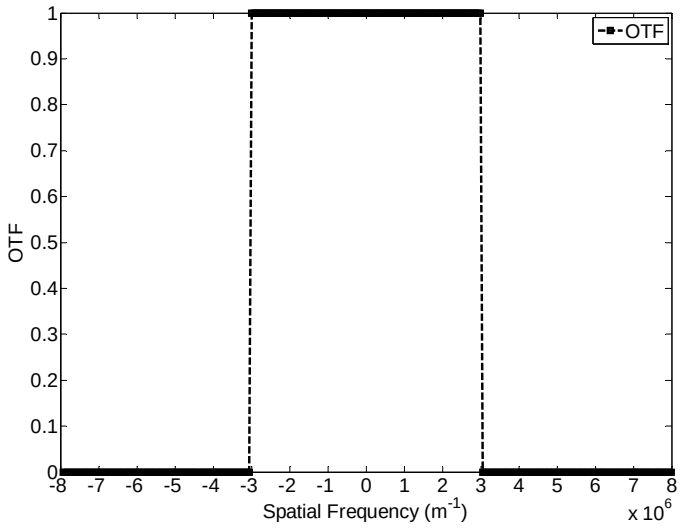


**Figure 4.3.1 OTF of an ideal fluorescence microscope**
OTF being 1 everywhere in the bandwidth and 0 outside the bandwidth

If we have a fine sinusoidal distribution fluorescent sample $S(r)$ that has the spatial frequency of $5\times10^6$ $m^{-1}$ (Figure 4.3.2), apparently it cannot be resolved by the microscope described above. In frequency domain, the two frequency components of the sample pattern lie outside the bandwidth of this microscope (Figure 4.3.3).

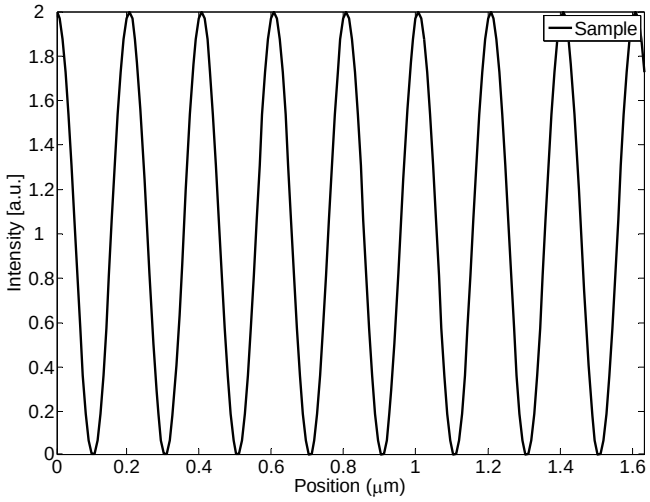


**Figure 4.3.2 A fine sinusoidal distribution fluorescent sample with spatial frequency of $5\times10^6$ $m^{-1}$ in spatial domain**

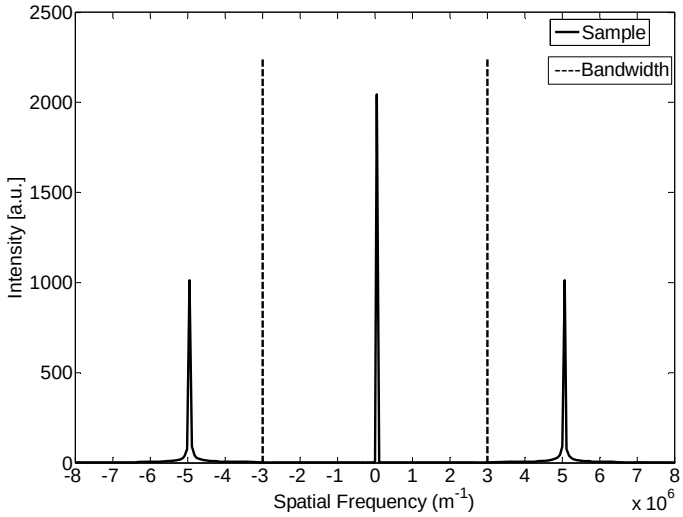


**Figure 4.3.3 A fine sinusoidal distribution fluorescent sample with spatial frequency of $5\times10^6$ $m^{-1}$ in frequency domain**

Now, we illuminate the fluorescent sample with a particularly simple structured illumination that is a sinusoidal pattern. The spatial phase of this illumination pattern is shifted by $\frac{\pi}{2}$ for three times, and then this gives:

$$I_1(r) = 1 + \cos(k_0 r) \quad (4.3.1a)$$
$$I_2(r) = 1 - \sin(k_0 r) \quad (4.3.1b)$$
$$I_3(r) = 1 - \cos(k_0 r) \quad (4.3.1c)$$
$$I_4(r) = 1 + \sin(k_0 r) \quad (4.3.1d)$$

here $k_0$ is the spatial frequency of the structured illumination pattern, $r$ is the space vector. The illumination pattern and its Fourier transform in the first case are shown in Figure 4.3.4 and 4.3.5 respectively. The structured illumination pattern has the spatial frequency of $2.5\times10^6$ $m^{-1}$ that is inside the bandwidth of the microscope, so the pattern is resolvable. The spatial frequency of the structured illumination pattern we choose is close to the conventional microscope bandwidth of $3\times10^6$ $m^{-1}$, we can expect a 1.8-fold

bandwidth improvement in SIM. If the spatial frequency of the structured illumination pattern is $3\times10^6$ $m^{-1}$ that is the same as the bandwidth of the conventional microscope, we would expect the bandwidth extension by a factor of 2.

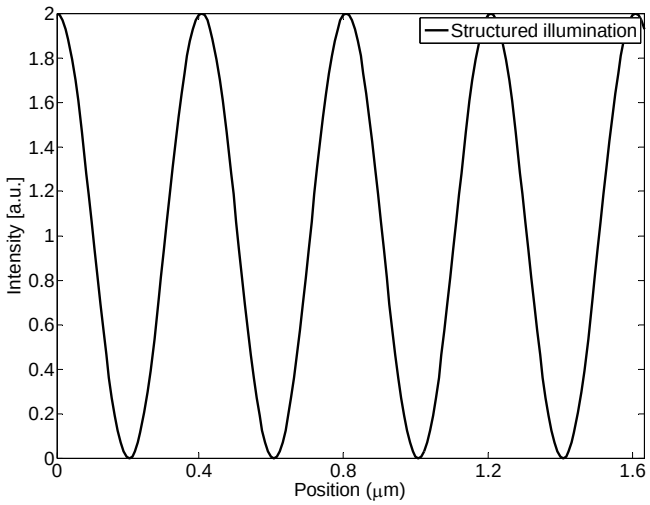


**Figure 4.3.4 A sinusoidal structured illumination pattern with spatial frequency of $2.5\times10^6$ $m^{-1}$ in spatial domain**

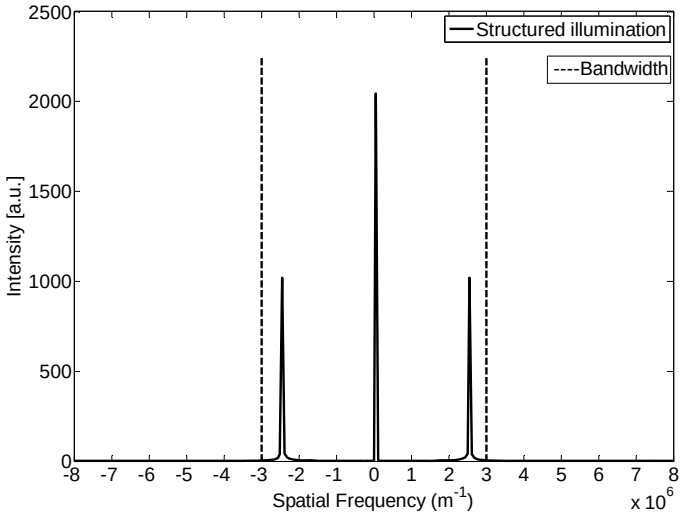


**Figure 4.3.5 A sinusoidal structured illumination pattern with spatial frequency of $2.5\times10^6$ $m^{-1}$ in frequency domain**

According to Equation (4.2.5), the products of the sample and the illumination are:

$$E_1(r) = S(r)[1+\cos(k_0 r)] \tag{4.3.2a}$$
$$E_2(r) = S(r)[1-\sin(k_0 r)] \tag{4.3.2b}$$
$$E_3(r) = S(r)[1-\cos(k_0 r)] \tag{4.3.2c}$$
$$E_4(r) = S(r)[1+\sin(k_0 r)] \tag{4.3.2d}$$

Their Fourier transforms are:

$$\tilde{E}_1(k) = \tilde{S}(k) + \frac{1}{2}\tilde{S}(k-k_0) + \frac{1}{2}\tilde{S}(k+k_0) \tag{4.3.3a}$$
$$\tilde{E}_2(k) = \tilde{S}(k) + \frac{i}{2}\tilde{S}(k-k_0) - \frac{i}{2}\tilde{S}(k+k_0) \tag{4.3.3b}$$
$$\tilde{E}_3(k) = \tilde{S}(k) - \frac{1}{2}\tilde{S}(k-k_0) - \frac{1}{2}\tilde{S}(k+k_0) \tag{4.3.3c}$$
$$\tilde{E}_4(k) = \tilde{S}(k) - \frac{i}{2}\tilde{S}(k-k_0) + \frac{i}{2}\tilde{S}(k+k_0) \tag{4.3.3d}$$

It is clear the product is made up of the sum and difference of their frequency components (Figure 4.3.6). In this way, the high frequency information of the object is shifted into the bandwidth of the conventional microscope.

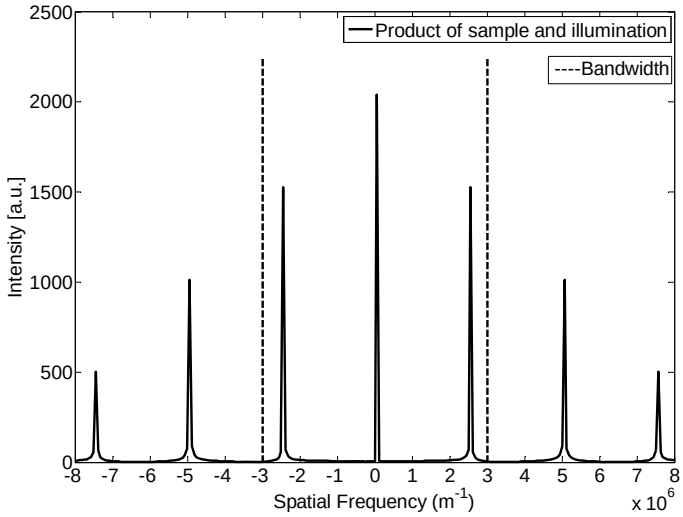


**Figure 4.3.6 Product of the sample and the illumination in frequency domain**
The product is made up of the sum and difference of their frequency components, so the high frequency information of the object is shifted into the bandwidth.

The observed image $D(r)$, in frequency domain (Figure 4.3.7), is made up of the multiplication of this product and OTF of the microscope:

$$\tilde{D}_1(k) = \tilde{E}_1(k\ )O(k) = \tilde{S}(k\ )O(k) + \frac{1}{2}\tilde{S}(k\ -k_0)O(k) + \frac{1}{2}\tilde{S}(k\ +k_0)O(k) \qquad (4.3.4a)$$

$$\tilde{D}_2(k) = \tilde{E}_2(k\ )O(k) = \tilde{S}(k\ )O(k) + \frac{i}{2}\tilde{S}(k\ -k_0)O(k) - \frac{i}{2}\tilde{S}(k\ +k_0)O(k) \qquad (4.3.4b)$$

$$\tilde{D}_3(k) = \tilde{E}_3(k\ )O(k) = \tilde{S}(k\ )O(k) - \frac{1}{2}\tilde{S}(k\ -k_0)O(k) - \frac{1}{2}\tilde{S}(k\ +k_0)O(k) \qquad (4.3.4c)$$

$$\tilde{D}_4(k) = \tilde{E}_4(k\ )O(k) = \tilde{S}(k\ )O(k) - \frac{i}{2}\tilde{S}(k\ -k_0)O(k) + \frac{i}{2}\tilde{S}(k\ +k_0)O(k) \qquad (4.3.4d)$$

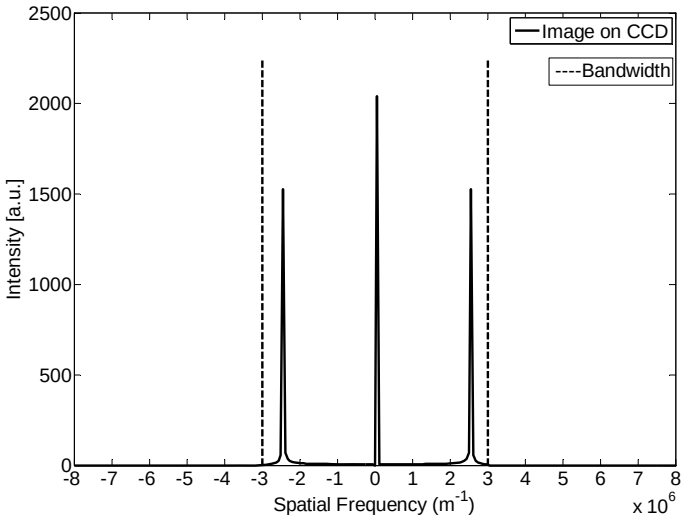


**Figure 4.3.7 Raw image captured on CCD under structured illumination in frequency domain**
The high frequency information is carried in the raw image.

Through (4.3.4a)-(4.3.4c) and (4.3.4b)-(4.3.4d), we can get:

$$\tilde{D}_1(k) - \tilde{D}_3(k) = \tilde{S}(k-k_0)O(k) + \tilde{S}(k+k_0)O(k) \qquad (4.3.5a)$$

$$\tilde{D}_2(k) - \tilde{D}_4(k) = i\tilde{S}(k-k_0)O(k) - i\tilde{S}(k+k_0)O(k) \qquad (4.3.5b)$$

Manipulating (4.3.5a)-$i$(4.3.5b) and (4.3.5a)+$i$(4.3.5b), we have:

$$\tilde{S}(k-k_0)O(k)=\frac{1}{2}\{[\tilde{D}_1(k)-\tilde{D}_3(k)]-i[\tilde{D}_2(k)-\tilde{D}_4(k)]\} \quad (4.3.6a)$$

$$\tilde{S}(k+k_0)O(k)=\frac{1}{2}\{[\tilde{D}_1(k)-\tilde{D}_3(k)]+i[\tilde{D}_2(k)-\tilde{D}_4(k)]\} \quad (4.3.6b)$$

Shifting these expressions by $-k_0$ and $k_0$ respectively, the frequency components can be moved to the correct positions:

$$\tilde{S}(k)O(k+k_0)=\frac{1}{2}\{[\tilde{D}_1(k+k_0)-\tilde{D}_3(k+k_0)]-i[\tilde{D}_2(k+k_0)-\tilde{D}_4(k+k_0)]\} \quad (4.3.7a)$$

$$\tilde{S}(k)O(k-k_0)=\frac{1}{2}\{[\tilde{D}_1(k-k_0)-\tilde{D}_3(k-k_0)]+i[\tilde{D}_2(k-k_0)-\tilde{D}_4(k-k_0)]\} \quad (4.3.7b)$$

The DC component can be calculated by summing up Equation (4.3.4a) to (4.3.4d):

$$\tilde{S}(k)O(k)=\frac{1}{4}[\tilde{D}_1(k)+\tilde{D}_2(k)+\tilde{D}_3(k)+\tilde{D}_4(k)] \quad (4.3.8)$$

According to Equation (4.3.7a), (4.3.7b) and (4.3.8), the original sample distribution can be reconstructed in frequency domain (Figure 4.3.8), correspondingly its inverse Fourier transform is the final reconstructed image that we intend to obtain (Figure 4.3.9). For the SIM, the bandwidth goes to $5.5\times10^6$ $m^{-1}$, corresponding to NA 1.375. Therefore the lateral resolution is improved by a factor of 1.8, which conforms to our expectation.

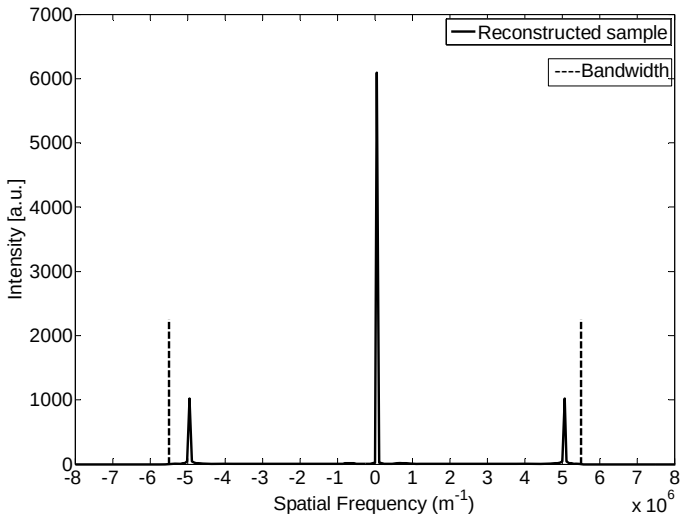


**Figure 4.3.8 Reconstructed image with spatial frequency of $5\times10^6$ $m^{-1}$ from the SIM in frequency domain**

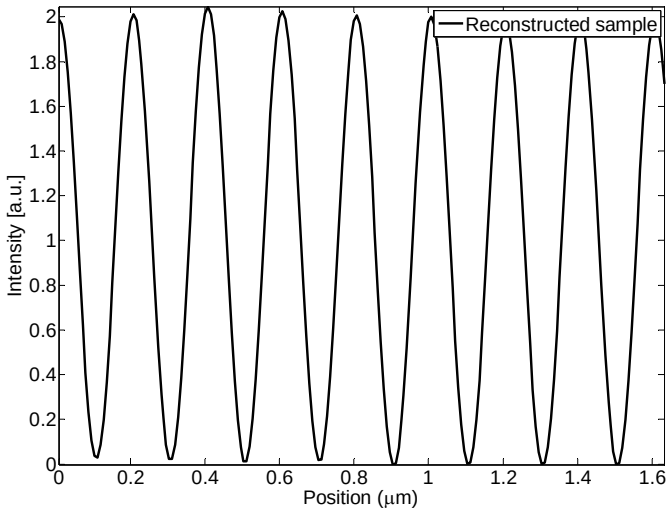


**Figure 4.3.9 Reconstructed image with spatial frequency of $5\times10^6$ $m^{-1}$ from the SIM in spatial domain**

In conclusion, the original unresolvable sample pattern (Figure 4.3.2) in a conventional fluorescence microscope now becomes resolvable (Figure 4.3.9) by mathematically processing four raw images captured in the conventional fluorescence microscope but

illuminated by a series of sinusoidal distribution structured pattern with $\frac{\pi}{2}$ phase difference.

The four-phase-step method ($\frac{\pi}{2}$ phase difference) we used to restore high frequency information does not make any real difference compared with the three-phase-step method ($\frac{2\pi}{3}$ phase difference [5] [6]) adopted by other researchers. In terms of signal to noise ratio and resolution enhancement performance, the two methods give the same results. Practically, four-phase-step method is a bit better to cancel the phase difference errors produced in phase stepping.

It is possible to retrieve a conventional image from the four raw images. The inverse Fourier transform of Equation (4.3.8) is:

$$S(r) \otimes H(r) = \frac{1}{4}[D_1(r) + D_2(r) + D_3(r) + D_4(r)] \qquad (4.3.9)$$

This means the average of the sum of the four raw images is equal to the conventional fluorescence image.

In above analysis, the final resolution-enhanced image is reconstructed by recombining the different frequency components and Fourier transforming back into the spatial domain, alternatively, the reconstruction procedure could entirely operate in the spatial domain [145].

The inverse Fourier transforms of Equation (4.3.7a) and (4.3.7b) are:

$$S(r)\otimes H(r)\exp(-ik_0 r)=\frac{1}{2}\{[D_1(r)-D_3(r)]-i[D_2(r)-D_4(r)]\}\exp(-ik_0 r) \quad (4.3.10a)$$

$$S(r)\otimes H(r)\exp(ik_0 r)=\frac{1}{2}\{[D_1(r)-D_3(r)]+i[D_2(r)-D_4(r)]\}\exp(ik_0 r) \quad (4.3.10b)$$

Summing Equation (4.3.9), (4.3.10a) and (4.3.10b), we obtain this:

$$S(r)\otimes\frac{1}{2}H(r)[1+\cos(k_0 r)]=$$
$$\frac{1}{8}[(1+2\cos k_0 r)D_1(r)+(1-2\sin k_0 r)D_2(r)+(1-2\cos k_0 r)D_3(r)+(1+2\sin k_0 r)D_4(r)] \quad (4.3.11)$$

In the left side of this equation, the cosine term gives rise to both upconversion and downconversion of the OTF of a conventional microscope in frequency domain, which means the OTF of conventional microscope plus two additional contributions from the structured illumination leads to an expanded OTF, i.e. the OTF belonging to SIM. The left side of this equation states the desired response from the structured illumination process and the right side tells us how to get this from four raw images. This result presents a simple expression which yields the reconstructed image from the raw images in the spatial domain without performing Fourier transforms. A potential advantage of this spatial domain method is to save some image processing time when reconstructing the SIM images.

# 4.4 Instrumentation

## 4.4.1 System design

In this chapter, the main purpose of our SIM experiments is to demonstrate the resolution improvement capability of SIM and our image reconstruction codes, therefore we just intend to experimentally implement SIM working in one dimension at this stage.

In contrast to conventional epi-fluorescence microscopy, the major difference in SIM is the structured illumination. Physically, it is possible to alter the illumination path of a conventional microscope to construct a structured illumination. In our experiments, we chose to employ a diffraction grating to produce structured illumination. The schematic diagram of our SIM configuration is shown in Figure 4.4.1. An expanded laser beam, which is designed to match the full field of view (FOV), is incident on a diffraction grating. Due to diffraction, the laser beam is separated into several orders through the grating. A mask, which is located on a conjugate plane of the back focal plane (BFP) of the objective, is applied to block all the diffracted beams except ±1 orders. Via the objective, ±1 order beams hit the sample symmetrically to the optical axis. As two coherent beams, they interfere to generate sinusoidal interference fringes on the sample.

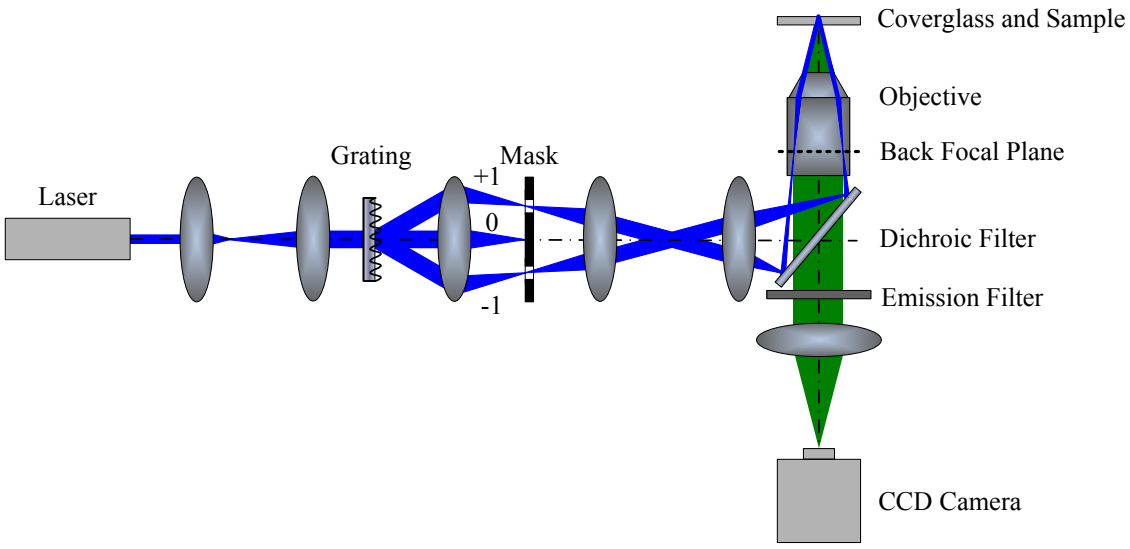


**Figure 4.4.1 Schematic of the SIM system**
The blue shading illustrates the scheme of producing sinusoidal structured illumination by a diffraction grating; the green shading illustrates the formation of fluorescence image.

Now we are going to numerically design the system. First, we determine the magnification of the microscope. The objective lens has an NA of 1.25, and the fluorescent sample for use has the peak emission wavelength $\lambda$ of 515 nm, the resolution of the microscope defined by Abbe limit is:

$$R = \frac{\lambda}{2NA} = 206nm$$

Considering the potential doubled lateral resolution in SIM, the theoretical resolution of our SIM system will be:

$$R_s = \frac{R}{2} = 103nm$$

The pixel size of our CCD camera is 8.6 μm ×8.3 μm, according to Nyquist criterion, the minimum magnification in imaging path is:

$$M = \frac{8.3\mu m \times 2}{103nm} = 161$$

Practically, we intend to make the magnification about twice as great as the minimum value, and then we adopt the magnification of 304.

Next, we are going to determine the magnification in the illumination path. The image area of our CCD is 6.47 mm× 4.83 mm, correspondingly, the FOV in the object plane is:

$$FOV = \frac{\sqrt{6.47^2 + 4.83^2}}{304} \approx 0.027mm = 27\mu m$$

The minimum (de)magnification is determined by the result of FOV dividing the laser beam size:

$$DM = \frac{27\mu m}{1mm} = 0.027$$

Practically we adopt the demagnification of 0.044.

## 4.4.2 Phase stepping

In order to decode the high frequency components encoded in the conventional fluorescence images, the spatial phase of the sinusoidal interference illumination pattern is required to alter $\frac{\pi}{2}$ for each image. Figure 4.4.2 shows the simulation images depicting this procedure. To implement this physically, the diffraction grating should be capable of moving laterally across the optical axis to execute phase stepping. In our system this was realised by mounting the grating on a linear translation stage.

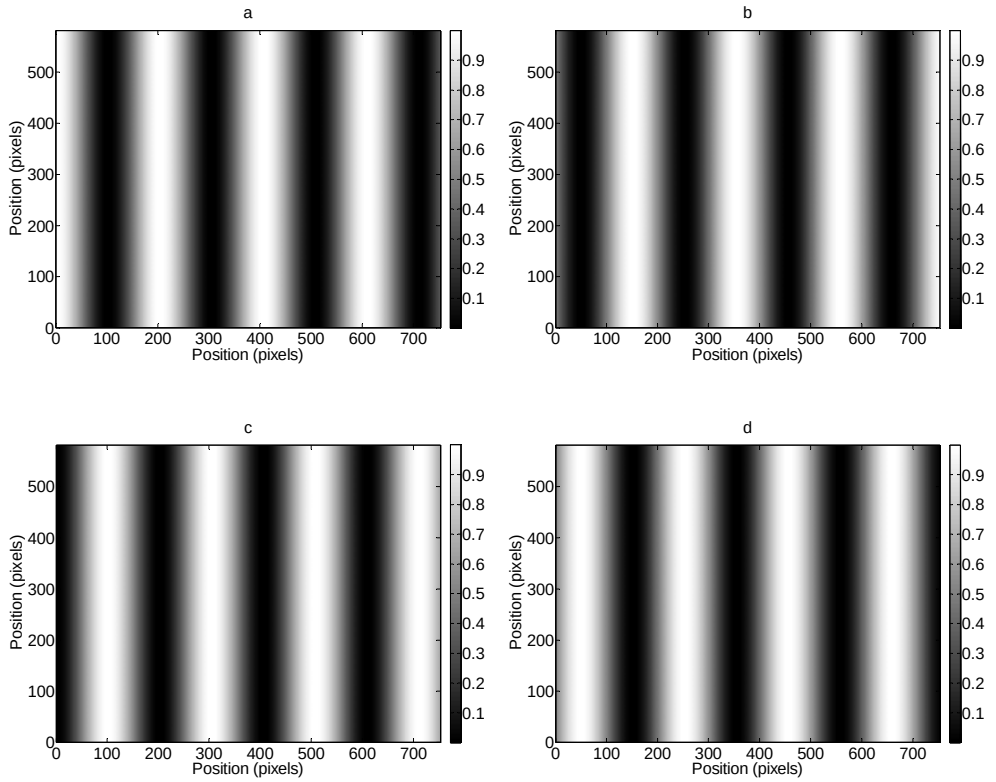


**Figure 4.4.2 Simulation images of sinusoidal structured illumination patterns with π/2 phase difference**
Sinusoidal fringes of structured illumination pattern have the period of 200 pixels. From (a) to (d), the patterns have π/2 phase difference successively, which is fulfilled by moving the pattern 1/4 of the period, i.e. 50 pixels, along the horizontal direction.

The scheme of using a diffraction grating to generate illumination pattern can be schematically expressed as shown in Figure 4.4.3. When the grating is moved along the X direction, the phase of the interference pattern on the object plane will change correspondingly. In order to choose a proper grating and correctly fulfil phase stepping, we are going to work out the relationship between the grating period and the interference pattern period.

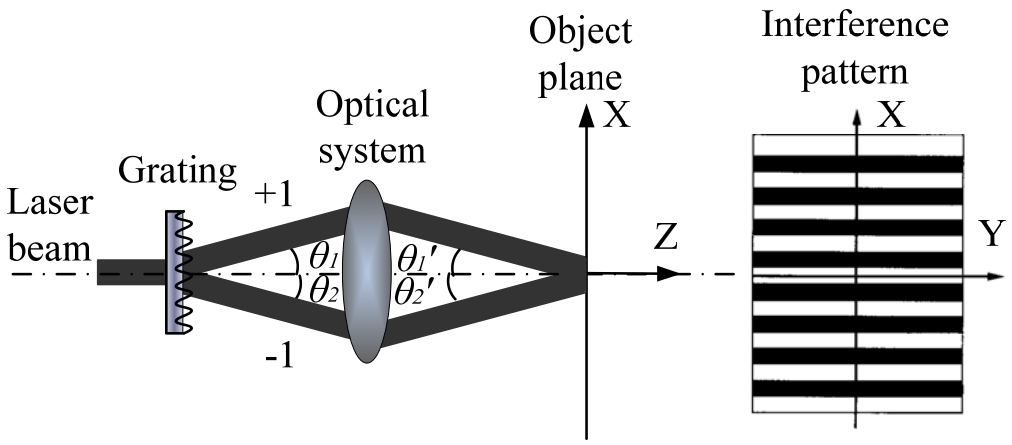


**Figure 4.4.3 Schematic of the structured illumination generation based on a diffraction grating**
The ±1 order diffracted beams from the diffraction grating produce interference pattern on the object plane. All the other diffraction orders are neglected.

For a diffraction grating, the relationship between the grating period and the angles of the incident and diffracted beams is expressed by the grating equation [148]:

$$\sin\theta_d = \sin\theta_i + m\frac{\lambda}{d}, \quad m = 0, \ \pm 1, \ \pm 2, \cdots \tag{4.4.1}$$

here $\theta_i$ is the angle between the incident beam and the normal to the grating surface, $\theta_d$ is the angle between the diffracted beam and the normal to the grating surface, $\lambda$ is the wavelength and $d$ is the grating period. In our case, $\theta_i = 0$, and $m = \pm 1$, then in Figure 4.4.3 there is:

$$\sin\theta_1 = -\sin\theta_2 = \frac{\lambda}{d} \tag{4.4.2}$$

The ±1 order diffracted beams go through the optical system and strike on the object plane symmetrically to the optical axis. Due to the same linear polarisation and frequency, the two beams produce interference pattern in the object plane. The intensity distribution of the interference pattern is:

$$I(x,y,z) = I_1 + I_2 + 2\sqrt{I_1 I_2}\cos[\Delta\phi(x,y,z)] \tag{4.4.3}$$

here $\Delta\phi = \phi_1 - \phi_2$ is the phase difference of the two beams. In our case, $I_1 = I_2 = I_0$, where $I_0$ is the intensity of the first order diffracted beam. And for simplicity we place the object plane at $z = 0$, then the phase difference between the two incident beams is:

$$\Delta\phi(x,y) = \frac{2\pi x}{\lambda}(\sin\theta_1' - \sin\theta_2') \tag{4.4.4}$$

and the resulting intensity of the interference pattern is:

$$I(x,y) = 2I_0\{1 + \cos[(\frac{2\pi x}{\lambda}(\sin\theta_1' - \sin\theta_2')]\} \tag{4.4.5}$$

The interference pattern is made up of straight fringes parallel to the Y axis with equal distance. The fringe period is:

$$p = \frac{\lambda}{\sin\theta_1' - \sin\theta_2'} \tag{4.4.6}$$

Since $\theta_2' = -\theta_1'$,

$$p = \frac{\lambda}{2\sin\theta_1'} \tag{4.4.7}$$

If the lateral magnification of the optical system is $M$, as a linear system, the angles $\theta_1$ and $\theta'_1$ have this relationship:

$$\sin\theta_1 = M\sin\theta_1' \tag{4.4.8}$$

According to Equation (4.4.2), (4.4.7) and (4.4.8), there is:

$$p = \frac{1}{2}Md \tag{4.4.9}$$

This is exactly the relationship between the grating period *d* and the period of the interference pattern *p* when using ±1 order diffracted beam to form structured illumination.

From the above result, we can conclude when the grating is moved the distance of 1/8 of one grating period along the X direction, the phase of the illumination pattern will change $\frac{\pi}{2}$ correspondingly. With four phase steps, four raw images with $\frac{\pi}{2}$ phase difference illumination can be acquired. Making use of the algorithm explained in the previous section, a new image with enhanced resolution in X direction can be reconstructed.

To maximise the resolution enhancement of the SIM, we should make the spatial frequency of the interference illumination pattern approach the bandwidth limit of the conventional microscope. The resolution, as the reciprocal of the bandwidth limit, of the conventional microscope is 206 nm (central emission wavelength: 515 nm), and the (de)magnification from the grating to the object plane was set as 0.022. If we intend to double the lateral resolution, from Equation (4.4.9), we need a grating with the period of:

$$d = \frac{2p}{M} = \frac{2 \times 206nm}{0.022} = 18.7\mu m$$

Practically we applied a grating with the period of 20 μm. With this grating, the interference pattern has the period of 220 nm that is quite close to the theoretical resolution of our conventional microscope.

### 4.4.3 Apparatus

Based on the system design above, an experimental SIF system was set up as shown in Figure 4.4.4. This system is a modification of a conventional epi-fluorescence microscope setup, adding a diffraction grating in the illumination path to produce structured illumination. The illumination and imaging path are indicated by blue and green dash-dot lines respectively in Figure 4.4.4.

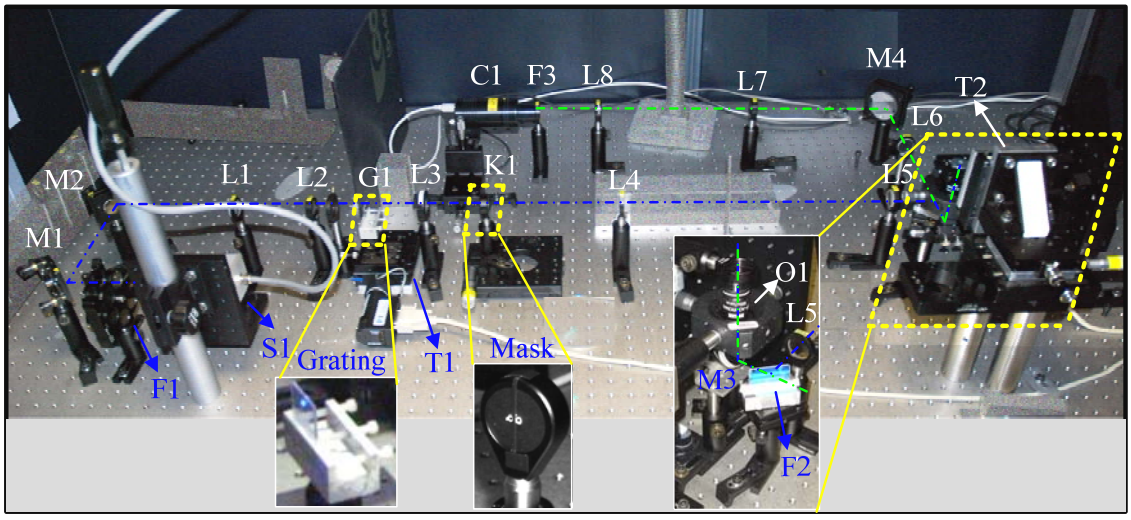


**Figure 4.4.4 Photograph of the 1D SIM system**
The illumination and imaging paths are indicated by blue and green dash-dot lines respectively.

The key apparatus in this setup include:

(1) Laser

The light source (S1) is a diode pumped solid state laser from Elforlight Ltd. Its brief specifications are given in Table 4.4.1.

**Table 4.4.1 Specifications of Elforlight diode pumped solid state laser**

| | |
|---|---|
| **Wavelength** | 473 nm |
| **Output power** | 20 mW |
| **Beam diameter(1/e$^2$ points)** | ~1 mm |
| **Beam divergence(full angle)** | <1 mrad |
| **Maximum noise (rms)** | <0.5% (typical 0.2%) |
| **Power stability** | <±2% over 8 hours |

(2) Objective lens

The objective lens (O1) we used is a 1.25 NA 100 × achromatic oil immersion objective from Carl Zeiss. Its brief specifications are given in Table 4.4.2.

**Table 4.4.2 Specifications of Zeiss achromatic objective lens**

| | |
|---|---|
| **Magnification** | 100× |
| **Numerical Aperture (NA)** | 1.25 |
| **Working Distance, WD** | 0.23 mm |
| **Coverglass Thickness** | 0.17 mm |
| **Immersion** | Oil |
| **Parfocal Length** | 45.06 mm |

(3) CCD camera

The CCD camera (C1) is from Starlight Xpress Ltd. Its major parameters are given in Table 3.3.3 in Subsection 3.3.2.

(4) Dichroic filter

The dichroic filter (F2) is from Chroma Technology Corporation. Its transmission curve is shown in Figure 4.4.5, from which we know the illumination (473 nm) is reflected while the emission (centred at 515 nm) is mostly transmitted.

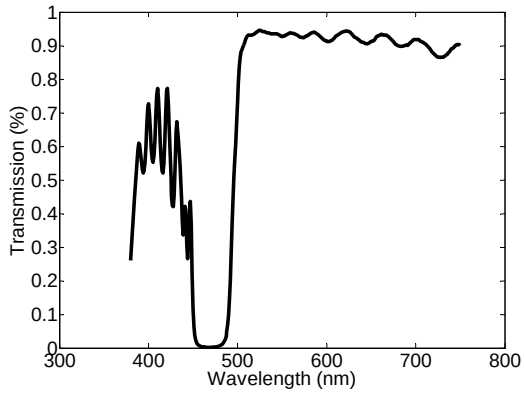


**Figure 4.4.5 Transmission curve of the dichroic filter**
Transmission at 473 nm (wavelength of laser beam): 2.8%, transmission at 515 nm (central emission wavelength): 93.2 %

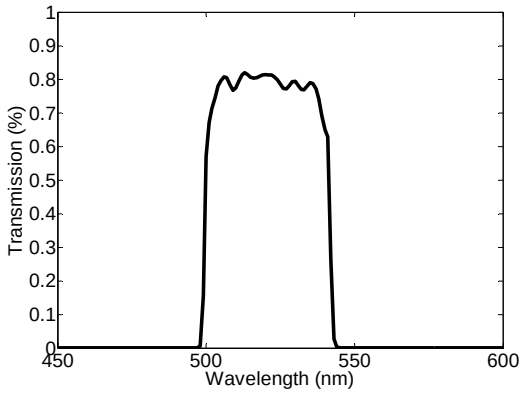


**Figure 4.4.6 Transmission curve of the emission filter**
Transmission at 515 nm (central emission wavelength): 80.6 %

(5) Emission filter

The emission filter (F3) is also from Chroma. Its transmission curve is shown in Figure 4.4.6, from which it is clear the emission (centred at 515 nm) is mostly transmitted and residual excitation is blocked.

(6) Translation stage

To fulfil phase stepping, the grating is mounted on a linear translation stage (T1, PI GmbH & Co.). The minimum incremental motion of this translation stage is 0.1 μm.

(7) Mask

The custom-designed mask (K1) contains two tiny holes from which the ±1 order diffracted beams can pass through, while all the other order diffracted beams are blocked.

# 4.5 Experiments and results

## 4.5.1 System calibration

The magnification is an important parameter of a microscope, which plays a key role in the evaluation of resolution. Two magnification parameters in our SIF were calibrated: one is the magnification in imaging path, i.e. the magnification from the object plane to the image plane; the other is the (de)magnification from the grating to the object plane. The standard resolution target we used was a 1951 USAF glass slide with positive chrome pattern. The images of this resolution target being placed on the object plane and in the grating position are shown in Figure 4.5.1 and 4.5.2 respectively. When imaging the resolution target, the spatial coherence of the laser beam was reduced by placing a rotating diffuser in the illumination path.

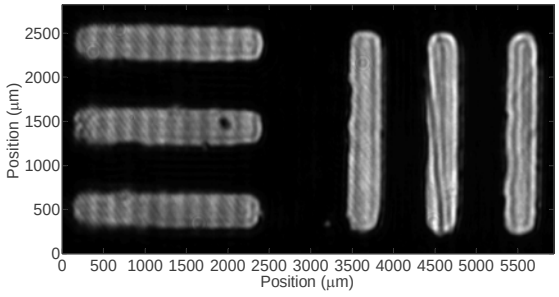


**Figure 4.5.1 Resolution target image used to calibrate the magnification in imaging path**
The coordinates correspond to the image plane on the CCD

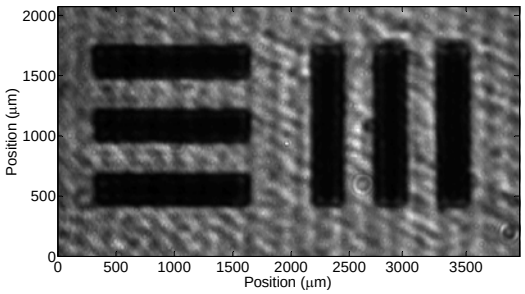


**Figure 4.5.2 Resolution target image used to calibrate the magnification from the grating to the object plane**
The coordinates correspond to the image plane on the CCD

The measurement value of the pattern period in Figure 4.5.1 and 4.5.2 is 946 μm and 531.2 μm respectively, and their nominal spatial frequency are 323 line pairs/mm and

12.7 line pairs/mm accordingly, then the magnification in the imaging path and the (de)magnification from the grating to the object are determined as 305 and 0.022.

Structured illumination pattern plays the most important role in SIM. Correct spatial frequency and accurate phase stepping of illumination patterns are the fundamental requirements to successfully fulfil high-resolution image reconstruction. In our experiments, we calibrated the spatial frequency and phase stepping accuracy of the interference illumination pattern before implementing the resolution examination experiments.

The structured illumination pattern (Figure 4.5.3) was captured by placing a mirror on the object plane, with the emission filter removed from the system. Its spatial frequency can be measured from its 1D Fourier transform (Figure 4.5.4). The measured value is $4.43\times10^{6}$ $m^{-1}$, corresponding to the period of 226 nm, which is very close to the designed value of 220 nm. Additionally, either from the experimental image of structured illumination pattern or its Fourier transform, it can be observed there is a low frequency stripe pattern mixed in the structured illumination pattern. This low frequency pattern comes from the interference of the multiple reflections from the dichroic filter.

Furthermore, the phase stepping procedure was also monitored in the same way. By Fourier transforming the four phase step images of the interference pattern, the relative phase angles are calculated from the corresponding complex numbers of the frequency

components. By comparing the relative phase angle of each pattern, the phase difference errors are worked out. From 20 measurements, the average phase difference error is $\pi/60$. In contrast to the theoretical phase difference of $\pi/2$, the error is just 3%. According to our simulation, this error would not lead to apparent deformation or artefacts in the reconstructed SIM images.

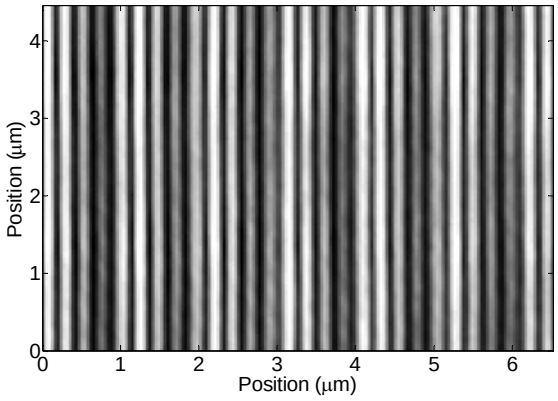


**Figure 4.5.3 Image of the interference illumination pattern**

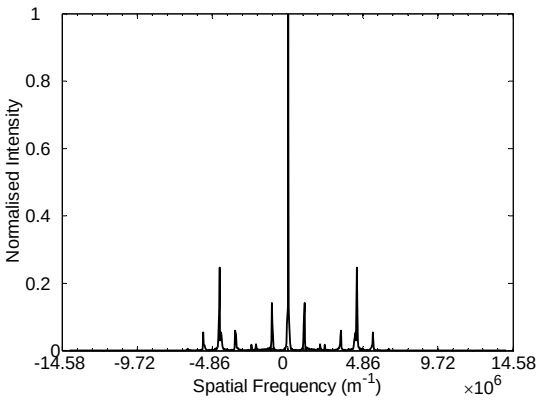


**Figure 4.5.4 1D Fourier transform of the image of structured illumination pattern**
Spatial frequency of structured illumination pattern: $4.43\times10^6$ m$^{-1}$

### 4.5.2 Raw image acquisition and processing

In our experiments, firstly four raw images were acquired with the phase of the interference illumination pattern shifted π/2 between each. Then these images were stored in a computer and processed in MATLAB to reconstruct a single high-resolution image. When processing these images, one way is to transform them into frequency domain, shift the displaced frequency components to their true positions, and then re-transform it back to spatial domain; the other way is to fulfil the reconstruction entirely in spatial domain as explained in Section 4.3. The latter method is more efficient due to the absence of Fourier transform. With this method, the typical processing time was about 4 seconds to reconstruct an 8 bit 752×580 pixel SIM image with 1D resolution improvement (phase-stepping happened in one dimension), and the image reconstruction was performed on a PC with a dual core 1.79GHz CPU and 1GB RAM. Practically on average we found it saved about 1/3 of the processing time in our case.

Although we employed the spatial domain method in practice, to demonstrate the inherent resolution enhancement mechanism in SIM, we illustrate the image reconstruction procedure in frequency domain in Figure 4.5.5 according to the Fourier transform method. The Fourier transform of a conventional fluorescence image (Figure 4.5.5a) shows no information can be detected outside the bandwidth (dashed circle) defined by the classical resolution limit. However, in the raw image with structured illumination (Figure 4.5.5b), high frequency components shifted from outside the

bandwidth into the bandwidth are contained as indicated by the arrows. From a sequence of four raw images, three different frequency component bands can be separated computationally (Figure 4.5.5c). By shifting them to their true positions, an expanded bandwidth (dashed ellipse), up to twice the size of the conventional one, can be constructed (Figure 4.5.5d). When transforming it back to spatial domain, an image with up to doubled lateral resolution can be obtained.

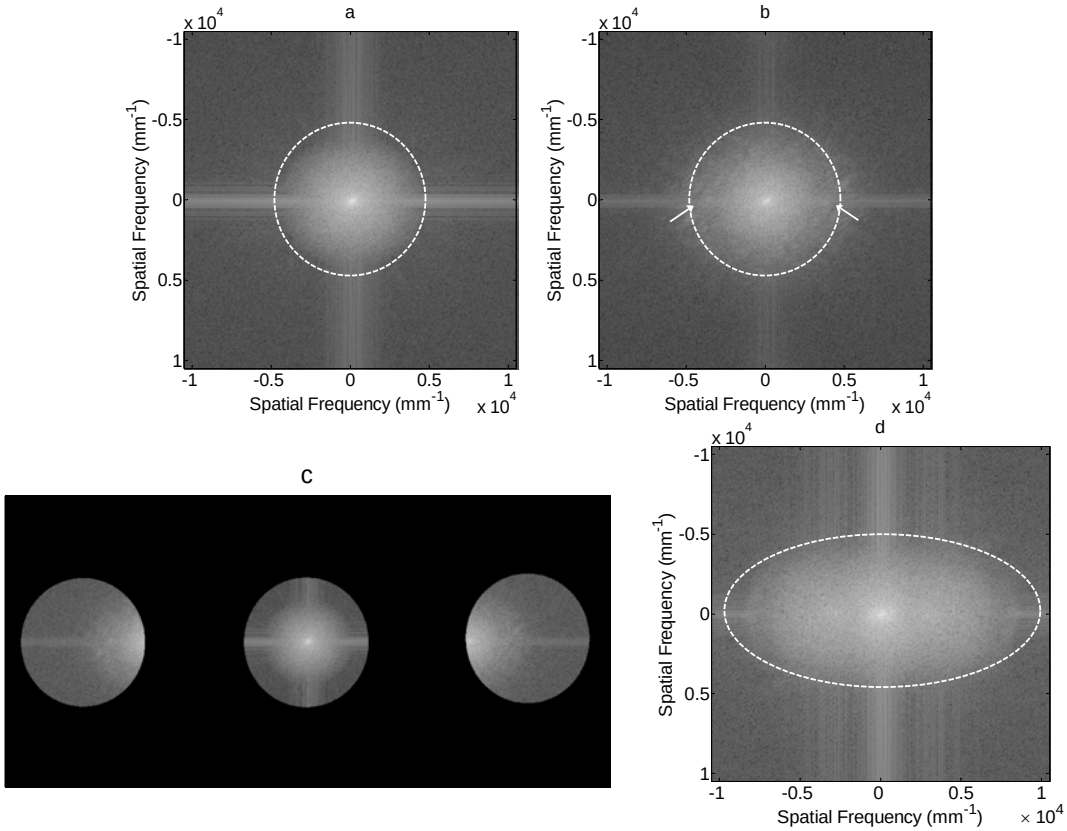


**Figure 4.5.5 High-resolution image reconstruction procedure in 1D SIM shown in frequency domain**

Fourier transforms of (a) a conventional image (dashed circle: bandwidth); (b) single raw image with structured illumination, in which the arrows indicate the shifted high frequency components from outside the conventional microscope bandwidth. (c) From four raw images, three bands of displaced information are separated. (d) The displaced bands are shifted to their true positions and form a new image with expanded bandwidth as indicated by the dashed ellipse.

When assembling the three different frequency component bands after moving the displaced frequency components back to their original positions, each frequency component should be compensated by the OTF of the microscope, averaging them with weights assigned according to their noise variances [5] [6] [53]. However, in our case we just assemble them by simple summing without implementing frequency component weighting.

### 4.5.3 Resolution evaluation method

Similar to the resolution evaluation method described in Subsection 3.4.1, the images of round fluorescent beads obtained with SIM are used to evaluate the resolution of the SIM system. We also model the convolution of a round-shaped object, with the same size as the fluorescent bead, and the PSF of a microscope with certain NA and wavelength. Then we compare the experimental image and a series of simulated images with different NAs. According to the best match between them, we can determine the corresponding resolution of the experimental system. Full Width at Half Maximum (FWHM) of the bead image profile is used here as the measurement in the comparison, instead of calculating 2D correlation coefficients. When the FWHM of the experimental bead image profile is same as, or practically close in (say $\leq$ 5 nm), the FWHM of a simulated bead image, we regard the practical NA of the experimental system as the parametrical NA in this simulation.

The method to compare FWHMs is a simplified approximation of the 2D correlation coefficient calculation method we used previously on the conditions of rather high SNR and sampling frequency in the images. Under such conditions, the cross-section profile of each bead image precisely depicts the resolution performance of the microscope.

### 4.5.4 Experimental results

In our experiments, 170 nm fluorescent beads (excitation/emission: 505/515 nm) were imaged by the 1D SIM. These beads were stored as suspensions in water and its concentration had been set by the factory in order to avoid aggregation. In each experiment, a drop of the bead solution was pipetted on a 0.17 mm thick coverglass, and then placed in an oven to heat-dry at 60 °C for 15 minutes.

To compare the resolution performance, the images of a number of 170 nm fluorescent beads were obtained with both conventional fluorescence microscope and 1D SIM. Moreover, the diffraction gratings with different periods were employed to demonstrate the computational resolution improvement in 1D SIM. In Figure 4.5.6, (a), (b) and (c) are the images of a single 170 nm fluorescent bead from conventional microscope, 1D SIM with 40 lp/mm (line pairs/mm) grating and 1D SIM with 50 lp/mm grating respectively. The cross-section profiles of these three single bead images are displayed in (e) for horizontal direction and (f) for vertical direction. In our experiments, the phase stepping of structured illumination happened in the horizontal direction, thus the resolution improvement should occur in the horizontal direction only. According to

these images, the width of the bead image in 1D SIM is clearly narrower in the horizontal direction in contrast to the one in conventional microscope image, while there is no observable difference in the vertical direction. The reduced size of the single bead in the horizontal direction in 1D SIM images indicates that the resolution in this direction has been improved thanks to the implementation of structured illumination.

We measure the FWHM of a single bead image in the horizontal direction to quantify the practical NA of the corresponding system. According to the measurements of ten isolated beads in each situation, the average FWHM of a single bead image is 247.7±3.9 nm for conventional microscope, 159.2±4.1 nm for 1D SIM with 40 lp/mm grating and 146.4±4.2 nm for 1D SIM with 50 lp/mm grating. Accordingly, the practical NA of each system is 1.14, 1.96 and 2.24 respectively. The deviation of the practical NA of the objective from its nominal value of 1.25 could be due to many causes, and the most common one is that high NA objective may not have an ideal OTF from manufacturing due to the strong attenuation of marginal rays [50]. Theoretically, when applying 40 lp/mm and 50 lp/mm grating in 1D SIM system, the spatial frequency of structured illumination pattern is $3.64 \times 10^6$ $m^{-1}$ and $4.55 \times 10^6$ $m^{-1}$ respectively, from which we expect a resolution improvement by a factor of 1.75 and 1.94 considering the central emission wavelength 515 nm and NA of 1.25. As stated by the measured NAs, the resolution is actually improved 1.72 and 1.96 times for 1D SIM with 40 lp/mm and 50 lp/mm grating respectively.

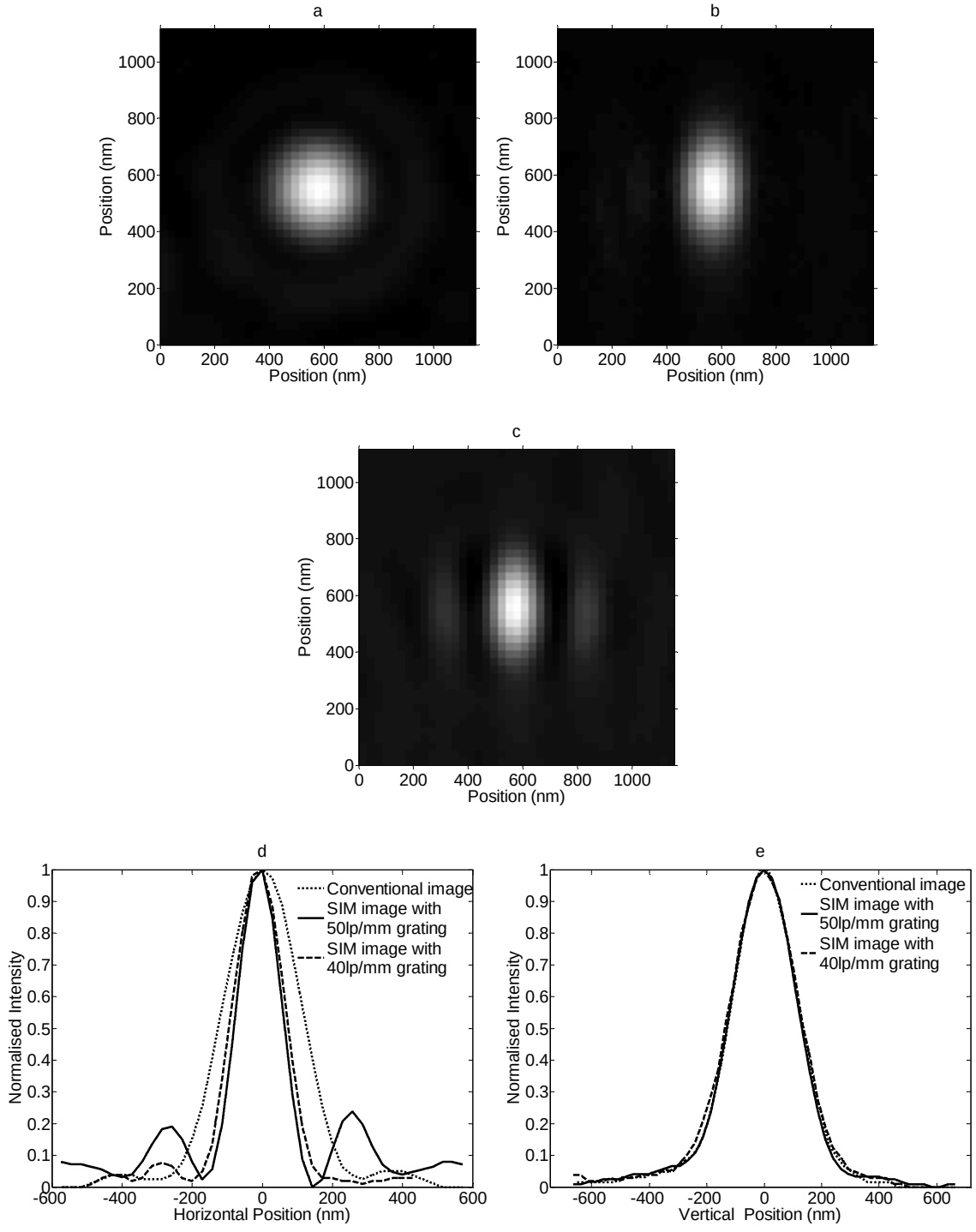


**Figure 4.5.6 Resolution comparison between conventional microscope and 1D SIM based on the images of a single 170 nm fluorescent bead**

The images of the same single bead are from (a) conventional microscope; (b) 1D SIM with 40 lp/mm grating; and (c) 1D SIM with 50 lp/mm grating. Cross-section profiles of (a), (b) and (c) in the horizontal direction are shown in (d), in which the FWHMs of the conventional image (dotted curve), 1D SIM with 40 lp/mm grating image (dashed curve) and 1D SIM with 50 lp/mm grating image (solid curve) are 247.7±3.9 nm, 159.2±4.1 nm and 146.4±4.2 nm respectively, corresponding to NA of 1.14, 1.96 and 2.24. Cross-section profiles of (a), (b) and (c) in the vertical direction are shown in (e). As the figure shows, there is no difference in resolution in this direction.

Moreover, the lateral resolution improvement in 1D SIM can be readily observed from the comparisons of two adjacent beads in the images shown in Figure 4.5.7. In this figure, the images of the same field of 170 nm fluorescent beads from conventional microscope, 1D SIM with 40 lp/mm grating and 1D SIM with 50 lp/mm grating are displayed in (a), (b) and (c). In region of interest A (ROI A), there are two adjacent beads lying along a non-orthogonal direction. In ROI B, there are two adjacent beads lying parallel to each other in the vertical direction. Neither of these two groups of adjacent beads in ROI A and ROI B can be resolved in conventional image (a). However, in 1D SIM image (b) and (c), the two adjacent beads in ROI A become resolvable in horizontal direction, but the two adjacent beads in ROI B are still unresolvable. The 3D surface plots of ROI A in each image are shown in (d), (e) and (f), and those of ROI B are shown in (g), (h) and (i). Clearly, the 1D SIM with 50 lp/mm grating has better resolution than the one with 40 lp/mm grating in the horizontal direction, while they have nothing to do with the resolution in the vertical direction. These images vividly demonstrate the 1D resolution improvement in our 1D SIM systems.

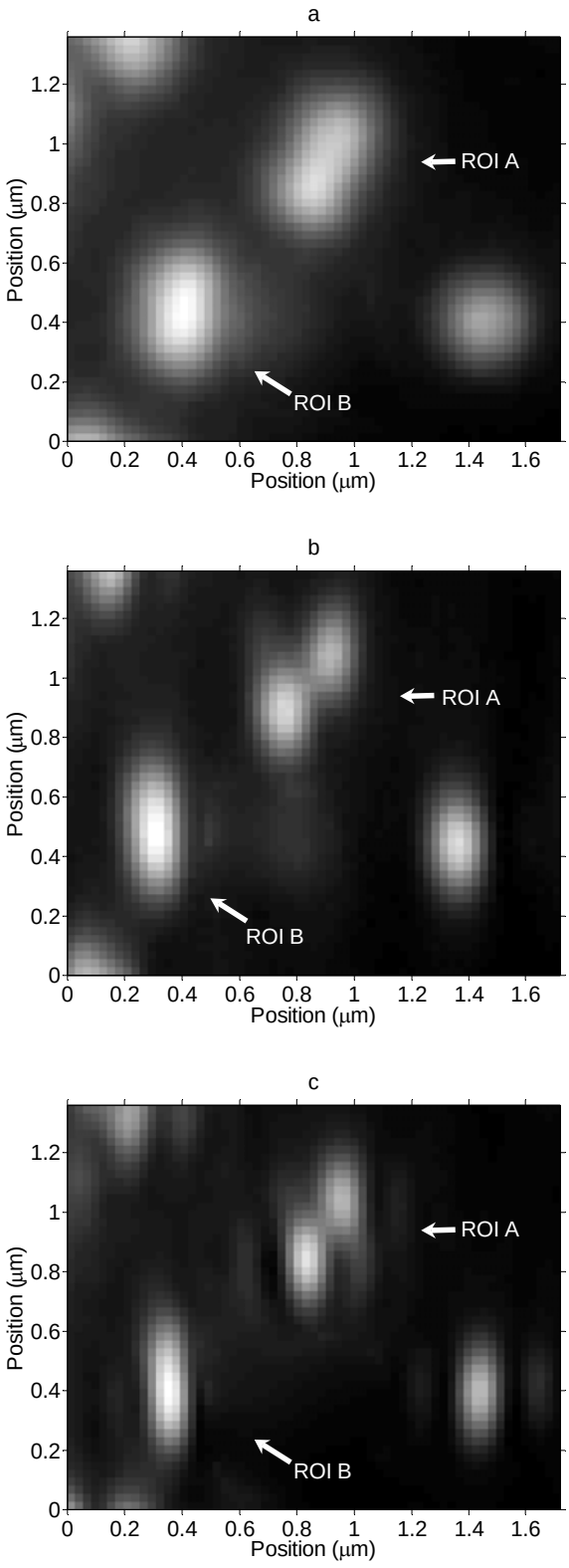


(Part of Figure 4.5.7, continued on the next page)

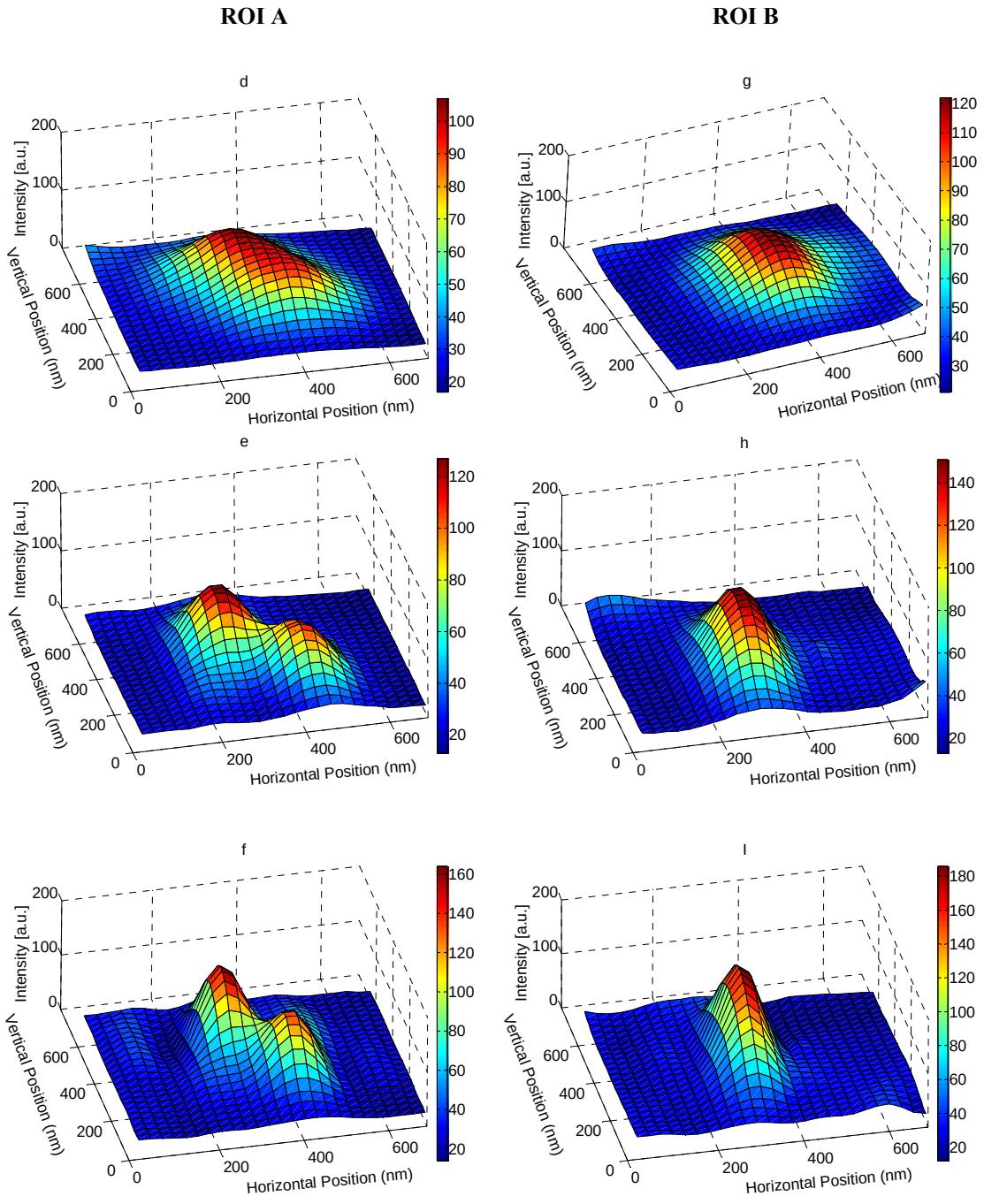


**Figure 4.5.7 Resolution comparisons between conventional microscope and 1D SIM based on the images of two adjacent 170 nm fluorescent beads**
The images of the same field of beads are from (a) conventional microscope; (b) 1D SIM with 40 lp/mm grating; and (c) 1D SIM with 50 lp/mm grating. In region of interest A (ROI A), two adjacent beads lie along a non-orthogonal direction; in ROI B, two adjacent beads lie parallel to each other in the vertical direction. The 3D surface plots of ROI A in each image are shown in (d), (e) and (f) respectively, and those of ROI B are shown in (g), (h) and (i) respectively. Apparently, the originally unresolvable adjacent beads in ROI A become resolvable in 1D SIMs in the horizontal direction, while nothing has happened in the vertical direction either in ROI A or in ROI B. Moreover, 1D SIM with 50lp/mm grating shows higher resolving power than 1D SIM with 40 lp/mm grating in the horizontal direction.

### 4.5.5 Discussion

In practice, we used a transmission amplitude diffraction grating to produce sinusoidal interference pattern as structured illumination pattern. This method is apparently inexpensive. Moreover, the transmission property of the grating maintains the whole system on-axis, which simplifies the optical alignment and eliminates the occurrence of geometrical aberrations. However, the optical power efficiency in this method is rather low. According to Kirchhoff's diffraction theory, in the Fraunhofer approximation, it is stated that, for the Ronchi gratings with rather large periods as we employed, the diffraction efficiency $\eta$ of incident light is given by the equation below [148]:

$$\eta_m = \frac{a}{d}\frac{\dfrac{\sin^2(\pi am/d)}{(\pi am/d)^2}}{\displaystyle\sum_m \frac{\sin^2(\pi am/d)}{(\pi am/d)^2}} \qquad (4.5.1)$$

here $a$ is the groove width, $d$ is the period, $m$ is the diffraction order. From this equation we know the diffraction efficiency is a function mainly of the ratio of $a$ to $d$. The results are plotted in Figure 4.5.8. From this figure, we know the diffraction efficiency of the first order is 11.1% in our case, where the ratio $a/d$ is 0.5. Therefore the two first orders deliver only 22.2% of the original laser beam power to illuminate the sample. Under this condition, a laser source with rather high power is needed in order to fulfil an efficient fluorescence excitation. Instead of an amplitude grating, a phase grating may perform much higher diffraction efficiency. Gustafsson's group applied a custom-made phase grating delivering 80% of the beam power into the two useful orders to generate structured illumination pattern [5] [6].

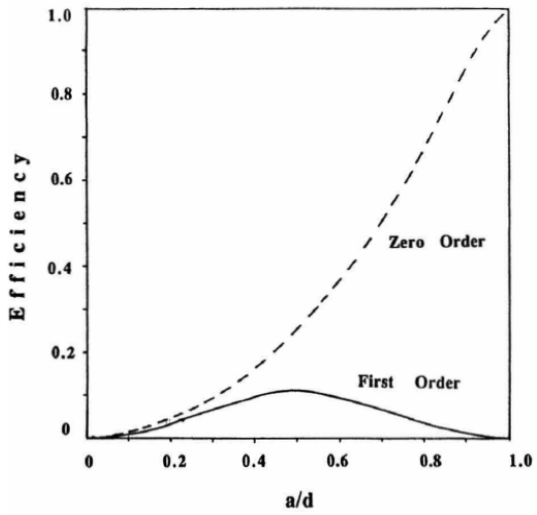


**Figure 4.5.8 Diffraction efficiency in zero and first order of a Ronchi ruling as the function of the ratio of groove width *a* to period *d* [148]**

Our 1D SIM system demonstrates the principle of how SIM improves the lateral resolution of a conventional microscope, however, 1D high-resolution images are inadequate in most practical cases. To extend 1D SIM to 2D SIM, we can apply the 1D structured illumination pattern repeatedly at different azimuthal angles. When mounting a diffraction grating on a rotation stage, we can change the azimuthal angles of the structured illumination pattern by rotating the rotation stage. Furthermore, we need to combine the rotation stage with a translation stage in order to implement 2D phase stepping. We will experimentally fulfil 2D SIM in the next chapter.

# 4.6 Artefacts

## 4.6.1 General analysis

In SIM, the final high-resolution image is a composite product of several raw images. When these raw images suffer relative position or intensity instability, the reconstructed image may contain some biases to the proper reconstructed image. Practically, the biases may be displayed in different forms of artefacts in SIM images. These artefacts could be the deformations of real samples, or the residual stripe patterns. It is necessary to analyse the causes of the artefacts and find out the solutions to eliminate or correct them.

In a paper on SIM artefact issue [64], the authors categorised the origins of artefacts as two groups: imprecise instrumental hardware and certain bleaching properties of the sample. The first group covers the problems like fluctuating intensity of light source, phase errors from grating shifts and so on; the second group contains the problems like decreased detection intensity due to homogeneous bleaching of sample, decreased detection intensity at different rates due to inhomogeneous bleaching of sample, superposition of illumination pattern on samples due to constant bleaching and so on. To tackle these problems, the authors developed a model-based method utilising parameter optimisation by minimising a merit function, meanwhile, a spatially adaptive bleaching correction method was also developed. It is worth noting that the artefact analysis in this paper is based on optical sectioning approach to fulfil SIM, in which the

axial resolution enhancement is the real aim, but it is still beneficial for our case due to the similar working mechanism in our SIM.

In our case, the artefacts induced by raw image displacements occurred in our preliminary experimental results. Although the problem was solved by refining the mechanical arrangement of the translation stages supporting samples soon after, we will investigate the artefact and the corresponding non-physical correction method in the next subsection.

### 4.6.2 Artefacts induced by raw image displacements

In our research, at least at this stage, we just aim to observe stationary samples by SIM. In other words, the samples always suppose not to change its position during the raw image acquisition. However, sometimes the sample (more accurately speaking, it is sample holder such as coverglass or coverslip) moves somehow during the raw image acquisition, and this leads to a series of relatively displaced raw images. Now, we are going to investigate how these displacements affect the final reconstructed SIM image through simulation.

Based on the 1D SIM simulation described in Section 4.3, we put a 1/5 period distance displacement on the sinusoidal distribution sample (spatial frequency: $5\times10^6$ $m^{-1}$) in each raw image one by one, then we obtain a very strange reconstructed SIM image. In Figure 4.6.1, the profiles of the original sample (black curves), the displaced sample

with 1/5 period distance displacement (blue curves) and the final reconstructed sample (red curves) are shown in the same figure. Here, the original sample and the displaced sample correspond to the objects in raw image No.1 and No.2, while the objects in raw image No.3 and No.4 which have 2/5 and 3/5 period distance displacements relative to that in raw image No.1 are omitted in this figure for clarity. From this figure, it is shown the reconstructed image is not a sinusoidal distribution any more, and the spatial frequency is halved. In this case, the SIM fails to perform high-resolution imaging. From this simulation, we know the displacements among the raw images can lead to the failure to correctly reconstruct original object and produce deformed artefacts in the reconstructed SIM image.

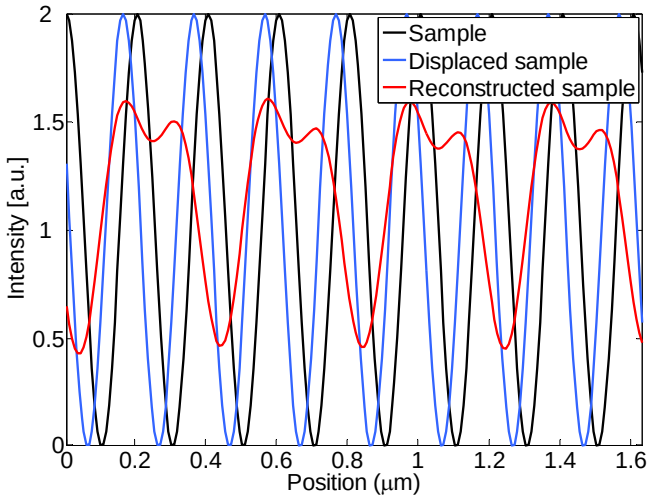


**Figure 4.6.1 Profiles of a sample (black curves), the displaced sample (blue curves) and the reconstructed sample (red curves) in 1D SIM simulation**
Sinusoidal distribution sample has the spatial frequency of $5\times10^6$ $m^{-1}$, which corresponds to the object in raw image No.1. The displaced sample has a displacement of 1/5 period distance relative to the original sample, which corresponds to the object in raw image No.2. The objects in raw image No.3 and No.4, which have the displacements of 2/5 and 3/5 period distance relative to the original sample, are omitted in this figure for clarity. The reconstructed sample image is from these displaced raw images.

Now let us have a look at a practical case on the artefacts induced by raw image displacements. In Figure 4.6.2, image (a) and (b) are the pseudocolor images of the same fluorescent bead in raw image No.1 and raw image No.3 in an experiment. Apparently, the position of this bead in raw image No.3 is different from that in raw image No.1. The corresponding reconstructed SIM image is shown in Figure 4.6.3 (a), obviously the bead is deformed. The displacements in the raw images could come from the mechanical drift, such as the static displacement from the translation stages on which the coverglass holder is mounted, or from the subtle movement of the coverglass due to the air disturbances or environmental vibrations. The displacement introduced by the former mechanism holds the feature that the movement direction and velocity is consistent; while if the reason is the latter one, the displacement direction and velocity should be random. According to the investigation on a series of 20 images taken at 1 second intervals, we find the displacements happen in a certain direction with constant velocity. Thus we conclude the artefacts come from the mechanical drift.

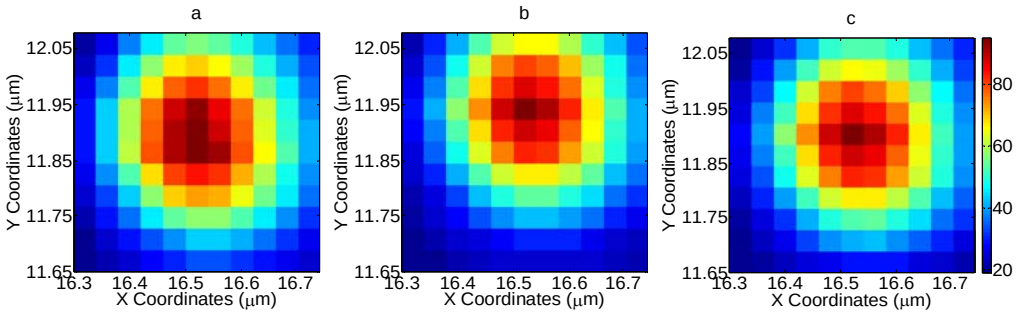


**Figure 4.6.2 Pseudocolor images of the same fluorescent bead in (a) raw image No.1, (b) raw image No.3, and (c) processed raw image No.3 in an experiment**
(c) is the processed image from (b) by shifting back 1 pixel in the vertical direction, through this procedure, the displacement between raw image No.3 and No.1 is offset.

Besides improving the translation stages to overcome the mechanical drift, we could correct the artefacts by image processing as well. The idea is to shift the displaced images back to their original places. In detail, firstly, we take the raw image No.1 as the reference image, which means the position of each fluorescent bead in this image is regarded as its original position. Secondly, we calculate the normalised cross-correlation coefficients between each other raw image and the raw image No.1. The displacement between them can be calculated according to the location of the peak of the cross-correlation matrix. Thirdly, we shift the displaced image back to their original position, using the displacement values determined in the previous step. For example, the Figure 4.6.2(c) is the processed image from Figure 4.6.2 (b) by shifting it back 1 pixel in the vertical direction. Comparing with Figure 4.6.2(a), the displacement has been offset. Finally, we use the raw image No.1 and three other processed images to reconstruct the final high-resolution image.

Figure 4.6.3 (a) and (b) are the 1D reconstructed images of a florescent bead from four non-processed and processed raw images respectively. In original non-processed raw images, image No.3 and 4 both displaced 1 pixel in the vertical direction relative to image No.1, after processing, they were both shifted back to the initial positions as defined in image No.1. In Figure 4.6.3, it is clear the artefact disappears in the reconstructed image from processed raw images, which demonstrates the good performance of the above correction method.

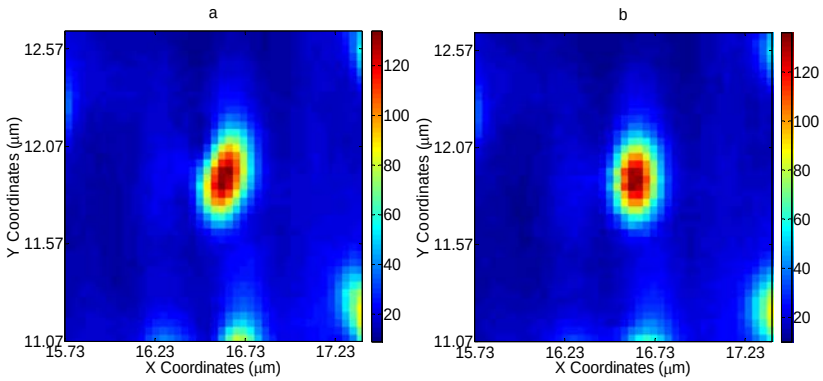


**Figure 4.6.3 Comparison of the reconstructed images of a fluorescent bead (a) with artefact and (b) without artefact induced by raw image displacements in 1D SIM**

# 4.7 Conclusions

In this chapter, we theoretically and experimentally examined high-resolution structured illumination microscopy (SIM) working in one dimension. With our prototype 1D SIM, we demonstrated effective NA of 2.24 by using an oil immersion objective lens with practical NA of 1.14 (nominal NA 1.25), which confirmed the doubled resolution capability of SIM in the lateral direction. The artefacts induced by raw image displacements and its correction method were also discussed and demonstrated.

In SIM, high spatial frequency information, which are originally out of the bandwidth of the conventional microscope, are mixed and shifted into the bandwidth through the structured illumination. In order to recover the high spatial frequency information, a four-phase-step method was applied in our case, in which the sinusoidal distribution structured illumination pattern was translated by four phase steps and one raw image

was captured at each value of the illumination phase. This four-phase-step method was testified to be robust in the presence of phase-stepping errors. The spatial domain algorithm used to reconstruct high-resolution SIM image in our case is simple and efficient. The two-beam interference method based on a diffraction grating to construct structured illumination not only provides high-contrast illumination patterns, but also makes the whole illumination path share the same optical axis, which simplifies the optical alignment and ensures the accuracy of structured illumination pattern formation. The nature of doubled spatial frequency in interference pattern relative to the spatial frequency in the original grating image is beneficial to construct a fine structured illumination pattern with a rather coarse diffraction grating. A coarse grating means not only low cost and high manufacture precision, but also fewer appearances of phase stepping errors. The two-beam interference method represents a cheap and reliable way to fulfil structured illumination.

The practical approach to the implementation of SIM has been successful developed, and the corresponding four-phase-step algorithm for high-resolution image reconstruction is examined as well, now we can take our research further.

# Chapter 5 Structured Illumination Solid Immersion Fluorescence Microscopy (SISIM)

## 5.1 Introduction

In the previous chapters, we have investigated two independent high-resolution fluorescence microscopic techniques − solid immersion fluorescence microscopy (SIF) employing an aplanatic solid immersion lens (ASIL) and structured illumination microscopy (SIM). In this chapter, we combine them in order to develop a new hybrid microscopic technique. This new technique, which is called structured illumination solid immersion fluorescence microscopy (SISIM), takes advantages of high NA of SIF and resolution enhancement capability of SIM, thus it is a promising technique to achieve exceedingly high lateral resolution.

In this chapter, we firstly explain the theoretical foundation of high-resolution performance of SISIM. Then we present the experimental considerations, implementations and results of 1D and 2D SISIM respectively. Finally we discuss the total internal reflection (TIR) illumination in SISIM.

## 5.2 Theory

According to our previous study, the SIF system can provide a numerical aperture (NA) as high as 1.85 (theoretically about 2) due to the high refractive index of the ASIL material that is around 2. Moreover, SIM can double the spatial bandwidth of a microscope system when applying the structured illumination pattern with the highest spatial frequency allowed by the NA of the microscope. In SIM, it is necessary to use as high a modulation frequency as possible in order to approach the highest resolution achievable, and this maximum modulation frequency of the structured illumination is limited by the NA of the objective lens. If we combine SIM and SIF, the modulation frequency in SIM could be improved dramatically due to the high NA of SIF in contrast with a conventional SIM using a conventional objective lens, and as a consequence, a higher lateral resolution, comparing with the individual SIF, could be achieved. In our case, their combination could achieve an effective NA approaching 4 in principle, which could lead to a spatial resolution below 100 nm if we use the light at the wavelength below 650 nm. A resolution at such level is clearly attractive in the research of light microscopy, especially in a wide-field system.

The combination of SIM and SIF, i.e. SISIM, certainly carries some legacy from its original systems. In Chapter 3, we analysed the aberration issues in SIF. Similarly, in SISIM, the size of the ASIL determines the range of fluorescence spectral width suitable for imaging and the valid FOV associated with aberrations when maintaining high-resolution performance. When maintaining the theoretical resolution, the feasible

fluorescence spectral width decreases with increasing the ASIL size, while the feasible FOV increases with increasing the ASIL size. It is necessary to find a trade-off between fluorescence spectral width and effective FOV. The conclusion on the fluorescence spectral width and FOV regarding ASIL size as summarised in Subsection 3.5.4 is still a practical reference on the ASIL selection when implementing SISIM. Accordingly, we retain the 5 mm diameter ASIL and the 3 nm passband (FWHM) emission filter in our SISIM system. Another character of SIF that is carried by SISIM is the near-field imaging property. When delivering a high-resolution performance in SISIM, the imaging must happen in near field because the air gap will severely degrade the resolution performance in the solid immersion system. For that reason, we apply 20 nm fluorescent beads as samples in our SISIM experiments.

In our SISIM system, we use the same method used in the SIM system to generate structured illumination. A diffraction grating is applied in the illumination path and the ± 1 order diffraction beams from it are used to produce interference pattern in the object plane as structured illumination pattern. When the grating is translated in one direction, one-dimensional (1D) phase stepping can be fulfilled. Furthermore, the grating is mounted on a rotation stage to perform phase stepping at different azimuthal angles, in this way, a two-dimensional (2D) SISIM can be achieved and the high-resolution images with two-dimensional resolution improvement can be obtained.

# 5.3 One-dimensional (1D) SISIM

## 5.3.1 System design

As a combination of SIF and 1D SIM, 1D SISIM can be constructed by modifying the conventional Köhler illumination in the SIF system to a 1D structured illumination. We put a diffraction grating in the illumination path in the SIF system to generate structured illumination pattern by the interference of ±1 order diffraction beams from the grating. The schematic diagram of the 1D SISIM system is shown in Figure 5.3.1.

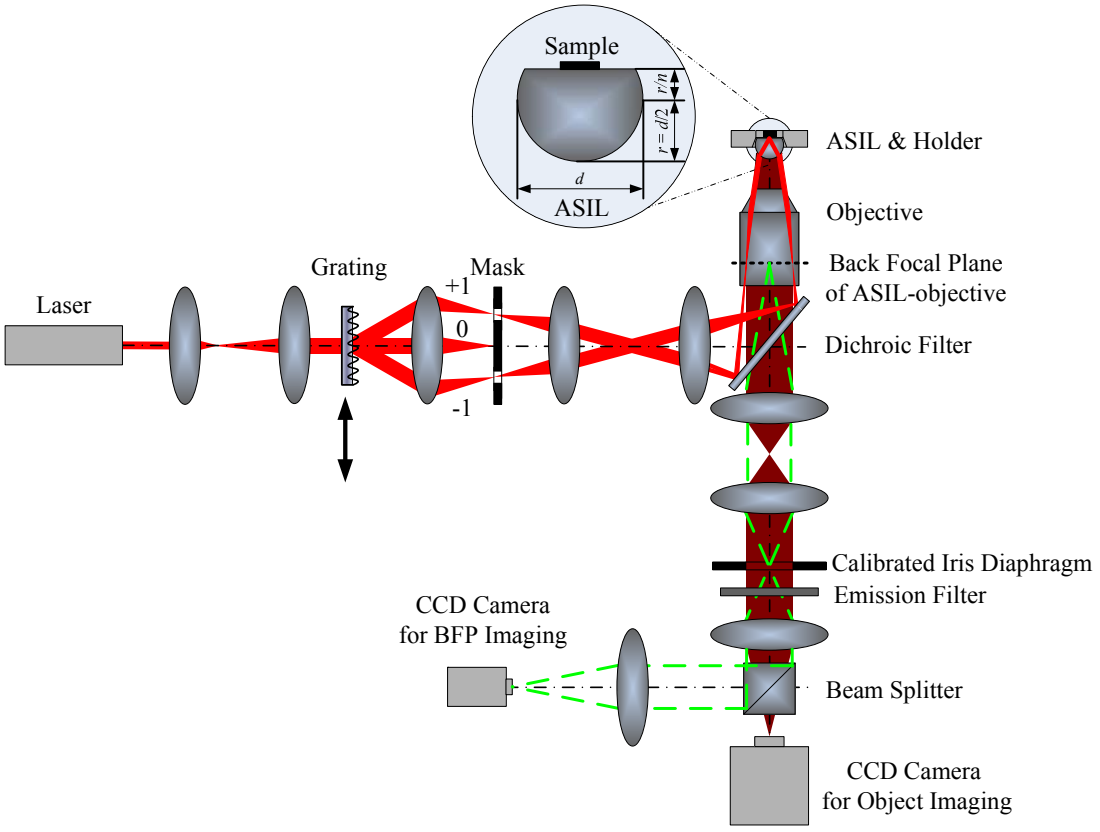


**Figure 5.3.1 Schematic of the 1D SISIM system**
The sharp red shading illustrates the construction of structured illumination; the dark red shading illustrates the fluorescent light forming specimen image; and the green dashed lines illustrate the fluorescent light forming BFP image. The ASIL configuration is also shown in the enlarged inset. The mask allows +1 and -1 order diffraction beams to pass through and form structured illumination pattern. The grating is translated along the direction perpendicular to the grating grooves to fulfil phase stepping.

The lens relay arrangement in the illumination path of the SISIM system needs careful design. On the one hand, the spatial frequency of the structured illumination pattern should approach the resolution limit of the ASIL-objective in order to improve the resolution as much as possible, which requires a proper demagnification from the grating to the object plane. On the other hand, to produce an efficient illumination that just covers the effective FOV, the demagnification from the output laser beam to the object plane is also required to be set properly. For the latter one, the demagnification is set as 0.06 as used in the previous SIF system, because it has been demonstrated to be an efficient value. The demagnification from the grating to the object plane is designed as 0.019. According to Equation 4.4.9 in Chapter 4, it is known the period of the interference pattern should be 190 nm (spatial frequency $5.26\times10^{6}$ $m^{-1}$) when applying a 20 μm period grating. Comparing with the theoretical bandwidth of the SIF system, which is $5.97\times10^{6}$ $m^{-1}$ considering the theoretical NA of 2 and emission wavelength of 670 nm, the spatial frequency of the structured illumination pattern is 88% of the bandwidth of the SIF system, therefore, theoretically the bandwidth could be improved by a factor of 1.88 with regard to the emission wavelength in the 1D SISIM system.

Regarding the imaging path, we keep it as the original design in the SIF system since the sampling frequency is already high enough even for the doubled resolution. The magnification from the object plane to the image plane has been calibrated as 210 (designed value: 200, see Subsection 3.3.3 in Chapter 3). The BFP imaging path is also

retained to observe the form of structured illumination on the BFP, and the magnification in this path is set as 1.

### 5.3.2 Apparatus

A 1D SISIM system (Figure 5.3.2) was built up based on our established bench-top SIF setup. The illumination, object imaging and BFP imaging paths are indicated by sharp red, dark red and green dash-dot lines respectively. In the illumination path, the bending section, i.e. from mirror 3 (M3) to mirror 6 (M6), is newly installed structured illumination generator. The 20 μm period diffraction grating (G1) diffracts the laser beam to several diffraction orders, but the custom-designed SISIM mask (A1) allows +1 and -1 order diffraction beams to get through only. These two beams interfere in the object plane to construct sinusoidal distribution structured illumination pattern. The combination of lenses from lens 3 (L3) to lens 6 (L6) maintains the demagnification in the illumination path as the value in the SIF system. Meanwhile, the combination of lenses from lens 5 (L5) to the ASIL-objective provides a demagnification of 0.019, which leads to a structured illumination pattern with the period of 190 nm.

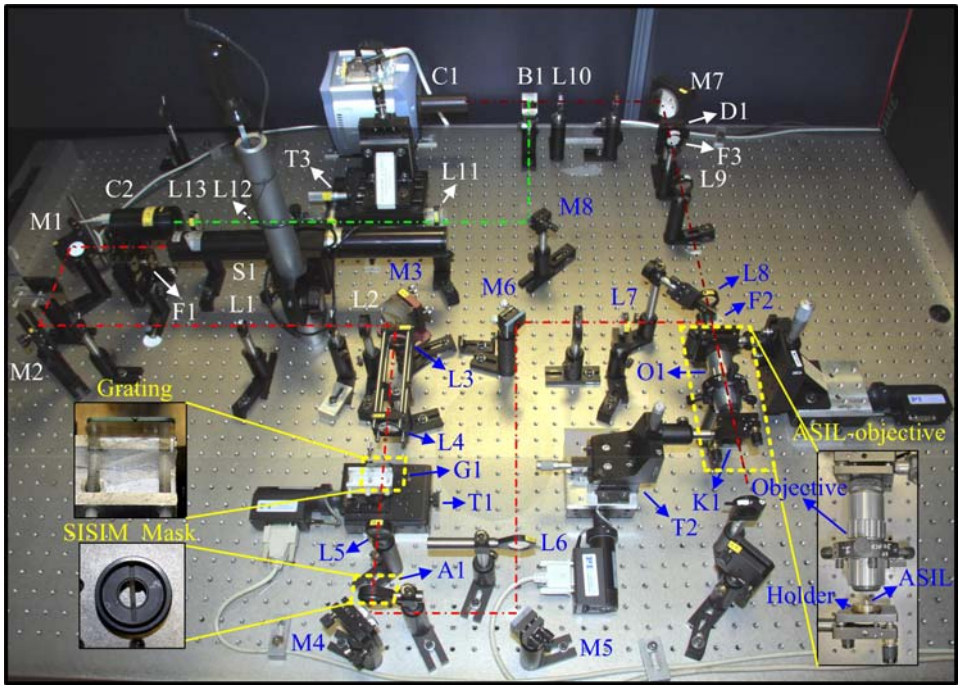


**Figure 5.3.2 Photograph of the 1D SISIM system**
Sharp red dash-dot line: illumination path; dark red dash-dot line: object imaging path; green dash-dot line: BFP imaging path. The grating, SISIM mask and ASIL-objective are shown in the enlarged insets. The SISIM mask allows +1 and -1 order diffraction beams to pass through and form structured illumination pattern. The grating is mounted on a translation stage to be translated along the direction perpendicular to the grating grooves to fulfil phase stepping.

This 1D SISIM system was built on the basis of our SIF system, the descriptions on the key apparatus can be found in Subsection 3.3.2 in Chapter 3. About the translation stage (T1), its information can be found in Subsection 4.4.3 in Chapter 4.

## 5.3.3 System calibration

Before experimentally investigating the resolution performance of the 1D SISIM system, we should calibrate the magnification of the system and structured illumination pattern. This system was constructed by modifying the illumination path of the original SIF system, thus it was just necessary to calibrate the magnification of the illumination

path. In the 1D SISIM system, the illumination beams are incident in the object plane, i.e. the flat surface of the ASIL, with large angles that surpass the critical angle at the interface (see Section 5.5 for more discussion). Therefore, the beams are totally reflected by the flat surface of the ASIL. At this time, the flat surface of the ASIL works like a mirror, when the emission filter is removed from the system, it is straightforward to observe the interference pattern from the camera. A part of the image of this pattern is shown in Figure 5.3.3. According to its Fourier transform as shown in Figure 5.3.4, it is known the spatial frequency of the pattern is $5.23\times10^{6}$ $m^{-1}$, in other words, the period of the pattern is 191.2 nm which is very close to the designed value of 190 nm. In this way, the magnification of the illumination path of the 1D SISIM system and the period of the structured illumination were calibrated. Additionally, from Figure 5.3.3 and 5.3.4, it can be observed there is a low frequency stripe pattern mixed in the structured illumination pattern. This low frequency pattern came from the interference of the multiple reflections from the dichroic filter. Regarding the phase difference errors when implementing phase stepping, it was similar to the situation in 1D SIM (see Subsection 4.5.1) since the same grating was employed.

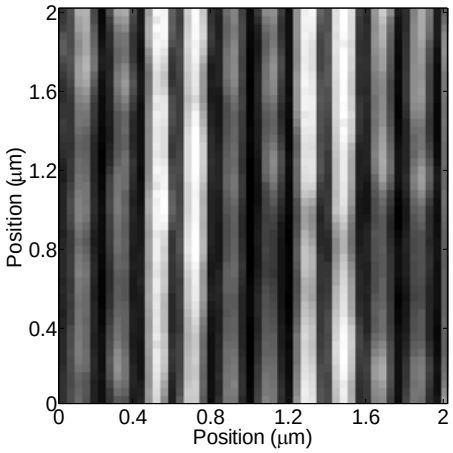


**Figure 5.3.3 Image of the structured illumination pattern in 1D SISIM**

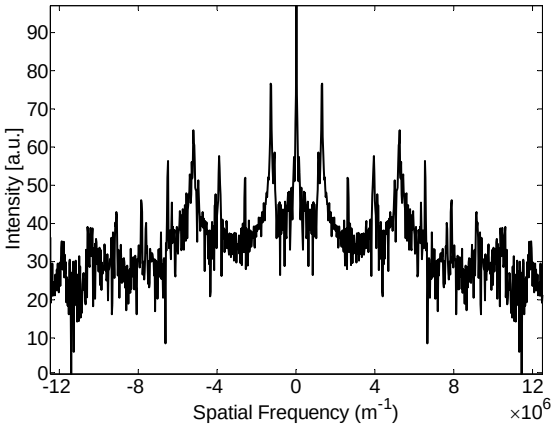


**Figure 5.3.4 1D Fourier transform of the image of structured illumination pattern in 1D SISIM**
Spatial frequency of structured illumination pattern: $5.23\times10^6$ $m^{-1}$.

## 5.3.4 Experiments and results

The samples we used to examine the resolution performance of the 1D SISIM system were 20 nm fluorescent beads (excitation/emission: 625/645 nm) which had been applied in previous SIF experiments. The samples were prepared in the same way as described in Subsection 3.4.2.

Fluorescent beads in 20 nm size contain quite small amount of fluorescent dye, the emission from each bead was considerably weak. Moreover, since only ±1 order diffraction beams from the diffraction grating were used to produce sinusoidal distribution pattern for illumination, the optical power of the laser source was not fully employed. For these reasons, a single frame image of these beads in the SISIM was usually quite noisy. To improve the SNR in each raw image, besides applying electron multiplying gain to multiply the signal with the help of the EMCCD, 16 frames with 0.5

seconds exposure time were averaged to be one raw image. Four raw images were captured to reconstruct a 1D SISIM image. Meanwhile the conventional SIF image could be derived by simply summing the four raw images.

The images of an isolated 20 nm fluorescent bead obtained with the SIF and the 1D SISIM are shown in Figure 5.3.5 and 5.3.6 respectively. Although the images are too noisy to quantify the resolution by means of FWHM measurement, it is still apparent the resolution in the horizontal direction has been improved in 1D SISIM image according to the narrower size of the bead image. Meanwhile it is hard to see any resolution change in the vertical direction. These results are exactly what we expected because we just fulfil phase stepping in the horizontal direction. Regarding the quantification of the resolution of our SISIM system, we will evaluate it later in the next section through 2D reconstructed images.

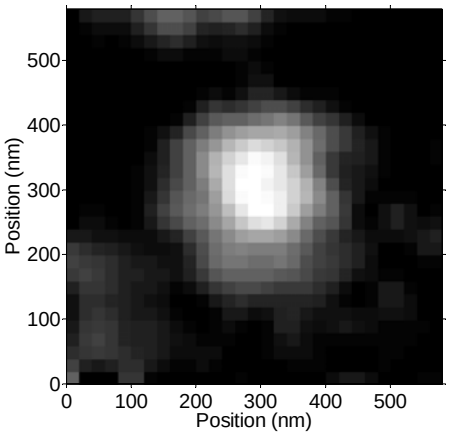


**Figure 5.3.5 20 nm fluorescent bead image obtained with SIF**

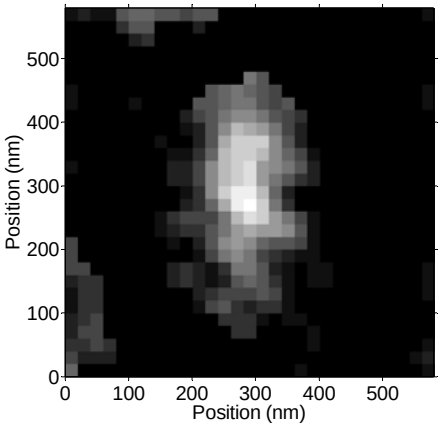


**Figure 5.3.6 20 nm fluorescent bead image obtained with 1D SISIM**

## 5.4 Two-dimensional (2D) SISIM

### 5.4.1 System design

To extend the resolution improvement ability of SISIM from one dimension to two dimensions, we need to repeat the phase stepping procedure with at least two other azimuthal angles as shown in Figure 4.2.2 in Chapter 4. By mounting the diffraction grating on a rotation stage, this aim can be achieved. The schematic diagram of a 2D SISIM system is shown in Figure 5.4.1. In contrast to the 1D SISIM system, the only difference is that the grating is able to rotate in the 2D SISIM system. As the same grating is employed, the resolution is expected to be improved by a factor of 1.88 with regard to the emission wavelength as well in the 2D SISIM system (see Subsection 5.3.1).

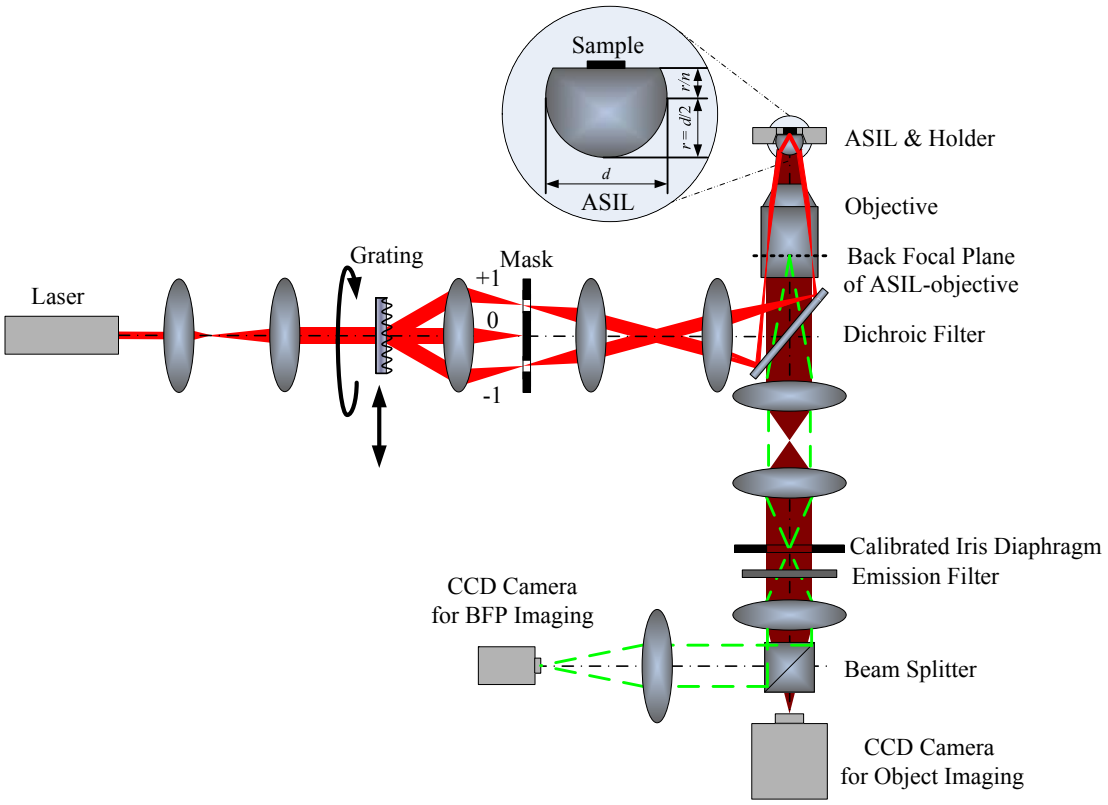


**Figure 5.4.1 Schematic of the 2D SISIM system**
The sharp red shading illustrates the construction of structured illumination; the dark red shading illustrates the fluorescent light forming specimen image; and the green dashed lines illustrate the fluorescent light forming BFP image. The ASIL configuration is also shown in the enlarged inset. The mask allows +1 and -1 order diffraction beams to pass through and form structured illumination pattern. The grating is translated along the direction perpendicular to the grating grooves to fulfil phase stepping. It is also rotatable in the plane perpendicular to the optical axis to fulfil 2D phase stepping.

In the 2D SISIM system, the diffraction grating is mounted on the assembly of a translation stage and a rotation stage in order to fulfil 2D phase stepping. This procedure is schematically shown in Figure 5.4.2. The rotation stage is used to rotate the grating in X-Y plane, and the translation stage is used to translate the grating in +X or –X direction. Firstly, the grating vector *k* (dashed line) is set to point towards +X direction (Figure 5.4.2, a), at this time, *k* has no component in the Y direction (Figure 5.4.2, d), and then the projections of the grating vector in the X and Y directions are:

$$k_x = k;\ k_y = 0.$$

The phase stepping happens in the +X direction with the translation distance of $\frac{1}{8}$ of the grating period each step. This action is exactly the same as those in the 1D SIM and 1D SISIM cases. Secondly, the grating is rotated by turning around the rotation stage, and the grating vector is set to point towards 120° azimuthal angle from the +X direction (Figure 5.4.2, b). Here, *k* has components in the both X and Y directions (Figure 5.4.2, e), and the projections of the grating vector in the X and Y directions are:

$$k_x = k\cos(120°) = -\frac{1}{2}k;\ k_y = k\sin(120°) = \frac{\sqrt{3}}{2}k.$$

At this time, the translation stage is driven towards the –X direction with the translation distance of $\frac{1}{4}$ of the grating period each step. In this way, the correct phase stepping happens along current grating vector orientation. Thirdly, the grating is rotated until its vector points towards 240° azimuthal angle from the +X direction (Figure 5.4.2, c). Now, the projections of the grating vector in the X and Y directions (Figure 5.4.2, f) are:

$$k_x = k\cos(240°) = -\frac{1}{2}k;\ k_y = k\sin(240°) = -\frac{\sqrt{3}}{2}k.$$

Thus the translation stage is driven towards the –X direction with the translation distance of $\frac{1}{4}$ of the grating period each step to implement correct phase stepping along current grating vector orientation. Following these steps, the 2D phase stepping is implemented.

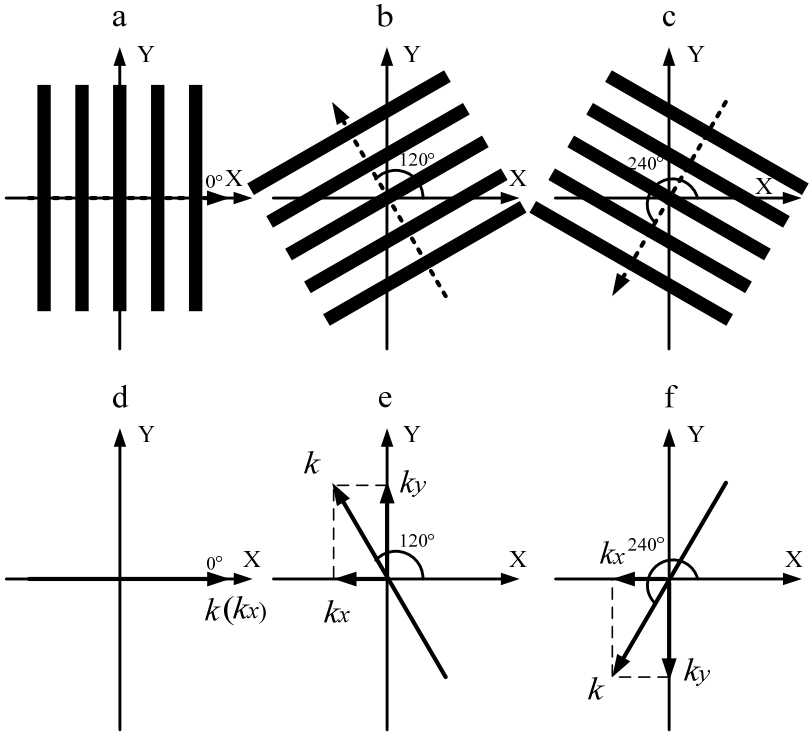


**Figure 5.4.2 Schematic depiction of 2D phase stepping**
(a) grating vector azimuthal angle: 0°, translation step: 1/8 of grating period, +X direction; (b) grating vector azimuthal angle: 120°, translation step: 1/4 of grating period, -X direction; (c) grating vector azimuthal angle: 240°, translation step: 1/4 of grating period, -X direction. (d-f) the projections of the grating vector at 0°,120° and 240° respectively.

## 5.4.2 Apparatus

By modifying the stages where the grating is mounted, the original 1D SISIM setup was transformed to a 2D SISIM setup, as shown in Figure 5.4.3. The Ø1" rotation stage (Thorlabs, T1 in the figure) utilises two precision bearings for smooth, backlash-free rotation. It features a knurled edge for adjusting rotation and a 360° laser-engraved scale marked at 2° increments allowed for precise, repeatable positioning and fine angular adjustment. A top-located setscrew can be tightened to lock the rotation of the stage.

The descriptions on other key apparatus can be found in Subsection 3.3.2 in Chapter 3 and Subsection 4.4.3 in Chapter 4.

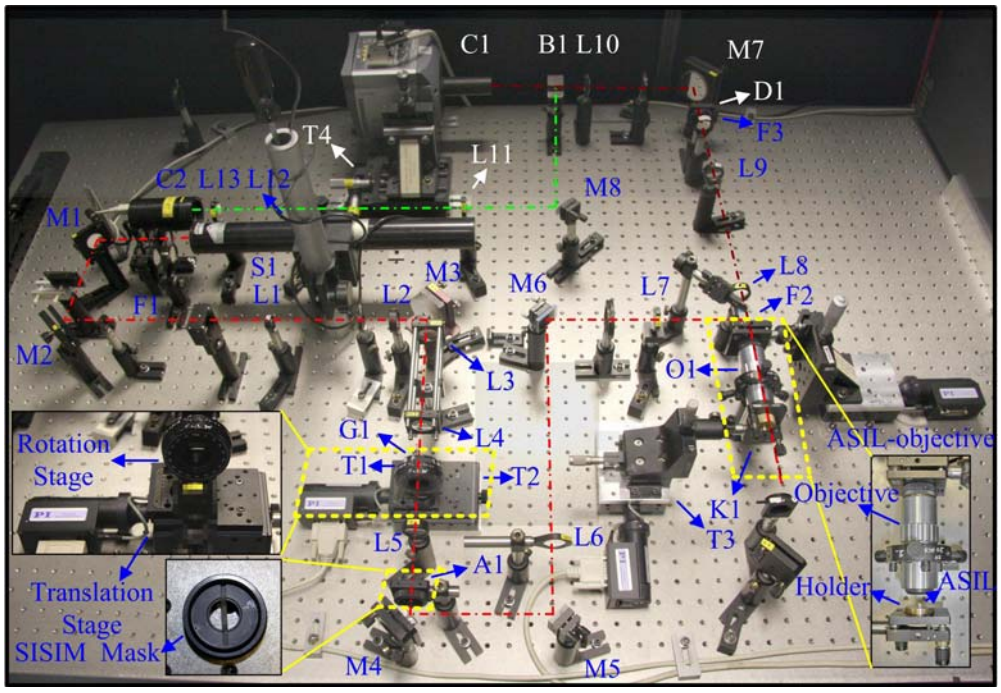


**Figure 5.4.3 Photograph of the 2D SISIM system**
Sharp red dash-dot line: illumination path; dark red dash-dot line: object imaging path; green dash-dot line: BFP imaging path. The assembly of translation stage and rotation stage, SISIM mask and ASIL-objective are shown in the enlarged insets. The rotatable SISIM mask allows +1 and -1 order diffraction beams to pass through and form structured illumination pattern. The grating is mounted on the assembly of a translation stage and a rotation stage to fulfil 2D phase stepping.

## 5.4.3 System calibration

As we implemented the calibrations in 1D SISIM experiments, here we calibrated the periods of structured illumination patterns by examining their images. The images of structured illumination patterns could be directly captured by removing the emission filter from the imaging path. Furthermore, the orientations of the structured illumination patterns were also calibrated from their images. The images of the structured illumination patterns at 0°, 120° and 240° azimuthal angle are shown in Figure 5.4.4 (a),

(b) and (c). According to their Fourier transforms, the period of the patterns was measured as 191.2 nm in all three orientations. Comparing to the designed value of 190 nm, the practical period was very close to the designed value. About the orientations, the errors were less than 0.5° according to 10 measurements at each azimuthal angle. Another parameter we should calibrate was the phase difference errors in phase stepping. For the phase stepping at 0° azimuthal angle, the errors were similar to that in 1D SISIM case, which was about 3.6%. Whereas, for the phase stepping at another two azimuthal angles, the errors were halved because the translation distance of the grating was doubled at each phase step.

From another perspective, the structured illumination pattern can be examined from the BFP images. As shown in Figure 5.4.1, the ± 1 order diffraction beams from the diffraction grating focus at the BFP of the ASIL-objective. The positions of these two focusing spots are determined by the period of the diffraction grating. The finer the diffraction grating, the closer the two focusing spots to the edge of the BFP. To achieve the full capacity of resolution enhancement in SISIM, it is required that the two focusing spots are positioned at the edge of the BFP. The advantage of examining structured illumination from the BFP images is that it provides a way to directly observe the relationship between structured illumination and the bandwidth of original fluorescence microscope. The potential resolution enhancement can be estimated by measuring the positions of the two focusing spots at the BFP. In our 2D SISIM setup, the BFP images can be captured by the CCD camera (C2 in Figure 5.4.3) in the BFP imaging path. The BFP images with structured illumination pattern at 0°, 120° and 240°

azimuthal angle are shown in Figure 5.4.4 (d), (e) and (f). The two focusing spots are indicated by the arrows in each image. From these images, we identify the two focusing spots are situated at 0.85 times the radius of the BFP image, in other words, the spatial frequency of the structured illumination pattern was 85% of the bandwidth of the SIF, therefore, we conclude the bandwidth could be improved by a factor of 1.85 in the 2D SISIM system. In addition, the orientations of the structured illumination patterns were also examined by measuring the orientations of the straight lines formed by the two focusing spots. It was shown the errors of the orientations were less than 0.5°.

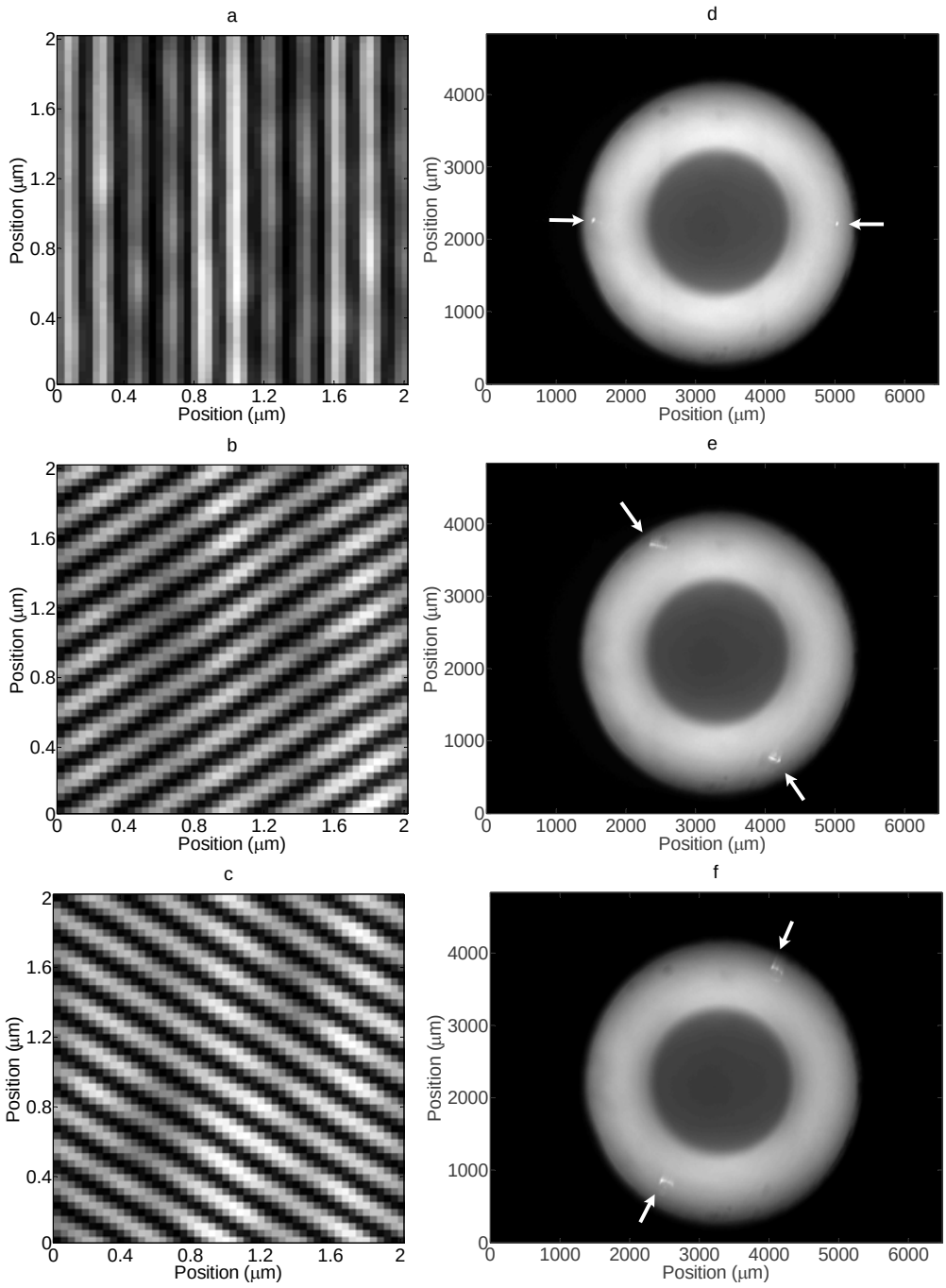


**Figure 5.4.4 Images of the structured illumination patterns and corresponding BFP images in 2D SISIM**

Images of structured illumination pattern orientated at azimuthal angle of (a) 0°, (b) 120° and (c) 240° and their BFP images (d-f). In BFP images, the two spots as indicated by the arrows in each image are the focusing spots of the two laser beams that construct structured illumination.

### 5.4.4 Resolution evaluation experiments and results

Similar to the method and experiments implemented to evaluate the resolution of the SIF system in Chapter 3, we employed some 20 nm fluorescent beads (excitation/emission: 625/645 nm) as samples, and then evaluated the resolution of the 2D SISIM system by calculating 2D correlation coefficients between the simulated images and the experimental image of a separate fluorescent bead. The sample preparation protocol was the same as described in Subsection 3.4.2. The raw image was composed of the average of 16 frames with 0.5 seconds exposure time each. Phase stepping was executed at three azimuthal angles: 0°, 120° and 240°. At each angle, 4 raw images were collected under the structured illumination with $\pi/2$ phase difference in sequence. After the phase stepping at each angle, the grating was translated back to its original position and then rotated to the next angle. Altogether 12 raw images were captured to reconstruct a high-resolution 2D SISIM image.

The image of an isolated 20 nm fluorescent bead from 2D SISIM is shown in Figure 5.4.5. For comparison, the simulated image of a 20 nm fluorescent bead from a NA of 3 microscope system is shown in Figure 5.4.6. By calculating 2D correlation coefficients between the experimental image and a series of simulated images of a 20 nm bead, and locating the simulated image with the highest correlation coefficient with the experimental image, the practical NA of our 2D SISIM was established. The simulation was executed with NA of from 2 to 4 at 0.1 intervals. The coefficient data and cubic curve fitting are shown in Figure 5.4.7. According to these data, we can conclude the practical NA of the 2D SISIM was $3.02 \pm 0.01$.

When evaluating the NA of the 2D SISIM system, in order to reduce the effect of random noise in each correlation coefficient, each data point of the coefficient was composed of the average of 5 original data from 5 individual 20 nm fluorescent bead images. These bead images were chosen randomly from different areas in a 2D SISIM image. Moreover, random noise were generated in each data point based on a normal distribution, in which the initial correlation coefficient data worked as the mean value of the normal distribution, and the norm of residuals from cubic curve fitting worked as the standard deviation of the normal distribution. With these noisy data, cubic curve fitting was performed and repeated for 100 times, at last the average peak value of the fitting curves was calculated. This value was employed as the practical NA of the 2D SISIM system.

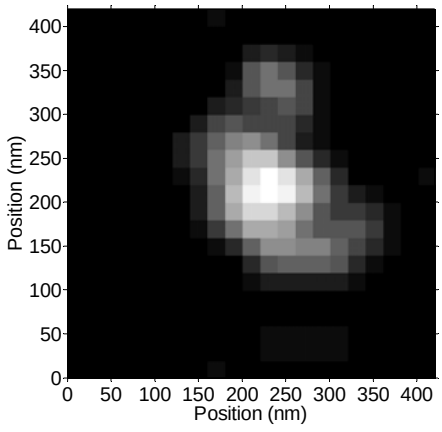


**Figure 5.4.5 20 nm fluorescent bead image obtained with 2D SISIM**

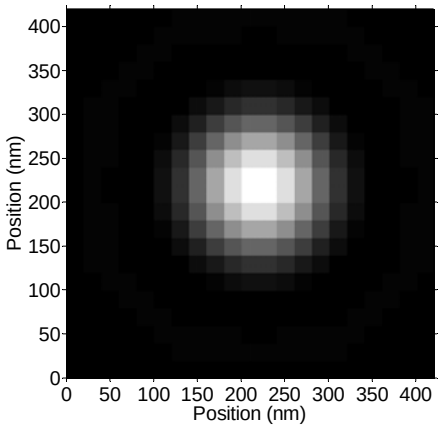


**Figure 5.4.6 Simulated 20 nm fluorescent bead image with NA of 3**

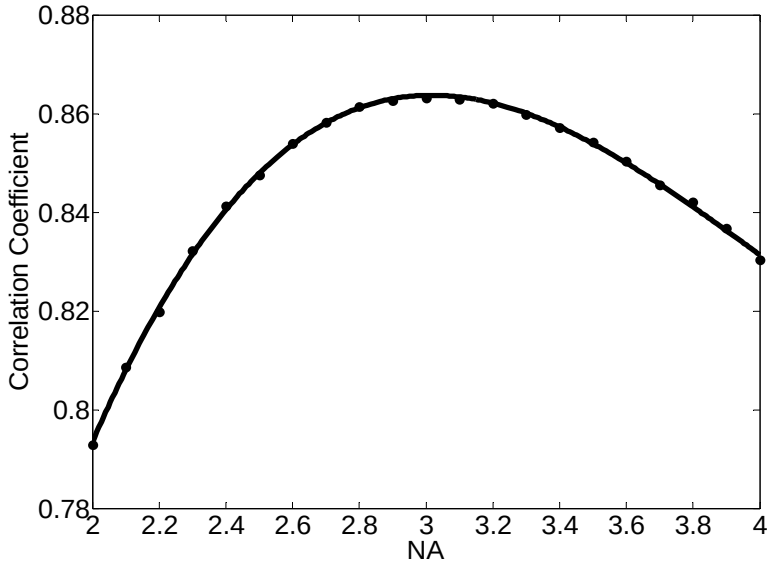


**Figure 5.4.7 Resolution evaluation data/curve of the 2D SISIM based on correlation coefficient method**
2D correlation coefficient data and cubic fitting curve between the experimental 2D SISIM image and a series of simulated images of a 20 nm bead under different NA, the peak value is found at (3.02, 0.8639).

Meanwhile, to readily demonstrate the resolution enhancement in 2D SISIM, the SIF image and the SISIM image of a field of 20 nm fluorescent beads are displayed together in Figure 5.4.8 to compare. Apparently, in the SIF image (Figure 5.4.8, a), it is difficult to distinguish two adjacent beads in the middle of the image from each other, while in the SISIM image (Figure 5.4.8, b), they are clearly resolved. This difference is also obviously seen in their 3D surface plots (Figure 5.4.8, c and d). Accordingly, the resolution enhancement in the 2D SISIM system is evident.

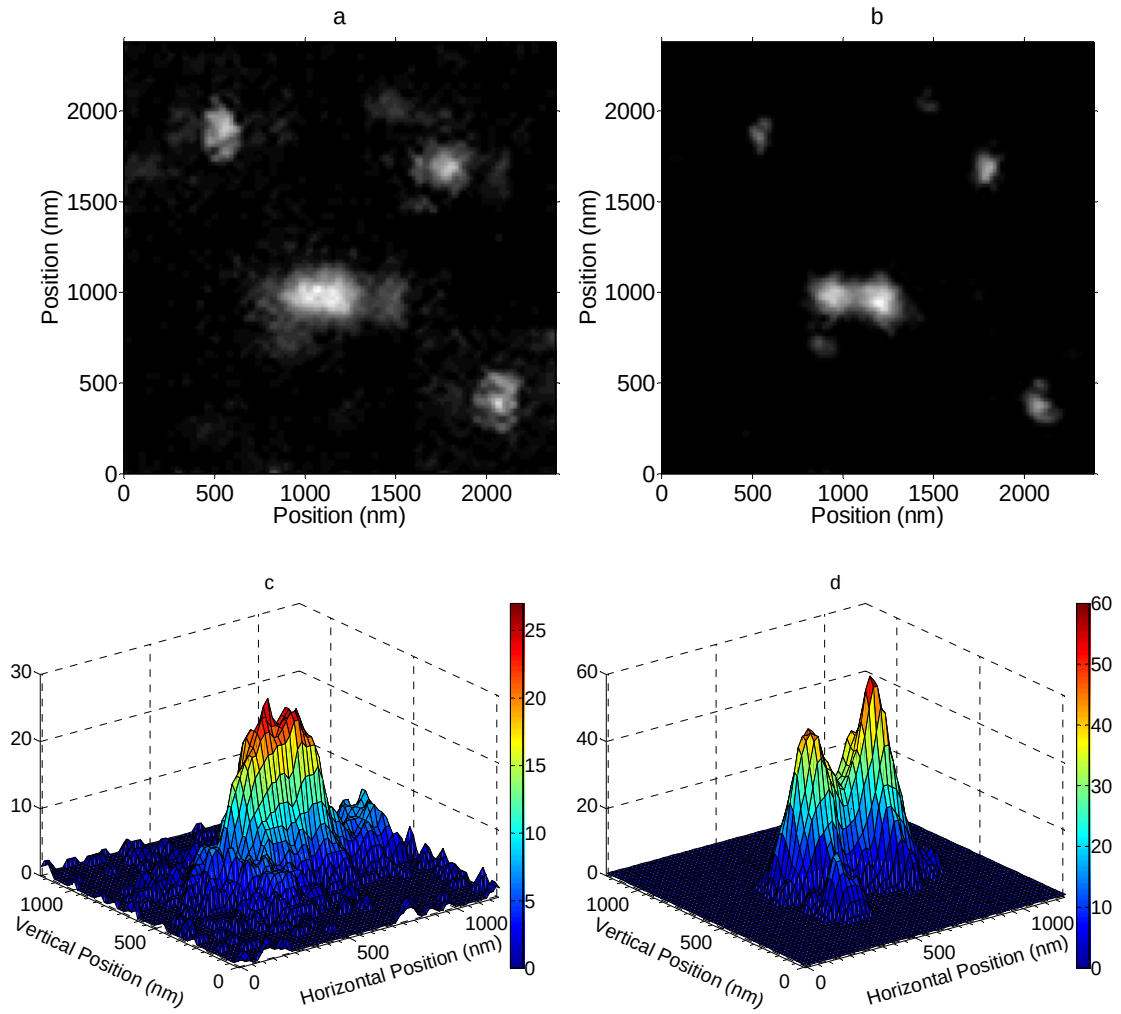


**Figure 5.4.8 Comparison of the images of a field of 20nm fluorescent beads obtained with SIF (a) and 2D SISIM (b)**
Two adjacent 20 nm fluorescent beads cannot be resolved in the SIF image (a), but can be resolved in the 2D SISIM image (b); this difference is obviously realised in the 3D surface plots of the two adjacent bead images obtained with SIF (c) and 2D SISIM (d).

In Chapter 3, we have verified the effective NA of the SIF system is 1.85. Now we demonstrate the NA of the 2D SISIM system is about 3. According to these values, we can draw a conclusion that the lateral resolution has been improved by a factor of 1.6 through transforming a SIF system to a SISIM system. Furthermore, considering the NA of the conventional objective lens we used is 0.55, we could also state that the lateral resolution has been improved 5.5 times in the SISIM system.

## 5.5 Discussion

In our SISIM system, two tilted incident beams strike the object plane symmetrically to the optical axis to produce the interference pattern as structured illumination pattern. Due to the large NA of the ASIL-objective, the incident angles of these beams are much larger than the critical angle between the two media − glass and air. Therefore, total internal reflection (TIR) illumination happens intrinsically.

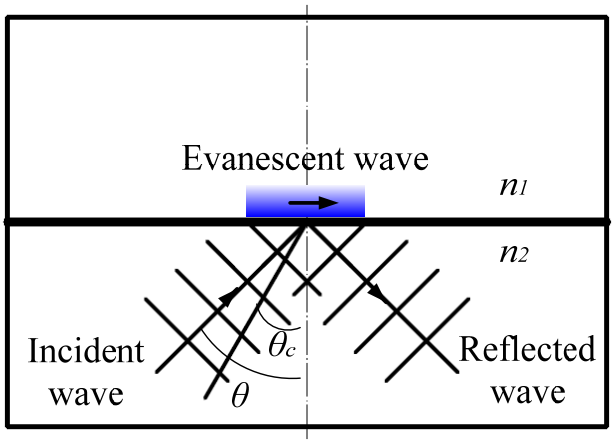


**Figure 5.5.1 TIR illumination scheme**
Refractive index $n_2$ must be greater than $n_1$. The incident angle $\theta$ must be larger than or equivalent to the critical angle $\theta c$ for TIR to occur. The exponentially-decaying evanescent field in the $n_1$ material is used to excite fluorophores.

The critical angle at the interface between two media with refractive indices $n_1$ and $n_2$ ($n_1 < n_2$) (Figure 5.5.1) is calculated by this equation [16]:

$$\theta_c = \arcsin(\frac{n_1}{n_2}) \qquad (5.5.1)$$

The evanescent wave is generated when the TIR illumination happens. The evanescent wave penetrates into the lower refractive index medium, and it decays exponentially

from the interface. The following equation [149] depicts the energy of evanescent wave as a function of distance from the interface:

$$E(z) = E(0)\exp(-\frac{z}{d}) \tag{5.5.2}$$

where $E(z)$ is the energy at a perpendicular distance $z$ from the interface, $E(0)$ is the energy at the interface. The intensity penetration depth $d$ is dependent on the wavelength of the incident illumination $\lambda$, the angle of incidence $\theta$, and the refractive indices of the media at the interface as expressed by the following equation [149]:

$$d = \frac{\lambda}{4\pi\sqrt{n_2^2 \sin^2\theta - n_1^2}} \tag{5.5.3}$$

The incident angle of the TIR illumination in our SISIM system is determined by the grating period. According to the grating equation (Equation 4.4.1) and our setup, the relationship between grating spatial frequency and incident angle of TIR illumination beam is depicted in Figure 5.5.2. It is shown only if the grating frequency is higher than 31.15 line pairs/mm (period 32.1 μm), TIR illumination can happen in our case. We practically applied a grating with 20 μm period (spatial frequency 50 line pairs/mm). This grating produced an incident angle of 50° that was significantly larger than the critical angle of 30°. According to Equation 5.5.3, the intensity penetration depth in this situation was about 43 nm that constrained the illumination depth in a very shallow region.

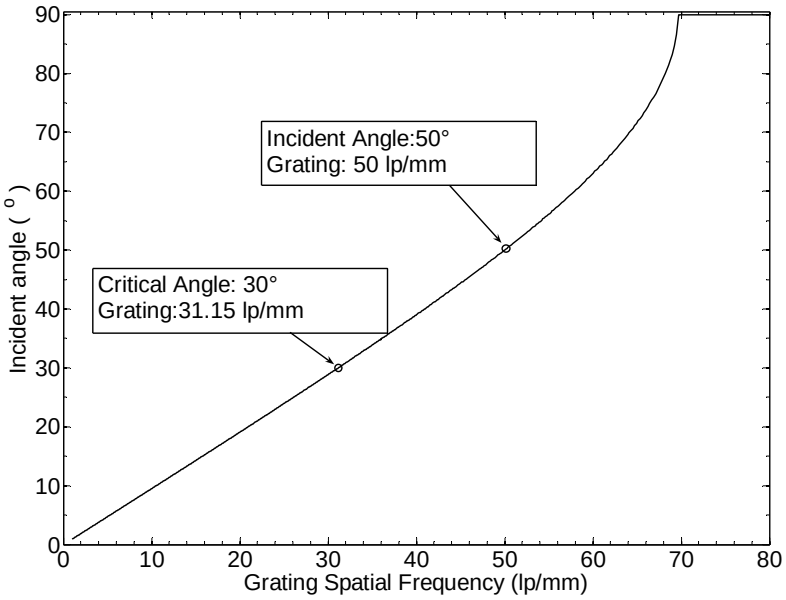


**Figure 5.5.2 Curve between diffraction grating spatial frequency and the incident angle of illumination beam in our SISIM setup**
The critical angle is 30°; the incident angle in our case is 50°, so TIR illumination happens. lp/mm: line pairs/mm

TIR illumination selectively illuminates and excites fluorophores in a near-field region of a sample due to the shallow penetration depth of evanescent wave. Elimination of background fluorescence from outside the focal plane can dramatically improve the image contrast. The highly depth-selective imaging property from the TIR illumination in the SISIM is significantly beneficial to cell biology. Due to the availability of novel membrane-specific fluorophores, imaging with TIR illumination is capable of visualising the delicate structures with fluorescent labels in and around cell membrane with high contrast. In the conventional fluorescence microscopes, these structures are usually submerged in massive fluorescent emission from background objects in out-of-focus planes.

In our experiments, we were unable to get high-resolution images of cells with the SISIM system, mainly because of the difficulty of cell sample positioning and the appearance of severe photobleaching during raw image acquisition. Although SISIM is a wide-field imaging system, the feasible high-resolution FOV is still limited to the central area, with the radius of about 25μm from the geometrical centre in our case, of the flat surface of an ASIL. In our current SISIM setup, it is a big challenge to position the cell samples inside this limited FOV. To address this problem, we propose several ideas in Subsection 6.2.2. Another problem is that the fluorescent cell samples usually bleach to emit the fluorescent signals much lower than the noise level in about two minutes during raw image acquisition. During this time, we can only capture less than six raw images which are apparently not enough to reconstruct high-resolution 2D SISIM images. To solve this problem, we need a refined immunofluorescence labelling protocol or to seek more fluorescently stable labelling materials, for example, quantum dots. Physically, we could use flashed illumination to decrease the overall exposure time for the samples, moreover, in Subsection 6.2.2, we also discuss the application of spatial light modulator to generate structured illumination pattern in order to improve the speed of raw image acquisition.

## 5.6 Conclusions

In this chapter, we developed a new hybrid microscopic technique – structured illumination solid immersion fluorescence microscopy (SISIM). SISIM is formed on the basis of two independent wide-field high-resolution microscopic techniques – solid

immersion fluorescence microscopy (SIF) employing an aplanatic solid immersion lens (ASIL) and structured illumination microscopy (SIM), both of which have been studied in the previous chapters. The SIF system, containing a NA 0.55 conventional objective lens and a 5 mm diameter ASIL made of optical glass S-LAH79 ($n_d$ = 2.0033), contributed an effective NA of 1.85. By modifying the illumination path of the SIF system, we constructed the structured illumination based on two-beam interference. With the help of the structured illumination and corresponding four-phase-step image reconstruction algorithm, we were able to expand the bandwidth of the SIF to obtain a higher lateral resolution. In this way, we set up a high-resolution SISIM system capable of working in 1D and 2D. By examining the response of the SISIM system to separate 20 nm fluorescent beads, we demonstrated the practical NA of this system was about 3. With this NA, the lateral resolution of our SISIM system was around 136 nm at 670 nm wavelength according to Rayleigh criteria. If the wavelength used for imaging was shorter than 500 nm, we could obtain the lateral resolution finer than 100 nm. The SISIM not only performs high-resolution imaging, but also provides high-contrast imaging due to its intrinsic supercritical angle TIR illumination characteristic, therefore it has broad application prospects in the research on intracellular and intercellular structures and processes in cell biology.

# Chapter 6 Conclusions and Future Work

## 6.1 Conclusions

### 6.1.1 Research overview

Seeing is believing. We are currently in the midst of an exciting revolution in optical microscopy because of a surge of innovation in microscopic techniques in the last decade or so. Solid immersion microscopy employing an aplanatic solid immersion lens is a wide-field high-resolution technique that has been investigated in our group, the wide spatial frequency bandwidth provided in this technique is beneficial when a large NA is needed; structured illumination microscopy, one of the newly emerging super-resolution microscopic techniques, requires a large NA in order to make the most of its resolution enhancement capability. We were interested in the potential high lateral resolution achievable through their combination, and therefore put this idea into practice.

The aim of this research is to develop a hybrid wide-field fluorescence microscopic technique with high lateral resolution based on the combination of solid immersion

fluorescence microscopy (SIF) employing an aplanatic solid immersion lens (ASIL) and structured illumination microscopy (SIM).

To develop this hybrid fluorescence microscopy, we completed the following steps: first, we investigated the application of an ASIL in wide-field fluorescence microscopy; second, we investigated the implementation of SIM; and at last, we developed a wide-field high-resolution microscopic system, which is called structured illumination solid immersion fluorescence microscopy (SISIM), by combining SIM with SIF.

### 6.1.2 Research contributions

In our research, we have effectively investigated three types of fluorescence microscopy: SIF, SIM and SISIM, so we summarise our research contributions in these three categories.

(1) SIF.

In the investigation on SIF, we applied an ASIL (radius $r$ = 2.5 mm) made of optical glass S-LAH79 ($n_d$ = 2.0033) with a NA 0.55 long working distance objective lens to demonstrate a wide-field high-resolution SIF system with effective NA of 1.85. The NA obtained in the SIF is superior to any kind of commercially available objective lenses so far. Different samples, including 20 nm fluorescent beads, dye grid with very fine structures and fluorescence labelled Jurkat cells, were imaged in the SIF system with high-resolution performance.

The severe dispersion of the high-index material of the ASIL makes the SIF suffer serious chromatic aberration (CA) that degrades the high-resolution performance of the SIF. We proposed several methods to eliminate or balance CA in the SIF in Subsection 3.5.3, and practically applied a super-narrow passband filter (FWHM = 3 nm) as the emission filter to overcome the drawback of CA successfully. The size of the ASIL determines the fluorescence spectral width suitable for imaging and the valid FOV associated with the aberrations when maintaining high-resolution performance. We theoretically analysed their relationships by means of hybrid simulations in both ray optics (in ZEMAX) and wave optics (in MATLAB). It is shown the feasible fluorescence spectral width decreases with increasing ASIL size; on the contrary, the feasible FOV increases with increasing ASIL size. From the application point of view, it is necessary to find a trade-off between fluorescence spectral width and effective FOV. The numerical results presented in Subsection 3.5.3 and 3.5.4 can be regarded as convenient references when applying an ASIL in fluorescence microscopes.

According to the analysis based on both ray tracing and dipole emitter simulation, we concluded SIF can deliver the best resolution performance only if working in near-field imaging mode. When there is a gap between the sample and the ASIL, the practical resolution of SIF will be degraded and dependent on the refractive index of the medium in the gap. This conclusion was experimentally demonstrated in our SIF system in Subsection 3.6.3.

In our SIF system, it was impossible to apply any type of traditional targets to calibrate system magnification due to the very limited sample accommodation space constrained by the ASIL holder. To solve this problem, we applied soft lithography to copy standard target structure on polydimethylsiloxane (PDMS) stamps, and then cast the structure to dye samples through micro contact printing (μCP) to calibrate system magnification. It was verified this method was reliable and accurate in our experiments.

The most important optical parameters, such as focal length and magnification, of ASILs and the combination of an ASIL and a conventional objective lens, i.e. ASIL-objective, were derived based on geometrical optics as described in Appendix III.

In the SIF system, the correct relative distance and position between the conventional objective lens and the ASIL relies on applicable alignment method and delicate alignment practice, which is described in Appendix IV.

(2) SIM.

In the investigation on SIM, we used a diffraction grating to generate two-beam interference pattern as structured illumination pattern to construct a SIM system in the epi-fluorescence configuration. With our bench-top one-dimensional SIM, we demonstrated effective NA of 2.24 by using an oil immersion objective lens with practical NA of 1.14 (nominal NA 1.25), which confirmed the doubled lateral resolution capability of SIM.

In our SIM experiments, to recover high spatial frequency information mixed in the conventional images, a four-phase-step raw image acquisition procedure was applied, in which the sinusoidal distribution structured illumination pattern was translated by four phase steps with $\pi/2$ phase difference and one raw image was captured at each value of the illumination phase. This four-phase-step method was shown to be robust in the presence of phase-stepping errors.

The spatial domain algorithm used to reconstruct high-resolution SIM image in our case is simple and efficient due to the absence of Fourier transform process. Practically on average we found it saved about 1/3 of the processing time in our case.

Artefacts could appear in SIM images when there are displacements among raw images. By moving back the displaced raw images to their initial positions determined by the calculated cross-correlation coefficients between the images, an artefact-free SIM image can be reconstructed from the processed raw images. We demonstrated the method in a practical case described in Subsection 4.6.2.

(3) SISIM.

In the research on SISIM, we developed a new hybrid wide-field high-resolution microscopic technique – structured illumination solid immersion fluorescence microscopy (SISIM). The SISIM was formed by combining two independent high-

resolution microscopic techniques – solid immersion fluorescence microscopy (SIF) employing an aplanatic solid immersion lens (ASIL) and structured illumination microscopy (SIM). Our SIF system, containing a NA 0.55 conventional objective lens and a 5 mm diameter ASIL made of optical glass S-LAH79 ($n_d$ = 2.0033), provided an effective NA of 1.85. By modifying the illumination path of the SIF system with a diffraction grating, a structured illumination based on two-beam interference was constructed. The four-phase-step raw image acquisition procedure and corresponding image reconstruction algorithm were applied to restore high-resolution images by expanding the bandwidth of the SIF system with the help of the structured illumination. The diffraction grating could be rotated and translated to implement phase stepping at different azimuthal angles. In this way, the SISIM system was capable of working in one dimension and two dimensions. The practical NA of our SISIM system was shown to be about 3, which corresponds to the lateral resolution of around 136 nm at the imaging wavelength of 670 nm according to Rayleigh criteria.

The aim of this research, which was to develop hybrid wide-field fluorescence microscopy with high lateral resolution based on the combination of SIF employing an ASIL and SIM, is successfully completed.

## 6.2 Future work

### 6.2.1 Further resolution enhancement

There are several promising ways to improve the SISIM in the future in terms of further resolution enhancement.

(1) Using optical glass with higher refractive index to fabricate ASILs.

The refractive index of the ASIL material effectively determines the numerical aperture (NA) of the SIF system, which accordingly governs the resolution of the SISIM system. The higher the refractive index of the ASIL material, the higher the potentially achievable resolution of the SISIM system. Although the optical glass S-LAH79 we used has the highest index of $n_d$ = 2.0033 among the readily available optical glasses, there are some other optical glasses with higher indices in market, for example, K-PSFn214 from Sumita Inc. has an extraordinary $n_d$ = 2.14352. Thus it is possible to use higher refractive index optical glass like K-PSFn214 to fabricate the ASIL to seek higher resolution in SISIM.

(2) Using finer structured illumination pattern.

For a SIM system, the best resolution performance, i.e. doubled resolution, occurs when the spatial frequency of the structured illumination pattern approaches the bandwidth of the conventional microscope. In our SISIM practice, the spatial frequency of the structured illumination pattern was 85% of the spatial frequency bandwidth of the SIF

system, which means the bandwidth of the SIF system could be expanded by a factor of 1.85 at most. If we use a finer diffraction grating to produce finer structured illumination pattern approaching the bandwidth of the SIF system, a SISIM system with doubled bandwidth in contrast to the SIF system should be achievable.

(3) Using shorter wavelengths for imaging.

The bandwidth of a microscope is inversely proportional to the imaging wavelength, which means a shorter wavelength can produce a wider bandwidth. In our case, the central imaging wavelength was 670 nm that is very long in the visible spectrum. Considering the practical NA of about 3 in our SISIM system, we could obtain the lateral resolution of about 100 nm if the imaging wavelength was 500 nm, nearly 30% higher than the resolution obtained in our case. In practice, there are many choices of fluorescent dyes or proteins working in short wavelengths, for example, Alexa Fluor 488 from Invitrogen Corp. has the peak excitation and emission wavelength of 499 nm and 519 nm respectively, which is an ideal fluorescent dye to obtain 100 nm or even better lateral resolution in SISIM if a 473 nm or 488 nm diode pumped solid state laser is used for illumination.

(4) Using micro-structured ASIL.

In Section 2.6, we reviewed the application of near-field gratings for high-resolution imaging. Our SISIM system intrinsically works in near-field mode because of the total internal reflection (TIR) illumination scheme, thus it has great potential to use a micro-structured ASIL (Figure 6.2.1), as the combination of an ASIL and a near-field grating,

in SISIM in order to pursue a lateral resolution far beyond the classical resolution limit. The micro-structured ASILs contain laterally patterned microstructures on the flat surface. The microstructures could be fabricated through physical vapour deposition (PVD) coating or chemical vapour deposition (CVD) coating, focused ion beam (FIB) [150], optical lithography [151], electron-beam lithography [59], soft lithography [136] or other micro-fabrication techniques. The micro-structured ASIL could also be used together with a conventional far-field diffraction grating to conduct the lateral resolution higher than that obtained using either of them only.

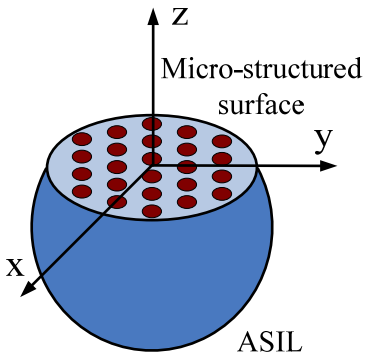


**Figure 6.2.1 Schematic of the micro-structured ASIL**
Laterally patterned microstructures are on the flat surface.

## 6.2.2 Instrumental improvements for routine use

For routine use, it is necessary to make SISIM more compact to improve experimental stability and repeatability, and more user-friendly. Here we propose some methods to make SISIM meet these requirements for future general use.

(1) Modification of the ASIL configuration.

From a biologist's point of view, it is inconvenient to make biological samples on the ball-shaped ASILs in contrast with conventional coverglasses or coverslides, especially in the procedure of tissue culture. However, this can be improved by modifying the ASIL configurations. In Figure 6.2.2, two modified ASIL configurations are displayed. The left one is a two-piece configuration [132] and the right one is a coverslide-like configuration. The two-piece configuration ASILs are composed of a flat thin plate (top) and a half ball (bottom). The flat plate is used as a common coverglass for the sample preparation. Similarly, the coverslide-like configuration ASILs are similar to regular coverslides thus allowing the sample preparation in the normal way. The total thicknesses of both of these two configurations satisfy the aplanatic condition. To adapt different fluorescent labelling, a series of flat plates, for the two-piece ASILs, or coverslide-like ASILs with different thicknesses regarding fluorescent wavelengths could be fabricated. When the imaging wavelength is determined, according to the fluorescent labels, researchers can simply choose the appropriate flat plates or coverslide-like ASILs to prepare biological samples.

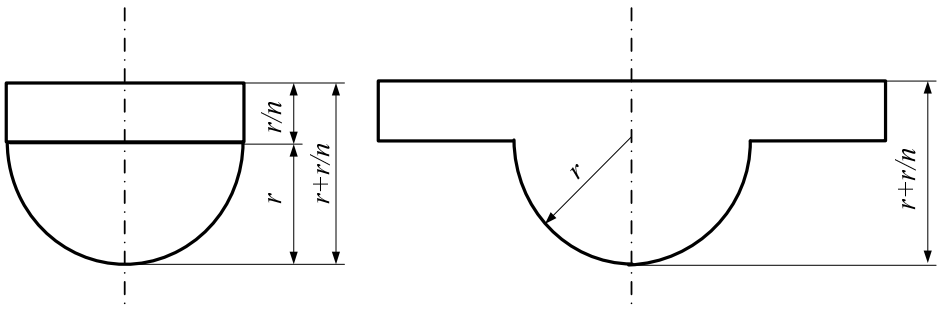


**Figure 6.2.2 Two modified ASIL configurations**
Two-piece configuration (left) and coverslide-like configuration (right)

(2) Integration of ASIL-objective.

In SISIM, the correct relative distance and position between the ASIL and the conventional objective lens is a crucial factor for high-resolution imaging. In practice, we employed a special procedure to align these two components as described in Appendix IV. Before taking images, we need to realign the ASIL because it has been taken out of the system for sample preparation. The realignment is quite subtle and time-consuming, which is not suitable for the routine use of SISIM. To solve this problem, it is possible to integrate the ASIL and the conventional objective lens (Figure 6.2.3). Here, the ASIL is effectively composed of an HSIL and a custom-designed coverglass with the sum of the thickness equivalent to the thickness of the ASIL, which is actually a two-piece configuration ASIL as described previously. The conventional objective lens and the HSIL are mechanically integrated to form a single unit. The relative distance between them is precisely set by the mechanical connection. Samples are mounted on the custom-designed cove glass that is easy to use. There is no need to realign the ASIL with this configuration.

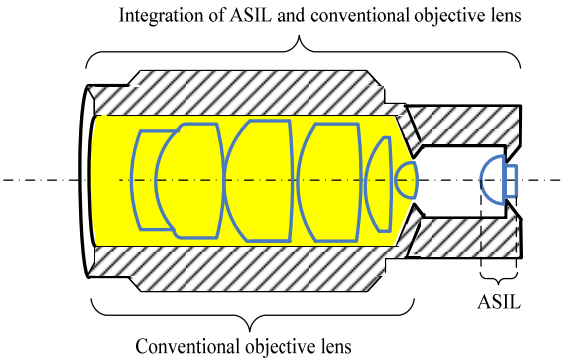


**Figure 6.2.3 Schematic of the integration of ASIL and conventional objective lens**
The ASIL is composed of an HSIL and a coverglass with certain thickness; the distance between the conventional objective lens and the HSIL is precisely set by the mechanical connection. There is no need to realign the ASIL with this configuration.

However, no matter what modified configuration ASILs we use, the feasible high-resolution FOV of an ASIL is limited to the central area of the flat surface, so it is very important to make the samples present in this area in order to obtain the high-resolution images of them. Next, we will discuss the possible ways to fulfil sample positioning.

(3) Combination of SISIM and laser tweezers for sample positioning.

In the application of SISIM, the feasible high-resolution imaging region is limited to the central area, with the radius of dozens of micrometers (depending on the ASIL size and fluorescence spectral width) from the geometrical centre, of the flat surface of an ASIL. Moreover, the location of the valid FOV is pre-determined in SISIM, in other words, there is no chance of adjusting the sample position during the imaging procedure. For genuine biological samples, for example cells, their high-resolution imaging by SISIM is directly dependent on the correct sample positions which should be located inside the limited central area of the ASIL flat surface.

When implementing sample positioning, a non-invasive approach is preferred because we always wish to observe the intrinsic nature of samples. One existing optical technique to fulfil non-invasive sample trap and manipulation are laser tweezers. Laser tweezers, also known as optical traps, are based on pico-newton force generation during the interaction of highly focused laser beams with dielectric particles, including cells and organelles [152]. The beam waist of a focused laser beam contains a very strong electric field gradient. Dielectric particles are attracted along the gradient to the region of strongest electric field at the beam waist. The laser beam also tends to apply a force

on particles in the beam along the beam propagation direction. An extensive review on laser tweezers theory and apparatus can be found in Neuman and Block's paper [153]. We propose to combine SISIM with laser tweezers in order to place the samples in the correct position before implementing imaging in SISIM. A hybrid system is schematically drawn in Figure 6.2.4. In this figure, the system is composed of a SISIM system with an independent laser tweezers system (above the ASIL). The laser for optical trap should have a longer wavelength than the one for excitation, ideally the same as the central wavelength of fluorescent emission or emission filter. In this way, the position of the focused laser beam can be directly monitored by the CCD camera. It is better to construct a sample chamber between the two objective lenses, and then the cell samples can be positioned by the optical trap during the cell culture or cell labelling procedure. The combination of ASIL and laser tweezers has been developed by Birkbeck *et al.*, which was applied in a scanning solid immersion microscope specially tailored for use in microfluidic systems [118]. Significantly different from that, the system we proposed here is a wide-field non-scanning microscope.

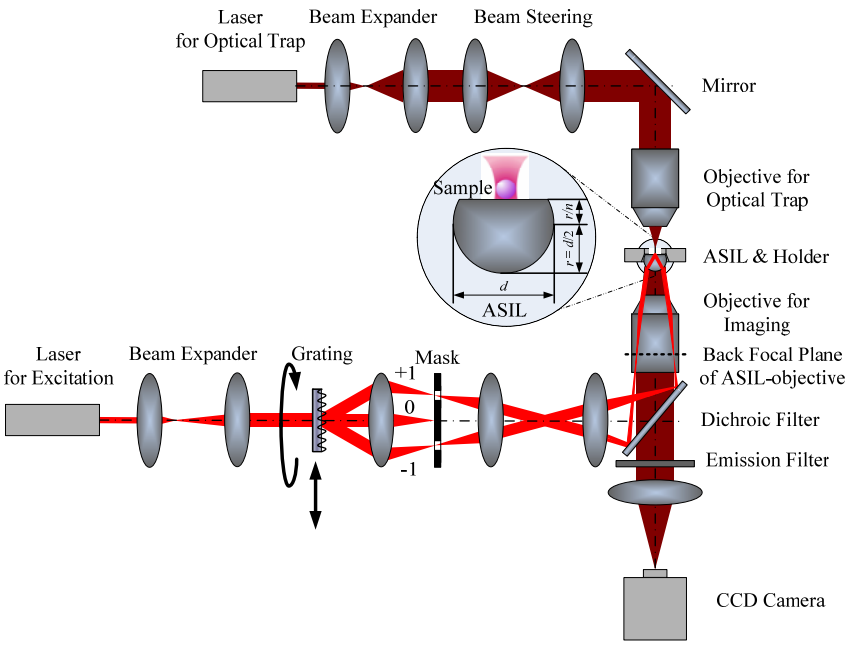


**Figure 6.2.4 Schematic of the combination of SISIM and laser tweezers**
Besides original SISIM system, another laser source is used to provide the necessary laser beam for optical trap, beam steering optics are used to steer the beam location, and another objective lens is used to create the optical trap in the object plane which is at the flat surface of the ASIL.

(4) Applying surface chemistry for sample positioning.

Another gateway to sample positioning, especially cell positioning, is surface chemistry. If we improve the cell adhesion inside the effective FOV region chemically by processing the flat surface of an ASIL locally, the cells can be positioned deliberately in a non-invasive way. A number of studies have demonstrated how the adhesion of cells may be determined. Common peptides, in particular Arg-Gly-Asp (RGD)-sequence [154], and proteins like fibronectin [155], albumin [156], or extra cellular matrix proteins [157] have been used as coating to improve the cell adhesion. The comprehensive technical details of biochemical surface modification are beyond the scope of this thesis. This will be a significant challenge for biologists and chemists.

(5) Using micro-structured ASIL for sample positioning.

Another attractive method to fulfil sample positioning is to use micro-structured ASILs. Topography can be used to gain control over cell adhesion [158]. Different micro-structures fabricated on different substrates have been used to demonstrate the confinement of cell positions [159-161]. An example is shown in Figure 6.2.5, in which a scanning electron microscope (SEM) image shows most of the adhered 3T3 fibroblast cells are confined to a square of patterned grid. Actually, the application of micro-structured ASILs is not only beneficial to sample positioning but also capable of implementing near-field structured illumination for further resolution enhancement.

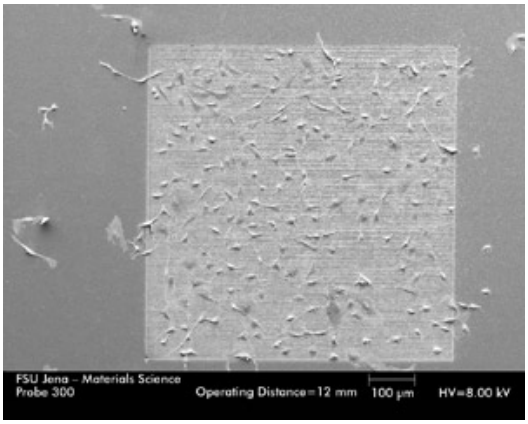


**Figure 6.2.5 Scanning electron microscope image of a patterned Teflon sample with 3T3 Swiss albino mouse fibroblasts on the surface [160]**
Most of the adhered cells are confined to the patterned area containing regular grids. Microstructure area: 1 $mm^2$, grid size: 4×4 µm, interval: 1 µm, depth: 0.5 µm.

(6) Using spatial light modulators (SLMs) to generate structured illumination pattern.

In contrast to a diffraction grating, a spatial light modulator (SLM), serving as an electrically configurable grating, is a better option to produce structured illumination pattern. An SLM is an instrument that imposes some form of spatially-varying

modulation on a beam. An SLM can be used to shift or rotate an illumination pattern precisely via corresponding electronic control system. The use of an SLM can thus overcome the shortcoming of imprecise mechanical motion when using a diffraction grating to generate structured illumination pattern, and therefore improve the precision of phase stepping. Meanwhile, SLMs can present a higher light efficiency. In a practical case, a pure phase modulating device based on liquid crystal on silicon (LCOS) is capable of delivering up to 52% illumination power [60].

The application of SLMs is also beneficial to improve the speed of raw image acquisition in SISIM. The movement of the diffraction grating in our case is dependent on a motorised translation stage for the phase stepping and a rotation stage for the orientation control. The mechanical movements of the rotation stages are rather slow, limiting the image acquisition speed of the SISIM. SLM is a good alternative to the diffraction grating for the purpose of increasing the raw image acquisition speed. In a practical case, a LCOS can shorten the pattern-switching time to less than 100 μs [43].

Another promising SLM device is a digital micro-mirror device (DMD). A typical DMD consists of hundreds of thousands of aluminium micro-mirrors arranged in a rectangular array. The mirrors are highly reflective and can be individually tilted to dozens of degrees in either direction, from which the reflected light is switched on or off to be modulated. To produce greyscale patterns, the mirrors are toggled on and off very quickly, and the ratio of ‘on’ time to ‘off’ time determines the grey scales of the generated patterns. DMDs usually have much higher frame rate than liquid crystal

SLMs, for example, a Discovery 1100 ALP1 DMD can display a sequence of binary XGA patterns at 8000 Hz [162], which is much faster than a ferroelectric liquid crystal SLM as reported hereinbefore. Furthermore, DMDs do not rely on the polarisation of the optical beams, so the apparatus will be potentially simpler compared to a system employing a liquid crystal SLM.

All in all, using an SLM, either an LCOS or a DMD, to generate structured illumination pattern contributes to more accurate phase stepping, higher light efficiency and faster pattern generation in contrast to the diffraction grating method we used.

(7) Using DSILs.

We mentioned diffractive solid immersion lenses (DSILs) in Subsection 3.2.1 and discussed the application of diffractive optical element to correct chromatic aberration (CA) in Subsection 3.5.3. A well designed DSIL can be used to not only increase the NA of a conventional microscope but also correct CA and other aberrations in a rather large FOV. Moreover, DSILs have the advantages of reduced height and weight than ASILs. With the development of aspherical fabrication in optics, DSILs will play more important role in the application of SISIM.

### 6.2.3 Total internal reflection fluorescence microscopy applying an ASIL (ASIL-TIRF) – a spin-off from SISIM

Finally, we discuss how the technology developed here can be applied to other forms of microscopy.

In the SISIM setup, it is possible to convert the structured illumination to a normal TIR illumination through simple modifications. Then, total internal reflection fluorescence microscopy (TIRF) applying an ASIL, i.e. ASIL-TIRF, can be constructed. As a spin-off from the SISIM, the ASIL-TIRF differs from the SISIM in that the former applies a tilted Köhler illumination from one laser beam while the latter applies a structured illumination from two-beam interference.

In biological research, the primary cellular component cytosol has a refractive index of 1.36-1.38 [163], an objective with NA exceeding that value is required in an objective-based TIRF. Objective lenses with higher NA can provide sufficient working margin for fine adjustment of angles exceeding the critical angle, which is beneficial to the observation of samples with complex components and elements. Furthermore, when TIR illumination happens, the penetration depth of evanescent wave into the sample depends on the incident illumination angle. A high selectivity in imaging is obtained only if the illumination angle exceeds the critical angle significantly. Our ASIL-objective could approach NA of nearly 2 that satisfies the requirement of high NA for objective-based TIRF in biological research.

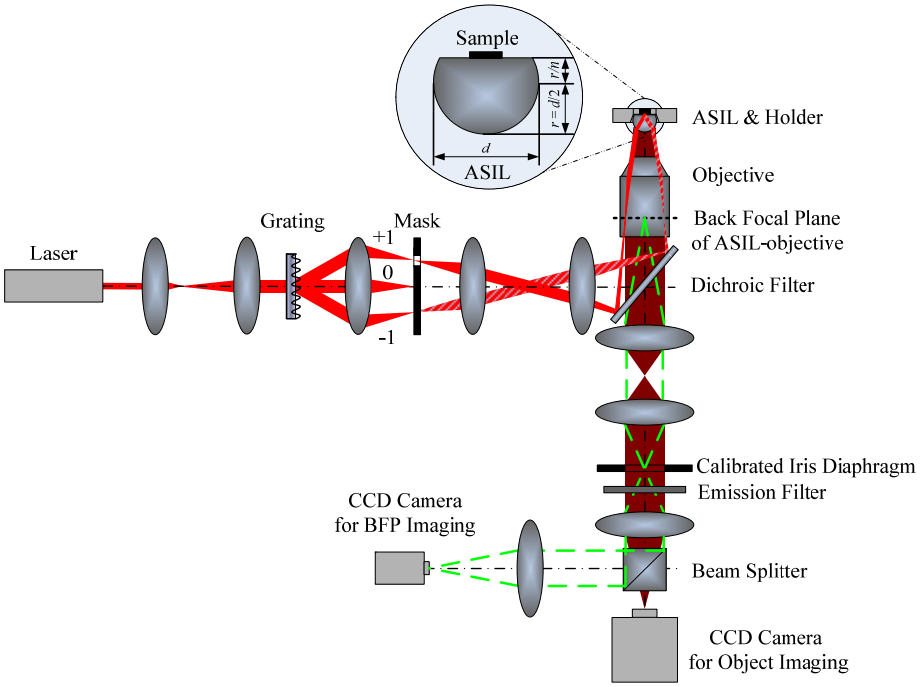


**Figure 6.2.6 Schematic of the ASIL-TIRF system**
The sharp red shading illustrates TIR illumination beam; the patterned sharp red shading illustrates the reflection of illumination beam; the dark red shading illustrates the fluorescent light forming specimen image; and the green dashed lines illustrate the fluorescent light forming BFP image. The ASIL configuration is also shown in the enlarged inset. The mask only allows +1 (or -1) order diffraction beam to pass through.

The schematic diagram of the ASIL-TIRF setup is shown in Figure 6.2.6. In contrast to our 1D SISIM setup (Figure 5.3.1), the only difference is the mask configuration. The mask used here only allows either +1 or -1 order diffraction beam to get through, while the mask used in the SISIM allows both +1 and -1 order diffraction beams through. In Figure 6.2.6, as illustrated by the sharp red shading, +1 order diffraction beam goes through the mask, and then focuses at the periphery of the BFP of ASIL-objective. After that, this collimated beam is cast on the sample with an incident angle larger than the critical angle. At the interface of the ASIL and the sample, illumination beam is totally

reflected to form the TIR illumination. The actual incident angle is dependent on the grating period once the lenses are decided.

We have obtained some preliminary results based on this setup that came from the modified SISIM setup. In our case, the incident angle was about 50° as discussed in Section 5.5. In Figure 6.2.7, SIF and ASIL-TIRF images of some 1 μm 625/645 fluorescent beads are displayed. In the SIF image, every single bead appears in a uniform intensity distribution due to the uniform Köhler illumination with the beam incident at 0° angle to the normal. While in the ASIL-TIRF image, every single bead appears in a gradient intensity distribution with increasing distance from the TIR plane at the contact point, and the periphery contour far from the centre of the bead partially disappears. This phenomenon happens because only the fluorophores within a very shallow depth, about 43 nm, from the interface of the ASIL flat surface and air can be efficiently excited by the evanescent wave, and theoretically all the fluorophores outside this region should be totally unexcited and therefore unseen. Practically these out-of-depth fluorophores are still weakly stimulated by a small portion of emission from the fluorophores in the region of evanescent wave, so they can still emit a small amount of fluorescent light.

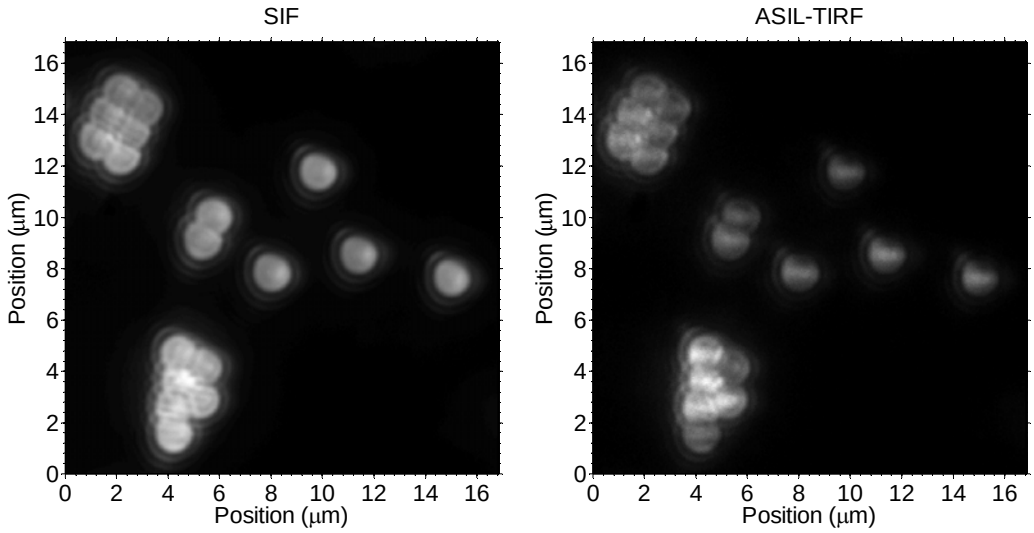


**Figure 6.2.7 Comparison of two images of several 1 μm fluorescent beads obtained with SIF (left) and ASIL-TIRF (right)**
In the SIF, the illumination beam was incident at 0° angle to the normal due to the conventional Köhler illumination; in the ASIL-TIRF, the illumination beam was incident at 50° angle to the normal due to the TIR illumination, then the intensity penetration depth was about 43 nm.

In Figure 6.2.8, Jurkat cell F-actin cytoskeleton images obtained with SIF and ASIL-TIRF are displayed. In the SIF image, the particular distribution of F-actin around the nucleus cannot be distinguished because of the diffusion of background fluorescence from the fluorophores conjugated to peripheral F-actin. On the contrary, in the ASIL-TIRF image, the F-actin distribution around the nucleus can be accurately observed, which means only the nucleus part in this cell was close enough to the interface and within the penetration depth of evanescent wave as depicted in Figure 6.2.9. Since the cytosol has a refractive index of approximately 1.38, the intensity penetration depth at the interface of the ASIL and the cell was about 76 nm. The remarkable differences in these two images vividly demonstrate the intense depth-selective imaging property of ASIL-TIRF.

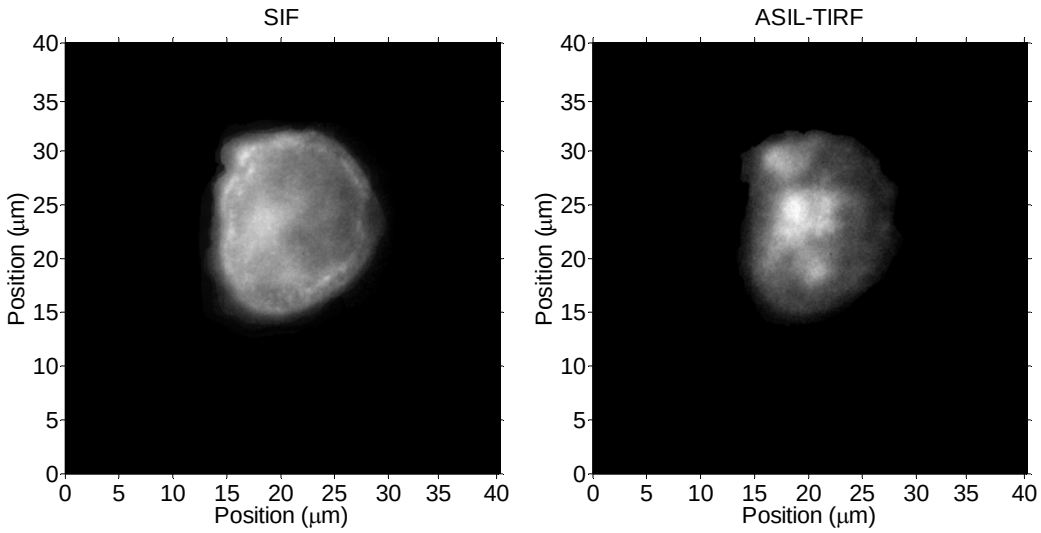


**Figure 6.2.8 Comparison of two fluorescent images of Jurkat cell F-action cytoskeleton obtained with SIF (left) and ASIL-TIRF (right)**
In the SIF, the illumination beam was incident at 0° angle to the normal due to the conventional Köhler illumination; in the ASIL-TIRF, the illumination beam was incident at 50° angle to the normal due to the TIR illumination, then the intensity penetration depth was about 76 nm.

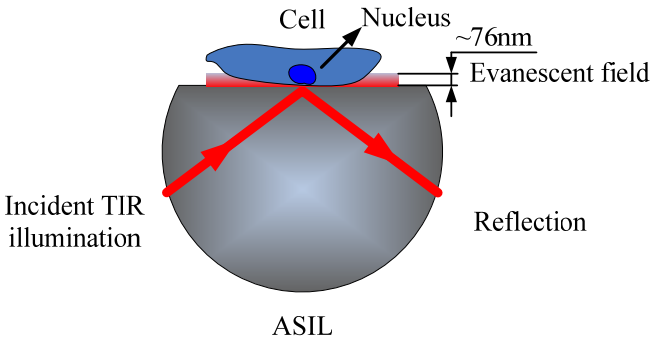


**Figure 6.2.9 Depiction of the relative position between the cell and the ASIL**
Only the nucleus part in this cell is close enough to the interface and within the penetration depth of evanescent wave.

The ASIL-TIRF, like conventional TIRF microscopes, can be used to image samples with much higher contrast, virtually no background fluorescence compared with normal epi-fluorescence images. This allows high-contrast imaging of fine intracellular and intercellular structures or processes that are not clearly visible in the conventional epi-fluorescence microscopes. Moreover, due to the high refractive index of the ASIL

material, an incident angle of the illumination beam that is much larger than the critical angle can be achieved. In this way, a much shallower penetration depth of evanescent wave, typically dozens of nanometres, can be fulfilled in contrast to the conventional TIRF. This feature makes highly-selective region of interest imaging possible.

Future refinements on ASIL-TIRF include every aspect mentioned in Subsection 6.2.2 in order to make it more suitable for routine use in biological research.

# References


1. R. Y. Tsien, *The green fluorescent protein.* Annual Review of Biochemistry, 2003. **67**(1): p. 509-544.
2. B. Huang, *Super-resolution optical microscopy: multiple choices.* Current Opinion in Chemical Biology, 2010. **14**(1): p. 10-14.
3. S. W. Hell and J. Wichmann, *Breaking the diffraction resolution limit by stimulated emission: stimulated-emission-depletion fluorescence microscopy.* Optics Letters, 1994. **19**(11): p. 780-782.
4. M. J. Rust, M. Bates, and X. W. Zhuang, *Sub-diffraction-limit imaging by stochastic optical reconstruction microscopy (STORM).* Nature Methods, 2006. **3**(10): p. 793-795.
5. M. G. L. Gustafsson, *Surpassing the lateral resolution limit by a factor of two using structured illumination microscopy.* Journal of Microscopy, 2000. **198**(2): p. 82-87.
6. M. G. L. Gustafsson, D. A. Agard, and J. W. Sedat. *Doubling the lateral resolution of wide-field fluorescence microscopy using structured illumination*. in *Three-Dimensional and Multidimensional Microscopy: Image Acquisition Processing VII*. 2000. San Jose, CA, USA: Proceedings of SPIE.
7. J. Zhang, 2006. *High resolution solid immersion lens microscopy and its application to surface plasmon resonance imaging*. PhD Thesis, The University of Nottingham.
8. J. Zhang, C. W. See, and M. G. Somekh, *Imaging performance of widefield solid immersion lens microscopy.* Applied Optics, 2007. **46**(20): p. 4202-4208.
9. T. Sasaki, M. Baba, M. Yoshita, and H. Akiyama, *Application of solid immersion lens to high-resolution photoluminescence imaging of patterned GaAs quantum wells.* Japanese Journal of Applied Physics, Part 2: Letters, 1997. **36**(7 B): p. L962-L964.
10. M. Yoshita, T. Sasaki, M. Baba, and H. Akiyama, *Application of solid immersion lens to high-spatial resolution photoluminescence imaging of GaAs quantum wells at low temperatures.* Applied Physics Letters, 1998. **73**(5): p. 635-637.
11. M. Baba, M. Yoshita, T. Sasaki, and H. Akiyama, *Application of solid immersion lens to submicron resolution imaging of nano-scale quantum wells.* Optical Review, 1999. **6**(3): p. 257-260.
12. F. Frischknecht, O. Renaud, and S. L. Shorte, *Imaging today's infectious animalcules.* Current Opinion in Microbiology, 2006. **9**(3): p. 297-306.
13. M. Abramowitz, *Microscope basics and beyond*. Revised 2003 ed. 2003, New York: Olympus America Inc.
14. J. R. Lakowicz, *Principles of fluorescence spectroscopy*. 3, illustrated ed. 2006, New York: Springer.

15. J. B. Pawley, *Handbook of biological confocal microscopy*. 3, illustrated ed. Language of science. 2006, New York: Springer.
16. M. Born and E. Wolf, *Principles of optics: electromagnetic theory of propagation, interference and diffraction of light*. 7th ed. 1999, Cambridge: Cambridge University Press.
17. J. W. Goodman, *Introduction to Fourier optics*. 3, illustrated ed. 2005, New York: Roberts and Company Publishers.
18. R. Wayne, *Light and Video Microscopy*. illustrated ed. 2009, San Diego: Academic Press/Elsevier.
19. S. G. Lipson, H. Lipson, and D. S. Tannhauser, *Optical physics*. 3, illustrated, revised ed. 1995, Cambridge: Cambridge University Press.
20. W. J. Smith, *Modern optical engineering: the design of optical systems*. 4, illustrated ed. 2007, New York: McGraw-Hill Professional.
21. J. M. Geary, *Introduction to lens design: With practical Zemax examples*. illustrated ed. 2002, Richmond: Willmann-Bell.
22. J. Lippincott-Schwartz and S. Manley, *Putting super-resolution fluorescence microscopy to work.* Nature Methods, 2009. **6**(1): p. 21-23.
23. T. A. Klar and S. W. Hell, *Subdiffraction resolution in far-field fluorescence microscopy.* Optics Letters, 1999. **24**(14): p. 954-956.
24. A. Yildiz, J. N. Forkey, S. A. McKinney, T. Ha, Y. E. Goldman, and P. R. Selvin, *Myosin V walks hand-over-hand: Single fluorophore imaging with 1.5-nm localization.* Science, 2003. **300**(5628): p. 2061-2065.
25. E. Betzig, G. H. Patterson, R. Sougrat, O. W. Lindwasser, S. Olenych, J. S. Bonifacino, M. W. Davidson, J. Lippincott-Schwartz, and H. F. Hess, *Imaging intracellular fluorescent proteins at nanometer resolution.* Science, 2006. **313**(5793): p. 1642-1645.
26. S. T. Hess, T. P. K. Girirajan, and M. D. Mason, *Ultra-high resolution imaging by fluorescence photoactivation localization microscopy.* Biophysical Journal, 2006. **91**(11): p. 4258-4272.
27. S. W. Hell, *Toward fluorescence nanoscopy.* Nature Biotechnology, 2003. **21**(11): p. 1347-1355.
28. M. Bates, B. Huang, and X. W. Zhuang, *Super-resolution microscopy by nanoscale localization of photo-switchable fluorescent probes.* Current Opinion in Chemical Biology, 2008. **12**(5): p. 505-514.
29. R. Heintzmann and C. Cremer, *Laterally modulated excitation microscopy: Improvement of resolution by using a diffraction grating.* Proceedings of SPIE - The International Society for Optical Engineering, 1999. **3568**: p. 185-196.
30. R. Heintzmann, T. M. Jovin, and C. Cremer, *Saturated patterned excitation microscopy-a concept for optical resolution improvement.* Journal of the Optical Society of America A: Optics and Image Science, and Vision, 2002. **19**(8): p. 1599-1609.
31. M. G. L. Gustafsson, *Nonlinear structured-illumination microscopy: Wide-field fluorescence imaging with theoretically unlimited resolution.* Proceedings of the National Academy of Sciences of the United States of America, 2005. **102**(37): p. 13081-13086.

32. M. A. A. Neil, R. Juskaitis, and T. Wilson, *Method of obtaining optical sectioning by using structured light in a conventional microscope.* Optics Letters, 1997. **22**(24): p. 1905-1907.
33. M. A. A. Neil, R. Juskaitis, and T. Wilson, *Real time 3D fluorescence microscopy by two beam interference illumination.* Optics Communications, 1998. **153**: p. 1-4.
34. M. Müller, *Introduction to confocal fluorescence microscopy*. 2 ed. 2006, Bellingham: SPIE Press.
35. E. Rittweger, K. Y. Han, S. E. Irvine, C. Eggeling, and S. W. Hell, *STED microscopy reveals crystal colour centres with nanometric resolution.* Nature Photonics, 2009. **3**(3): p. 144-147.
36. G. Donnert, J. Keller, R. Medda, M. A. Andrei, S. O. Rizzoli, R. Lurmann, R. Jahn, C. Eggeling, and S. W. Hell, *Macromolecular-scale resolution in biological fluorescence microscopy.* Proceedings of the National Academy of Sciences of the United States of America, 2006. **103**(31): p. 11440-11445.
37. B. Huang, W. Q. Wang, M. Bates, and X. W. Zhuang, *Three-dimensional super-resolution imaging by stochastic optical reconstruction microscopy.* Science, 2008. **319**(5864): p. 810-813.
38. M. G. L. Gustafsson, L. Shao, P. M. Carlton, C. J. R. Wang, I. N. Golubovskaya, W. Z. Cande, D. A. Agard, and J. W. Sedat, *Three-dimensional resolution doubling in wide-field fluorescence microscopy by structured illumination.* Biophysical Journal, 2008. **94**(12): p. 4957-4970.
39. L. Schermelleh, P. M. Carlton, S. Haase, L. Shao, L. Winoto, P. Kner, B. Burke, M. C. Cardoso, D. A. Agard, M. G. L. Gustafsson, H. Leonhardt, and J. W. Sedat, *Subdiffraction multicolor imaging of the nuclear periphery with 3D structured illumination microscopy.* Science, 2008. **320**(5881): p. 1332-1336.
40. W. Lukosz and M. Marchand, *Optischen Abbildung Unter Überschreitung der Beugungsbedingten Auflösungsgrenze.* Optica Acta 1963. **10**(3): p. 241-255.
41. W. Lukosz, *Optical Systems with Resolving Powers Exceeding the Classical Limit.* Journal of the Optical Society of America, 1966. **56**(11): p. 1463-1471.
42. L. Shao, B. Isaac, S. Uzawa, D. A. Agard, J. W. Sedat, and M. G. L. Gustafsson, *$I^5S$: Wide-field light microscopy with 100-nm-scale resolution in three dimensions.* Biophysical Journal, 2008. **94**(12): p. 4971-4983.
43. P. Kner, B. B. Chhun, E. R. Griffis, L. Winoto, and M. G. L. Gustafsson, *Super-resolution video microscopy of live cells by structured illumination.* Nature Methods, 2009. **6**(5): p. 339-342.
44. P. Kner, B. Chhun, E. Griffis, L. Winoto, L. Shao, and M. G. L. Gustafsson. *Live TIRF microscopy at 100nm resolution through structured illumination*. in *Three-Dimensional and Multidimensional Microscopy: Image Acquisition and Processing XVI* 2009. San Jose, CA, USA SPIE.
45. J. T. Frohn, H. F. Knapp, and A. Stemmer, *True optical resolution beyond the Rayleigh limit achieved by standing wave illumination.* Proceedings of the National Academy of Sciences, 2000. **97**(13): p. 7232-7236.
46. R. Fedosseev, Y. Belyaev, J. Frohn, and A. Stemmer, *Structured light illumination for extended resolution in fluorescence microscopy.* Optics and Lasers in Engineering, 2005. **43**(3-5): p. 403-414.

47. A. Stemmer, M. Beck, and R. Fiolka, *Widefield fluorescence microscopy with extended resolution.* Histochemistry and Cell Biology, 2008. **130**(5): p. 807-817.
48. G. E. Cragg and P. T. C. So, *Lateral resolution enhancement with standing evanescent waves.* Optics Letters, 2000. **25**(1): p. 46-48.
49. P. T. C. So, H. S. Kwon, and C. Y. Dong, *Resolution enhancement in standing-wave total internal reflection microscopy: A point-spread-function engineering approach.* Journal of the Optical Society of America A: Optics and Image Science, and Vision, 2001. **18**(11): p. 2833-2845.
50. E. Chung, D. Kim, and P. T. C. So, *Extended resolution wide-field optical imaging: Objective-launched standing-wave total internal reflection fluorescence microscopy.* Optics Letters, 2006. **31**(7): p. 945-947.
51. E. Chung, D. Kim, Y. Cui, Y.H. Kim, and P. T. C. So, *Two-dimensional standing wave total internal reflection fluorescence microscopy: Superresolution imaging of single molecular and biological specimens.* Biophysical Journal, 2007. **93**(5): p. 1747-1757.
52. R. Heintzmann, *Saturated patterned excitation microscopy with two-dimensional excitation patterns.* Micron, 2003. **34**(6-7): p. 283-291.
53. R. Heintzmann and P. A. Benedetti, *High-resolution image reconstruction in fluorescence microscopy with patterned excitation.* Applied Optics, 2006. **45**(20): p. 5037-5045.
54. A. Sentenac, K. Belkebir, H. Giovannini, and P. C. Chaumet, *Subdiffraction resolution in total internal reflection fluorescence microscopy with a grating substrate.* Optics Letters, 2008. **33**(3): p. 255-257.
55. A. Sentenac, K. Belkebir, H. Giovannini, and P. C. Chaumet, *High-resolution total-internal-reflection fluorescence microscopy using periodically nanostructured glass slides.* Journal of the Optical Society of America A: Optics and Image Science, and Vision, 2009. **26**(12): p. 2550-2557.
56. S. G. Liu, C. J. Chuang, C. W. See, G. Zoriniants, W. L. Barnes, and M. G. Somekh, *Double-grating-structured light microscopy using plasmonic nanoparticle arrays.* Optics Letters, 2009. **34**(8): p. 1255-1257.
57. A. Sentenac, P. C. Chaumet, and K. Belkebir, *Beyond the rayleigh criterion: Grating assisted far-field optical diffraction tomography.* Physical Review Letters, 2006. **97**(24): p. 243901.
58. M. W. Docter, P. M. van den Berg, P. F. A. Alkemade, V. G. Kutchoukov, O. M. Piciu, A. Bossche, I. T. Young, and Y. Garini. *Structured illumination microscopy using extraordinary transmission through sub-wavelength hole-arrays*. in *1st Joint Israeli-Turkish Workshop on Nanophotonics*. 2007. Ramat Gan, ISRAEL: Spie-Soc Photoptical Instrumentation Engineers.
59. Z. Liu, S. Durant, H. Lee, Y. Pikus, N. Fang, Y. Xiong, C. Sun, and X. Zhang, *Far-field optical superlens.* Nano Letters, 2007. **7**(2): p. 403-408.
60. R. Fiolka, M. Beck, and A. Stemmer, *Structured illumination in total internal reflection fluorescence microscopy using a spatial light modulator.* Optics Letters, 2008. **33**(14): p. 1629-1631.
61. L. M. Hirvonen, K. Wicker, O. Mandula, and R. Heintzmann, *Structured illumination microscopy of a living cell.* European Biophysics Journal, 2009. **38**(6): p. 807-812.

62. M. R. Beversluis, G. W. Bryant, and S. J. Stranick, *Effects of inhomogeneous fields in superresolving structured-illumination microscopy.* Journal of the Optical Society of America A: Optics and Image Science, and Vision, 2008. **25**(6): p. 1371-1377.
63. B. J. Chang, L. J. Chou, Y. C. Chang, and S. Y. Chiang, *Isotropic image in structured illumination microscopy patterned with a spatial light modulator.* Optics Express, 2009. **17**(17): p. 14710-14721.
64. L. H. Schaefer, D. Schuster, and J. Schaffer, *Structured illumination microscopy: artefact analysis and reduction utilizing a parameter optimization approach.* Journal of Microscopy, 2004. **216**(2): p. 165-174.
65. S. A. Shroff, J. R. Fienup, and D. R. Williams. *OTF compensation in structured illumination superresolution images*. in *Unconventional Imaging IV*. 2008. San Diego, CA, United states: SPIE.
66. S. A. Shroff, J. R. Fienup, and D. R. Williams, *Phase-shift estimation in sinusoidally illuminated images for lateral superresolution.* Journal of the Optical Society of America A: Optics and Image Science, and Vision, 2009. **26**(2): p. 413-424.
67. W. Kim, Y. Yoon, H. Choi, N. Park, K. Park, and Y. Park, *Feasibility analysis of solid immersion lens-based dual-layer near-field recording optics with a numerical aperture of 1.84.* Optics Communications, 2009. **282**(4): p. 540-545.
68. N. Bozinovic, C. Ventalon, T. Ford, and J. Mertz, *Fluorescence endomicroscopy with structured illumination.* Optics Express, 2008. **16**(11): p. 8016-8025.
69. C. C. Wang, K. L. Lee, and C. H. Lee, *Wide-field optical nanoprofilometry using structured illumination.* Optics Letters, 2009. **34**(22): p. 3538-3540.
70. W. G. Hartley, *The light microscope: its use and development*. 1993, Oxford: Senecio.
71. B. R. Masters and P. T. C. So, *Handbook of biomedical nonlinear optical microscopy*. illustrated ed. 2008, New York: Oxford University Press US.
72. B. D. Terris, H. J. Mamin, D. Rugar, W. R. Studenmund, and G. S. Kino, *Near-field optical data storage using a solid immersion lens.* Applied Physics Letters, 1994. **65**(4): p. 388-390.
73. S. M. Mansfield and G. S. Kino, *Solid immersion microscope.* Applied Physics Letters, 1990. **57**(24): p. 2615-2616.
74. S. M. Mansfield, 1992. *Solid immersion microscopy*. PhD Thesis, Standford University.
75. S. M. Mansfield, W. R. Studenmund, G. S. Kino, and K. Osato, *High-numerical-aperture lens system for optical storage.* Optics Letters, 1993. **18**(4): p. 305-307.
76. J. A. H. Stotz and M. R. Freeman, *Stroboscopic scanning solid immersion lens microscope.* Review of Scientific Instruments, 1997. **68**(12): p. 4468-4477.
77. D. A. Fletcher, K. B. Crozier, C. F. Quate, G. S. Kino, K. E. Goodson, D. Simanovskii, and D. V. Palanker, *Near-field infrared imaging with a microfabricated solid immersion lens.* Applied Physics Letters, 2000. **77**(14): p. 2109-2111.
78. K. B. Crozier, D. A. Fletcher, G. S. Kino, and C. F. Quate, *Micromachined silicon nitride solid immersion lens.* Journal of Microelectromechanical Systems, 2002. **11**(5): p. 470-478.

79. S. Moehl, Hui Zhao, B. D. Don, S. Wachter, and H. Kalt, *Solid immersion lens-enhanced nano-photoluminescence: Principle and applications.* Journal of Applied Physics, 2003. **93**(10): p. 6265-6272.
80. L. P. Ghislain and V. B. Elings, *Near-field scanning solid immersion microscope.* Applied Physics Letters, 1998. **72**(22): p. 2779-2781.
81. L. P. Ghislain, V. B. Elings, K. B. Crozier, S. R. Manalis, S. C. Minne, K. Wilder, G. S. Kino, and C. F. Quate, *Near-field photolithography with a solid immersion lens.* Applied Physics Letters, 1999. **74**(4): p. 501-503.
82. K. Karrai, X. Lorenz, and L. Novotny, *Enhanced reflectivity contrast in confocal solid immersion lens microscopy.* Applied Physics Letters, 2000. **77**(21): p. 3459-3461.
83. S. B. Ippolito, B. B. Goldberg, and M. S. Unlu, *High spatial resolution subsurface microscopy.* Applied Physics Letters, 2001. **78**(26): p. 4071-4073.
84. S. B. Ippolito, S. A. Thorne, M. G. Eraslan, B. B. Goldberg, M. S. Unlu, and Y. Leblebici, *High spatial resolution subsurface thermal emission microscopy.* Applied Physics Letters, 2004. **84**(22): p. 4529-4531.
85. F. Zijp, J. Lee, C. A. Verschuren, J. M. A. Van Den Eerenbeemd, and D. M. Bruls, *Improved near-field recording system for first-surface media with an NA = 1.9 solid immersion lens.* Japanese Journal of Applied Physics, Part 1: Regular Papers and Short Notes and Review Papers, 2006. **45**(2 B): p. 1336-1340.
86. Q. Wu, G. D. Feke, R. D. Grober, and L. P. Ghislain, *Realization of numerical aperture 2.0 using a gallium phosphide solid immersion lens.* Applied Physics Letters, 1999. **75**(26): p. 4064-4066.
87. Q. Wu, L. P. Ghislain, and V. B. Elings, *Imaging with solid immersion lenses, spatial resolution, and applications.* Proceedings of the IEEE, 2000. **88**(9): p. 1491-1498.
88. S. B. Ippolito, 2004. *High spatial resolution subsurface microscopy*. PhD Thesis, Boston University.
89. S. B. Ippolito, B. B. Goldberg, and M. S. Unlu, *Theoretical analysis of numerical aperture increasing lens microscopy.* Journal of Applied Physics, 2005. **97**(5): p. 053105.
90. M. Yoshita, K. Koyama, Y. Hayamizu, M. Baba, and H. Akiyama, *Improved high collection efficiency in fluorescence microscopy with a Weierstrass-sphere solid immersion lens.* Japanese Journal of Applied Physics, Part 2: Letters, 2002. **41**(7 B): p. 858-860.
91. V. Zwiller and G. Bjork, *Improved light extraction from emitters in high refractive index materials using solid immersion lenses.* Journal of Applied Physics, 2002. **92**(2): p. 660-665.
92. R. Brunner, J. Bischoff, K. Rudolf, and M. Ferstl. *Diffractive solid immersion lenses characterization and manufacturing*. in *Optical Metrology Roadmap for the Semiconductor, Optical, and Data Storage Industries II* 2001. San Diego, CA, United states: SPIE.
93. K. Cohn, D. Simanovskii, T. Smith, and D. Palanker, *Transient photoinduced diffractive solid immersion lens for infrared microscopy.* Applied Physics Letters, 2002. **81**(19): p. 3678-3680.

94. R. Brunner, M. Burkhardt, A. Pesch, O. Sandfuchs, M. Ferstl, S. Hohng, and J. O. White, *Diffraction-based solid immersion lens.* Journal of the Optical Society of America A, 2004. **21**(7): p. 1186-1191.
95. N. Choi, S. Shim, T. D. Milster, and J. Kim, *Optical design for the optimum solid immersion lens with high numerical aperture and large tolerance.* Japanese Journal of Applied Physics, Part 1-Regular Papers Brief Communications & Review Papers, 2007. **46**(6 B): p. 3724-3728.
96. Y. Yoon, W. Kim, H. Choi, N. Park, S. Kang, and Y. Park, *Design and analysis of replicated solid immersion lens for large thickness tolerance in near-field recording.* Japanese Journal of Applied Physics, 2008. **47**(7 Part 2): p. 5927-5932.
97. J. Bischoff and R. Brunner. *Numerical investigation of the resolution in solid immersion lens systems*. in *Optical Metrology Roadmap for the Semiconductor, Optical, and Data Storage Industries*. 2000. San Diego, CA, USA: SPIE.
98. Y. Zhang, *Design of high-performance supersphere solid immersion lenses.* Applied Optics, 2006. **45**(19): p. 4540-4546.
99. T. D. Milster, *Chromatic correction of high-performance solid immersion lens systems.* Japanese Journal of Applied Physics, Part 1: Regular Papers and Short Notes and Review Papers, 1999. **38**(3B): p. 1777-1779.
100. M. Baba, T. Sasaki, M. Yoshita, and H. Akiyama, *Aberrations and allowances for errors in a hemisphere solid immersion lens for submicron-resolution photoluminescence microscopy.* Journal of Applied Physics, 1999. **85**(9): p. 6923-6925.
101. J. S. Jo, T. D. Milster, and J. K. Erwin. *Characteristics of gap-induced aberration in solid immersion lens systems*. in *Conference on Optical Data Storage (ODS2000)*. 2000. Whistler, Canada: IEEE.
102. C. A. Verschuren, F. Zijp, J. Lee, J. M. A. Van Den Eerenbeemd, M. B. Van Der Mark, and H. P. Urbach, *Near field recording on first-surface write-once media with a NA = 1.9 solid immersion lens.* Japanese Journal of Applied Physics, Part 1: Regular Papers and Short Notes and Review Papers, 2005. **44**(5 B): p. 3564-3567.
103. A. N. Vamivakas, R. D. Younger, B. B. Goldberg, A. K. Swan, M. S. Unlu, E. R. Behringer, and S. B. Ippolito, *A case study for optics: The solid immersion microscope.* American Journal of Physics, 2008. **76**(8): p. 758-768.
104. M. Lang, E. Aspnes, and T. D. Milster, *Geometrical analysis of third-order aberrations for a solid immersion lens.* Optics Express, 2008. **16**(24): p. 20008-20028.
105. S. H. Goh, C. J. R. Sheppard, A. C. T. Quah, C. M. Chua, L. S. Koh, and J. C. H. Phang, *Design considerations for refractive solid immersion lens: Application to subsurface integrated circuit fault localization using laser induced techniques.* Review of Scientific Instruments, 2009. **80**(1): p. 013703.
106. S. H. Goh and C. J. R. Sheppard, *High aperture focusing through a spherical interface: Application to refractive solid immersion lens (RSIL) for subsurface imaging.* Optics Communications, 2009. **282**(5): p. 1036-1041.
107. W. Kim, Y. Yoon, H. Choi, N. Park, and Y. Park, *Effects of optical variables in immersion lens-based near-field optics.* Optics Express, 2008. **16**(18): p. 13933-13948.

108. Y. J. Zhang and Y. Y. Zhuang, *Dispersion effect in optical microscopy systems with a supersphere solid immersion lens.* Chinese Physics B, 2009. **18**(7): p. 2788-2793.
109. S. Hasegawa, N. Aoyama, A. Futamata, and T. Uchiyama, *Optical tunneling effect calculation of a solid immersion lens for use in optical disk memory.* Applied Optics, 1999. **38**(11): p. 2297-2300.
110. T. D. Milster, J. S. Jo, and K. Hirota, *Roles of propagating and evanescent waves in solid immersion lens systems.* Applied Optics, 1999. **38**(23): p. 5046-5057.
111. T. D. Milster, J. S. Jo, K. Hirota, K. Shimura, and Y. Zhang, *The nature of the coupling field in optical data storage using solid immersion lenses.* Japanese Journal of Applied Physics, Part 1: Regular Papers and Short Notes and Review Papers, 1999. **38**(3B): p. 1793-1794.
112. F. Guo, T. E. Schlesinger, and D. D. Stancil, *Optical field study of near-field optical recording with a solid immersion lens.* Applied Optics, 2000. **39**(2): p. 324-332.
113. M. Yoshita, K. Koyama, M. Baba, and H. Akiyama, *Fourier imaging study of efficient near-field optical coupling in solid immersion fluorescence microscopy.* Journal of Applied Physics, 2002. **92**(2): p. 862-865.
114. L. E. Helseth, *Roles of polarization, phase and amplitude in solid immersion lens systems.* Optics Communications, 2001. **191**(3-6): p. 161-172.
115. K. Koyama, M. Yoshita, M. Baba, T. Suemoto, and H. Akiyama, *High collection efficiency in fluorescence microscopy with a solid immersion lens.* Applied Physics Letters, 1999. **75**(12): p. 1667-1669.
116. S. Matsuo and H. Misawa, *Direct measurement of laser power through a high numerical aperture oil immersion objective lens using a solid immersion lens.* Review of Scientific Instruments, 2002. **73**(5): p. 2011-2015.
117. A. L. Birkbeck, S. Zlatanovic, M. Ozkan, and S. C. Esener. *Laser tweezer controlled solid immersion lens for high resolution imaging in microfluidic and biological samples*. in *BioMEMS and nanotechnology*. 2004. Perth, WA, Australia: The International Society for Optical Engineering.
118. A. L. Birkbeck, S. Zlatanovic, S. C. Esener, and M. Ozkan, *Laser-tweezer-controlled solid immersion microscopy in microfluidic systems.* Optics Letters, 2005. **30**(20): p. 2712-2714.
119. T. Chen, T. D. Milster, S. Yang, and D. Hansen, *Evanescent imaging with induced polarization by using a solid immersion lens.* Optics Letters, 2007. **32**(2): p. 124-126.
120. K. A . Serrels, E. Ramsay, R. J . Warburton, and D. T . Reid, *Nanoscale optical microscopy in the vectorial focusing regime.* Nature Photonics, 2008 **2** (5 ): p. 311-314.
121. S. H. Goh, A. C. T. Quah, C. J. R. Sheppard, C. M. Chua, L. S. Koh, and J. C. H. Phang. *Effect of Refractive Solid Immersion Lens parameters on the enhancement of laser induced fault localization techniques*. in *International Symposium on the Physical and Failure Analysis of Integrated Circuits*. 2008. Singapore, Singapore: Institute of Electrical and Electronics Engineers Inc.

122. C. D. Poweleit, A. Gunther, S. Goodnick, and Jose Menendez, *Raman imaging of patterned silicon using a solid immersion lens.* Applied Physics Letters, 1998. **73**(16): p. 2275-2277.
123. E. Ramsay, N. Pleynet, D. Xiao, R. J. Warburton, and D. T. Reid, *Two-photon optical-beam-induced current solid-immersion imaging of a silicon flip chip with a resolution of 325 nm.* Optics Letters, 2005. **30**(1): p. 26-28.
124. K. A. Serrels, E. Ramsay, and D. T. Reid, *70 nm resolution in subsurface optical imaging of silicon integrated-circuits using pupil-function engineering.* Applied Physics Letters, 2009. **94**(7): p. 073113.
125. A. Serov, R. Rao, M. Gosch, T. Anhut, D. Martin, R. Brunner, R. Rigler, and T. Lasser, *High light field confinement for fluorescent correlation spectroscopy using a solid immersion lens.* Biosensors and Bioelectronics, 2004. **20**(3): p. 431-435.
126. R. Rao, J. Mitic, A. Serov, R. A. Leitgeb, and T. Lasser, *Field confinement with aberration correction for solid immersion lens based fluorescence correlation spectroscopy.* Optics Communications, 2007. **271**(2): p. 462-469.
127. D. Simanovskii, D. Palanker, K. Cohn, and T. Smith, *Transient optical elements: application to near-field microscopy.* Journal of Microscopy, 2003. **210**(3): p. 307-310.
128. M. Tseng, L. Chen, and C. Liu, *Improvement of optical imaging resolution by a negative refraction photonic crystal with a solid immersion lens.* Physica B: Condensed Matter, 2008. **403**(21-22): p. 4123-4127.
129. Y. J. Zhang, C. W. Zheng, and H. C. Xiao, *Improving the resolution of a solid immersion lens optical system using a multiphase Fresnel zone plate.* Optics & Laser Technology, 2005. **37**(6): p. 444-448.
130. B. B. Goldberg, S. B. Ippolito, L. Novotny, Z. Liu, and M. S. Unlu, *Immersion lens microscopy of photonic nanostructures and quantum dots.* IEEE Journal on Selected Topics in Quantum Electronics, 2002. **8**(5): p. 1051-1059.
131. J. Zhang, C. W. See, M. G. Somekh, M. C. Pitter, and S. G. Liu, *Wide-field surface plasmon microscopy with solid immersion excitation.* Applied Physics Letters, 2004. **85**(22): p. 5451-5453.
132. J. Zhang, M. C. Pitter, S.G. Liu, C. W. See, and M. G. Somekh, *Surface-plasmon microscopy with a two-piece solid immersion lens: bright and dark fields.* Applied Optics, 2006. **45**(31): p. 7977-7986.
133. M. J. Weber, *Handbook of optical materials*. illustrated ed. The CRC Press laser and optical science and technology series. 2002, Boca Raton: CRC Press.
134. L. Dai, I. Gregor, I. Von Der Hocht, T. Ruckstuhl, and J. Enderlein, *Measuring large numerical apertures by imaging the angular distribution of radiation of fluorescing molecules.* Optics Express, 2005. **13**(23): p. 9409-9414.
135. J. Chen, 2009. *Towards single photon detection with a practical EMCCD*. MSc Thesis, The University of Nottingham.
136. Y. N. Xia, J. Tien, D. Qin, and G. M. Whitesides, *Non-photolithographic methods for fabrication of elastomeric stamps for use in microcontact printing.* Langmuir, 1996. **12**(16): p. 4033-4038.
137. Q. Wu, F. A. Merchant, and K. R. Castleman, *Microscope Image Processing*. illustrated ed. 2008, San Diego: Academic Press.

138. D. Axelrod, *Carbocyanine dye orientation in red-cell membrane studied by microscopic fluorescence polarization.* Biophysical Journal, 1979. **26**(3): p. 557-573.
139. O. Haeberle, M. Ammar, H. Furukawa, K. Tenjimbayashl, and P. Török, *Point spread function of optical microscopes imaging through stratified media.* Optics Express, 2003. **11**(22): p. 2964-2969.
140. P. Török, P. R. T. Munro, and Em E. Kriezis, *High numerical aperture vectorial imaging in coherent optical microscopes.* Optics Express, 2008. **16**(2): p. 507-523.
141. P. Török, S. J. Hewlett, and P. Varga, *The role of specimen-induced spherical aberration in confocal microscopy.* Journal of Microscopy-Oxford, 1997. **188**: p. 158-172.
142. P. Török and F. J. Kao, *Optical imaging and microscopy: techniques and advanced systems*. 2, illustrated ed. Volume 87 of Springer series in optical sciences. 2007, New York: Springer.
143. E. Wolf, *Progress in Optics, Volume 49*. illustrated ed. Progress in Optics. 2006, Amsterdam: Elsevier.
144. M. A. Heald and J. B. Marion, *Classical electromagnetic radiation*. 3rd ed. 1995, Philadelphia: Saunders College Publishing.
145. M. G. Somekh, K. Hsu, and M. C. Pitter, *Resolution in structured illumination microscopy: A probabilistic approach.* Journal of the Optical Society of America A: Optics and Image Science, and Vision, 2008. **25**(6): p. 1319-1329.
146. K. Hsu, M. G. Somekh, and M. C. Pitter, *Stochastic transfer function: Application to fluorescence microscopy.* Journal of the Optical Society of America A: Optics and Image Science, and Vision, 2009. **26**(7): p. 1622-1629.
147. M. G. Somekh, K. Hsu, and M. C. Pitter, *Stochastic transfer function for structured illumination microscopy.* Journal of the Optical Society of America A: Optics and Image Science, and Vision, 2009. **26**(7): p. 1630-1637.
148. E. G. Loewen and E. Popov, *Diffraction gratings and applications*. illustrated ed. Volume 58 of Optical engineering. 1997, New York: Marcel Dekker Inc.
149. J. J. Correia and H. W. Detrich, *Biophysical tools for biologists, Volume 2*. illustrated ed. Methods in Cell Biology. Vol. 89. 2008, San Diego: Academic Press.
150. S. Matsui, T. Kaito, J. Fujita, M. Komuro, K. Kanda, and Y. Haruyama. *Three-dimensional nanostructure fabrication by focused-ion-beam chemical vapor deposition*. in *Papers from the 44th international conference on electron, ion, and photon beam technology and nanofabrication*. 2000. Rancho Mirage, California, (USA): AVS.
151. J. A. Rogers, K. E. Paul, R. J. Jackman, and G. M. Whitesides, *Using an elastomeric phase mask for sub-100 nm photolithography in the optical near field.* Applied Physics Letters, 1997. **70**(20): p. 2658-2660.
152. K. König, *Laser tweezers and multiphoton microscopes in life sciences.* Histochemistry and Cell Biology, 2000. **114**(2): p. 79-92.
153. K. C. Neuman and S. M. Block, *Optical trapping.* Review of Scientific Instruments, 2004. **75**(9): p. 2787-2809.
154. A. J. Garcia, *Get a grip: integrins in cell-biomaterial interactions.* Biomaterials, 2005. **26**(36): p. 7525-7529.

155. N. Faucheux, R. Schweiss, K. Lutzow, C. Werner, and T. Groth, *Self-assembled monolayers with different terminating groups as model substrates for cell adhesion studies.* Biomaterials, 2004. **25**(14): p. 2721-2730.
156. Y. Z. Yang, R. Cavin, and J. L. Ong, *Protein adsorption on titanium surfaces and their effect on osteoblast attachment.* Journal of Biomedical Materials Research - Part A, 2003. **67**(1): p. 344-349.
157. D. Lehnert, B. Wehrle-Haller, C. David, U. Weiland, C. Ballestrem, B. A. Imhof, and M. Bastmeyer, *Cell behaviour on micropatterned substrata: limits of extracellular matrix geometry for spreading and adhesion.* Journal of Cell Science, 2004. **117**(1): p. 41-52.
158. P. Clark, P. Connolly, A. S. G. Curtis, J. A. T. Dow, and C. D. W. Wilkinson, *Topographical control of cell behavior.1. Simple step cues.* Development, 1987. **99**(3): p. 439-448.
159. M. J. Dalby, M. O. Riehle, H. Johnstone, S. Affrossman, and A. S. G. Curtis, *Investigating the limits of filopodial sensing: a brief report using SEM to image the interaction between 10 nm high nano-topography and fibroblast filopodia.* Cell Biology International, 2004. **28**(3): p. 229-236.
160. J. Reichert, S. Bruckner, H. Bartelt, and K. D. Jandt, *Tuning cell adhesion on PTFE surfaces by laser induced microstructures.* Advanced Engineering Materials, 2007. **9**(12): p. 1104-1113.
161. G. Fu and W. O. Soboyejo, *Cell/surface interactions of human osteo-sarcoma (HOS) cells and micro-patterned polydimelthylsiloxane (PDMS) surfaces.* Materials Science and Engineering C, 2009. **29**(6): p. 2011-2018.
162. S. H. Jiang and J. G. Walker, *Speckle-illuminated fluorescence confocal microscopy, using a digital micro-mirror device.* Measurement Science and Technology, 2009. **20**(6): p. 065501.
163. D. Toomre and D. J. Manstein, *Lighting up the cell surface with evanescent wave microscopy.* Trends in Cell Biology, 2001. **11**(7): p. 298-303.

# Appendix I Three conjugate pairs free from spherical aberration

A paraxial ray propagation model is shown in Figure AI.1. The ray emitted from an on-axis point $A$ propagates from medium with refractive index $n$ to another medium with refractive index $n'$ through a spherical surface $BP$. Being refracted by the spherical surface, the ray hits the optical axis at $A'$ and forms the image of $A$.

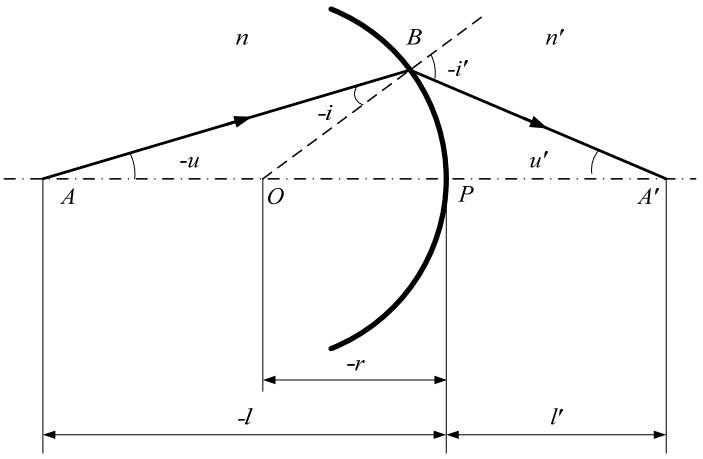


**Figure AI.1 The paraxial ray propagation model of a single refractive spherical surface**

In the triangle $ABO$, from the law of sines, there is:

$$\frac{r}{L-r}=\frac{\sin U}{\sin I}$$

Due to the approximation property of paraxial rays, it can be expressed as:

$$\frac{r}{l-r}=\frac{u}{i}$$

Adding the numerators to the denominators on both sides of this, there are:

$$\frac{r}{l}=\frac{u}{i+u}=1-\frac{i}{i+u} \tag{1}$$

and

$$\frac{l-r}{l}=\frac{i}{i+u} \tag{2}$$

Multiplying throughout (1) by $n/r$, there is:

$$\frac{n}{l}=\frac{n}{r}-\frac{n}{r}\cdot\frac{i}{i+u} \tag{3}$$

In the triangle *A'BO*, there is:

$$\frac{r}{l'-r}=\frac{\sin u'}{\sin i'}$$

Due to the approximation property of paraxial rays, it can also be expressed as:

$$\frac{r}{l'-r}=\frac{u'}{i'}$$

Following the similar deduction procedure as above, it can be derived that there is:

$$\frac{n'}{l'}=\frac{n'}{r}-\frac{n'}{r}\cdot\frac{i'}{i'+u'} \tag{4}$$

(4)-(3), there is:

$$\frac{n'}{l'}-\frac{n}{l}=\frac{n'-n}{r}+\left[\frac{ni}{r(i+u)}-\frac{n'i'}{r(i'+u')}\right]$$

or in this form:

$$\frac{n'}{l'}=\frac{n}{l}+\frac{n'-n}{r}+\left[\frac{ni}{r(i+u)}-\frac{n'i'}{r(i'+u')}\right] \tag{5}$$

From Snell's law, there is:

$$n\sin i = n'\sin i'$$

This can be expressed as:

$$ni = n'i'$$

From trigonometric relations, there is:

$$i + u = i' + u'$$

With the help of the two equations above, it is clear the last term in (5) is zero, so it can be rewritten as:

$$\frac{n'}{l'} = \frac{n'-n}{r} + \frac{n}{l} \tag{6}$$

Now, a real ray propagation model is shown in Figure AI.2.

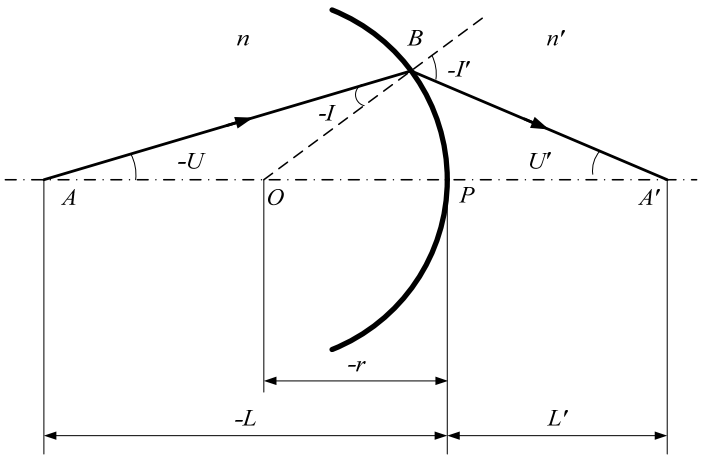


**Figure AI.2 The real ray propagation model of a single refractive spherical surface**

In the triangle *ABO*, from the law of sines, there is:

$$\frac{r}{L-r} = \frac{\sin U}{\sin I}$$

Adding the numerators to the denominators on both sides of this, there are:

$$\frac{r}{L}=\frac{\sin U}{\sin I+\sin U}=1-\frac{\sin I}{\sin I+\sin U} \tag{7}$$

and

$$\frac{L-r}{L}=\frac{\sin I}{\sin I+\sin U} \tag{8}$$

Multiplying throughout (7) by $n/r$, there is:

$$\frac{n}{L}=\frac{n}{r}-\frac{n}{r}\cdot\frac{\sin I}{\sin I+\sin U} \tag{9}$$

In the triangle *A'BO*, there is:

$$\frac{r}{L'-r}=\frac{\sin U'}{\sin I'}$$

Following the similar deduction procedure as above, it can be derived that there is:

$$\frac{n'}{L'}=\frac{n'}{r}-\frac{n'}{r}\cdot\frac{\sin I'}{\sin I'+\sin U'} \tag{10}$$

(10)-(9), there is:

$$\frac{n'}{L'}-\frac{n}{L}=\frac{n'-n}{r}+\left[\frac{n\sin I}{r(\sin I+\sin U)}-\frac{n'\sin I'}{r(\sin I'+\sin U')}\right]$$

or in this form:

$$\frac{n'}{L'}=\frac{n'-n}{r}+\frac{n}{L}+\left[\frac{n\sin I}{r(\sin I+\sin U)}-\frac{n'\sin I'}{r(\sin I'+\sin U')}\right] \tag{11}$$

For the image of an on-axis object, there are no aberrations besides spherical aberration in paraxial field. When the angles of the emitted rays from the object increase and excess paraxial field, spherical aberration takes place. Equation (6) and (11) are the mathematical expressions of the image distance in paraxial and real field respectively. Comparing these two equations, it is clear the only difference is the long final term in Equation (11), which exactly represents the spherical aberration.

Here, this final term of Equation (11), i.e. the spherical aberration, is defined as *SA* and transformed for further analysis. From Snell's law, there is:

$$n\sin I = n'\sin I'$$

Substitute it into Equation (11), there is:

$$SA = \frac{n\sin I}{r(\sin I + \sin U)} - \frac{n'\sin I'}{r(\sin I' + \sin U')} = \frac{n\sin I}{r(\sin I + \sin U)}\left(1 - \frac{\sin I + \sin U}{\sin I' + \sin U'}\right)$$

From Equation (8), there is:

$$SA = \frac{n(L-r)}{rL}\left(1 - \frac{\sin I + \sin U}{\sin I' + \sin U'}\right)$$

According to sum-to-product identities, there is:

$$SA = \frac{n(L-r)}{rL}\left(1 - \frac{2\sin\frac{U+I}{2}\cos\frac{I-U}{2}}{2\sin\frac{U'+I'}{2}\cos\frac{I'-U'}{2}}\right)$$

From trigonometric relations, there is:

$$I + U = I' + U'$$

then

$$SA = \frac{n(L-r)}{rL}(1 - \frac{\cos\frac{I-U}{2}}{\cos\frac{I'-U'}{2}})$$

According to sum-to-product identities again, there is:

$$SA = \frac{2n(L-r)}{rL}\frac{\sin\frac{I-U+I'-U'}{4}\sin\frac{I-U-I'+U'}{4}}{\cos\frac{I'-U'}{2}} = \frac{2n(L-r)}{rL}\frac{\sin\frac{I'-U}{2}\sin\frac{I-I'}{2}}{\cos\frac{I'-U'}{2}}$$

In conclusion, there is:

$$SA = \frac{2n(L-r)}{rL}\frac{\sin\frac{I'-U}{2}\sin\frac{I-I'}{2}}{\cos\frac{I'-U'}{2}} \qquad (12)$$

From Equation (11) and (12), it can be concluded there are three cases in which spherical aberration does not exist:

(1) The first case is $L$=0. In this case, according to Equation (11), image distance $L'$ and object distance $L$ both equal zero, which means there is no longitudinal aberration. In this way, spherical aberration does not exit.

(2) The second case is $L$=$r$. In this case, according to Equation (12), $SA$=0, which means no spherical aberration. From Equation (11), we know:

$$\frac{n'}{L'} = \frac{n'-n}{r} + \frac{n}{L}$$

Due to $L=r$, so:

$$\frac{n'}{L'}=\frac{n'-n}{r}+\frac{n}{r}=\frac{n'}{r}$$

then

$$L'=r$$

Which means the image point $A'$ coincides with object point $A$ at the centre of curvature of the spherical surface.

(3) The third case is $I'=U$. In this case, according to Equation (12), $SA=0$, which means no spherical aberration.

Due to:

$$\frac{r}{L-r}=\frac{\sin U}{\sin I}$$

and

$$n\sin I=n'\sin I'$$

There is:

$$\sin I'=\frac{n}{n'}\frac{L-r}{r}\sin U$$

here $I'=U$, then from above equation we know:

$$\frac{n}{n'}\frac{L-r}{r}=1$$

or

$$\frac{L-r}{r}=\frac{n'}{n}$$

then

$$L = r\frac{n'+n}{n}$$

This equation expresses the object distance in this case. Substitute it in Equation (11), we know:

$$\frac{n'}{L'} = \frac{n^2}{r(n'+n)} + \frac{n'-n}{r} = r\frac{n'^2}{n'+n}$$

then there is:

$$L' = r\frac{n'+n}{n'}$$

This is the image distance in this case.

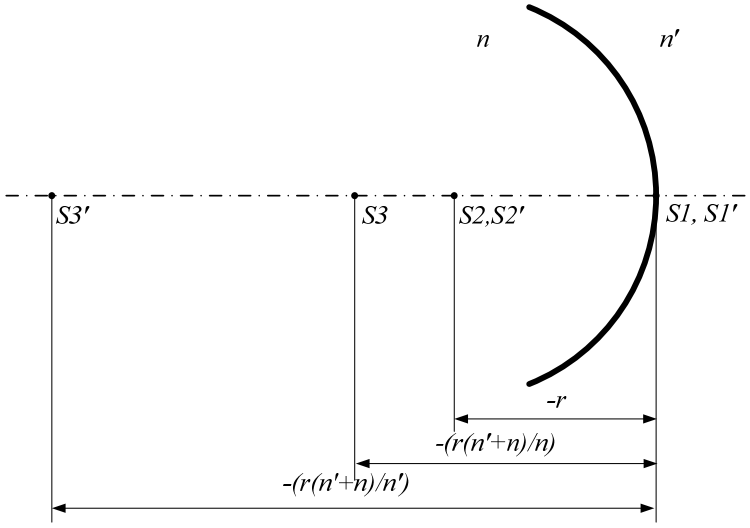


**Figure AI.3 Three conjugate pairs free from spherical aberration with a single refractive spherical surface**

In conclusion, for a single refractive spherical surface, there are three conjugate pairs that are free from spherical aberration (Figure AI.3):

(1) Object point lies on the vertex of the spherical surface (*S1*), and the conjugate image point lies on the vertex too (*S1′*).

(2) Object point lies on the centre of curvature of the spherical surface (*S2*), and the conjugate image point lies on the centre too (*S2′*).

(3) Object point lies on the concave side of the spherical surface at the distance of $r\frac{n'+n}{n}$ from the vertex of the surface (*S3*), and the conjugate image point lies on the same side at the distance of $r\frac{n'+n}{n'}$ from the vertex of the surface (*S3′*).

# Appendix II Data sheet of optical glass S-LAH79*

## S-LAH79

Code(d) **003283**
Code(e) **011281**

| | | | | | | | | |
|---|---|---|---|---|---|---|---|---|
| Refractive Index | $n_d$ | **2.00330** 2.003300 | Abbe Number | $\nu_d$ | **28.3** 28.27 | Dispersion | $n_F-n_C$ | **0.03549** 0.035486 |
| Refractive Index | $n_e$ | 2.011689 | Abbe Number | $\nu_e$ | 28.07 | Dispersion | $n_{F'}-n_{C'}$ | 0.036041 |

| Refractive Indices | | |
|---|---|---|
| λ(μm) | | |
| $n_{2325}$ | 2.32542 | 1.93904 |
| $n_{1970}$ | 1.97009 | 1.94642 |
| $n_{1530}$ | 1.52958 | 1.95518 |
| $n_{1129}$ | 1.12864 | 1.96486 |
| $n_t$ | 1.01398 | 1.96873 |
| $n_s$ | 0.85211 | 1.97630 |
| $n_{A'}$ | 0.76819 | 1.98195 |
| $n_r$ | 0.70652 | 1.98739 |
| $n_C$ | 0.65627 | 1.99301 |
| $n_{C'}$ | 0.64385 | 1.99461 |
| $n_{He-Ne}$ | 0.6328 | 1.99613 |
| $n_D$ | 0.58929 | 2.00299 |
| $n_d$ | 0.58756 | 2.00330 |
| $n_e$ | 0.54607 | 2.01169 |
| $n_F$ | 0.48613 | 2.02850 |
| $n_{F'}$ | 0.47999 | 2.03066 |
| $n_{He-Cd}$ | 0.44157 | 2.04682 |
| $n_g$ | 0.435835 | 2.04972 |
| $n_h$ | 0.404656 | 2.06844 |
| $n_i$ | 0.365015 | |

| Deviation of Relative Dispersions Δθfrom "Normal" | |
|---|---|
| $\Delta\theta_{C,t}$ | 0.0049 |
| $\Delta\theta_{C,A'}$ | 0.0015 |
| $\Delta\theta_{g,d}$ | 0.0020 |
| $\Delta\theta_{g,F}$ | 0.0023 |
| $\Delta\theta_{i,g}$ | |

| Constants of Dispersion Formula | |
|---|---|
| $A_1$ | 2.32557148E+00 |
| $A_2$ | 5.07967133E-01 |
| $A_3$ | 2.43087198E+00 |
| $B_1$ | 1.32895208E-02 |
| $B_2$ | 5.28335449E-02 |
| $B_3$ | 1.61122408E+02 |

| Other Properties | |
|---|---|
| Bubble Quality Group B | |
| Specific Gravity d | 5.23 |
| Remarks | |

| Partial Dispersions | |
|---|---|
| $n_C-n_t$ | 0.024281 |
| $n_C-n_{A'}$ | 0.011059 |
| $n_d-n_C$ | 0.010289 |
| $n_e-n_C$ | 0.018678 |
| $n_g-n_d$ | 0.046416 |
| $n_g-n_F$ | 0.021219 |
| $n_h-n_g$ | 0.018725 |
| $n_i-n_g$ | |
| $n_C-n_t$ | 0.025885 |
| $n_e-n_{C'}$ | 0.017074 |
| $n_F-n_e$ | 0.018967 |
| $n_i-n_{F'}$ | |

| Thermal Properties | | |
|---|---|---|
| Strain Point StP (℃) | | |
| Annealing Point AP (℃) | | |
| Transformation Temperature Tg (℃) | | 699 |
| Yield Point At (℃) | | 731 |
| Softening Point SP (℃) | | |
| Expansion Coefficients | (-30~+70℃) | 60 |
| α ($10^{-7}$/℃) | (+100~+300℃) | 71 |
| Thermal Conductivity k (W/m·K) | | 0.957 |

| Mechanical Properties | | |
|---|---|---|
| Young's Modulus E ($10^3$N/m$^2$) | 1255 | |
| Rigidity Modulus G ($10^3$N/m$^2$) | 484 | |
| Poisson's Ratio σ | 0.297 | |
| Knoop Hardness Hk[Class] | 700 | 7 |
| Abrasion Aa | 61 | |
| Photoelastic Constant β (nm/cm/$10^7$Pa) | | 1.89 |

| Chemical Properties | |
|---|---|
| Water Resistance(Powder) Group RW(P) | 1 |
| Acid Resistance(Powder) Group RA(P) | 1 |
| Weathering Resistance(Surface) Group W(S) | 2 |
| Acid Resistance(Surface) Group SR | 1.0 |
| Phosphate Resistance PR | 1.0 |

| Relative Partial Dispersions | |
|---|---|
| $\theta_{C,t}$ | 0.6842 |
| $\theta_{C,A'}$ | 0.3116 |
| $\theta_{d,C}$ | 0.2899 |
| $\theta_{e,C}$ | 0.5263 |
| $\theta_{g,d}$ | 1.3080 |
| $\theta_{g,F}$ | 0.5980 |
| $\theta_{h,g}$ | 0.5277 |
| $\theta_{i,g}$ | |
| $\theta'_{C',t}$ | 0.7182 |
| $\theta'_{e,C'}$ | 0.4737 |
| $\theta'_{F',e}$ | 0.5263 |
| $\theta'_{i,F}$ | |

| Coloring | | | |
|---|---|---|---|
| $\lambda_{80}$ | | $\lambda_5$ | 37 |
| $\lambda_{70}$ | 46 | | |

| Internal Transmittance | |
|---|---|
| λ(nm) | τ10mm |
| 280 | |
| 290 | |
| 300 | |
| 310 | |
| 320 | |
| 330 | |
| 340 | |
| 350 | |
| 360 | |
| 370 | 0.03 |
| 380 | 0.16 |
| 390 | 0.33 |
| 400 | 0.50 |
| 420 | 0.72 |
| 440 | 0.83 |
| 460 | 0.88 |
| 480 | 0.921 |
| 500 | 0.945 |
| 550 | 0.979 |
| 600 | 0.988 |
| 650 | 0.991 |
| 700 | 0.993 |
| 800 | 0.996 |
| 900 | 0.997 |
| 1000 | 0.997 |
| 1200 | 0.998 |
| 1400 | 0.998 |
| 1600 | 0.997 |
| 1800 | 0.994 |
| 2000 | 0.986 |
| 2200 | 0.966 |
| 2400 | 0.89 |

OHARA 02-06

| Temperature Coefficients of Refractive Index | | | | | | | |
|---|---|---|---|---|---|---|---|
| Range of Temperature (℃) | dn/dt relative ($10^{-6}$/℃) | | | | | | |
| | t | C' | He-Ne | D | e | F' | g |
| -40~20 | 6.5 | 8.0 | 8.1 | 8.6 | 9.2 | 10.7 | 12.4 |
| -20~ 0 | 6.7 | 8.2 | 8.3 | 8.9 | 9.5 | 11.1 | 12.9 |
| 0~20 | 6.9 | 8.5 | 8.6 | 9.2 | 9.8 | 11.5 | 13.4 |
| 20~40 | 7.0 | 8.7 | 8.9 | 9.4 | 10.1 | 11.9 | 13.8 |
| 40~60 | 7.2 | 9.0 | 9.1 | 9.7 | 10.4 | 12.2 | 14.3 |
| 60~80 | 7.4 | 9.2 | 9.4 | 10.0 | 10.7 | 12.6 | 14.8 |

* From Ohara's catalogue of optical glass data sheets.

# Appendix III Optical parameters of ASILs and ASIL-objectives

We are going to deduce some important optical parameters, including focal length, magnification, etc, of the ASIL and ASIL-objective based on rigorous geometric optics equations.

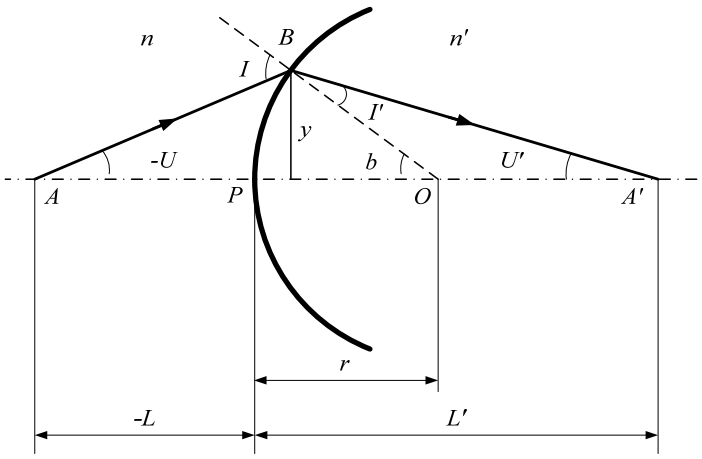


**Figure AIII.1 The signs and their conventions with a single refractive spherical surface**

(1) First, we will work out the focal length, or optical power, of an ASIL. For a single refractive surface (Figure AIII.1), the optical power is given by:

$$\phi = (n' - n)c \tag{1}$$

here, $c$ is the curvature of the refractive surface, $n'$ represents the refractive index to the right of the surface, and $n$ represents the refractive index to the left.

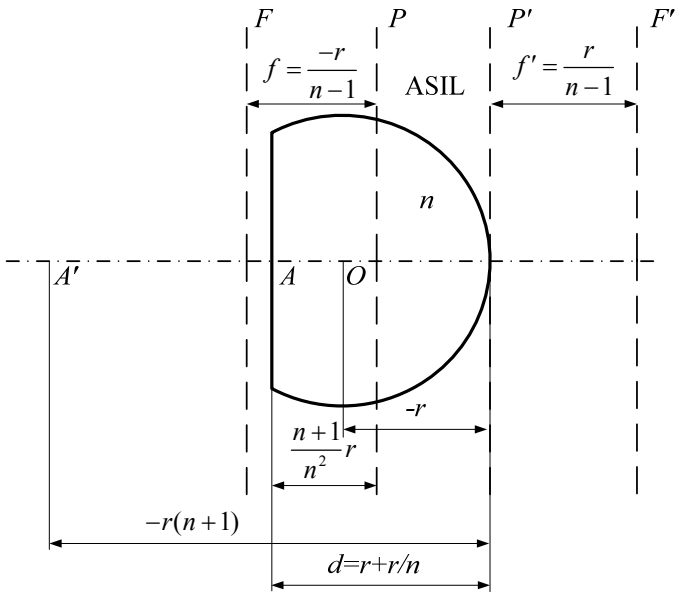


**Figure AIII.2 The locations of the front (*P*) and rear principal planes (*P*′), the front (*F*) and rear focal planes (*F*′), and the object (*A*) and its image (*A*′) of an ASIL**

For an ASIL (Figure AIII.2), the left-side surface, i.e. the flat surface, has the power of:

$$\phi_L = (n-1)c_L = (n-1)\cdot 0 = 0 \tag{2}$$

The right-side, i.e. the curved surface, has the power of:

$$\phi_R = (1-n)c_R = \frac{1-n}{-r} = \frac{n-1}{r} \tag{3}$$

The optical power of the whole ASIL can be calculated by the formula of the power of a thick lens:

$$\phi = \phi_L + \phi_R - \frac{d}{n}\phi_L\phi_R = 0 + \phi_R - \frac{d}{n}\cdot 0\cdot\phi_R = \phi_R = \frac{n-1}{r} \tag{4}$$

From this, we know the rear focal length is:

$$f' = \frac{r}{n-1} \tag{5}$$

and the front focal length is:

$$f = -f' = -\frac{r}{n-1} \tag{6}$$

(2) Next, we will explore the principal plane locations of the ASIL. The principal planes are crucial in defining the optical properties of the system, since the distances of the object and image from the front and rear principal planes determine the magnification of the system. It is also necessary to work out the locations of principal plane for the further derivation of the optical parameters of the ASIL-objective.

The principal plane locations of the ASIL can be calculated by the equation of the principal plane locations of a two-element system. Here, we use $\delta'$ to denote the separation between the rear principal plane and the vertex of the curved surface of the ASIL, and then the rear principal plane location can be determined as:

$$\delta' = -\frac{d}{n}\frac{\phi_L}{\phi} \tag{7}$$

Substitute (2) into (7):

$$\delta' = -\frac{d}{n}\frac{\phi_L}{\phi} = -\frac{d}{n}\frac{0}{\phi} = 0$$

From this result, we know the rear principle plane coincides with the vertex of the curved surface of the ASIL.

Similarly, we use $\delta$ denote the separation between the front principal plane and the flat surface of the ASIL, and then the front principal plane location is determined as:

$$\delta = \frac{d}{n}\frac{\phi_R}{\phi} \tag{8}$$

Due to

$$d = r + \frac{r}{n} \tag{9}$$

Substitute (3), (4) and (9) into (8):

$$\delta = \frac{d}{n}\frac{\phi_R}{\phi} = \frac{r + \frac{r}{n}}{n}\frac{\frac{n-1}{r}}{\frac{n-1}{r}} = \frac{n+1}{n^2}r \tag{10}$$

From this result, we know the front principle plane locates to the right of the flat surface of the ASIL in the distance of $\frac{n+1}{n^2}r$.

Here, according to the front and rear focal lengths we have derived previously, we realise the front focal plane locates to the left of the front principal plane in the distance of $\frac{r}{n-1}$, and the rear focal plane locates to the right of the rear principal plane in the distance of $\frac{r}{n-1}$. The locations of the front ($P$) and rear ($P'$) principal planes as well as the front ($F$) and rear ($F'$) focal planes of the ASIL are all shown in Figure AIII.2.

(3) Then, we will see what the magnification is when the object is situated at the aplanatic point of the ASIL.

From Gaussian equation:

$$\frac{1}{l'}-\frac{1}{l}=\frac{1}{f'} \tag{11}$$

here $l$ is the object distance, $l'$ is the image distance. Rearrange it and solve $l'$:

$$l'=\frac{lf'}{l+f'} \tag{12}$$

The object is at the aplanatic point in the object space, so we know:

$$l=-\frac{n+1}{n^2}r \tag{13}$$

Substitute (13) into (12):

$$l'=\frac{(-\frac{n+1}{n^2}r)f'}{(-\frac{n+1}{n^2}r)+f'}=-r(n+1) \tag{14}$$

From this result, we see the image locates to the left of the rear principal plane, which coincides with the vertex of the curved surface of the ASIL, in the distance of $r(n+1)$. Considering the conclusion in Appendix I, we know the aplanatic point in image space is situated to the left of the vertex of the curved surface of the ASIL in the distance of $r(n+1)$. Apparently, the image is exactly located at the aplanatic point in image space, which proves the object and its image are conjugated at the two aplanatic points of the ASIL. The object ($A$) and its image ($A$') location are also shown in FigureAIII.2.

Moreover, we can simply derive the magnification in this case:

$$m=\frac{l'}{l}=\frac{-r(n+1)}{-\frac{n+1}{n^2}r}=n^2 \tag{15}$$

(4) Furthermore, we will investigate the focal length, or optical power, of the ASIL-objective lens, i.e. the combination of the ASIL and the conventional objective lens.

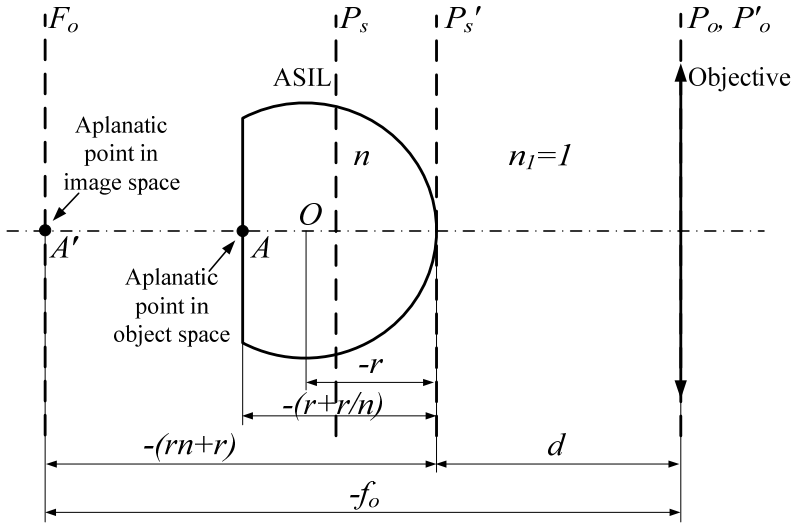


**Figure AIII.3 The configuration of the ASIL-objective and corresponding principal plane positions**

The ASIL-objective configuration is shown in Figure AIII.3. The objective lens is simplified as a thin lens, therefore its front principal plane ($P_o'$) and rear principal plane ($P_o'$) coincide with the lens centre. As described before, the ASIL works under the aplanatic conditions, the object is situated at the aplanatic point in the object space ($A$), and its conjugate image is situated at the aplanatic point in the image space ($A$'). For an infinite conjugate objective lens, this image needs to be placed at the front focal point of the objective lens. In conclusion, the ASIL-objective works in a two-step imaging procedure. The object at the aplanatic point in object space ($A$) first forms a virtual image at the aplanatic point in image space ($A'$), then this image works as the object of the conventional objective lens and forms a real image.

The distance between the rear principal plane ($P_s'$) of the ASIL and the front principal plane ($P_o'$) of the conventional objective lens is:

$$d = f_o' - (r + rn) \tag{16}$$

here $f_o'$ denotes the rear focal length of the conventional objective lens.

The ASIL-objective can be regarded as a two-element system. Its optical power can be calculated by the formula of a two-element system's power:

$$\phi = \phi_s + \phi_o - \frac{d}{n_1}\phi_s\phi_o \tag{17}$$

Here $\phi_s$ is the optical power of the ASIL, $\phi_o$ is the optical power of the conventional objective lens, $n_1$ is the refractive index of the medium between the ASIL and the conventional objective lens, which is 1 in this case (in air).

Substitute Equation (4), (16) into (17) and cancel out some same items, we know:

$$\phi = \frac{n-1}{r} + \frac{1}{f_o'} - \frac{f_o' - (r + rn)}{1}\frac{n-1}{r}\frac{1}{f_o'} = \frac{n^2}{f_o'} \tag{18}$$

The rear focal length and the front focal length are:

$$f' = \frac{1}{\phi} = \frac{f_o'}{n^2} \tag{19}$$

$$f = -f' = -\frac{1}{\phi} = -\frac{f_o'}{n^2} \tag{20}$$

(5) At last, we will see the magnification of the ASIL-objective. For a series of optical imaging elements, the magnification of the group is the product of each system. If the magnification of the conventional objective lens is $m_o$, and from Equation (15) we know the magnification of the ASIL $m_s$ is $n^2$, it is concluded that the magnification of the ASIL-objective is:

$$m = m_s \cdot m_o = n^2 m_o \tag{21}$$

which means the ASIL-objective is $n^2$ times the magnification of the conventional objective lens.

# Appendix IV SIF alignment

One significant difference in setting up a prototype system between SIF and a conventional epi-fluorescence microscope is that the alignment of the SIF is not based on the conventional objective lens, but the ASIL-objective. Comparing with the conventional objective lens, the combination of an ASIL and a conventional objective lens produces new principal planes, focal planes and focal length. Therefore, the positions of all the other optics are determined by the optical parameters of the ASIL-objective instead of the conventional objective lens.

In our research, the alignment of the SIF started from the alignment of the ASIL-objective, and then other optics were aligned with the ASIL-objective to form telecentric configurations. The key alignment procedures are explained as follows:

(1) The alignment of the ASIL-objective. The scheme to correctly align the ASIL-objective is shown in Figure AIV.1. A collimated beam (non-patterned red shading) generated by a laser diode is expanded to cover the full aperture of the BFP of ASIL-objective by the beam expander 1. When the distance between the ASIL and the conventional objective lens is adjusted to $f_o$-($r$+$rn$) as the Equation (16) shows in Appendix III, the incident beam is reflected by the flat surface of the ASIL and propagates back along the incident optical path. This reflection (patterned red shading) is separated by a beam splitter and half of it is reflected into the beam expander 2. The

output beam is an expanded collimated beam, and then parallel interference pattern can be observed in a shear plate.

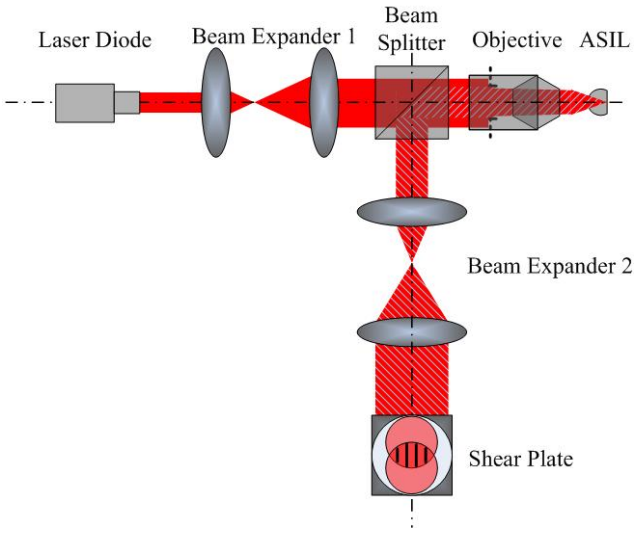


**Figure AIV.1 Schematic diagram of the ASIL-objective alignment scheme**
The non-patterned red shading represents the input collimated beam; the patterned red shading represents the reflected collimated beam by the ASIL. When the parallel pattern appears in the shear plate, the ASIL is in position.

A photo of our ASIL-objective alignment apparatus is shown in Figure AIV.2. The laser diode generated 2 mm diameter laser beam with 635nm wavelength. This beam was expanded to 10 mm diameter through lens 1 and 2. The back aperture of the conventional objective lens was 4.4 mm in diameter, so this expanded collimated beam could cover the full BFP sufficiently. When the ASIL was in position, the flat surface of it reflected this collimated input beam. And the reflected beam was expanded to 11 mm in diameter through lens 3 and 4. This expanded beam shined in the shear plate and formed parallel interference fringes as shown in the inset of Figure AIV.2.

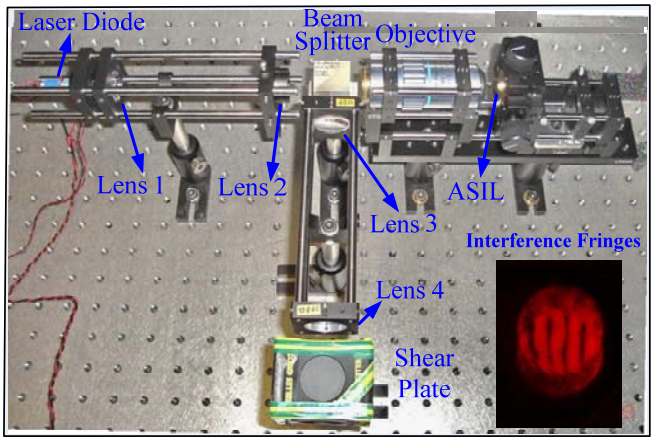


**Figure AIV.2 Photograph of the ASIL-objective alignment apparatus**
Parallel interference fringes appear on the screen of the shear plate when ASIL is in position as shown in the inset.

(2) The alignment of laser. The laser is set as the reference as it defines the optical axis of the system. By moving a mounted small aperture along the laser beam path and adjusting the laser beam to pass the aperture anywhere, a laser beam parallel to the bench can be achieved.

(3) The alignment of other lenses. All the lenses are settled as telecentric system. In a telecentric system, the entrance pupil and the exit pupil are located at infinity. The telecentric system can reduce the measurement or position error caused by a slight defocusing of the system. In the alignment, it is fulfilled by adjusting the separation of each two adjacent lenses as the sum of their focal lengths. When shining an expanded collimated laser beam in one lens from the front, a collimated beam, which can be examined by a shear plate, will emerge after the other lens when the separation is right.